An Investigation of Some Mechanical and Optical Properties of Materials for Test Masses in Laser Interferometric Gravitational Wave Detectors

by

Jennifer Elizabeth Logan

Department of Physics and Astronomy
University of Glasgow.

Presented as a thesis for the degree of
Ph.D. in the University of Glasgow.
March 1993.

Contents

List of Figures

Tables

Acknowledgements

I would like first and foremost to thank my supervisor, Norna Robertson, for all her help, advice and encouragement whilst carrying out the research for and the writing of this thesis. I would equally like to thank Jim Hough for all the help and encouragement he has given me throughout my time as a research student in his group. Thanks also go to Peter Veitch for his interest in and useful discussions about my work. I am grateful for the support of all the other members of the gravitational waves group, namely Gavin Newton, Harry Ward, Anne Campbell, Brian Meers, David Robertson, Caroline Cantley, Kenneth Strain, Euan Morrison, Sheila Rowan, Kenneth Skeldon and Alison McLaren. I would also like to thank the group technicians, Jim Pittilo, Angus McKellar, Allan Latta and David Edwards as well as Tom Neil and the workshop staff for all their assistance.

My thanks go to the Science and Engineering Research Council who made the Ometron Vibration Pattern Imager available through their Engineering Loan Pool. I am grateful to Dr. John Brandon of the University of Wales College of Cardiff, for making available laboratory facilities and technical support, and for assistance in the operation of the V.P.I.. I am also grateful to Professor Bernard Schutz, also of the University of Wales College of Cardiff, for useful discussions about this work.

Thanks go to the Physics department of Strathclyde University for the loan of the Soleil compensator.

I am grateful for the support given to me by Professor R.P. Ferrier during my time as a research student in his department.

I would like to thank the S.E.R.C. for financial support throughout the period of this work.

Finally I would like to say a big thank you to my family, especially my mum and dad, for all their encouragement and support throughout my time at university.

Preface

Chapter 1 of this thesis contains a brief introduction to the nature of gravitational waves. The two main prototype detection systems currently being developed are reviewed, with emphasis on laser interferometric detectors. The relevant noise sources which limit the sensitivity of such detectors are discussed and in particular the importance of thermal noise from the test masses is stressed. The material presented in this chapter is mainly derived from the literature.

Chapter 2 contains a derivation by the author of an expression for the thermal motion of a test mass. It is noted that the equation is a factor of two greater than had been assumed up until now. A method of measuring the quality factor, Q, of materials using laser interferometry is described. The idea for this was originally suggested by Professor Jim Hough and the technique was developed by the author.

In chapter 3 the effect of coupling between the normal modes of test masses is discussed. The Q measurements presented in this chapter were made by the author and the vibration pattern images of the coupled modes were produced with the help Dr Norna A. Robertson and Professor Jim Hough. The electrical model of the coupled system was developed by the author at the suggestion of Professor Jim Hough and with advice from Dr Norna A. Robertson, Professor Jim Hough and Dr Peter J. Veitch.

The investigation of the effect of suspension wire resonances on the measured Q of a test mass, presented in chapter 4, was carried out at the instigation of the author. The electrical modelling of the system was at the suggestion of Professor Jim Hough with advice from both him and Dr. Norna A. Robertson.

Chapter 5 contains a brief review of anelastic materials. The information in this section was derived from the literature. The measurements and analysis of Q as a function of frequency for aluminium and fused silica were carried out by the author with help from Dr. Norna A. Robertson and Professor Jim Hough.

In chapter 6 measurements of stress induced birefringence in fused silica are presented. An experimental method using balanced photodiodes to measure this effect is described. This technique was suggested by Professor Jim Hough and was developed by the author with the help of Dr. Norna A. Robertson. The final birefringence results presented in this chapter were made by the author using a Soleil Compensator. These results were analysed with advice from Dr. Norna A. Robertson and Professor Jim Hough.

Chapter 7 is a summary of the results from the previous chapters and draws the main conclusions of this thesis together.

Summary

Gravitational waves are one of the predictions of Einstein's General Theory of Relativity (Einstein, 1916). They are produced when mass accelerates asymmetrically resulting in quadrupole, or higher order, gravitational radiation and the production of a strain in space. This is in principle detectable by measuring the change in distance, ΔL, between two free test masses a distance L apart. Despite considerable experimental effort which has gone into developing suitable detectors, gravitational waves remain as yet undetected. This is due to their weakness of interaction with matter. Gravitational waves which are emitted from a violent astrophysical event, such as a supernova, are predicted to produce a strain at the earth of at most ~ 10^{-21} in the frequency range accessible to terrestrial detectors (greater than approximately 100 Hz), assuming that a reasonable event rate is required. The most promising type of detector currently under development uses laser interferometry to monitor the displacement of freely suspended test masses - a technique which exploits the quadrupole nature of gravitational waves. Construction of large-scale detectors of this type will soon commence in several places around the world. These should have the required sensitivity to detect gravitational waves from astrophysical sources leading to the opening of a new field of astronomy.

The ultimate sensitivity of such detectors will be limited by various noise sources. Above about 100 Hz, thermal motion of the test masses is predicted to make the dominant contribution to the detector noise level when searches for continuous sources of gravitational waves are made. The investigation of such thermal motion forms a substantial part of this thesis. To minimise thermal noise, it is important that the test masses are fabricated from a material which has low internal losses, i.e. a high quality factor Q. The dimensions of each test mass should also be such that its lowest resonant frequency is well above the frequency range of interest for the detection of gravitational waves (approximately 100 Hz to a few kilohertz). As it is important to investigate the Q values of possible materials of interest, an experimental method using laser interferometry to measure the Q of samples of material suspended as pendulums, was developed.

The effect of coupling between normal modes in samples of materials was studied and it was noted that the Q values of the coupled system were degraded by the more lossy pure mode. The structure of the coupled modes was studied with the aid of a vibration pattern imager. Information gained from this was then used in order to develop an electrical model of the coupling, in order that its effect on thermal motion of a test mass, in the frequency band of interest for the detection of gravitational waves, could be assessed. It was found that depending on the exact nature of the coupling, thermal motion of the mass, at frequencies well below its lowest resonance, could be increased above that for the uncoupled system. Thus as a general guideline, it is wise to choose the dimensions of a test mass such that its resonant frequencies do not lie close together.

Columnar silicon, a particular type of polycrystalline silicon, has been found by the author to have a suitably high Q for it to be considered as a possible material from which to form the test masses for a long base-line interferometric gravitational wave detector. It was found however that the measured Q of the fundamental longitudinal mode of a sample of this material varied, apparently randomly, when the mass was re-suspended. After some experimental investigation it was found that variation in measured Q was due to resonances in the suspension wires. An electrical model of the system was developed and this allowed an evaluation to be made of the effect of wire resonances on the thermal motion of the test mass, at frequencies much lower than the lowest resonant frequency of the mass. It was found that if the mass was suspended such that its measured Q was low due to resonances in the suspension wires, thermal motion of the mass, at frequencies of interest for the detection of gravitational waves, was not increased. This model was then used as a basis from which to construct a second equivalent circuit which was used to predict the thermal motion of the pendulum which is formed by a test mass on its suspension wires. The two models were then used in conjunction to predict the sensitivity of a long baseline detector limited only by thermal motion of the pendulums and of the test masses.

It has been assumed in all the proposals worldwide for large scale interferometric gravitational wave detectors, that the Q of a material is inversely proportional to frequency. This implies that the spectral density of the thermal motion of the test mass is frequency independent below the lowest resonance of the mass. However there is evidence that the Q of many materials may in fact be independent of frequency, leading to

the thermal motion spectral density being inversely proportional to the square root of frequency, below the lowest resonance of the mass. This would have serious implications for the sensitivity of long baseline detectors. It is thus clear that, in order to predict the thermal noise limited sensitivity of a gravitational wave detector, a knowledge of Q as a function of frequency for possible materials is required. Experimental investigation by the author indicates that the Q values of both aluminum and fused silica are constant over large frequency bandwidths. If this behaviour is found to continue to low frequencies this will be of serious concern.

It is not only the mechanical properties of the test masses which are important. Optical homogeneity of the beamsplitter and of the test masses themselves, depending on the particular optical scheme being employed in the interferometer, is also essential. One of the limiting factors to optical homogeneity is due to birefringence. Two experimental methods of measuring stress induced birefringence are described. Measurements of birefringence due to the stress induced in a fused silica mass by its supports, are given and the implications of these measurements for a long baseline interferometer are discussed. It is found that stress birefringence could be a limiting factor to the sensitivity of interferometric gravitational wave detectors.

A number of points important to the ultimate sensitivity of long baseline laser interferometric gravitational wave detectors are addressed in this thesis. This work has helped to increase knowledge about the thermal motion of suspended test masses and of the magnitude of stress induced birefringence in such masses. It has also served to highlight the need for further investigation of the properties of possible test mass materials.

Chapter 1

The Nature, Sources and Detection of Gravitational Waves

1.1 Introduction

Gravitational waves are a prediction of Einstein's General Theory of Relativity (Einstein, 1916) or indeed of any relativity theory in which gravitational effects propagate with finite velocity. As yet there has only been indirect experimental evidence for the existence of gravitational waves. This comes from observations of the orbital period of the binary pulsar PSR 1913 + 16 (Taylor and Weisberg, 1982). It has been found that this period is becoming progressively shorter and it is believed that this is consistent with the two stars losing energy via the emission of gravitational radiation[1] and spiralling in towards each other.

Direct detection of gravitational waves remains one of the most challenging problems in experimental physics today. Currently there are several groups around the world working towards this aim. Success in this field will allow some of the predictions of General Relativity to be tested and will lead to the opening of a new window on the universe.

In this chapter the nature of gravitational waves as predicted by Einstein's theory, possible sources for its production, and means of detection will be discussed. A more comprehensive review of this material is given by e.g. Thorne (Thorne, 1987) and Blair (Blair, 1991).

[1] The terms gravitational waves and gravitational radiation are used interchangeably

1.2 The Nature of Gravitational Waves

Gravity is one of the four fundamental forces of nature. It is the weakest of the forces (e.g. the electromagnetic force between two stationary protons is 10^{36} times greater than the gravitational force between them). However since gravity is always attractive, the effects accumulate and so it is this force which dominates on large scales. Newton's law of gravity, like Coulomb's law for electrostatic forces, does not, however, describe the propagation of field effects. A generalisation of Coulomb's law is given in Maxwell's equations. In the case of gravity, the generalisation is given by Einstein's field equations of General Relativity. In these the local curvature of spacetime is identified with the local densities of energy, mass and momentum. One of the solutions to these equations describes plane waves propagating in a vacuum at the speed of light. These are gravitational waves which may be described as ripples in the curvature of spacetime.

By analogy with electromagnetism where waves are produced by the acceleration of charge, so gravitational waves are produced by the acceleration of mass. However unlike charge, mass only occurs in one sign and since linear and angular momentum must be conserved, the acceleration which the mass undergoes must be asymmetric in order to produce any net flux of gravitational waves. The resulting radiation is quadrupole, or higher order, in nature. As will be indicated in the next section, the production of detectable levels of gravitational radiation requires very large masses undergoing very high accelerations. This can occur in astrophysical systems. Waves from such a source will, to a very high accuracy, be plane when they impinge on the earth. They will also be very weak and thus, to a good approximation, a linearised version of Einstein's equations suffices to describe the properties of the waves.

Consider the effect of a plane gravitational wave on a test mass a proper distance x^k away from an observer. An earth-based detector is in a situation of low background curvature. In this case, to a good approximation, the Riemann curvature tensor, $R_{\alpha\beta\gamma\delta}$, which describes the curvature of spacetime, may be considered to be composed of two components: one due to the background curvature $R^B_{\alpha\beta\gamma\delta}$, and the other due to small perturbations caused by gravitational waves. The background curvature is the average of $R_{\alpha\beta\gamma\delta}$ over several wavelengths. The curvature due to the waves is then given by

$$R^{GW}_{\alpha\beta\gamma\delta} \equiv R_{\alpha\beta\gamma\delta} - R^{B}_{\alpha\beta\gamma\delta} \tag{1.1}$$

Consider a freely falling observer at the origin of a Cartesian coordinate frame in a region of spacetime where gravitational waves provide the only source of spacetime curvature. A test mass positioned at a distance x^k away will suffer small oscillations relative to her position. The change in the position of the test mass is given by

$$\delta\ddot{x}^j = - R^{GW}_{j0k0}\, x^k \tag{1.2}$$

where the dot notation represents differentiation with respect to time.

Since the interaction is a tidal effect, it is more conventional to describe gravitational radiation by a dimensionless strain amplitude, h_{jk}. This is defined by

$$\delta\ddot{x}^j = \frac{1}{2}\ddot{h}_{jk}x^k \tag{1.3}$$

From General Relativity it is predicted that the amplitude of the wave $h << 1$. Thus the oscillatory changes δx^j are very much smaller than the distance of the particle from the observer. x^k can therefore be regarded as essentially constant and eq. (1.3) may be integrated to give

$$\delta x^j = \frac{1}{2} h_{jk}x^k \tag{1.4}$$

Thus h_{jk} is proportional to a strain in space the exact nature of which is governed by General Relativity and the properties of the Riemann curvature tensor. These imply that gravitational waves are transverse with two independent polarisations known as h_+, the 'plus' polarisation and h_x, the 'cross' polarisation. The 'plus' polarisation is defined by

$$\delta\ddot{x} = \frac{1}{2}\ddot{h}_+ x \quad \text{and} \quad \delta\ddot{y} = \frac{1}{2}\ddot{h}_+ y \tag{1.5a}$$

and the 'cross' polarisation by

$$\delta\ddot{x} = \frac{1}{2}\ddot{h}_x y \quad \text{and} \quad \delta\ddot{y} = \frac{1}{2}\ddot{h}_x x \tag{1.5b}$$

In order to visualise the effect of gravitational radiation consider a 'plus' polarised wave normally incident on a ring of test particles as shown in figure 1.1. An observer located at the centre of the ring would observe the proper distances of the test particles to vary with time such that the ring oscillates between a circle and an ellipse, which alternates between the orientations as indicated in figure 1.1. The 'cross' polarisation has the same effect but the pattern is rotated round by 45°.

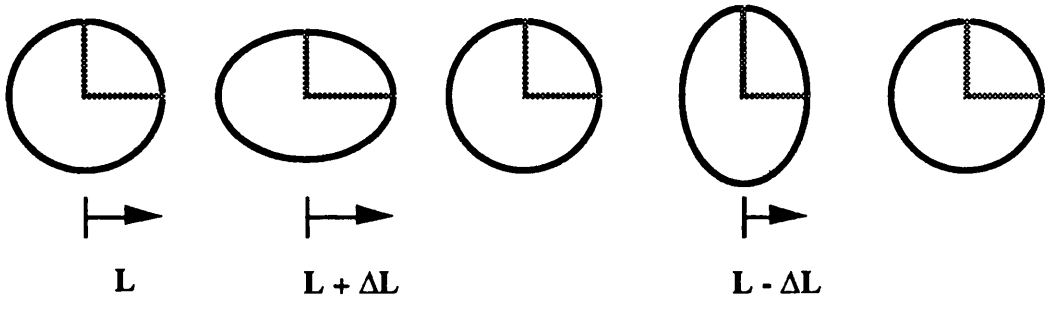

Figure 1.1: ***The Effect of a Gravitational Wave on a Ring of Test Particles.*** *The amplitude of the wave* $h = 2\Delta L/L$ *where* $L << \lambda_{GW}$, *the wavelength of the gravitational wave.*

The energy flux of a wave of frequency f and amplitude h is given by (Schutz, 1989a)

$$\mathcal{F}_{GW} \approx \frac{c^3}{16\pi G}|\dot{h}|^2 \approx \frac{\pi c^3}{4G} f^2 h^2 \qquad (1.6)$$

where c is the speed of light,

G is the gravitational constant.

Using values which might be expected from possible sources discussed later, eq. (1.6) may be expressed as

$$\mathcal{F}_{GW} \approx 3.2 \times 10^{-3} \left[\frac{f}{1\ \text{kHz}}\right]^2 \left[\frac{h}{10^{-22}}\right]^2 \text{W m}^{-2} \qquad (1.7)$$

Thus a gravitational wave of amplitude 10^{-22} and frequency 1 kHz is approximately 10^5 brighter than the brightest star in the night sky. Hence gravitational waves carry enormous amounts of energy.

At present nearly all the information about our universe and the events in it, is gathered from electromagnetic waves i.e. from photons which come from individual atoms. By contrast gravitational waves are emitted from and carry information about the bulk movement of matter. This radiation is very penetrating and passes through everything virtually unattenuated and thus the waves carry unique information about astrophysical sources. Note however that this very property i.e. the weakness of interaction, makes gravitational waves very difficult to detect.

In the following section a brief review of some possible sources of gravitational waves will be given.

1.3 Sources of Gravitational Waves

In the previous section it was noted that the production of gravitational waves requires the asymmetric acceleration of mass. This raises the question, is it possible to create detectable amounts of gravitational radiation in the laboratory? Consider a high tensile steel bar of mass 500 tonnes, 20 m long by 1 m in radius, which is rotated about its middle. If the frequency of rotation is such that the internal stresses are close to the breaking stress of steel, the resulting gravitational wave luminosity would be ~ 10^{-30} W (Misner et al, 1973). Since a detector will only absorb a tiny fraction of this power, the detection of laboratory produced gravitational waves seems rather unrealistic. It is more natural instead to look to astrophysical sources with high masses and accelerations. Some such possible sources are detailed below. These are divided into three categories: burst, periodic, also known as continuous, and stochastic. For a more comprehensive review of sources see e.g. Thorne (Thorne, 1987) and Schutz (Schutz, 1989b)

1.3.1 Burst Sources

The form of the gravitational waves which are emitted from such sources are typically a few cycles of a characteristic frequency or frequencies. Two possible types of source are outlined below.

Supernovae

The first gravitational wave detectors were optimised to look for signals from these sources. There are two categories of supernovae. A type I supernova is thought to occur when a white dwarf, which is accreting material from a companion star, undergoes a nuclear explosion in which the core may or may not collapse to form a neutron star. By contrast a type II supernova occurs when the radiation pressure from nuclear reactions in a massive, highly evolved star is no longer great enough to prevent gravitational collapse of the core.

The strength of the gravitational radiation which is emitted by such an event depends on the degree of asymmetry and on the speed of the collapse. A perfectly spherical collapse would yield no gravitational waves. If however the core is rotating, centrifugal forces will lead to an axisymmetric collapse. If the angular momentum of the core is large enough, nonaxisymmetric instabilities may set in, leading to possible bifurcation of the core (Schutz, 1989a). Note that in type I supernovae, the white dwarf may have high angular momentum due to accretion and thus if a neutron star is formed, there may be strong emission of gravitational waves.

The magnitudes of both the degree of asymmetry and the speed of collapse are difficult to quantify but an estimate of the gravitational wave amplitude impinging on the earth from such an event is given by (Hough et al, 1987)

$$h = 5 \times 10^{-22} \left[\frac{E}{10^{-3} M_{\odot} c^2}\right]^{1/2} \left[\frac{15\ \text{MPc}}{r}\right] \left[\frac{1\ \text{kHz}}{f}\right] \left[\frac{1\ \text{ms}}{\tau}\right]^{1/2} \qquad (1.8)$$

where E is the energy emitted in the form of gravitational waves in a time τ,

$M_{\odot}$ is a solar mass,

r is the distance to the source (15 MPc is the distance to the Virgo cluster of galaxies) and

f is the frequency of the emitted waves.

Note that estimates of E, f and τ vary according to the the type of collapse which is envisaged.

In a typical spiral galaxy there is predicted to be approximately one supernova of each type every 40 years. This would imply that out to the distance of the Virgo cluster there should be several of each type per year. Note that the event rate might in fact be much higher than this since some supernovae may be optically quiet, e.g. a white dwarf may accrete enough mass until it exceeds the Chandrasekhar limit (1.4 $M_\odot$) and collapse to form a neutron star without exploding.

Coalescing Binaries

Since a large fraction of all stars begin as members of a binary system, it is probable that a significant fraction remain as binaries after the individual stars have completed their evolutionary cycle and become compact objects. Small numbers of these will have been brought so close together during the evolution of the binary that, due to the energy loss from the system by the emission of gravitational waves, the orbital period decays leading to coalescence of the two stars. Note that systems containing white dwarves are not of interest for terrestrial detectors since coalescence occurs before the emitted gravitational radiation reaches an observable frequency.

A binary emits gravitational waves at twice the orbital frequency of the system. In the few seconds prior to collision, the signal from the system will take the form of a chirp as both the frequency and amplitude of the emitted wave sweep towards a maximum. The predictability of this waveform will allow matched filters to be used to search the output of a broadband detector for these signals. This allows the detection threshold to be reduced for a given detector noise level.

For two neutron stars the frequency of the signal will change from ~ 100 Hz to ~ 1 kHz in about 3 seconds. These systems may be modelled using General Relativity. It is found that for a binary at a distance r = 100 MPc with a total mass $m_T M_\odot$ and reduced mass $\mu M_\odot$ emitting gravitational waves at a instantaneous frequency of f = 100 Hz, the r.m.s. amplitude of the waves is given by

$$h_{rms} = 1 \times 10^{-23} \left[\frac{m_T}{M_\odot}\right]^{2/3} \left[\frac{\mu}{M_\odot}\right] \left[\frac{f}{100\ \text{Hz}}\right]^{2/3} \left[\frac{100\ \text{MPc}}{r}\right] \qquad (1.9)$$

and the frequency of the waves will change on a timescale

$$\tau = \frac{f}{\dot{f}} = 7.8 \left[\frac{M_\odot}{m_T}\right]^{2/3} \left[\frac{M_\odot}{\mu}\right] \left[\frac{100\ Hz}{f}\right]^{8/3} \text{ seconds} \qquad (1.10)$$

Schutz (Schutz, 1986) has pointed out that the product of h_{rms} and τ is independent of the total and reduced masses. With a worldwide network of at least three detectors measurements of h_{rms}, τ and f may be made and from this information a value of the distance to the source, r, may be found i.e. coalescing binaries act as standard distance indicators. Note that the direction to the source may be determined by analysing the differences in arrival times of the waves at the detectors. If an optical signal is also observed then the exact source is known and by measuring the red shift of this source, a value for Hubble's constant may be found directly. Even if there is no observed optical flash, a statistical value of Hubble's constant may still be found. A worldwide network of four detectors with a strain sensitivity of 10^{-22} over millisecond timescales should be able to determine the position of the source to within approximately 25 square degrees. By calculating the red shift of each galaxy cluster within this error box (there is approximately 1 galaxy per square degree out to 100 MPc) a statistical value for Hubble's constant may be found (Schutz, 1986).

At present there are three precursors of such systems: PSR 1913 + 16 (Taylor and Weisberg, 1982), PSR 2127 + 11C (Anderson et al 1990) and PSR 1534 + 12 (Wolszczan, 1991) all of which will coalesce on a timescale less than the age of the universe. There are approximately 450 known pulsars in our galaxy and if a steady state is assumed (i.e. pulsar birth rate equals the stellar death rate so that there is new pulsar approximately every 40 years) and given further that the density of galaxies is $\sim 0.02\ MPc^{-3}$ a crude estimation of the birthrate of coalescing binaries is given by

$$\frac{3}{450} \times \frac{1}{40} \times 0.02\ MPc^{-3} \times \frac{4\pi(100\ MPc)^3}{3} \times \frac{1}{2} \approx 7 \text{ per year out to } 100\ MPc \qquad (1.11)$$

with the error on this number being -5 or +11.

The factor of 1/2 is included since this represents the fraction of non-elliptical galaxies in the universe. Coalescing compact binaries are formed from massive, highly evolved stars which have exploded in type II supernovae. Such events do not occur in elliptical galaxies.

The Implication of γ-ray Bursts

There has recently been much interest in the source of production for γ-ray bursts which have been observed in satellite experiments, in particular by the Burst and Transient Source Experiment (BATSE) currently being undertaken on the Compton Gamma-ray Observatory. The number of bursts observed suggests a full-sky rate of about 800 bursts per year. Results from this show that sources of γ-ray bursts are distributed isotropically, rather than clustering in the galactic plane, but are radially non-uniform. There is also a good indication that some sources are at cosmological rather than intergalactic distances (Meegan et al, 1992). The form of the bursts indicates that they originate from neutron stars, however it is likely that no one type of source will explain all the observations. The coalescence of neutron star - neutron star or neutron star - black hole binaries has been suggested as one possible mechanism (Mochkovitch et al, 1993). If this is the case, this would suggest an event rate for coalescing binaries of possibly 1 or 2 per day out to cosmological distances.

1.3.2 Periodic Sources

Periodic gravitational wave signals are emitted from stably rotating systems. The emitted gravitational radiation is characterised by a signal at one or more discrete frequencies. If the signal from such a source is observed for a time τ, the achievable sensitivity of the detector increases by $\sqrt{\tau}$.

For gravitational waves produced by binary systems to be detectable at the earth, the orbital time would have to be less than ~ 10^{-1} s. Binaries with such an orbit time would be close to coalescing and would therefore not be continuous sources of gravitational waves. Rotating neutron stars will emit gravitational waves if the star in question is either non-symmetric or axisymmetric but rotating around an axis that is not a symmetry axis. These are the most likely sources of periodic gravitational radiation and will be considered in more detail below.

Spindown of Neutron Stars

If a gravitational collapse results in the formation of a neutron star, the star may initially have a very high angular momentum. If its period of rotation is less than approximately 1 ms, a gravitational radiation instability will set in and create strong hydrodynamic waves in the surface layers and mantle of the star. These waves propagate in the opposite direction to the star's rotation (Schutz, 1989b). This leads to radiation of gravitational waves until the star loses enough angular momentum for its rotation period to decrease and the star's condition to stabilise.

Elliptical Neutron Stars

The crust of neutron star may have lumps in it due to starquakes (Pandharipande et al, 1976). If the neutron star is a pulsar, the crust may also be deformed due to the presence of a magnetic field which is misaligned with the rotation axis (Zimmermann, 1978). Thus a neutron star may have some ellipticity, δ. For a neutron star of mass 1.4 $M_\odot$ and radius 10 km, which is emitting gravitational waves at a frequency f (equal to twice the spin frequency), it is estimated that the amplitude of the waves at the earth will be (Schutz, 1989a)

$$h \sim 6 \times 10^{-22}\, \delta \left[\frac{f}{100\ \text{Hz}}\right]^2 \left[\frac{10\ \text{kPc}}{r}\right] \qquad (1.12)$$

where r is the distance of the source from the earth and δ is probably $\leq 10^{-3}$.

Wagoner Stars

If a rotating neutron star in a binary system is accreting from its companion, it may be spun up until it reaches the gravitational wave instability point. Further accretion will drive the instability until a steady state is reached in which angular momentum lost by the radiation of gravitational waves, equals the accreted angular momentum. Since accretion is involved, the system should also be an X-ray source. Since both the X-ray luminosity and the intensity of gravitational radiation are proportional to the accretion rate this implies that the gravitational wave luminosity is proportional to the X-ray luminosity. Such a source of X-ray flux F_x emitting gravitational waves at a frequency f, will produce a

gravitational wave amplitude at the earth given by (Wagoner, 1984)

$$h \sim 2 \times 10^{-27} \left[\frac{300\ \text{Hz}}{f}\right] \left[\frac{F_X}{10^{-11}\ \text{W m}^{-2}}\right]^{1/2} \qquad (1.13)$$

1.3.3 Stochastic Sources

It is expected that there will be a background of gravitational waves due to a superposition of signals from many sources separated in time and space. Two possible sources which may contribute to this are noted below. For example, the vibration of cosmic strings formed in closed loops would generate gravitational waves over a wide range of frequencies as loops of different sizes decayed (Vachaspati and Vilenkin, 1985). Observation of this radiation may yield information about the formation of galaxies since it is postulated that cosmic strings may act as the seeds for galaxy formation. Another possibility is primordial gravitational waves. These are remnants of activity in the early universe (Allen, 1988).

To look for signals from stochastic sources requires correlation between at least two detectors. These should be separated by less than half a wavelength of the detected gravitational radiation, if coherence in their responses to random waves is to be maintained.

1.4 The Detection of Gravitational Waves

A direct detection of gravitational waves requires a measurement to be made of the strain in space induced by the wave. Currently there are various groups around the world working towards this end with two distinct laboratory based methods being pursued: resonant bar detectors and laser interferometric detectors. These will be outlined below.

1.4.1 Resonant Bar Detectors

Resonant bar detectors were originally proposed and developed by Weber (Weber, 1960). This detection technique is now being extended by groups in America, Europe, Asia and Australia.

A resonant bar gravitational wave detector is generally formed from a massive (~ few tonnes) right circular cylinder of material (usually aluminium). The passage of a suitably oriented gravitational wave through the detector will excite the mechanical modes of the bar giving rise to a potentially detectable motion of its ends. This motion is sensed by some form of transducer, generally either parametric or resonant in nature, which converts the signal into an electrical voltage which may then be amplified. The bar is designed so that its fundamental longitudinal mode is resonant at about 1 kHz, a reasonable frequency to expect gravitational waves.

The sensitivity of the detector is limited by noise in the sensors and by the thermal noise of the bar itself. Note that the effects of seismic and acoustic noise are minimised by suspending the bar in vacuum. Thermal noise may be minimised by the use of a high mass bar fabricated from material which has low internal damping (i.e. a high quality factor) and is operated at cryogenic temperatures (a few Kelvin or less). To detect a gravitational wave requires a measurement to be made of the very small displacements of the ends of the bar induced by the wave. This has to be carried out against the slowly changing background of thermal motion of the bar. In order to pick out a pulse against this background, it is desirable to have a short measurement time of approximately the duration of a gravitational wave wave pulse. However a short measurement time implies a large measurement bandwidth and this introduces more electronic noise from the sensor. Thus there is an optimum measurement bandwidth which is typically ~ 1/100 of the resonant frequency of the bar. This leads to resonant bar detectors being rather narrowband. To have greater frequency coverage, an array of such detectors resonant at different frequencies could be used. The current gravitational wave amplitude sensitivity of the resonant bar detector at CERN (the University of Rome) is 7×10^{-19} for millisecond pulses (Astone et al, 1993).

A more fundamental limit to the sensitivity of bar detectors is, however, set by the Heisenberg Uncertainty Principle. The displacement of the end of the bar may be expressed in terms of its quadrature components as

$$x(t) = X_1 \cos \omega_o t + X_2 \sin \omega_o t \qquad (1.14)$$

where the complex amplitude of the bar, $X = X_1 + i\,X_2$.

The position of the end of the bar changes in response to the passage of a gravitational wave. The momentum of the bar may be expressed as

$$p(t) = m\omega_o(-X_1 \sin \omega_o t + X_2 \cos \omega_o t) \tag{1.15}$$

Thus a new coordinate system may be defined from eqs. (1.14) and (1.15) as

$$X_1 = x(t)\cos \omega_o t - \frac{p(t)}{m\omega_o} \sin \omega_o t \tag{1.16a}$$

$$X_2 = x(t)\sin \omega_o t + \frac{p(t)}{m\omega_o} \cos \omega_o t \tag{1.16b}$$

It may be shown that the Heisenberg Uncertainty relation gives

$$\Delta X_1 \, \Delta X_2 \geq \frac{h}{2m\omega_o} \tag{1.17}$$

where ΔX_1 and ΔX_2 are the uncertainties in X_1 and X_2 respectively and h is the reduced value of Planck's constant. Thus the minimum uncertainty in the complex amplitude of the bar and so also in the displacement of the end of the bar, is

$$|\Delta x| = |\Delta X| = \left[(\Delta X_1)^2 + (\Delta X_2)^2\right]^{1/2} = \sqrt{\frac{h}{m\omega_o}} \tag{1.18}$$

where $\Delta X_1 = \Delta X_2$. This limits the strain sensitivity of bar detectors to $\sim 10^{-20}$ (Thorne et al, 1979).

It may, however, be possible to achieve greater sensitivity by the use of back-action evasion techniques (Thorne et al, 1979, Caves, 1982). To understand the principle of this idea consider again eq. (1.17). Instead of carrying out a symmetric measurement with $\Delta X_1 = \Delta X_2$, one could instead measure X_1, say, with arbitrarily high accuracy, which by back-action produces a large uncertainty in X_2. Note that X_1 is independent of the motion of the bar and thus if it is accurately measured once, it remains precisely known (unlike the position of the bar, x(t)). Two detectors may be used, one which

measures X_1 and one which measures X_2 to high accuracy. Thus in principle the quantum limit may be circumvented. Considerable experimental development remains to be carried out before such techniques can be implemented.

1.4.2 Laser Interferometric Detectors

Laser interferometric detectors were pioneered by Forward (Forward, 1978) and Weiss (Weiss, 1972). This type of detector is based on a Michelson interferometer as shown in figure 1.2

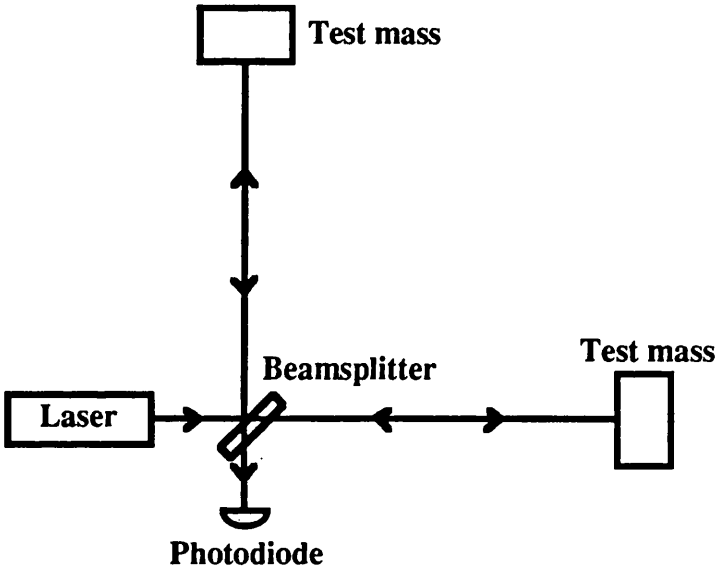

Figure 1.2: Schematic of a Michelson Interferometer. *The test masses incorporate the mirrors for the interferometer.*

A Michelson interferometer consists of two mirrors and a beamsplitter and is illuminated by light from a laser. The beamsplitter divides the incident light evenly between the two arms of the interferometer. The two beams of light are reflected by the mirrors back towards the beamsplitter where they recombine. Any differential change in the lengths of the arms will produce a relative phase shift in the two interfering beams. This is then detected as a change in intensity in the light at the output of the interferometer. Note that this type of detector is particularly well suited to the quadrupole nature of gravitational radiation. Consider the arms of the interferometer aligned to the axes indicated in figure 1.1. The detector is optimally sensitive to radiation propagating perpendicular to the arms

of the interferometer in the 'plus' polarisation. If one arm of the detector is shortened by ΔL then the other is lengthened by the same amount i.e. a differential change in the arm length of $2\Delta L$ is introduced by the passage of the wave.

The test masses must be free to move under the influence of a gravitational wave without being disturbed by external influences such as ground or acoustic vibrations or air pressure fluctuations. For this reason the test masses are suspended as pendulums in vacuum. Thus above the resonant frequency of the pendulums, the test masses are essentially free and hence interferometric detectors are broadband in nature.

The sensitivity of such detectors to strains in space induced by a gravitational wave may be increased by using long arm lengths. (This type of detector can obviously be much bigger than resonant bar detectors since it employs separated masses.) The maximum signal response is obtained if light is stored in the arms for a half a period of a gravitational wave i.e. when the arm length is $\lambda_{GW} / 4$. For a 1 kHz signal this implies an arm length of 75 km. It is not practical to build such large detectors on earth, thus instead of using a single bounce Michelson as indicated in figure 1.2, the optical path may be folded in each arm by the use of either delay lines or resonant cavities as detailed below.

Delay Lines

This type of detector was first proposed by Weiss (Weiss, 1972). Groups at the Max-Planck-Institut für Quantenoptik (MPQ), Germany, and the Institute of Space and Astronautical Science, Japan, are currently developing prototype detectors which employ delay lines (e.g. Winkler, 1991). The layout of such an interferometer is shown in figure 1.3. Light is repeatedly reflected between the delay line mirrors and traces a path in which the beams do not overlap. The intensity of light at the output port is kept on a null by the use of feedback techniques which control the arm lengths of the interferometer. A gravitational wave would change the length of the arms and hence the intensity of the output light. Thus the feedback signal, which opposes the change in arm length, would contain the gravitational wave signal.

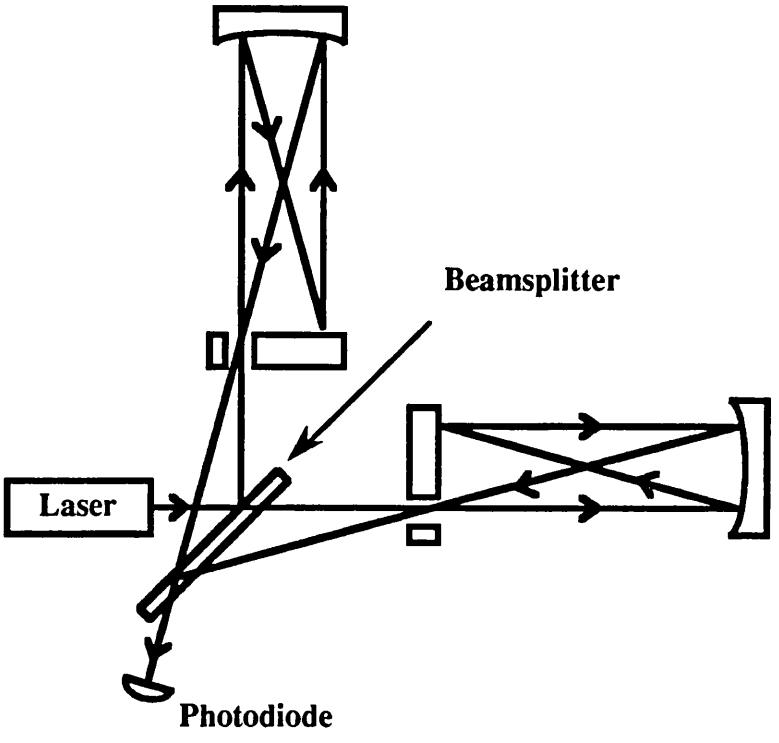

Figure 1.3: Schematic Layout of an Interferometric Gravitational Wave Detector Employing Delay Lines in the Arms. *For clarity only 4 beams in each cavity are shown.*

The main drawback of such a system is the requirement for large mirror diameters and therefore vacuum pipe diameters. For a 3 km detector, ultra-high quality mirrors of the order of 75 cm diameter would be required. Note also that a mirror of this size will have low resonant frequencies. If these are close to the frequencies of interest for gravitational wave detection, their thermal motion will degrade the sensitivity of the detector.

In principle, if the optical path length in each arm is exactly the same, then the interferometer would be insensitive to any fluctuations in the frequency of the laser light. In practice however, light which is scattered in the arms of the interferometer, and which may have a significantly different path length to the main beam, can leak back to the beamsplitter and cause noise in the phase of the output light. This effect may be reduced by stabilising the frequency of the laser light.

The MPQ prototype detector has an arm length of 30 m and an optical path length in each

arm of 3 km. Its best gravitational wave amplitude sensitivity to date is 1 x 10^{-19} / $\sqrt{Hz}$ above 1.5 kHz (Shoemaker et al, 1988).

Resonant Cavity Interferometers

Another multi-pass scheme in interferometric detectors uses Fabry-Perot cavities in the arms. This technique was first developed at Glasgow (Drever et al, 1983) on a 10 m prototype and later at the California Institute for Technology on a 40 m prototype. The layout of such a detector is shown in figure 1.4. In this scheme the laser beams in each Fabry-Perot cavity all lie on top of each other.

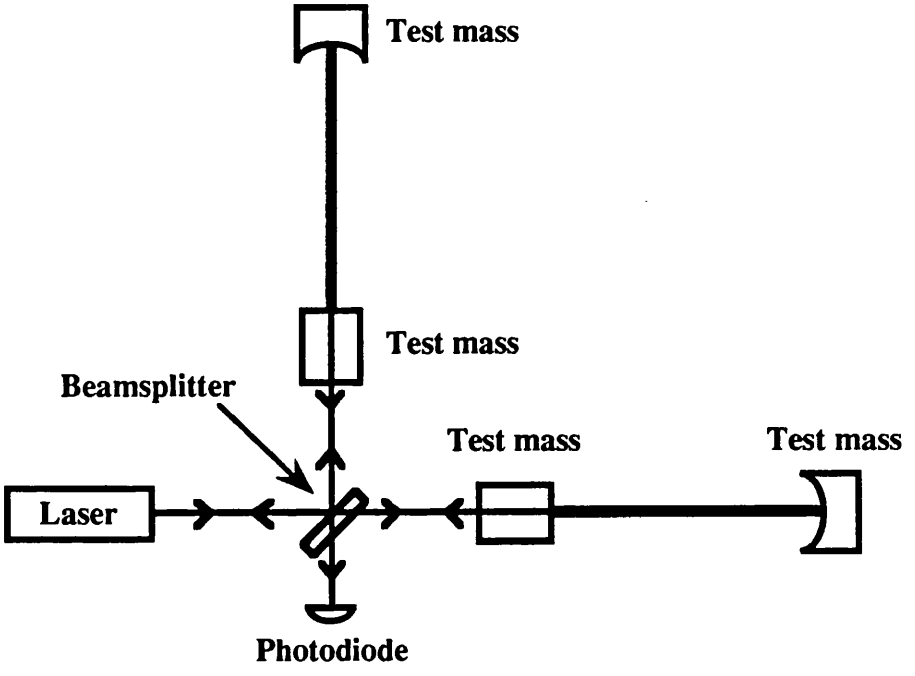

Figure 1.4: Schematic Layout of an Interferometric Gravitational Wave Detector Employing Fabry-Perot Cavities in the Arms.

One of the cavities (the primary cavity) is held on resonance by locking the frequency of the laser to a resonance of the cavity. The length of the secondary cavity is then controlled by keeping it on resonance with the highly stabilised laser light. Any relative changes in the lengths of the arms will tend to move the secondary off resonance. This is compensated for by a control signal which would thus contain the gravitational wave signal.

The operation of such a detector requires more sophisticated control systems, as compared to an interferometer using delay lines, since the two cavities must be held on resonance with the laser light. This requires precise orientation of the test masses and very high frequency stabilisation of the laser light. However smaller mirrors and hence vacuum tubes may be used and since the laser light is so highly stabilised, scattered light is less of a problem.

The Glasgow prototype detector currently has a gravitational wave amplitude sensitivity of $6 \times 10^{-20} / \sqrt{\text{Hz}}$ above 600 Hz.

1.5 Noise Sources in Interferometric Gravitational Wave Detectors

There are several proposals to build long baseline interferometric gravitational wave detectors with arm lengths of up to 4 km and with a planned amplitude sensitivity of 10^{-22} from pulses in a frequency range of several tens of hertz to a few kilohertz. The ultimate sensitivity of these detectors, and also of the present prototype detectors, is limited by various noise sources. The more important of these will be outlined below. A more comprehensive review of possible noise sources is contained in proposals submitted by the various groups to their funding bodies (Giazotto et al, 1989 (the VIRGO project), Hough et al, 1989 (the GEO project), Vogt et al, 1989 (the LIGO project), Blair et al, 1990 (the AIGO project)).

1.5.1 The Heisenberg Uncertainty Principle

The Heisenberg Uncertainty Principle places a fundamental limit on the accuracy of any measurement of the position of a free test mass. The minimum differential displacement of the two end masses of the detector, each of mass m, over a bandwidth Δf at a frequency f is given by (Edelstein, 1978)

$$\langle x_{up} \rangle = \left[\frac{h}{m\pi^2 f^2}\right]^{1/2} m/\sqrt{\text{Hz}} \qquad (1.19)$$

Thus the sensitivity of an interferometric detector of arm length L is given by

$$\langle h \rangle = 2 \times 10^{-25} \left[\frac{50\ \text{kg}}{m}\right]^{1/2} \left[\frac{1\ \text{kHz}}{f}\right] \left[\frac{3\ \text{km}}{L}\right] / \sqrt{\text{Hz}} \qquad (1.20)$$

It is noted that the sensitivity of such a detector will increase linearly with increasing arm length. Note however that other noise sources will impose more significant limitations to the sensitivity of proposed detectors.

1.5.2 Photon Counting Statistics

The effect of a gravitational wave, of the correct orientation, passing through an interferometric detector is to produce a differential displacement of the end masses. This in turn induces a relative phase shift between the light beams in the two arms of the interferometer and hence a change in the intensity of the light at the output port. Thus the minimum detectable change in the output light in a time τ determines the minimum detectable differential displacement of the test masses. This is limited by the $\sqrt{n}$ uncertainty associated with counting n photons in a time τ. The effect of photon counting statistics, or photon shot noise, is decreased by keeping the output of the detector on a dark fringe. The photon shot noise limited sensitivity of an interferometric detector is given by (Hough et al, 1989)

$$\langle h \rangle \approx \left[\frac{\pi h \lambda}{\varepsilon I_o c}\right]^{1/2} \frac{f}{\sin(\pi f \tau_s)} / \sqrt{\text{Hz}} \qquad (1.21)$$

where λ is the wavelength of the laser light,

ε is the quantum efficiency of the photodiode,

I_o is the light power entering the interferometer,

c is the speed of light,

f is the gravitational wave frequency and

τ_s is the time for which light is stored in the arms of the interferometer.

It may be seen from eq. (1.21) that the effect of shot noise is reduced by using high laser power. Note also that the sensitivity of the interferometer is optimised by setting the storage time of the light in the arms to be half the period of the gravitational wave. If this is the case then (Hough et al, 1989)

$$\langle h \rangle \approx 2.4 \times 10^{-21} \left[\frac{\varepsilon I_o}{50\ \mathrm{W}}\right]^{-1/2} \left[\frac{f}{1\ \mathrm{kHz}}\right]^{3/2} / \sqrt{\mathrm{Hz}} \qquad (1.22)$$

Since the detector is operated on a dark fringe, virtually all of the light from the arms of the interferometer travels back towards the laser. By careful positioning of an extra mirror at the input port, as indicated in figure 1.5, this unused light may be coherently added to the input light, a technique known as standard recycling (Drever, 1983).

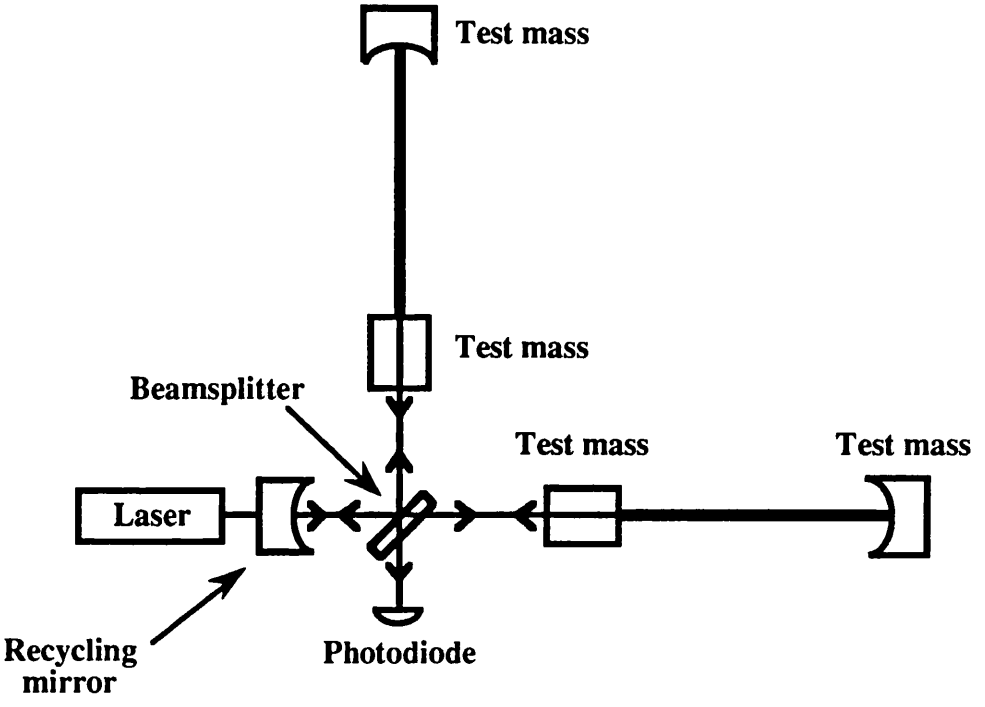

Figure 1.5: Schematic Layout for a Gravitational Wave Detector with Fabry-Perot Cavities using Standard Recycling.

This increases the light power in the interferometer thereby reducing photon shot noise. The limit to the sensitivity for such a detector for a choice of $\Delta f = f/2$ is then (Hough et al, 1989)

$$\langle h \rangle \approx 10^{-22} \left[\frac{\varepsilon I_o}{50\ \mathrm{W}}\right]^{-1/2} \left[\frac{f}{1\ \mathrm{kHz}}\right] \left[\frac{1-R}{5 \times 10^{-5}}\right]^{1/2} \left[\frac{L}{3\ \mathrm{km}}\right]^{-1/2} \qquad (1.23)$$

where (1 - R) is the mirror loss.

Other methods have been proposed to improve the sensitivity of interferometric gravitational wave detectors. These include dual recycling (Meers, 1988). This technique involves the careful positioning of a mirror at the output port of the interferometer, in front of the photodiode, to recycle the optical sidebands which result from the gravitational wave signal. These sidebands are effectively increased in size by this recycling, and thus this technique may be used to improve the narrowband shot noise limited sensitivity of the detector, or to enhance the broad band sensitivity when the storage time in the arms of the interferometer is not well matched to the period of the gravitational wave. This scheme has recently been experimentally demonstrated to increase the sensitivity of an interferometer (Strain and Meers, 1990). Another possible method of improving detector sensitivity is by the use of squeezed light (Caves, 1981). This technique, however, still requires much experimental development.

1.5.3 Thermal Noise

Another limit to the sensitivity of interferometric detectors is that imposed by thermal motion of the pendulum suspensions and of the internal modes of the suspended masses.

Thermal Motion of the Pendulum Suspensions

The maximum thermal motion of a simple pendulum occurs at its resonant frequency, f_{pend}, which is typically about 1 Hz for the suspended masses under consideration here. For frequencies much higher than this the spectral density of the thermal motion of the pendulum is given by (Weiss, 1972)

$$\langle x_{pend} \rangle = \left[\frac{f_{pend} k_B T}{2\pi^3 f^4 m Q_{pend}} \right]^{1/2} m/\sqrt{Hz} \qquad (1.24)$$

where k_B is Boltzmann's constant,

T is the temperature,

f is the frequency of interest

m is the mass of the pendulum bob and

Q_{pend} is the quality factor of the pendulum.

It is noted that eq. (1.24) is derived using the conventional assumption that the damping coefficient of the pendulum suspension is independent of frequency. The implications of this assumption for the sensitivity of an interferometric gravitational wave detector will be discussed in detail in chapters four and five of this thesis.

Thus the conventional limit to the sensitivity of an interferometric detector, due to thermal motion of the pendulums, is given by

$$\langle h \rangle = 8 \times 10^{-26} \left[\frac{f_{pend}}{1\ Hz}\right]^{1/2} \left[\frac{1\ kHz}{f}\right]^{2} \left[\frac{50\ kg}{m}\right]^{1/2} \left[\frac{10^{8}}{Q_{pend}}\right]^{1/2} \left[\frac{3\ km}{L}\right] / \sqrt{Hz} \qquad (1.25)$$

Hence the thermal noise limited sensitivity of a detector due to thermal motion of the pendulum suspensions, may be increased by using high Q pendulum suspensions and having a detector with long arms.

Thermal Motion of the Internal Modes of the Test Masses

The dimensions of the test masses should be chosen such that the lowest resonant frequency is well above the frequency bandwidth of interest for the detection of gravitational waves (~ 100 Hz to a few kHz). It will be shown in chapter two that the spectral density of the thermal motion of a test mass of mass m and quality factor Q_{mass}, at frequencies much less than fundamental longitudinal mode, f_o, is given by

$$\langle x_{mass} \rangle = \left[\alpha \frac{k_B T}{\pi^3 f_o^3 m Q_{mass}}\right]^{1/2} m/\sqrt{Hz} \qquad (1.26)$$

where $\alpha \sim 2.5$ is a factor to allow for a summation of the effect of a number of different modes (Hough et al, 1989). Again it has been assumed that the damping coefficient of the material is frequency independent.

Note that eq. (1.26) is a factor of 2 higher than has been conventionally assumed up until now. This is since a test mass has in general been treated as a simple harmonic oscillator consisting of a mass on a spring. However in reality it is not - it is a distributed mechanical system. If the correct calculation is carried out eq. (1.26) is obtained. The limit to the sensitivity of an interferometric gravitational wave detector is then given by

$$\langle h \rangle = 1 \times 10^{-24} \left[\frac{15\ \text{kHz}}{f_o}\right]^{3/2} \left[\frac{50\ \text{kg}}{m}\right]^{1/2} \left[\frac{10^6}{Q_{mass}}\right]^{1/2} \left[\frac{3\ \text{km}}{L}\right] / \sqrt{\text{Hz}} \qquad (1.27)$$

Thus, assuming that the temperature is fixed, the effect of thermal motion of the internal modes of the mass on the sensitivity of the detector can be decreased by using high Q material and again having a detector with a long baseline. Investigation of the Q of possible materials for use as test masses is one of the chief objectives of this thesis.

1.5.4 Seismic Noise

Seismic noise will limit the sensitivity of all earth-based detectors especially at low frequencies. The test masses and other optical components must therefore be isolated to a great a degree as possible from ground vibrations. This may be achieved by connecting the components to ground via mechanical isolators such as pendulum suspensions and vibration isolation stacks (e.g. Robertson, 1991). However even with these measures it is likely that seismic noise will limit the sensitivity of terrestrial interferometric gravitational wave detectors at frequencies below a few tens of hertz.

1.5.5 Other Noise Sources

There is a variety of other noise sources which will affect the sensitivity of laser interferometric gravitational wave detectors. For example fluctuations in the residual gas pressure of the vacuum can give rise to changes in the optical path length in the detector. Frequency and intensity fluctuations of the laser light can introduce noise and both of these must be stabilised using feedback techniques. In addition to this, variation of the laser beam position, orientation and geometry are important. Such effects may be attenuated by the use of a mode cleaning device such as a single mode fibre or a mode cleaning cavity. Rotation and tilting of the suspended masses can cause misalignment of the optical cavities. This could lead to fluctuations in the phase of the detected output light and hence a reduction in the sensitivity of the detector. Thus such effects have to be strictly controlled.

1.5.6 Summary of Predicted Noise Sources and the Importance of Thermal Noise

Figure 1.6 shows a graph of the predicted sensitivity of a 3 km arm length detector to continuous sources of gravitational waves. From this it is observed that, at frequencies less than approximately 100 Hz, the sensitivity of the detector is severely limited by seismic noise. Above this, the sensitivity is limited by thermal noise. The thermal motion of the pendulum suspensions is important for frequencies between approximately 100 and 150 Hz. Above this frequency, the thermal motion of the internal modes of the test masses will limit the sensitivity of the proposed detector. As noted in section 1.5.3, it is important that the test masses have a high Q in order to minimise the effects of thermal motion. Part of this thesis is devoted to investigation of the quality factor of some possible materials of interest for use as test masses. Note that the sensitivity graph shown in figure 1.6, has been drawn for the conventional assumption that the damping coefficients of both the pendulum suspension and test mass material are independent of frequency. As will be discussed later in this thesis, there is strong evidence that this assumption is invalid for some materials. A different model of damping predicts a different frequency distribution of thermal noise and it is thus very important to find experimental evidence as to mechanical damping mechanisms. Part of this thesis describes work aimed in this direction.

In chapter two, consideration will be given to the criteria for choosing the material from which the test masses are formed and in particular consideration is given as to how to minimise the thermal motion of the masses.

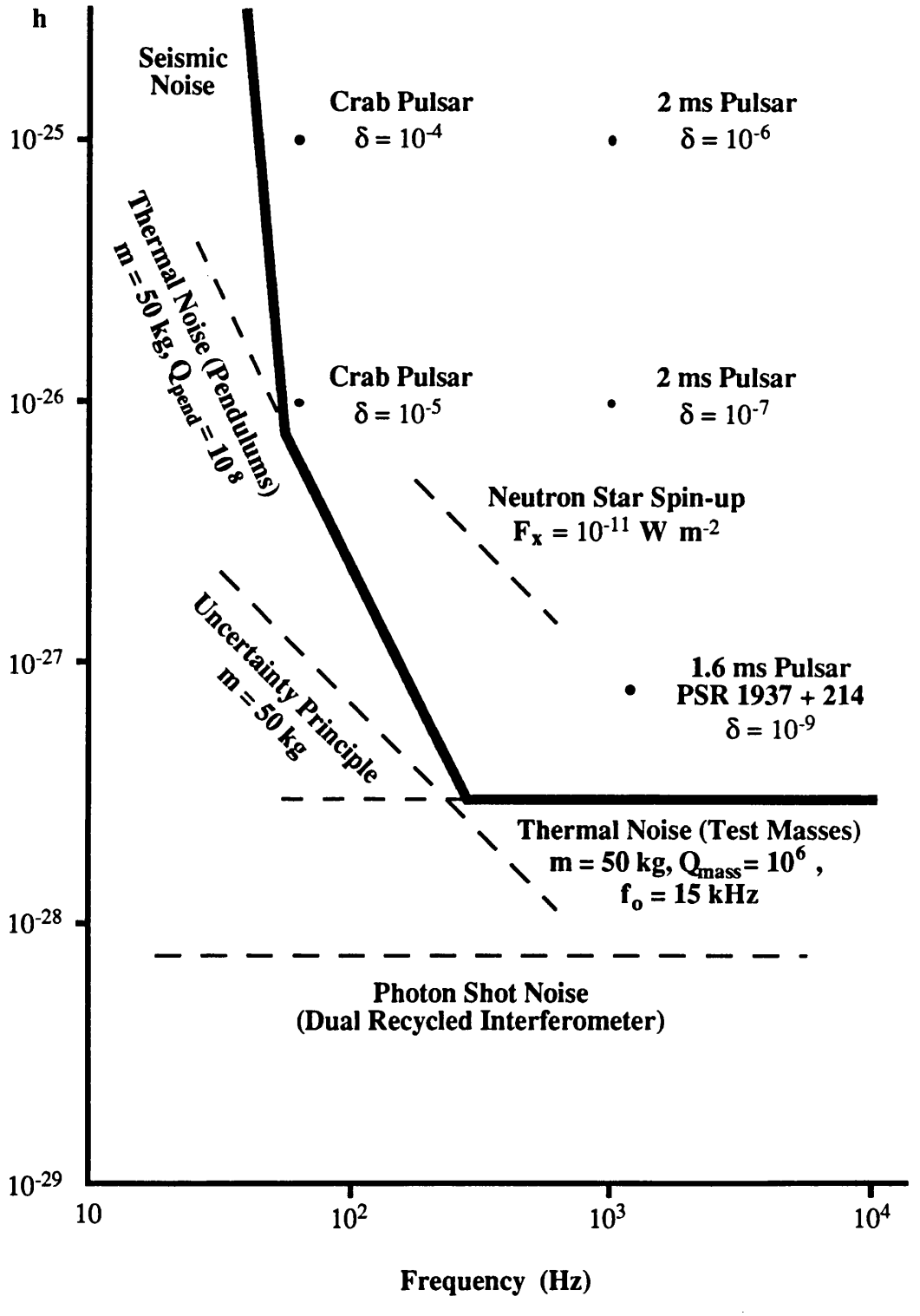

Figure 1.6: Predicted Sensitivity of a 3 km Baseline Detector to Continuous Sources of Gravitational Waves. *An integration time of 10^7 s is assumed. Note that due to possible non-optimum orientation of source and detector, signal strengths shown on the graph may need to be reduced by up to a factor of $\sqrt{5}$. Possible values for the ellipticity, δ, of some pulsars are shown.*

Chapter 2

An Introduction to Quality Factor Measurements and the Minimisation of Thermal Motion of Test Masses

2.1 Introduction

Thermal motion is one of the fundamental noise sources in precision mechanical experiments. To understand how this motion arises, consider a resonant system in thermal equilibrium with its surroundings at temperature T. According to the equipartition theorem such a system will have internal thermal energy corresponding to k_BT energy per resonant mode, where k_B is Boltzmann's constant, giving rise to thermal excitation of these modes. In laser interferometric gravitational wave detectors this noise source appears via two routes; through thermal motion associated with the pendulum modes of the suspended test masses and through thermal motion associated with the internal modes of the test masses themselves, as outlined in section 1.5.3. A more detailed analysis of the spectral density of the thermal noise from the test masses is presented in this chapter and consideration is given as to how the resulting thermal motion may be minimised by the choice of material used.

2.2 The Thermal Motion Power Spectrum of a Test Mass

It is conventionally assumed that the damping force in a material is proportional to velocity and that the form of the power spectral density for the thermal motion associated with an internal mode of a mass, is directly related to the Q of the mode. In deriving the form of this power spectral density it is thus useful to first derive an expression for the Q of an internal mode of a test mass.

2.2.1 The Quality Factor of a Material

The quality factor of any mode of a resonant system is defined to be (e.g. Duffin, 1980, p. 278)

$$Q = 2\pi \frac{\text{energy stored}}{\text{energy lost per cycle}} \tag{2.1}$$

Consider the longitudinal vibrations of an elastic, right circular cylindrical mass of uniform cross-sectional area S, density ρ and length L. It is assumed that the length of the mass is much greater than its radius, r. If the mass is subjected to an initial excitation which is then abruptly removed, the motion of the mass resonating freely is described by

$$\frac{\partial^2 \xi}{\partial x^2} = \frac{1}{c^2}\left(\frac{\partial^2 \xi}{\partial t^2} + \beta \frac{\partial \xi}{\partial t}\right) \tag{2.2}$$

where x is the equilibrium distance of each point in the mass from a fixed reference plane which is parallel to the end faces of the mass,

ξ is the displacement of each point in the mass, with respect to x, from its equilibrium position,

t is the time,

c is the velocity of sound in the mass and

β is the coefficient of damping per unit mass.

It can be shown, by separation of variables, that the solution to eq. (2.2) is given by

$$\xi = Ae^{-\beta t/2} \cos(kx + \alpha) \cos\left(\sqrt{c^2k^2 - \frac{\beta^2}{4}}\, t + \varepsilon\right) \tag{2.3}$$

where A is the maximum amplitude of motion,

k, α and ε are constants which remain to be determined.

Consider now the case of a freely suspended mass in a gravitational wave detector. The ends of such a mass, at x = 0 and x = L, are free from tension and if, in addition, the mass is subject to an excitation such that its maximum amplitude of oscillation is A, at

t = 0, the following boundary conditions apply:

i) $\frac{\partial \xi}{\partial x} = 0$ at x = 0 and x = L for all t and

ii) $\xi = A$ at x = 0 and $\xi = -A$ at x = L when t = 0.

It is then found that

$$\alpha = \varepsilon = 0$$

and

$$k = \frac{n\pi}{L} \qquad \text{for n odd} \qquad (2.4)$$

Without loss of generality, consider the equation of the fundamental longitudinal mode of the mass given by n = 1 in eq. (2.4)

$$\xi = Ae^{-\beta t/2} \cos\left(\frac{\pi x}{L}\right) \cos\left(\sqrt{\frac{c^2\pi^2}{L^2} - \frac{\beta^2}{4}}\, t\right) \qquad (2.5)$$

If the mass had no damping present, ξ would represent simple harmonic motion with a natural resonant angular frequency of $\omega_o = c\pi/L$. It is noted however, that the treatment detailed here is in fact an approximation since when the mass elongates in the longitudinal direction, the accompanying radial contraction has been neglected. The amount of radial contraction for a given elongation is given by Poisson's ration, ν, for the material

$$\nu = \frac{\text{lateral contractile strain}}{\text{longitudinal strain}} \qquad (2.6)$$

The radial motion of the mass results in a non-uniform distribution of stress across sections of the mass leading to distortions of these sections. The longitudinal vibrations of long thin bars were analysed by Pochhammer (Pochhammer, 1876) and independently by Chree (Chree, 1886) who showed that the resonant angular frequency of the fundamental longitudinal mode of vibration of such an undamped bar is given, to a closer approximation, by

$$\omega_o = \frac{\pi c}{L}\left[1 - \left(\frac{\nu \pi r}{2L}\right)^2\right] \qquad (2.7)$$

Eq. (2.5) describes motion with an angular resonant frequency

$$\omega^2 = \omega_o^2 - \frac{\beta^2}{4} \tag{2.8}$$

Thus for a mass with very low damping, it is observed that $\omega^2 \approx \omega_o^2$. Indeed for this case, the oscillations of the mass can be described over several cycles by simple harmonic motion of constant amplitude and eq. (2.5) may be written as

$$\xi \approx A \cos\left(\frac{\pi x}{L}\right) \cos \omega_o t \tag{2.9}$$

The kinetic energy of the mass, E_k, is given by

$$E_k = \int_0^L \frac{1}{2} \rho S \left(\frac{\partial \xi}{\partial t}\right)^2 dx$$

$$= \frac{1}{4} m \omega_o^2 A^2 \sin^2 \omega_o t \tag{2.10}$$

where m is the mass.

The total energy, E_T, in the mass is equal to its maximum kinetic (or potential) energy. Thus

$$E_T = \frac{1}{4} m \omega_o^2 A^2 \tag{2.11}$$

The power, P, dissipated in the mass is given by

$$P = \int_0^L \left(\frac{\partial \xi}{\partial t}\right)^2 S \rho \beta \, dx \tag{2.12}$$

and the energy lost per cycle

$$E_L = \int_0^{2\pi/\omega_o} P\,dt$$

$$= \frac{1}{2}\pi\, m\, \beta\, \omega_o\, A^2 \qquad (2.13)$$

Thus from eqs. (2.1), (2.11) and (2.13) the quality factor of the mass

$$Q = \frac{\omega_o m}{b} \qquad (2.14)$$

for the low damping situation where $\omega_o^2 >> \frac{b^2}{4m^2}$ and where $b = \beta m$ is the total damping in the mass. From eq. (2.14) it can be seen that the condition for low damping is equivalent to $Q >> \frac{1}{2}$.

From eq. (2.5) it is observed that the amplitude of motion of the mass falls to e^{-1} of its original value in a decay time

$$\tau_d = \frac{2}{\beta} \qquad (2.15)$$

Combining this with eq. (2.14) the Q of the mass may also be defined as

$$Q = \pi f_o \tau_d \qquad \text{for } Q >> \frac{1}{2} \qquad (2.16)$$

where f_o is the resonant frequency of the mode under study.

By experimentally determining f_o and τ_d, the Q for the longitudinal mode of the mass may be calculated. Eq. (2.16) is in fact used in general to calculate the Q of any mode of a mass, where f_o is the resonant frequency of the mode under study.

2.2.2 The Fluctuation-Dissipation Theorem

It is well known that when a system is dissipative it also exhibits fluctuations. This was most clearly illustrated in electrical systems by Johnson who found experimentally that the

random motion of the electrons in a conductor produced a fluctuating voltage, v_{th}, across the conductor (Johnson, 1928). Nyquist theoretically showed these fluctuations to have a power spectral density (Nyquist, 1928)

$$\langle v_{th}^2 \rangle = 4k_B TR \tag{2.17}$$

where R is the resistance of the conductor and the conventional 1 Hz bandwidth is assumed.

In fact the dissipative property of a system is the large scale manifestation of the microscopic fluctuations of the charge carriers or atoms of the system, and therefore the magnitude of the dissipation is dependent upon the size of these fluctuations. Such dissipation necessarily implies the presence of a fluctuating voltage, in the case of an electrical system or, in the case of a mechanical system, a fluctuating force.

These ideas are the essence of the fluctuation-dissipation theorem of Callen (Callen and Welton, 1951 and Callen and Greene, 1952) who showed that any linear, dissipative system with generalized resistance $R(\omega)$, equal to the real part of the impedance of the system, $Z(\omega)$, exhibits a fluctuating thermal force with power spectral density

$$\langle F_{th}^2 \rangle = 4k_B TR(\omega) \tag{2.18}$$

This is the generalized form of the more familiar Nyquist theorem

A system is said to be dissipative if it has densely distributed energy levels and if, when subjected to a force which is periodic in time, it absorbs energy. The system is said to be linear if the power dissipated in it is proportional to the square of the magnitude of the applied force.

Consider now the resonant mass of the previous section. If the mass is subject to a damping force $F = F_o \cos\omega t$, where $F = bv$, the power dissipated in it is

$$P = \frac{F_o^2 \cos^2\omega t}{b} \tag{2.19}$$

It is evident that P is proportional to F_0^2 and the presence of damping implies that the mass is capable of absorbing energy. Thus from the definitions given above, such a resonant mass is a linear, dissipative system and equation (2.18) applies.

The spectral density of the fluctuations themselves, for a mechanical system, are given by (Callen and Greene, 1952)

$$\langle x_{th}^2 \rangle = \frac{4k_B T G(\omega)}{\omega^2} \tag{2.20}$$

where $G(\omega)$ is the conductance of the system (equal to the real part of the admittance, $Z^{-1}(\omega)$)

2.2.3 The Relation Between Q and the Thermal Motion of a Test Mass

In this section an expression will be developed for the thermal motion power spectral density of a mass. From analysis of a simple harmonic oscillator and by consideration of the similarity between such an oscillator and a mass resonating in its fundamental longitudinal mode, the required expression for the mass may be derived.

Consider a simple harmonic oscillator, such as the system shown in figure 2.1, formed by a mass on a spring. When such a system is subjected to an oscillatory driving force, F, with frequency ω, the motion of the mass is described by

$$M\frac{d^2x}{dt^2} + B\frac{dx}{dt} + Kx = F \tag{2.21}$$

where $K = \omega_0^2 m$ is the spring constant and

ω_o is the angular resonant frequency of the system.

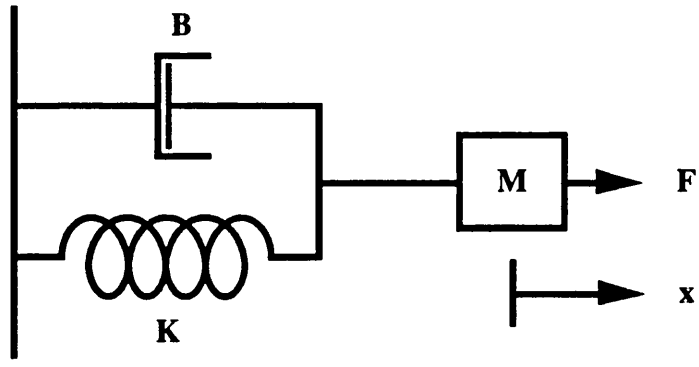

Figure 2.1: A Simple Harmonic Oscillator. *This is formed by a mass, M, attached to a damper of damping coefficient B, and a spring of spring constant K. x shows the displacement of the mass from its equilibrium position.*

The impedance of the system, defined to be (e.g. French, 1986, p. 262)

$$Z = \frac{F}{v} \tag{2.22}$$

is thus

$$Z = j\omega M + B + \frac{K}{j\omega} \tag{2.23}$$

and hence the conductance

$$G(\omega) = \frac{\omega^2 B}{(K - \omega^2 M)^2 + \omega^2 B^2} \tag{2.24}$$

If the driving force is thermal in origin, from eqs. (2.18) and (2.23)

$$\langle F_{th}^2 \rangle = 4k_B TB \tag{2.25}$$

From eqs. (2.20) and (2.24) the thermal motion power spectral density of the simple harmonic oscillator is given by

$$\langle x_{sho}^2 \rangle = \frac{4k_B TB}{(K - \omega^2 M)^2 + \omega^2 B^2} \tag{2.26}$$

The exact form of this equation is shown in figure 2.2, in which is is assumed that B is a constant, independent of frequency.

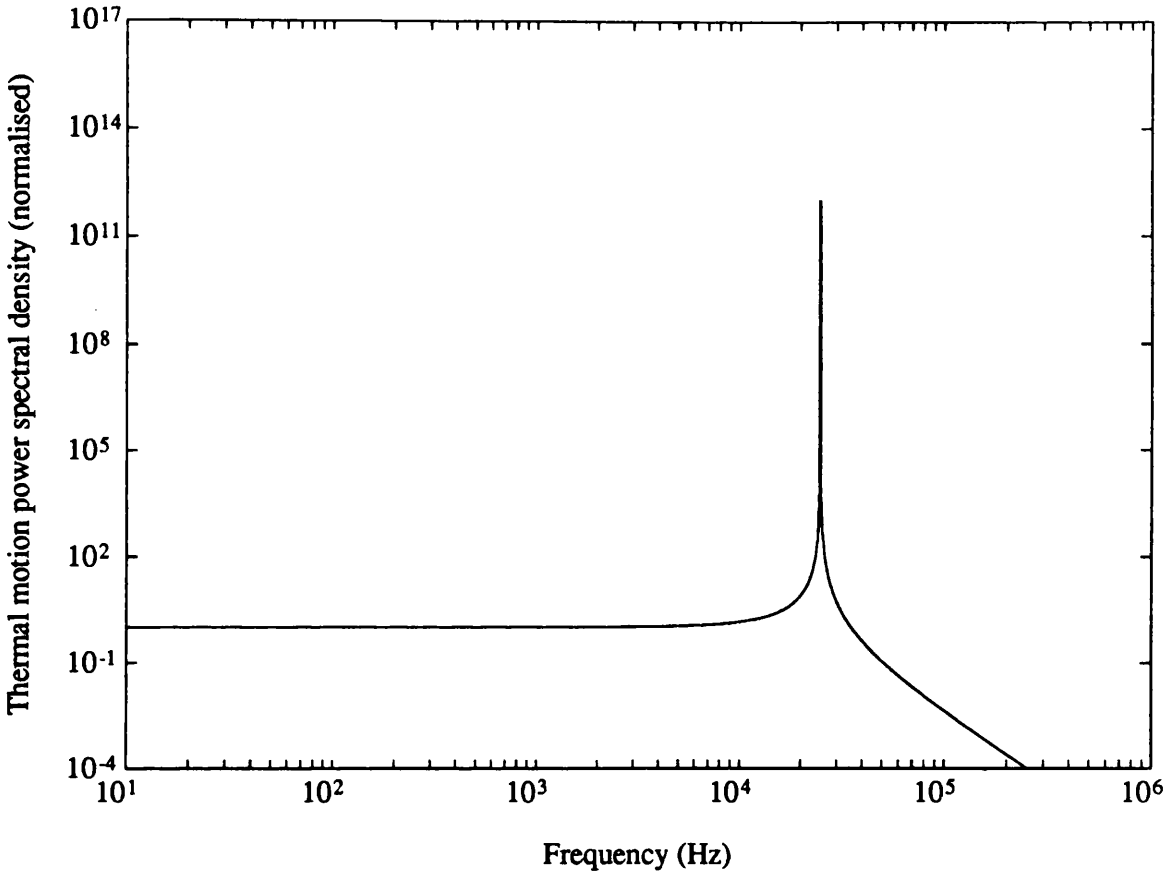

Figure 2.2: The Form of the Thermal Motion Power Spectral Density of a Simple Harmonic Oscillator with a Frequency Independent Damping Coefficient. *The oscillator has a Q of 1 x 10^6 and a resonant frequency of 25 kHz. The spectrum is normalized such that the curve is equal to 1 at low frequencies.*

From the figure it is evident that the thermal motion is essentially frequency independent below the resonance of the system. Using eqs.(2.14) and (2.26) it can be shown that for $\omega << \omega_o$

$$\langle x^2_{sho} \rangle = \frac{4k_B T}{QM\omega_o^3} \tag{2.27}$$

The energy of the system, E_{sho}, at its angular resonant frequency

$$E_{sho} = \frac{1}{2} M\omega_o^2 x_{sho}^2 \tag{2.28}$$

where x_{sho} is the peak amplitude of motion of the oscillator on resonance.
From the equipartition theorem such a system has $k_B T$ internal energy per resonant mode and hence

$$x_{sho}^2 = \frac{2k_B T}{M\omega_o^2} \tag{2.29}$$

Consider now the mass described in section 2.2.1, the energy of which is given by eq. (2.11). By the equipartition theorem the peak amplitude of one end of the mass, x_{mass} is given by

$$x_{mass}^2 = \frac{4k_B T}{M\omega_o^2} \tag{2.30}$$

Since the end of the mass resonating its fundamental longitudinal mode, behaves like a simple harmonic oscillator, eq. (2.9), the ratio of the level of motion below resonance to that at resonance must equal that of the simple harmonic oscillator. This is given by the ratio of eqs. (2.27) and (2.29). This leads to the thermal motion spectral density of one end of the mass, at frequencies very much less than the fundamental longitudinal resonance, neglecting the effect of other modes, being of the form

$$\langle x_{mass}^2 \rangle = \frac{8k_B T}{Qm\omega_o^3} \tag{2.31}$$

It is important to note that the level of thermal motion of a test mass as predicted by eq. (2.31) is a factor of 2 greater than has been previously assumed (e.g. Weiss, 1972). This arises since in previous calculations, a test mass has been treated as a simple harmonic oscillator leading to eq. (2.27) for the thermal noise of the mass at frequencies well below its lowest resonant frequency. In reality, however, a test mass is a distributed mechanical system not a simple harmonic oscillator. When this difference is fully considered, as shown above, eq. (2.31) is reached, a factor of 2 greater than eq. (2.27).

Thus, given that the test masses are at room temperature, in order to have low thermal motion it is desirable to have masses with high values of Q, m and ω_o. Note however that increasing the mass will tend to lower the resonant frequency of each test mass.

The contribution to the level of thermal motion due to higher order longitudinal modes is small. Recall that eq. (2.26) was obtained using the conventional assumption that the damping force in a material is proportional to velocity. As will be shown in chapter 5, this assumption implies that, for a particular mode in a material, Q is inversely proportional to frequency. Thus the level of thermal motion, at frequencies very much less than the resonant frequencies of the test mass, due to the summation of all the higher order longitudinal modes yields

$$\langle x^2_{mass} \rangle = \frac{8k_BT}{m\omega_1 Q_1}\left[\sum_{n=1}^{\infty}\frac{1}{\omega_n^2}\right] \tag{2.32}$$

where ω_1 is the angular resonant frequency of the fundamental longitudinal mode and
Q_1 is the Q of the fundamental longitudinal mode.

The resonant angular frequency of the nth longitudinal mode of the mass is given by

$$\omega_n = \omega_1 n \tag{2.33}$$

However only the odd numbered longitudinal modes contribute to the level of thermal motion in a gravitational wave detector since the end faces of the mass are nodes for even numbered modes. Thus

$$\langle x^2_{mass} \rangle = \frac{8k_BT}{m\omega_1^3 Q_1}\left[\sum_{m=1}^{\infty}\frac{1}{(2m-1)^2}\right]$$

$$= \frac{\pi^2}{8}\frac{8k_BT}{m\omega_1^3 Q_1}$$

$$\approx 1.2\,\frac{8k_BT}{m\omega_1^3 Q_1} \tag{2.34}$$

Any other modes in which there is a net movement of the parts of the face interrogated by the sensing beam will also contribute to this level of thermal motion. Note that modes in which the average movement in a circle concentric with the face of the test mass is zero, are not so important since their effect is much smaller. In order to allow for the effects of more complicated modes, such as drum modes (see chapter 3, figure 3.10), the level of thermal noise is usually taken to be

$$\langle x^2_{mass} \rangle \approx \alpha \frac{8k_BT}{m\omega_1^3 Q_1} \tag{2.35}$$

where $\alpha \sim 2.5$ (Hough et al, 1989).

Recall that eq. (2.35) was derived using the assumption that, for a particular mode in a material, Q is inversely proportional to frequency. There is some experimental evidence for this behaviour (Abramovici, 1990). However for some materials there is evidence that Q is constant over a wide frequency range (e.g. Kimball and Lovell, 1927 and Mason, 1971, p. 348). This would lead to a different form of thermal noise spectrum to that shown in figure 2.2, as pointed out by Saulson (Saulson, 1990). This topic will be fully discussed in chapter 5.

2.3 The Choice of Material for the Test Masses

There are various constraints on the choice of material to be used for the test masses, some of which have been mentioned in the previous section. In summary:

a) in order to minimise thermal noise from the test masses, the material is required to have a high Q. Further, the dimensions of the test mass should be chosen such the lowest resonant frequency lies above the frequency band of interest for the detection of gravitational waves. It is thus important to choose a material with a high velocity of sound, c. In order to derive a figure of merit that may be used in the consideration of possible materials, the expression for the thermal motion of a test mass, eq. (2.35) may be rewritten. Eq. (2.7), to a first approximation, gives the angular frequency of the first longitudinal mode to be $\omega_1 = \pi c/L$. If it is further assumed that the length of the test mass is of the order

of the diameter, the mass $m \sim \rho L^3$, where ρ is the density of the test mass material. Eq. (2.35) may then be expressed as

$$\langle x^2_{mass} \rangle \sim \alpha \frac{8 k_B T}{\pi^3 \rho c^3 Q_1} \tag{2.36}$$

Thus to have low thermal motion it is necessary to choose a material with a high product of $\rho c^3 Q$.

b) the material should have high thermal conductivity, κ, and a low coefficient of thermal expansion, α, in order to minimise distortion when high light power is incident upon it (Winkler et al, 1991). The ratio of κ / α is often used as a figure of merit in the consideration of possible materials.

c) the material should be such that it may be polished to make ultra-high quality, low loss mirrors with surface roughness ~ 1 Å rms.

d) it must be possible to manufacture / grow suitable sized samples (~ 0.5 m diameter and ~ 0.25 m thick) to form the mirrors for a long baseline interferometer.

Table 2.1 shows a comparison of some of the above qualities for possible materials of interest.

Since the Q of a material is so important in minimising thermal motion from the test masses, it is essential to understand the factors which limit the Q and how to minimise these effects. It is also of interest to investigate different forms of materials such as polycrystalline rather than single crystal silicon which has been widely studied. In order to do this an experimental method of measuring the Q of materials has been developed.

Notes on table 2.1

1) All values are given for room temperature

2) The velocity of sound is given for longitudinal waves in the material. The value quoted for silicon is for waves propagating along the [111] axis.

3) Values for k/α and the speed of sound for sapphire are given for a direction along the c axis. Light propagating through a sapphire crystal in such a direction suffers minimal birefringence effects. The importance of this is discussed in chapter 6.

4) There is a wide variety of aluminium alloys. The 6061 alloy (U.S.A. specification) considered here is known to have a high Q and is used for some resonant bar gravitational wave detectors.

5) Beryllium has the disadvantage of being toxic. The author is not aware of any published Q measurements for this material in the literature.

6) All Q values are for the longitudinal mode of the sample of material with the exception of the fused silica value marked (*). This is believed to be some sort of bending mode (Dialinas, 1991). The frequency at which the Q measurements were made is indicated in the neighbouring right-hand column.

7) Three measurements of Q for fused silica are quoted. Chapter 5 contains details of the author's investigation of the Q of this material.

8) Whilst sapphire clearly has the highest figure of merit, $\rho c^3 Q$, its thermal properties are not so good. It is also not clear whether large enough pieces of this material will be available for use as mirrors in a 3 km baseline interferometric detector.

Material	k / α ($\times 10^6$ W m^{-1})	ρ ($\times 10^3$ kg m^{-3})	c ($\times 10^3$ m s^{-1})	Q ($\times 10^5$)	f_Q (kHz)	$\rho c^3 Q$ ($\times 10^{20}$ kg s^{-3})	References
Aluminium (Alloy 6061)	6.5	2.64	5.00	2	8	0.66	[1], [2], [7]
Beryllium	19.8	1.83	12.90	?	-	$3.9 \times 10^{-5} \times Q$	[1], [3]
Fused silica	2.7	2.20	5.72	44	7	18	[4], [8]
				10 *	4	4.1	[9]
				0.88	29	0.36	[10]
Sapphire	4.3	3.97	10.50	1800	34	8.3×10^3	[3], [5], [11]
Silicon (single crystal)	59.2	2.33	8.98	300	19	500	[1], [3], [12]
Silicon Carbide	46.5	3.10	11.5	1	19	4.7	[6], [13]

References for values of physical constants :

[1] Gray, 1972

[2] American Society for Metals, 1984

[3] Kaye and Laby, 1986

[4] Heraeus

[5] Braginsky et al, 1985

[6] British Nuclear Fuels

References for Q measurements :

[7] Amaldi et al, 1977

[8] Mitrovanov and Frontov, 1974

[9] Brillet, 1992

[10] Cadez and Abramovici, 1988

[11] Bagdasarov et al, 1977

[12] McGuigan et al, 1978

[13] Michelson, 1992

Table 2.1: Comparison of Some Possible Materials for Use as Test Masses

2.4 An Experimental Technique for Measuring the Q of Materials

Figure 2.3 shows the experimental arrangement used for measuring the Q values of materials. The sample under test was suspended on a single loop of hard drawn, stainless steel wire from a support structure with the suspension wires constrained, at the top, in grooves and breaking away over sharp edges as indicated in figure 2.4. The orientation of the breakaway points was chosen to be as shown in figure 2.4, in order to minimise any damping of radial motion of the mass. The samples were, in general, right circular cylinders and the suspension wires were made to break away from the mass above its centre of gravity in order to provide stability. Different conditions where the wire broke free from the mass were investigated. These will be detailed later in the text. The diameter of wire used is chosen such that when loaded by the mass, the stress induced in the wire is a few times smaller than its breaking stress.

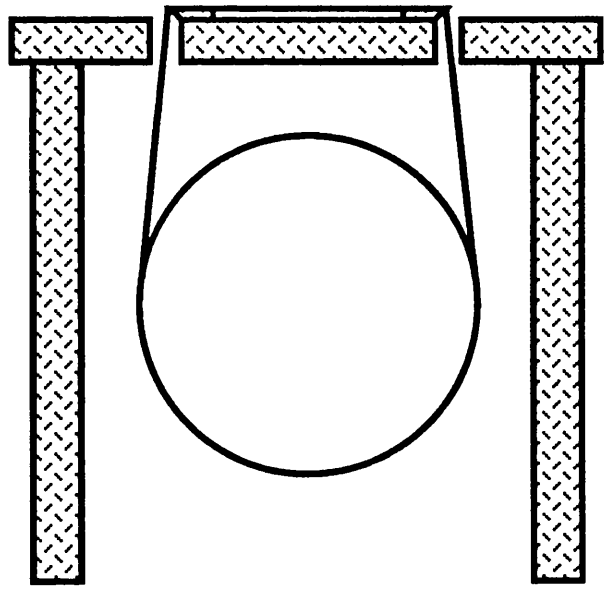

Figure 2.4: The Method of Suspension of a Sample of Material Under Test.

The mass was excited in one of three ways, with the method chosen depending on the material under test:

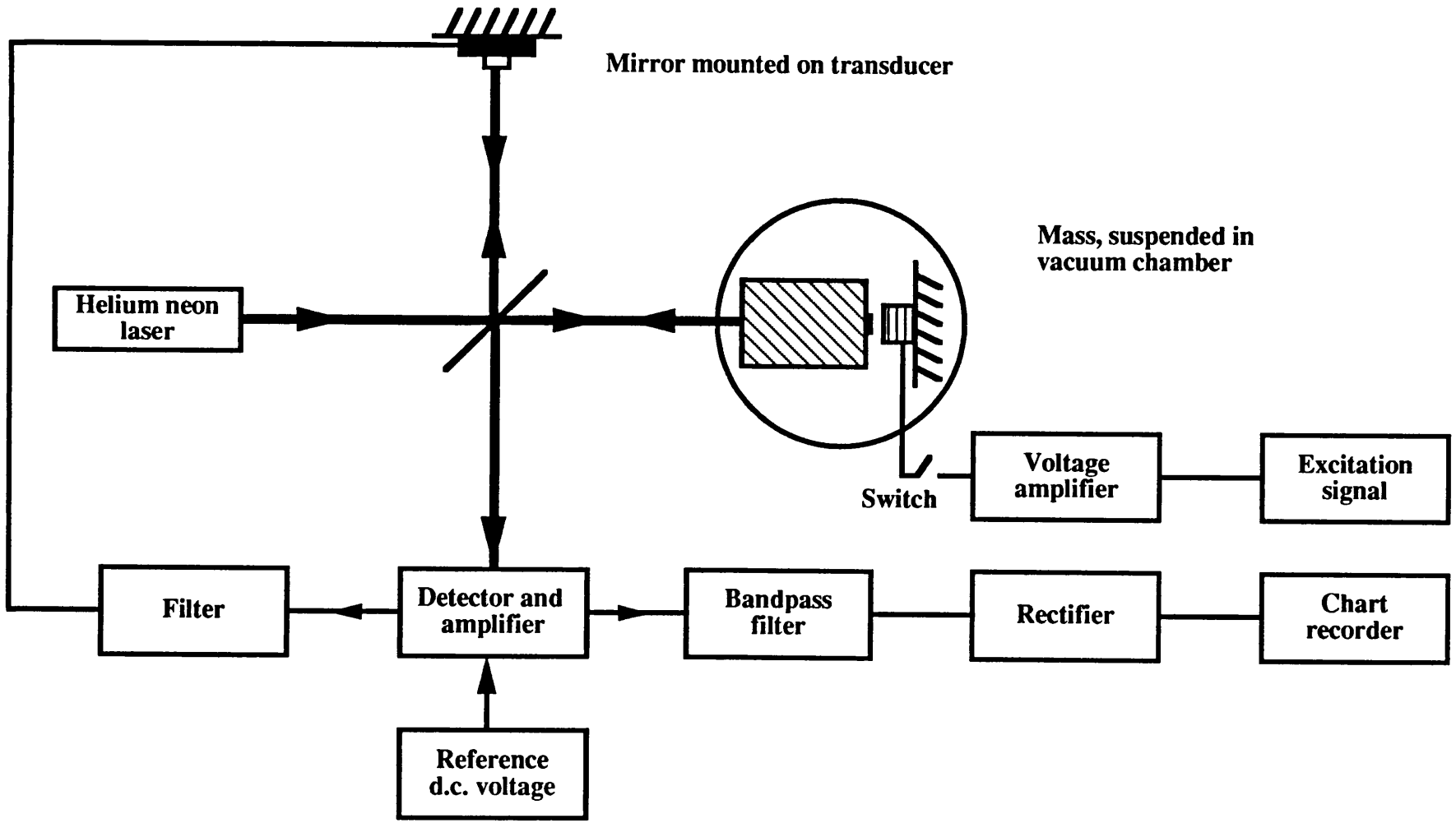

Figure 2.3: Schematic of Experimental Arrangement for Measuring the Quality Factor of a Suspended Sample of Material.

a) magnetically, as indicated in figure 2.3, using a small (approximately 3 mm square) samarium cobalt magnet glued to the mass with cyanoacrylate adhesive, and a drive coil of d.c. resistance 24 Ω and inductance 7 mH. The coil was placed about 5 mm from the magnet. The applied a.c. voltage varied depending of the level of excitation required but was typically in the range of 1 - 30 V peak to peak. Appendix A contains a calculation of the level of damping produced by such an excitation mechanism. This was not predicted to be a limitation to any of the Q measurements made by the author.

b) capacitively using the capacitance between a copper plate and its image formed in the dielectric bulk of the material under test. The plate was circular, with diameter slightly smaller than that of the mass, and was placed a few millimetres away from the mass. A d.c. offset voltage of about 200 V and an a.c. voltage of about 400 V peak to peak was applied to the capacitor plate in order to excite the mass. A large resistor, R, was also inserted in series between the high voltage amplifier and the capacitor plate in order to protect the high voltage supply should the capacitor short circuit. The value of R was chosen so that $(2\pi RC)^{-1} >> f_o$ where C is the size of the capacitance formed between the mass and the plate and f_o is the resonant frequency of the mode of interest of the mass. Appendix B contains a calculation of the level of damping produced by such an excitation mechanism. This was not predicted to be a limit to the Q measurements made.

c) inductively using the force produced between a drive coil, with the same parameters as (a), and the image coil formed in the sample. Note that the drive coil produces a force, F, that is proportional to the square of the current, i, passing through it and hence if $i = i_o \sin\omega t$, the force produced will be proportional to $\cos 2\omega t$. Thus in order to excite the sample at its resonant frequency, the signal applied to the drive coil must be at half the sample's resonant frequency. The drive coil was placed a few millimetres away from the mass and again the applied a.c. voltage was varied according to the level of excitation required but was typically in the range of of 1 - 30 V peak to peak.

The sensing system used a Michelson interferometer, one arm of which was formed

between the beamsplitter and the mass, which was either polished or had a small mirror (approximately 5 mm by 3 mm) glued to it using cyanoacrylate adhesive. The other arm was formed between the beamsplitter and a mirror mounted on a piezo-electric transducer (PZT). A d.c. bias was applied to the fringe signal from the interferometer in order to make it symmetrical about zero volts. By feeding back a fraction of the signal from the interferometer to the PZT at frequencies up to 1 kHz, the mirror attached to it was made to follow the pendulum motion of the suspended mass, thereby locking the output signal from the interferometer to the side of a fringe. This then allowed linear measurements of small amplitude motions of the mass to be made at higher frequencies. Appendix C contains a diagram of the feedback circuit which was used. The amplified output signal from the detector was then filtered and rectified before being displayed on a chart recorder. In order to measure the Q of a mass, the excitation signal applied to it was abruptly removed using a switch with a short disconnection time (approximately 0.5 ms). This then allowed the free decay of the amplitude of oscillation of the mode under study to be recorded on the chart recorder. From this the decay time was measured and hence the Q for the mode of the sample calculated using eq. (2.16).

Note on the Electronics used

The PZT was covered in a damping compound in order to reduce the effect of its resonances in the output signal of the detector. When this was done the PZT was capable of providing 1.8×10^{-7} m V^{-1} and had its first resonance at about 3 kHz. Note that an active rather than a passive rectifier was used since at voltages less than approximately 0.6 V a semiconductor diode will cease to conduct and hence a passive rectifier would be non-linear at low signal voltages. The circuit diagram for the active rectifier used is contained in Appendix C.

'Self-oscillation' - An Alternative Method of Exciting the Mass

It was found that the mass could be made to 'self-oscillate' in its fundamental longitudinal mode i.e. to resonate without the use of a signal generator. The method relied on the interferometer detecting small motions of the front face of the mass. After the output signal from the interferometer had been amplified and filtered, a fraction of this signal was fed back to the drive mechanism leading to the amplitude of oscillation of the mass

building up and sustaining itself. It was found that in order for this method to work the amplifier needed to have a wide frequency passband (~ 10 kHz - 1 MHz) and high gain (~ 10^4) and that the lower cut-off frequency of the bandpass filter had to be just below the frequency of the longitudinal mode. Self-oscillation of the mass was tested and found to work with both a magnetic and a capacitive drive. Thus the problem of trying to tune onto a high Q resonance was eliminated. However this method of exciting the mass had the disadvantage that the output signal from the interferometer had to remain very well locked to the side of a fringe. Since no damping is applied to the suspended mass, this was sometimes difficult to achieve and so in practice this method of resonating the mass was seldom used.

Gas Damping

Note that experiments were conducted in vacuum, typically ~ 10^{-2} mbar, in order to reduce gas damping to a level where it does not degrade the Q. The limit to the Q of a mass due to such a damping mechanism may be written as follows, based on Suzuki's calculation for gas damping of a right circular cylindrical mass (Suzuki, 1983)

$$Q_g = \left[\frac{4P}{\pi c \rho} \sqrt{\frac{3M}{RT}} + \frac{S}{m} \sqrt{\frac{2\eta PM}{\omega_o RT}} \right]^{-1} \qquad (2.37)$$

where P is the pressure of the gas,

M is the molecular weight of the gas (M = 0.029 kg mol^{-1} for air),

R is the gas constant (R = 8.314 J K^{-1} mol^{-1}),

T is the temperature (300 K),

c is the speed of sound in the mass,

ρ is the density of the mass,

S is the surface area of the mass,

m is the mass,

η is the viscosity of the gas (η = 1.8 x 10^{-5} kg m^{-1} s^{-1} for air at 300 K) and

ω_o is the angular frequency of the mass.

The first term in this equation represents losses due to individual gas molecules striking the mass. The second term represents frictional losses due to the viscosity of the gas.

The latter term will dominate if the mean free path of the gas molecules is less than or of the order of the dimensions of the mass. For pressures of ~ 10^{-2} mbar the mean free path of nitrogen molecules is ~ 1 cm.

The highest Q value measured by the author was for a sample of polycrystalline silicon, as discussed in chapter 4. This mass was 4 inches in diameter by 2.9 inches long with its first longitudinal mode at a frequency of 47.7 kHz. From eq. (2.37) it is thus predicted that the Q of such a mass, at a pressure of 10^{-2} mbar, is limited to a value of 7 x 10^{8} by gas damping alone. This is two orders of magnitude higher than the measured value and thus gas damping is not predicted to be a limitation to the measurements.

2.5 Preliminary Measurements

The modes which are most important in a laser interferometric gravitational wave detector are those in which there is a net movement of the parts of the face interrogated by the sensing beam. One of the chief modes of interest for these quality factor measurements was therefore the fundamental longitudinal mode.

In the course of developing the method described in section 2.4 for measuring the Q of materials, an aluminium mass was used to test the experimental technique. The mass, of alloy 6082 (U.S.A. specification), was 3 inches in diameter by 3 inches long and was suspended on a single loop of wire 0.006 inches in diameter in order to allow a measurement of the Q of its fundamental longitudinal mode. The suspension wire was allowed to breakaway naturally from the sides of the mass. A magnetic excitation was employed with the magnet used being 9 mm in diameter and 3 mm thick. It was found that if the magnet was not fully adhered to the mass, the Q of the longitudinal mode was significantly reduced. Indeed it was possible to damp the resonance so heavily that the sensing system could not detect it. In bonding the magnet to the mass it is important that both surfaces are clean and that the entire surface of the magnet is covered by a thin coat of glue. It was thus decided when magnetically exciting subsequent samples of material to use a piece of magnet with a smaller surface area (~ 3 mm square) since it would be easier to achieve a good contact between the mass and the magnet.

For the aluminium mass under consideration here, the problem was eliminated by replacing the magnetic drive with an inductive drive. With this, the Q of the pure fundamental longitudinal mode was found to be $(3.3 \pm 0.1) \times 10^4$ at a frequency of 31.358 kHz. This particular aluminium alloy was thus found to have a low Q compared to the alloy detailed in table 2.1. Note that another aluminium sample of alloy 2014, 1 inch in diameter by 3 inches long, excited in the same way, yielded a Q of $(4.3 \pm 0.1) \times 10^5$ when resonating in its longitudinal mode, which occurred at frequency of 32.010 kHz. This Q value compares well with the alloy of table 2.1 and is also in agreement with a previous measurement of this material, made using a different experimental method (McCourt, 1976). A typical decay trace from this mass is shown in figure 2.5.

2.6 Conclusion

In this chapter the importance of choosing a high Q material for the test masses in an interferometric gravitational wave detector in order to minimise thermal noise, has been discussed. A method for measuring the Q of possible materials has also been outlined and preliminary measurements on aluminum samples have been presented.

In the course of measuring the Q of the fundamental longitudinal mode of the first aluminum sample, coupling between two internal modes of the mass was observed. It was found that the Q values of the coupled system were degraded by that of the more lossy mode (see also Braginsky et al, 1985, p. 25). This then raises the question, is the thermal motion of such a mass, at frequencies well below its resonant frequencies, increased by the apparent degradation in Q? This forms the subject of chapter 3.

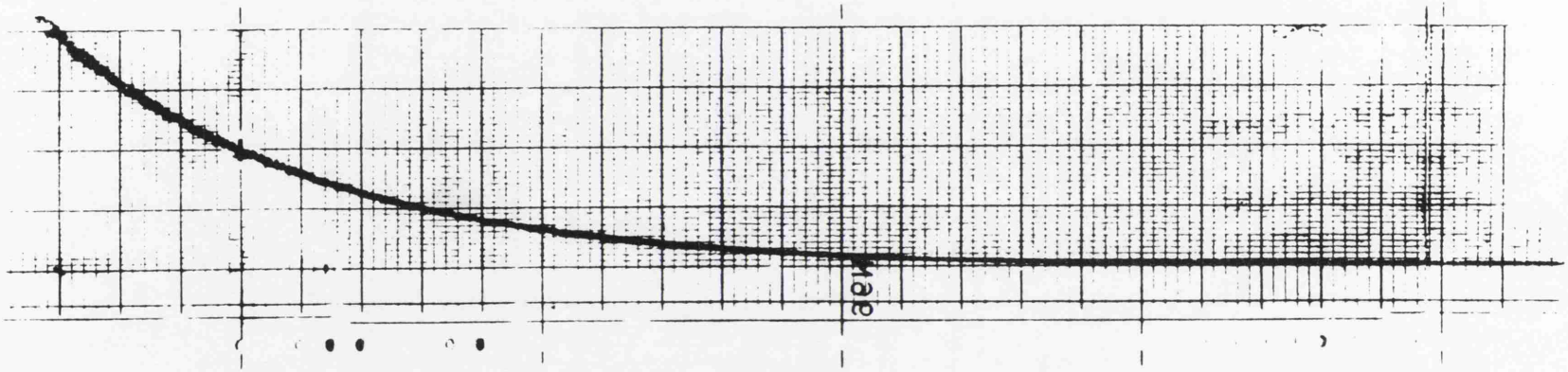

Figure 2.5: A Typical Decay Trace. *The trace shown is for an aluminum mass of alloy 2014 as detailed in the text. The x axis is in units of 10 mm s^{-1} and the y axis is in units of 50 mV cm^{-1} (one major division is equivalent to 1 cm). The frequency of the longitudinal mode of the sample is 32.010 kHz. The decay time recorded on the trace is (4.4 ± 0.1) s implying that the Q of the longitudinal mode is $(4.4 \pm 0.1) \times 10^5$.*

Chapter 3

An Investigation of Coupling Between Internal Modes of Test Masses

3.1 Introduction

Coupling between internal modes of masses has been observed in two samples each of a different material but the same aspect ratio (aspect ratio = height / radius). In this chapter details are given of experimental investigations of mode coupling and theoretical modelling, using equivalent circuits, to determine the effect, if any, of such coupling on the level of thermal motion of a mass at frequencies well below its resonant frequencies. Details of this work are also presented in a paper (Logan et al, 1991) which is contained in Appendix D.

3.2 Mode Coupling in Aluminium

In the course of measuring the Q value of the aluminium mass of alloy 6082, 3 inches in diameter by 3 inches long, as described in section 2.5, two small aluminium lugs were glued onto the sides of the mass, as indicated in figure 3.1, using toughened acrylic adhesive. This was done in order to define the point at which the suspension wire broke free from the mass and to minimise friction between the mass and the suspension wire at the breakaway point A small mirror was also attached to the centre of the front face of the mass.

Excitation of the mass was achieved using a magnetic drive (section 2.4). It was found that at frequencies close to the expected frequency of the fundamental longitudinal mode of the mass, instead of only one resonance being observed, there were in fact two, only

70 Hz apart at a frequency of ~ 31 kHz. A typical response is shown in figure 3.2.

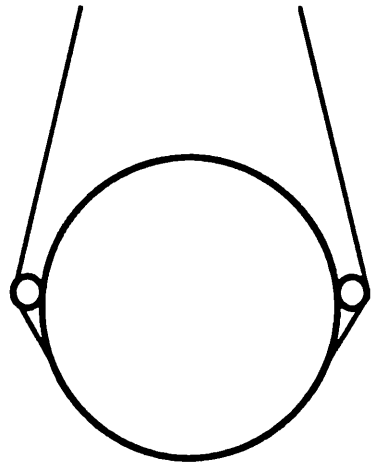

Figure 3.1: The Position of the Lugs used in the Suspension of the Aluminium Mass.

3.2.1 The Effect of Different Lugs on the Observed Mode Coupling

It was discovered that if the lugs were removed from the mass only one resonance was observed at this frequency and furthermore that if the lugs were glued onto a mass of the same alloy but of aspect ratio 1.8 rather than 2, once more only one resonance was observed. The effect of first suspending the mass and then gluing the lugs on top of the wire was also investigated to establish whether the coupling was due to the inward force of the suspension wire on the mass. Decreasing the inward force in this manner made no apparent difference to the frequency separation or shape of the two resonances. Thus it became clear that the lugs themselves were acting to couple together two normal modes of the unloaded mass.

Investigations were carried out to determine the effect of different lengths and diameters of lugs on the coupled modes by observing in each case a spectrum of amplitude of motion of the centre of the front face of the mass against frequency of excitation. Six sets of lugs were used; three of diameter 6.5 mm with lengths 4 mm, 8 mm and 14 mm and three sets of length 9 mm with diameters 6.5 mm, 8 mm and 10 mm. In both cases it was noted that as the mass of the lugs became smaller

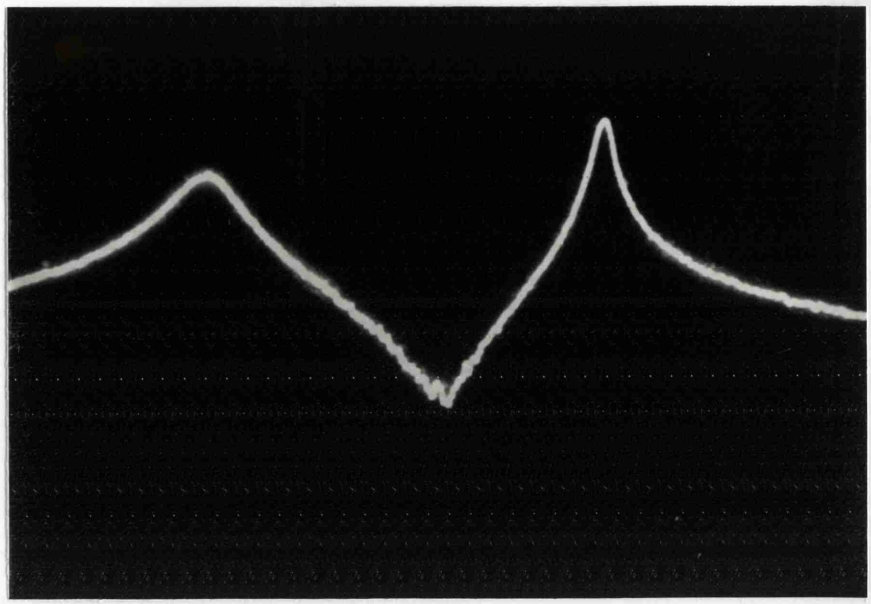

Figure 3.2: A Typical Spectrum of the Amplitude of Motion of the Central Point of the Front Face versus Frequency of Excitation of the Aluminium Bar. *The lugs used were 9 mm in length and 8 mm in diameter and the resonances occurred at 31.102 and 31.196 kHz. Note that the y axis is a log scale. The spectrum was accumulated using a spectrum analyser with a tracking oscillator which was used to drive the mass.*

1) the lower frequency mode, f_1, approached the frequency of the longitudinal mode as seen without lugs, f_o ($f_1 < f_o$). The resonance was observed to increase in both amplitude and Q.

2) The upper frequency mode, f_2, remained at the same frequency, approximately f_o, but decreased in amplitude.

It was also observed that if the lugs were not properly adhered to the mass, the Q of only the lower frequency resonance was lowered. This indicated that the glue joint was being flexed more by this mode.

3.2.2 Prediction of the Modes Involved

McMahon's work on resonant frequencies and modes of vibrations of cylinders (McMahon, 1964) allowed prediction of which normal modes of the mass were involved in the coupled system. With this knowledge it was postulated that the lugs were acting to couple the fundamental longitudinal mode and the n = 2 symmetric radial contour mode, where the order, n, of the mode denotes the circumferential wave number. These modes are shown schematically in figure 3.3(a) and (b). It should be noted that without coupling, the measurement technique would not be expected to detect the radial contour mode since the centre of the front face, the point under study, is a node.

In order to try to experimentally verify this premise, the lugs were attached to the mass in the position shown in figure 3.4 such that they made an angle of 90° with the centre of the mass. This arrangement resulted in only one mode being observed. It was therefore concluded that the radial contour mode was oriented such that the lugs, when positioned as indicated in figure 3.4, were located on the nodal lines.

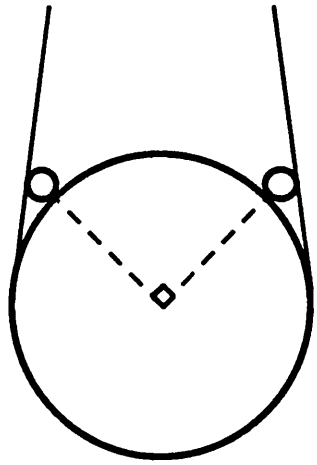

Figure 3.4 Lugs Attached to the Aluminium Mass. *The lugs are positioned such that they Make an Angle of 90° with the Centre of Mass.*

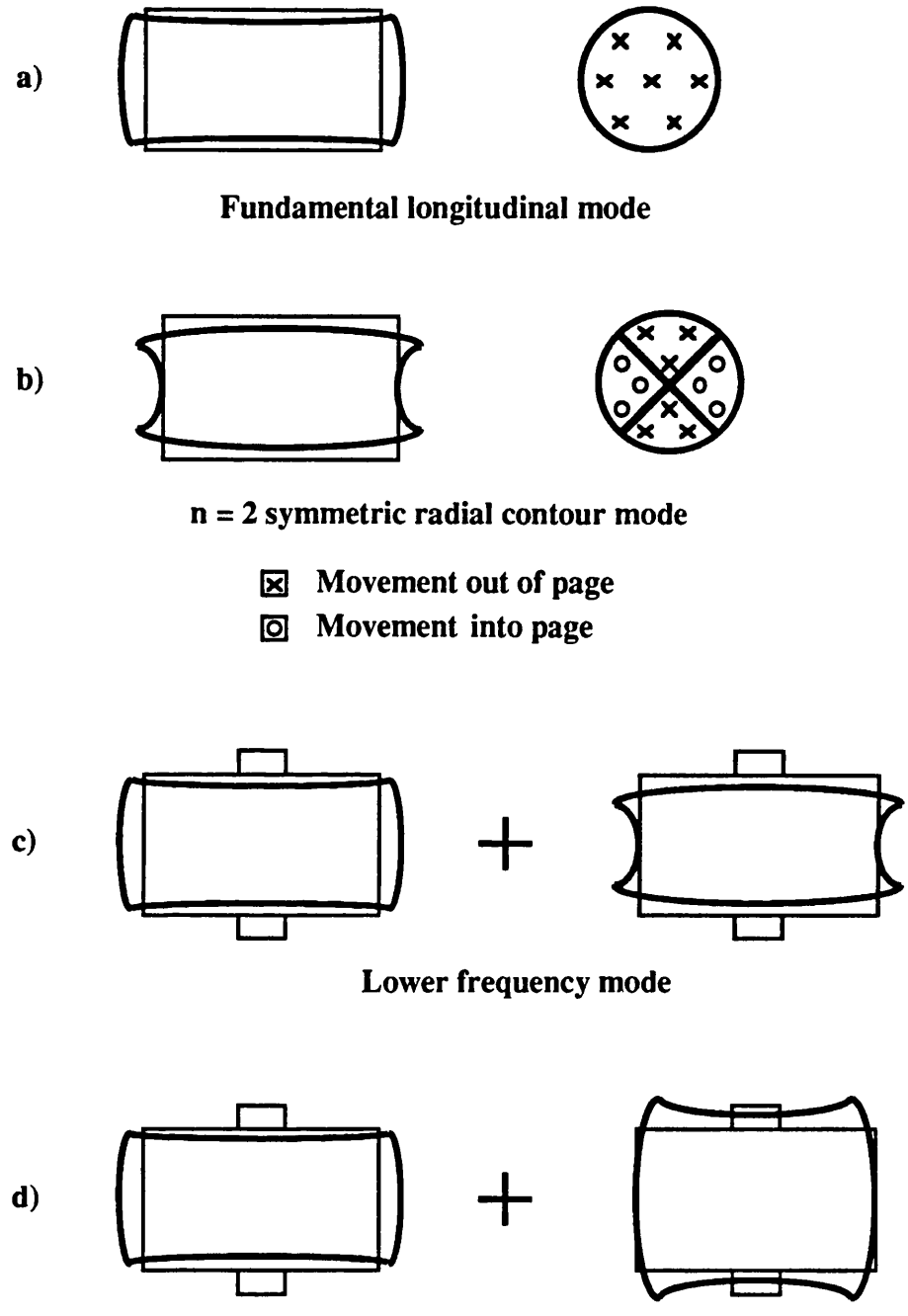

Figure 3.3: The Formation of Coupled Modes in Aluminium. *(a) and (b) Pure modes in aluminium. (c) and (d) Coupled modes, viewed from above, formed by the addition of lugs on the sides of the bar as indicated.*

Since the glue joint was apparently flexed more by the lower frequency coupled mode, it was postulated that this mode was formed by the two pure modes coupling in such a way that, at the position of the lugs, the modes were in phase with respect to longitudinal extension and compression. The predicted forms for the coupled modes are thus as shown in figures 3.3(c) and (d). Note that for the upper frequency coupled mode, the two pure modes are longitudinally out of phase at the position of the lugs, and thus the lugs are not flexed very much. It would therefore be expected that the lugs would have less effect on the upper frequency coupled mode. This agrees with the observation that, as the coupling changed, this mode remained at approximately the same frequency.

3.3 Q Measurements of Columnar Silicon

3.3.1 The Structure of Columnar Silicon

Columnar silicon is a possible material for the test masses in laser interferometric gravitational wave detectors. It is well known that single crystal silicon has a very high Q at room temperature (table 2.1), however as yet pieces of this material large enough to form the mirrors for a 3 km detector (~ 0.5 m diameter and 0.25 m thick) have not been produced. A possible alternative to this may be columnar silicon. This is a material which consists of numerous columns of single crystal silicon, with each column grown in the same direction. In the samples studied by the author, these columns were grown preferentially in the [111] direction but may deviate from this by up to 10°. Note that the crystals were all grown approximately parallel to the axis of the cylinder. A sample of columnar silicon is shown in figure 3.5.

3.3.2 Observation of a Coupled Mode System

The first columnar silicon mass to be studied was 3 inches in diameter by 3 inches long i.e. the same dimensions as the aluminium mass of section 3.2. It was suspended on a single loop of wire 0.0035 inches in diameter. No lugs were used in the suspension. The mass was excited magnetically and had a small mirror attached to the centre of the front face.

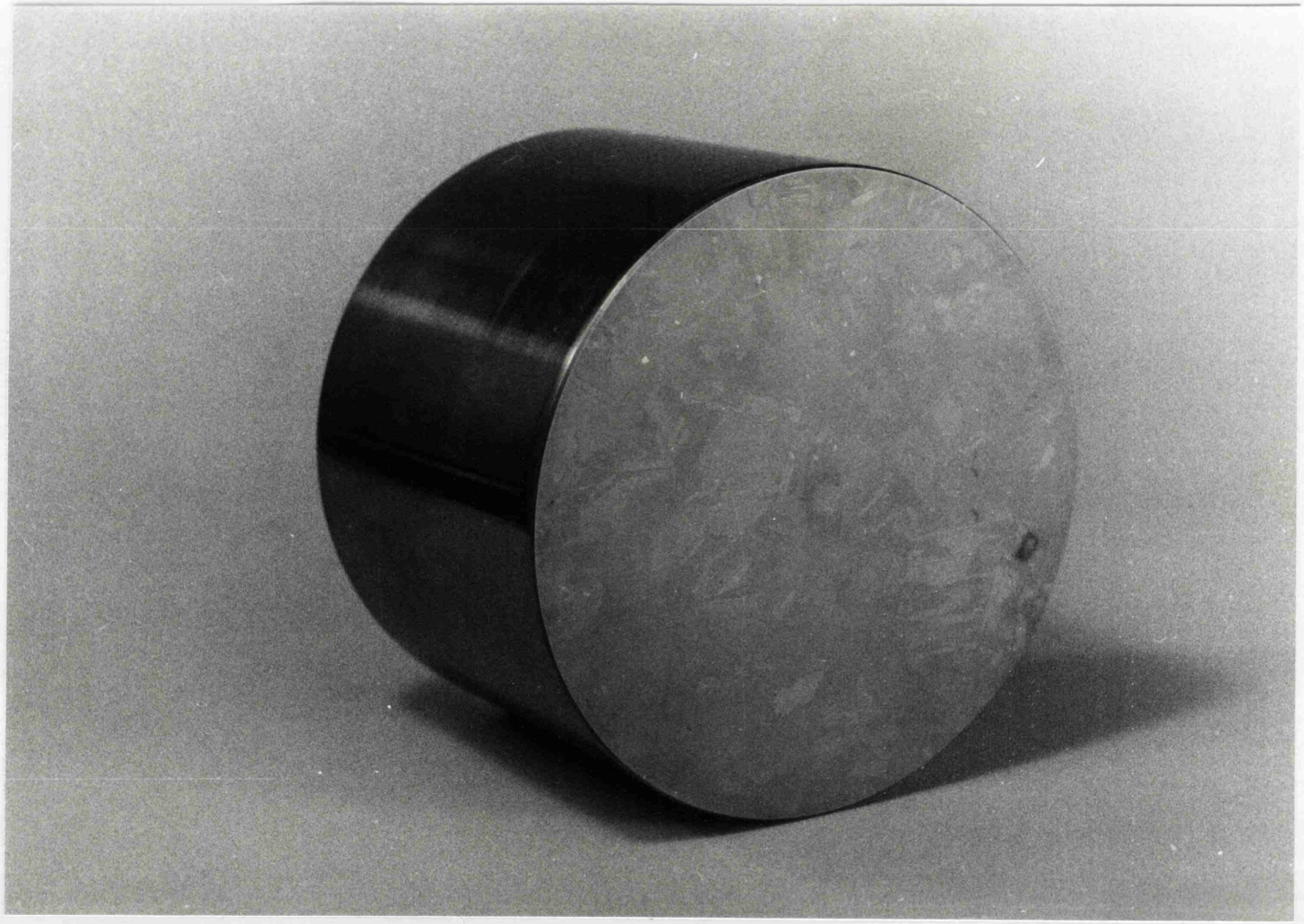

Figure 3.5: A Columnar Silicon Mass. The sample shown is 4 inches in diameter by 2.9 inches long.

It was found that when the mass was excited, instead of observing only one resonance at frequencies close to the expected frequency of the longitudinal mode, there were in fact two resonances, this time only 40 Hz apart at a frequency of ~ 52 kHz. The highest measured Q for the mode at 52.516 kHz was $(4.3 \pm 0.1) \times 10^5$ and the highest measured Q for the mode at 52.556 kHz, $(7.3 \pm 0.1) \times 10^5$. Some variation in the measured Q was observed with the smallest measured values being approximately 20% less than the values quoted above for each mode. Possible reasons for such a variation will be the subject of chapter 4.

It was postulated that the observed modes were in fact coupled modes and since the silicon mass had the same aspect ratio as the aluminium mass, the modes involved were again thought to be the fundamental longitudinal mode and the n = 2 symmetric radial contour mode shown in figures 3.3(a) and (b).

It was desirable to try to measure the Q of the modes with both magnet and mirror removed since this would eliminate any worry about limitations to the measured Q due to badly formed glue joints. The first stage of this investigation was to remove the mirror. The front face of the silicon was then polished, in order to reflect laser light, using a lapping wheel and diamond paste. Unfortunately during polishing the mass sustained surface damage and thus it was not possible to compare the Q values of the modes with earlier measurements since it was found that these values had both been degraded to a value of about 1×10^5.

However once the front face of the mass was polished, it was possible to align the interferometer, used to sense the motion of the mass, with any part of the face. Thus it was possible to make spot measurements of the amplitude of motion across the face of the mass.

The amplitude of motion may be calculated with consideration of figure 3.6.

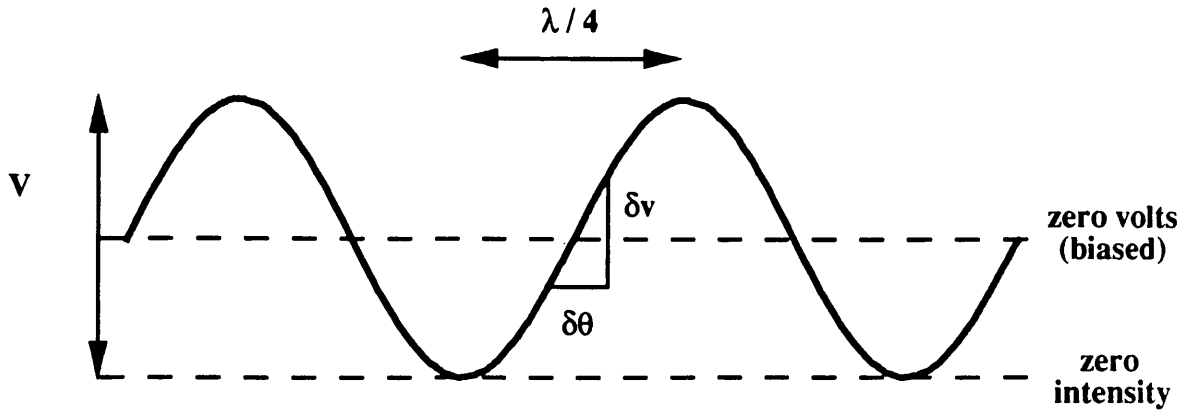

Figure 3.6: Conversion of the Fringe Intensity Signal to a Relative Displacement. *The interferometer arm lengths are stabilised relative to each other to give an output half of the maximum intensity from the interferometer. Symbols as defined in the text.*

The size of the fringe signal, when no feedback is employed to stabilise the arm lengths of the interferometer, is V volts peak to peak. Thus the output signal, v, from the interferometer may be described by

$$v = \frac{V}{2} \sin\theta \tag{3.1}$$

where θ represents the phase of the signal.

Hence the gradient of the fringe signal about zero volts

$$\left(\frac{\delta v}{\delta \theta}\right)_{v=0} = \frac{V}{2} \tag{3.2}$$

Now consider the separation of the mirrors changing by an amount δx. The difference between the path lengths in each arm of the interferometer is thus $2\delta x$. Hence the phase difference between the two interfering beams, $\delta\theta$, is given by

$$\delta\theta = \frac{2\pi}{\lambda} 2\delta x \tag{3.3}$$

Thus by combining eqs. (3.2) and (3.3), the following expression for δx may be obtained

$$\delta x = \frac{\lambda}{2\pi} \frac{\delta v}{V} \tag{3.4}$$

Crude maps of the amplitude of motion of the face of the mass resonating in air were drawn with 10 data points for each mode as shown in figure 3.7. The lower frequency mode has generally a higher amplitude of motion across the face of the mass than the upper frequency mode. It is also noted that the ratio of maximum to minimum amplitude for the lower frequency mode is about 2 whereas for the upper frequency mode this ratio is about 5. It was thus predicted that since there was a smaller variation in amplitude across the face of the mass, the lower frequency mode was predominantly due to the fundamental longitudinal mode with a lesser amount of the radial contour mode. The larger variation in amplitude observed across the face of the mass for the upper frequency mode indicated that this mode was formed mainly by the radial contour mode with a lesser amount of the longitudinal mode.

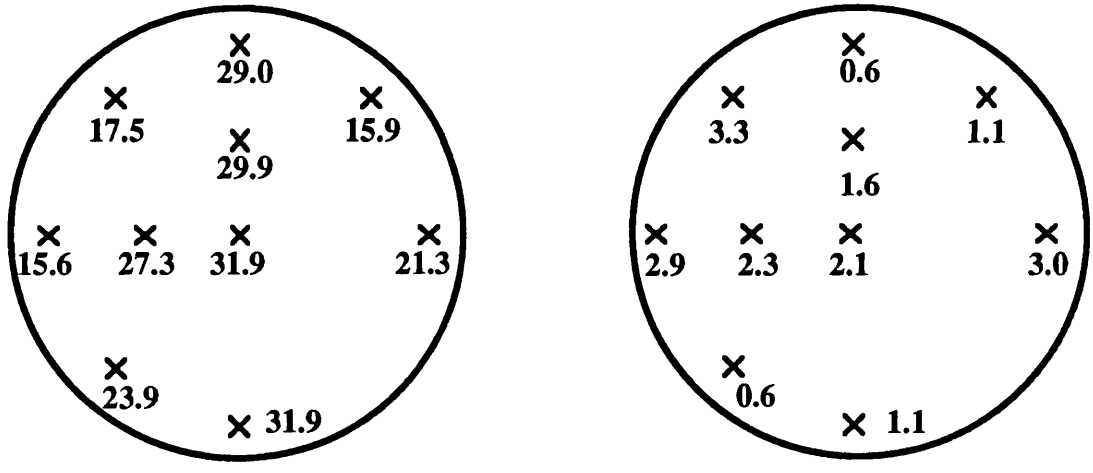

Lower frequency mode **Upper frequency mode**

Figure 3.7: Diagram Indicating the Level of Motion Across the Face of the Silicon Mass for the Two Coupled Modes. *The crosses mark the approximate position at which the measurement was made. All amplitudes are in angstroms. Note that the diagrams contain no phase information.*

The magnet was then removed from the mass and the silicon was excited capacitively.

The Q values for both coupled modes were found to gradually increase over a period of a few weeks from 1 x 10^5 to 4 x 10^5. It is probable that this drift in the value of Q was due to loosely adhered flakes of silicon on the damaged surface of the mass which gradually fell off. Whilst the Q values after the mass was damaged were not comparable with earlier results it is to be noted that the two modes were still present and were still 40 Hz apart. Thus the coupling mechanism could not be loading of the mass by the mirror and / or magnet.

3.3.3 Columnar Silicon of Aspect Ratio 1.45

The dimensions of a new piece of columnar silicon were chosen to be 2.9 inches long by 4 inches in diameter since the work of McMahon (McMahon, 1964) indicated that an aspect ratio of 1.45 would seem to leave a reasonable gap in frequency between the fundamental longitudinal resonance and the nearest modes on either side of it. It should be noted that McMahon's work was carried out for isotropic aluminium and steel and thus any predictions drawn from it will not be exact for silicon which is anisotropic.

As predicted, only one resonance was observed at frequencies close to the expected frequency of the fundamental longitudinal mode. Using magnetic excitation, initial measurements yielded a Q of $(3.6 \pm 0.1) \times 10^6$ at a frequency of 47.791 kHz for this mode. Note that the face of this mass had been polished and hence no mirror was required. Chapter 4 contains greater details of the investigations of the Q of this mass.

It is evident that this value is considerably higher than those measured for the coupled modes. In the 3 inch mass, energy would be shared between the contributing pure modes and thus the Q values of the coupled system are degraded by that of the more lossy pure mode. This is in agreement with a finding of Braginsky's (Braginsky et al, 1985, p. 25).

3.4 Verification of the Modes Using a Vibration Pattern Imager

3.4.1 The Vibration Pattern Imager

A commercial vibration pattern imager (VPI), (VPI 9000, Ometron Limited), was used to investigate the structure of the modes in the aluminium and silicon samples. The VPI is based on a Michelson interferometer in which a laser beam is reflected from a test structure and is then recombined with a reference laser beam which is entirely contained within the VPI unit. The direction and magnitude of motion of the test surface is determined from the resulting optical signal using a quadrature phase sensitive optical scheme with the drive signal for the mass acting as a reference signal (VPI 9000, Ometron Limited). The test surface is repeatedly scanned by the laser beam in order to build up an image of the velocity distribution, which is then processed and displayed by computer.

The sample to be studied was suspended as a pendulum in air, with excitation provided via the rear face. A magnetic drive was employed for this purpose since this provided the high level of drive required in order for the VPI to be able to detect the motion of the silicon masses resonating at frequencies close to 50 kHz, which is on the border of the VPI's operating range. Of the order of 5 A was passed through the drive coil in order to achieve this. To ensure that the mass was on resonance, the Michelson interferometer, used for the Q measurements, was employed to sense the motion of the rear face of the mass.

3.4.2 Aluminium

Figure 3.8(a) shows the VPI picture of the aluminium mass resonating in the pure fundamental longitudinal mode at 31.240 kHz. The form of this is as expected with the centre undergoing more motion than the edges.

Figures 3.8(b) and (c) show the coupled modes which resulted when lugs 9 mm long by 8 mm in diameter were attached to the sides of the mass. Figure 3.8(b) shows the lower frequency mode at 31.120 kHz and figure 3.8(c) the upper frequency mode at 31.239 kHz. These frequencies are slightly different to those quoted in section 3.2.

ORIGINAL IN COLOUR

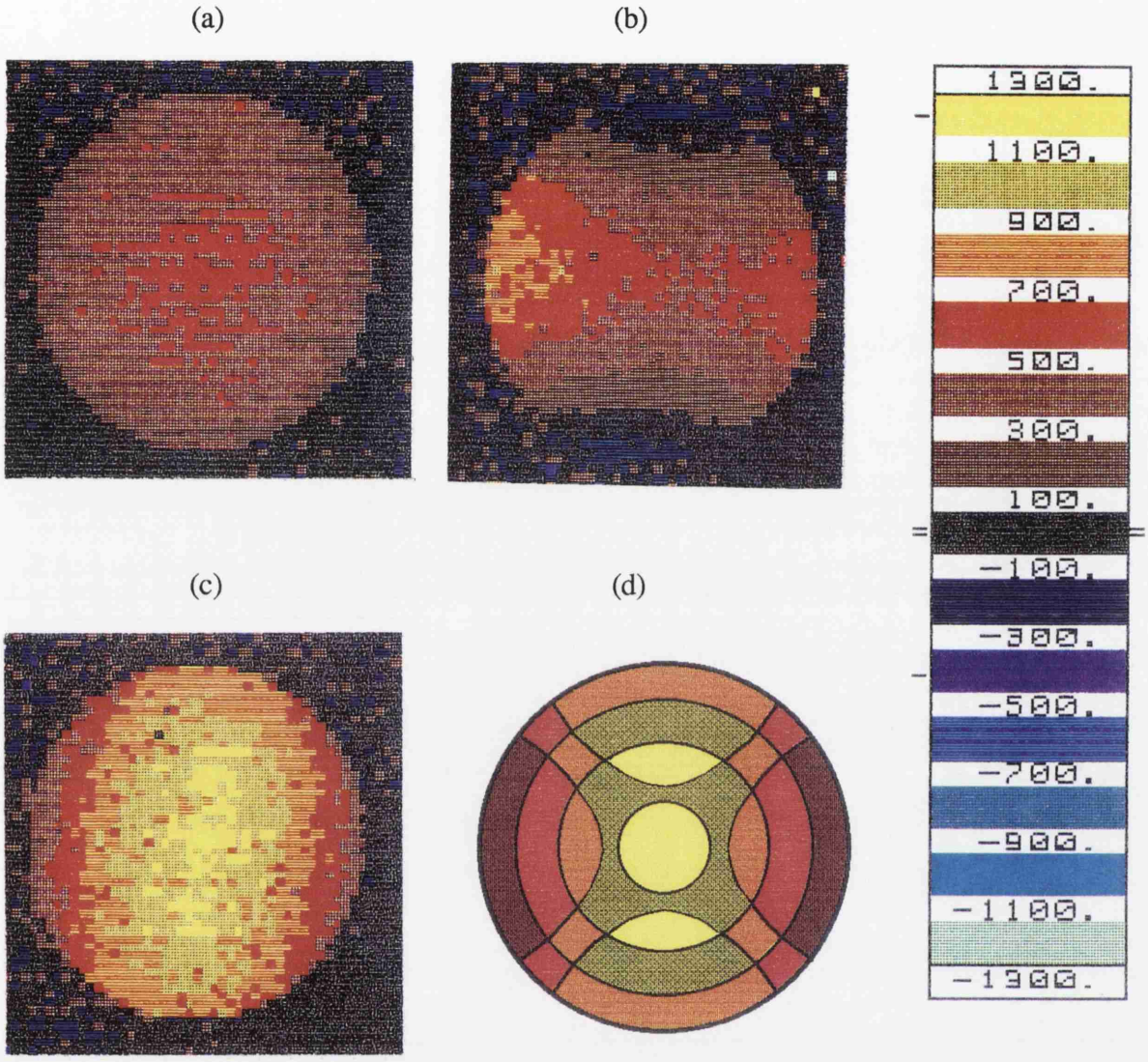

Figure 3.8: V.P.I. Images of the Front Face of the Aluminium Mass. *The mass is shown resonating in (a) its fundamental longitudinal mode (31.240 kHz), (b) its coupled lower frequency mode (31.120 kHz), (c) its coupled upper frequency mode (31.239 kHz). The scale shows arbitrary units. (d) Reconstruction of the upper coupled frequency mode. When the resolution of the imager is taken into consideration, this velocity map shows a picture very similar to that of (c).*

This is probably due to the mirror being glued onto the rear, instead of the front face of the mass, leading to the mass being asymmetrically loaded. The lower frequency mode shows obvious characteristics of the radial contour mode. Since backward moving quarters are still evident it is clear that this mode is composed mainly of the radial contour mode with a lesser amount of longitudinal motion adding in the phase shown in figure 3.3(c).

What is taking place in the upper frequency mode is not immediately clear. Based on the earlier deduction that this mode is formed by the radial contour mode adding to the longitudinal mode in the phase shown in figure 3.3(d), an attempt was made to reconstruct the pattern of figure 3.8(c) using the velocity information which this picture contains. This was done using the fact that the centre of the pure radial contour mode is a node and thus all the movement at the centre of figure 3.8(c) is due to the longitudinal mode. The velocity at the top and bottom of the VPI picture must then be due to the quarters of the radial contour mode adding in phase with the longitudinal mode whereas the velocity at the left and right-handsides are from the radial contour quarters adding in the opposite phase to the longitudinal mode. This gave enough information to draw an approximate map of the velocities of each of these two modes. These maps were then superimposed giving the result shown in figure 3.8(d) which is very similar to figure 3.8(c). Thus it was deduced that this mode is composed mainly of the longitudinal mode with a small amount of the radial contour mode.

3.4.3 Columnar Silicon

Columnar Silicon of Aspect ratio 2

Figures 3.9(a) and (b) show the mode patterns for the lower and upper resonances, 52.270 and 52.436 kHz respectively, of the silicon mass of aspect ratio 2. Note that the frequency split between the resonances is larger than the 40 Hz mentioned in section 3.3.2. This is due to the loading of an extra magnet which was added to provide the necessary level of excitation to allow the VPI to detect the motion of the mass.The similarity to the mode shapes observed for aluminium is immediately obvious. The lower mode is mainly due to the longitudinal mode with a lesser contribution from the radial contour mode, as was shown in the previous section for the similar mode pattern in

ORIGINAL IN COLOUR

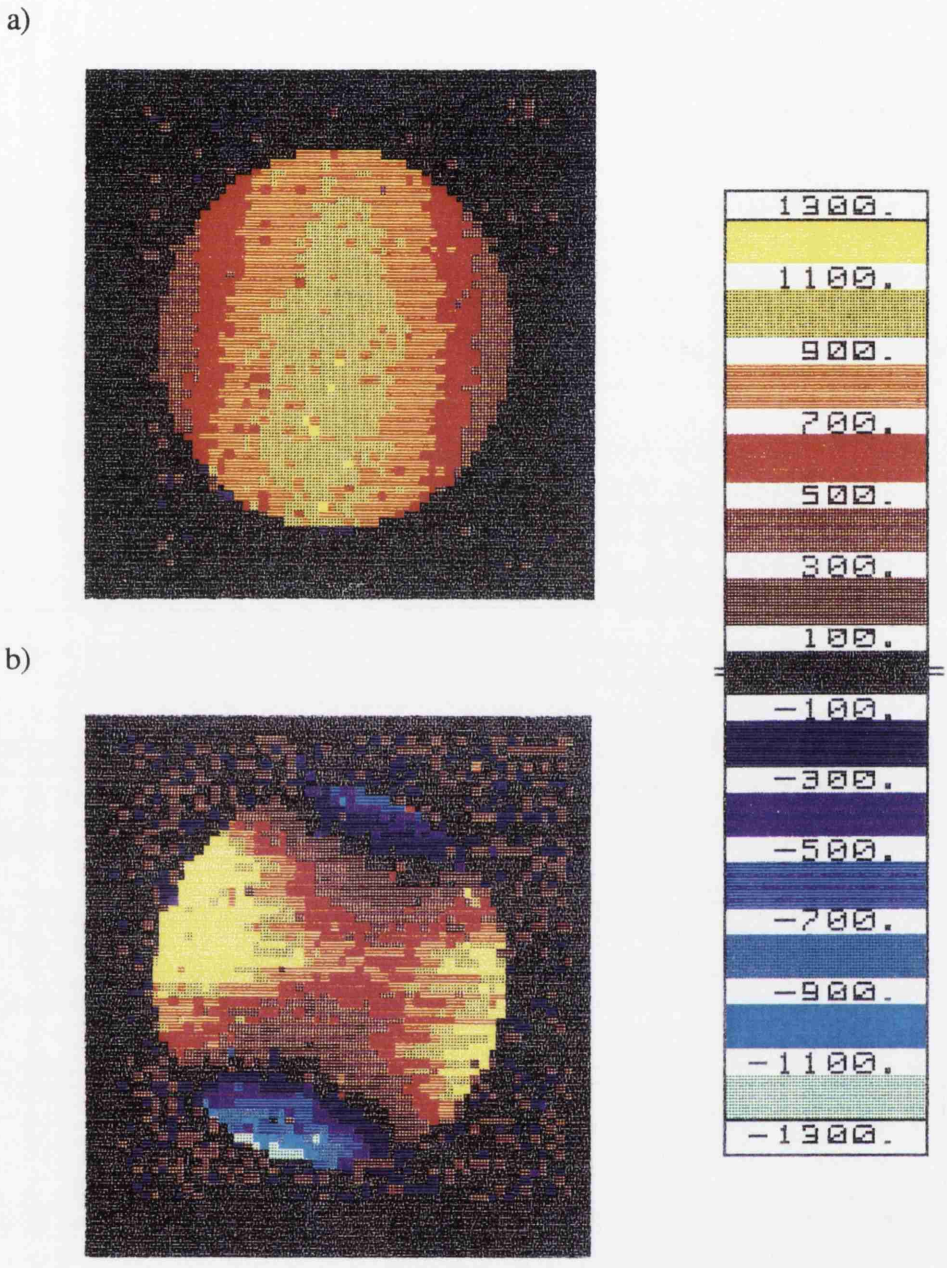

Figure 3.9: V.P.I. Images of the Front Face of the 3 inch Diameter Columnar Silicon Mass. *The mass is shown resonating in (a) its lower coupled frequency mode (52.270 kHz) and (b) its upper coupled frequency mode (52.436 kHz). Scale shows arbitrary units.*

aluminium. The upper mode is immediately observed to be predominantly due to the radial contour mode with a lesser amount of the longitudinal mode. These findings agree with the observations of section 3.3.2.

It is believed that the coupling in the columnar silicon is due to misalignments of the individual crystals in the mass together with the natural anisotropy of silicon itself. To verify this, the cylinder was rotated about its axis in order to observe the effect on the mode patterns. It was found that the patterns rotated in the same direction and by the same angle as the mass. It must be noted however that the surface damage which the mass had previously sustained may determine where the nodes of the system lie.

Columnar Silicon of Aspect Ratio 1.45

The columnar silicon mass of aspect ratio 1.45 was also studied using the VPI. Figure 3.10(a) shows the fundamental longitudinal mode which occurred at 47.773 kHz. It is observed that this is indeed a pure mode as expected.

Figure 3.10(d) and (e) show the expected form of the modes which lie, in frequency, on either side of the fundamental longitudinal mode (McMahon, 1964). Figures 3.10(b) and (c) show the VPI pictures of the front face of the mass for these modes, which occur at 42.764 and 55.824 kHz respectively. It is again observed that these are pure modes. It is also noted that the anisotropic nature of the mass did not distort the mode patterns from the shapes that would be predicted for an isotropic cylinder.

ORIGINAL IN COLOUR

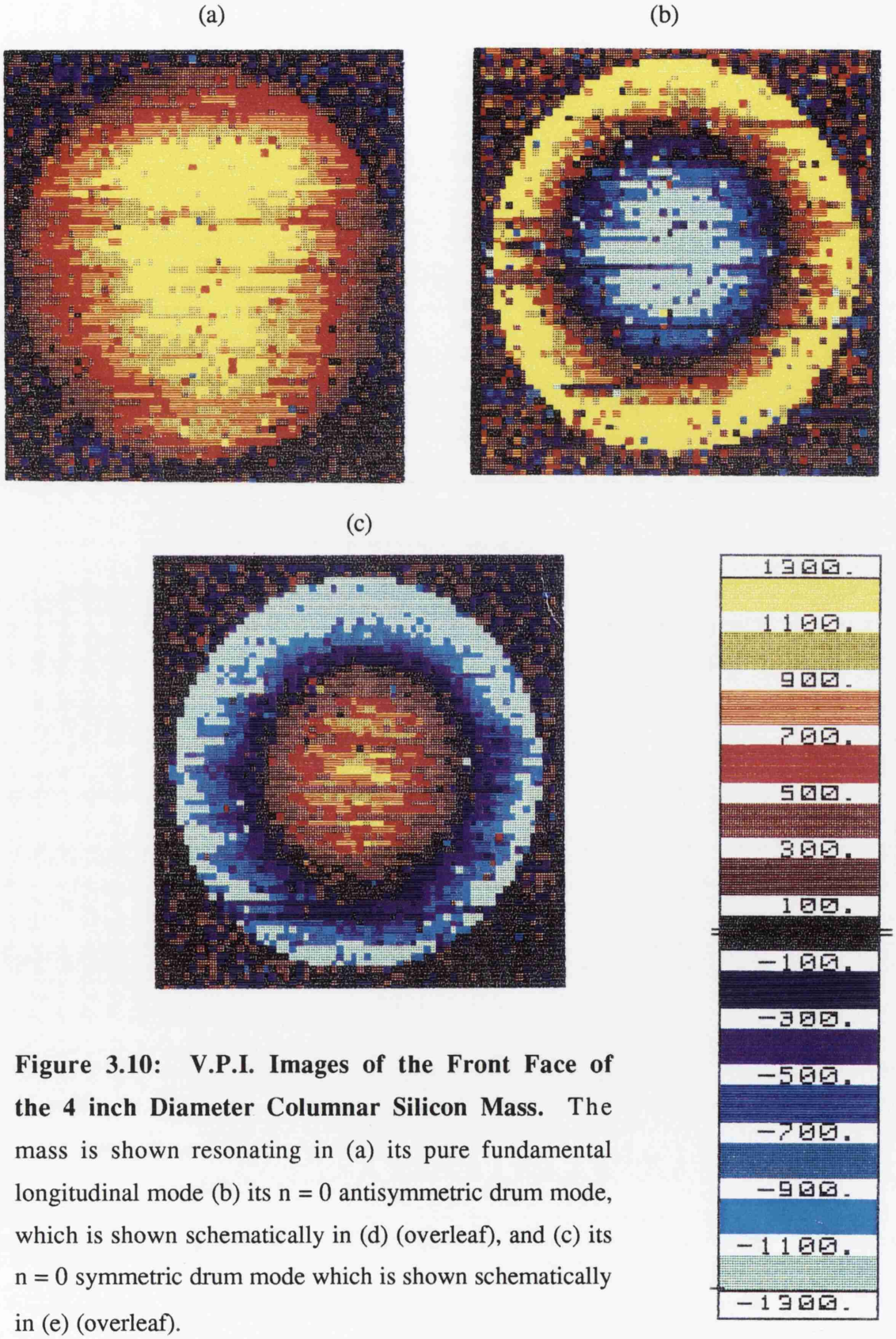

Figure 3.10: V.P.I. Images of the Front Face of the 4 inch Diameter Columnar Silicon Mass. The mass is shown resonating in (a) its pure fundamental longitudinal mode (b) its n = 0 antisymmetric drum mode, which is shown schematically in (d) (overleaf), and (c) its n = 0 symmetric drum mode which is shown schematically in (e) (overleaf).

Side view of mass

View of front face of mass

d)

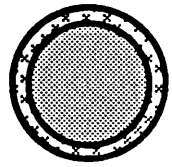

n = 0 antisymmetric drum mode

e)

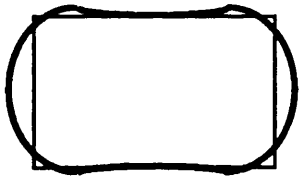

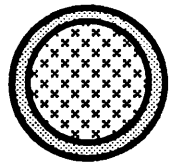

n = 0 symmetric drum mode

movement out of page

movement into page

Figure 3.10 continued.

3.5 Electrical Modelling of the Coupled Mode System in Aluminium

For the columnar silicon samples studied, it was observed that the Q values of the coupled modes were considerably lower than the Q value for the pure fundamental longitudinal mode measured at a similar frequency. Does this apparent degradation in Q cause an increase in the level of thermal motion, from that which would be expected from the pure modes, at frequencies well below the resonant frequencies of the mass? In order to gain insight into this problem, the mode coupling which was observed in the aluminium sample due to the presence of lugs was modelled using an equivalent circuit.

Consider the series resonant circuit of figure 3.11.

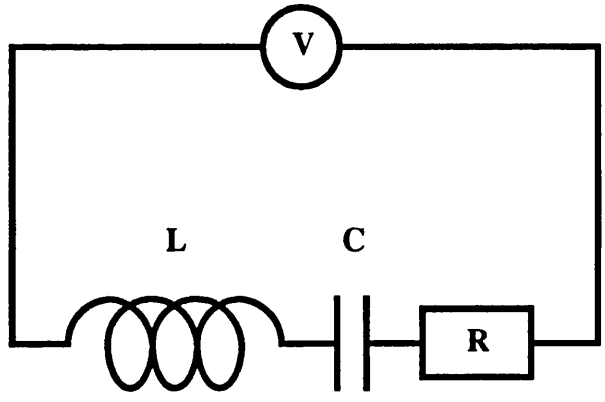

Figure 3.11: A Series Resonant Circuit. *This is formed by an inductor, L, a capacitor, C, a resistor, R, and a voltage source, V.*

The voltage, V, in the circuit is of the form

$$V = L\frac{d^2q}{dt^2} + R\frac{dq}{dt} + \frac{1}{C}q \tag{3.5}$$

where q is the charge flowing in the circuit.

If this equation is compared to the equation for a driven simple harmonic oscillator, eq. (2.21)

$$F = m\frac{d^2x}{dt^2} + b\frac{dx}{dt} + kx \qquad (3.6)$$

it is observed that

voltage	≡ force	inductance	≡ mass
charge	≡ displacement	resistance	≡ damping
current	≡ velocity	capacitance	≡ compliance = k^{-1}

$$Q = \frac{\omega_o L}{R} \equiv Q = \frac{\omega_o m}{b}$$

3.5.1 A Simple Coupling Model

Figure 3.12 shows the first circuit that was considered.

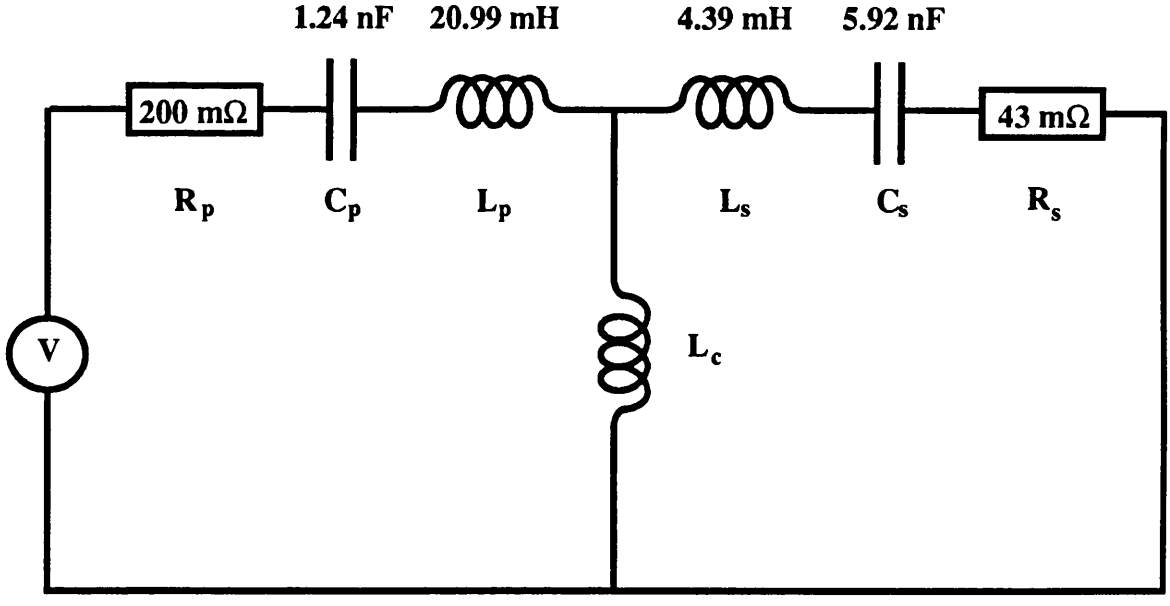

Figure 3.12: Circuit with Simple Inductive Coupling. *L_c was varied from 6.2 μH to 63 μH to fit the whole curve shown in figure 3.13.*

Algebraic analysis of this circuit with no damping present and with the resonant frequencies of the primary and secondary circuits chosen to be equal to f_o, gave the two resonant frequencies of the coupled circuit to be

$$f_1 = \frac{f_o}{\sqrt{1 + 4\pi^2 f_o^2 L_c (C_p + C_s)}} \qquad (3.7a)$$

$$f_2 = f_o \qquad (3.7b)$$

where $f_o = \frac{1}{2\pi\sqrt{L_p C_p}} = \frac{1}{2\pi\sqrt{L_s C_s}}$

From these equations it is observed that as the coupling inductor, L_c,decreases in value, the lower frequency resonance, f_1, increases in frequency towards f_o whilst the higher frequency resonance, f_2, remains at f_o. Thus the general behaviour of the circuit agrees with the observations of the coupled mode frequencies in aluminium as described in section 3.2.1.

For the lower frequency mode, the current in the primary circuit, i_p, and the secondary circuit, i_s, are in the ratio

$$\frac{i_s}{i_p} = -\frac{C_s}{C_p} \qquad \text{for } f = f_1 \qquad (3.8)$$

Thus the currents are 180° out of phase which in fact means that these currents flow in the same direction through L_c. This implies that for the lower frequency coupled mode in aluminium, the velocity of both of the pure modes are in phase with respect to longitudinal extension and compression at the position of the lugs, as shown in figure 3.3(c). Thus the phasing of the mode is as predicted in section 3.2.2.

For the upper frequency mode,

$$\frac{i_s}{i_p} = 1 \qquad \text{for } f = f_2 \qquad (3.9)$$

The currents are equal and in phase with each other. This means that equal currents flow in opposite directions through L_c and hence the net current through the coupling inductor is zero. The physical interpretation of this is that for the upper frequency coupled mode in aluminium, the velocity of the longitudinal extension of the mass, at the position of the lugs, of one of the pure modes, is the same as the velocity of the longitudinal

compression of the other pure mode as indicated in figure 3.3(d). Thus the lugs remain stationary. This condition defines the 'amount' of each pure mode that is present in the coupled modes. Since the lugs have no longitudinal velocity the glue joints between the lugs and the mass are not flexed. This agrees with the observation that a badly adhered glue joint did not appear to affect the Q value of the upper frequency mode. The phasing of the mode is again as predicted in section 3.2.2.

Suitable values for the circuit components must be selected in order to test the behaviour of the equivalent circuit with the experimental data. When no lugs are present only the longitudinal mode is excited. This situation is equivalent to L_c in the equivalent circuit being replaced by a wire i.e. shorting out the secondary circuit. Thus the frequency of the primary circuit is determined by that of the pure longitudinal mode. Hence the current in the primary circuit is equivalent to the velocity of the longitudinal mode, v_L. Since the mass is a distributed rather than a discrete system, a constant of proportionality, α, is introduced to allow for uncertainty in the interpretation of the current i_p, and

$$v_L = \alpha i_p \tag{3.10}$$

The current in the secondary circuit is equivalent to the velocity of the radial contour mode which is similarily written

$$v_R = \beta i_s \tag{3.11}$$

where β is a constant of proportionality.

Thus

$$\frac{v_R}{v_L} = \frac{\beta i_s}{\alpha i_p} = \gamma \frac{i_s}{i_p} \tag{3.12}$$

where γ is a constant given by the ratio of α to β.
Now from eqs. (3.9) and (3.12)

$$\frac{v_R}{v_L} = \gamma \qquad \text{for } f = f_2 \tag{3.13}$$

Average values for the magnitude of v_L and v_R across the face of the mass were obtained from the VPI picture for the upper frequency mode, figure 3.8(c), in a similar manner to that discussed in section 3.4.2. This yielded a value of $\gamma = 9$. The ratio of the capacitor values in the primary and secondary circuits could then be calculated, since from eqs. (3.8) and (3.12)

$$\left|\frac{v_R}{v_L}\right| = \gamma\left|\frac{i_s}{i_p}\right| = \gamma\frac{C_s}{C_p} \tag{3.14}$$

Average values for the magnitude of v_L and v_R across the face of the mass were obtained from the VPI picture for the lower frequency mode, figure 3.8(b). This gave

$$C_s = 5C_p \tag{3.15}$$

Note that this result is obtained using either peak or average velocities since the introduction of α and β allowed for either interpretation.

This information together with the fact that the Q in air for the aluminium mass was approximately 2×10^4, allowed the values for the circuit components to be chosen as indicated in figure 3.12. Note that if the resonant frequencies of the primary and secondary circuits were chosen to be identical, then the heights of the coupled resonances remained equal to each other irrespective of the value of L_c. Thus it was found that in order to obtain resonance curves which closely resembled in shape the experimental spectra, such as that shown in figure 3.2, it was necessary to make the frequency of the secondary circuit slightly higher (20 Hz) than that of the primary.

Since the spectra of amplitude of motion versus frequency of excitation were taken with the Michelson interferometer aligned to the centre of the front face of the mass, the contribution to the spectra from the radial contour mode would be negligible since this is a nodal point. Hence the amplitude information which these spectra contain comes predominantly from the longitudinal mode. Thus when the circuit was analysed using a computer package (Matlab, The MathsWork Inc.) the behaviour of the current i_p was studied.

It was found that with a frequency split matching that in the VPI data (110 Hz), the coupling strength of the circuit was (Duffin, 1980, p288)

$$k_{elec} = \frac{L_c}{\sqrt{L_p L_s}} = 3.0 \times 10^{-3} \qquad (3.16)$$

This compared favourably with a coupling strength postulated for the mechanical system

$$k_{mass} = \frac{\text{mass of lugs}}{\text{mass of aluminium}} = 2.6 \times 10^{-3} \qquad (3.17)$$

Having thus established the model using information from the VPI data, the circuit was tested further using the results from the amplitude of motion versus frequency spectra obtained for the set of lugs which had the same length but differing radii, section 3.2.1. The data from this set were used since the lugs which were attached to the aluminium when the VPI images were taken, were from this set. Table 3.1 gives the relevant information for these lugs and figure 3.13 shows a comparison of these data and the behaviour of the equivalent circuit.

mass of lugs (x 10^{-3} kg)	f_1 (kHz)	f_2 (kHz)	$f_2 - f_1$ (Hz)	h_1 / h_2
1.63	31.129	31.200	71	1.46
2.4	31.102	31.196	94	0.32
4.29	30.944	31.189	245	0.12

Table 3.1: The Behaviour of the Coupled Resonances in Aluminium when Three Sets of Lugs of Length 9 mm with Diameters 6.5 mm, 8 mm and 10 mm were Attached to the Sides of the Mass. *f_1 is the frequency of the lower coupled resonance and f_2 the frequency of the upper coupled resonance. h_1 / h_2 is the amplitude ratio of the lower to upper frequency resonance. The pure longitudinal resonance was observed at 31.200 kHz.*

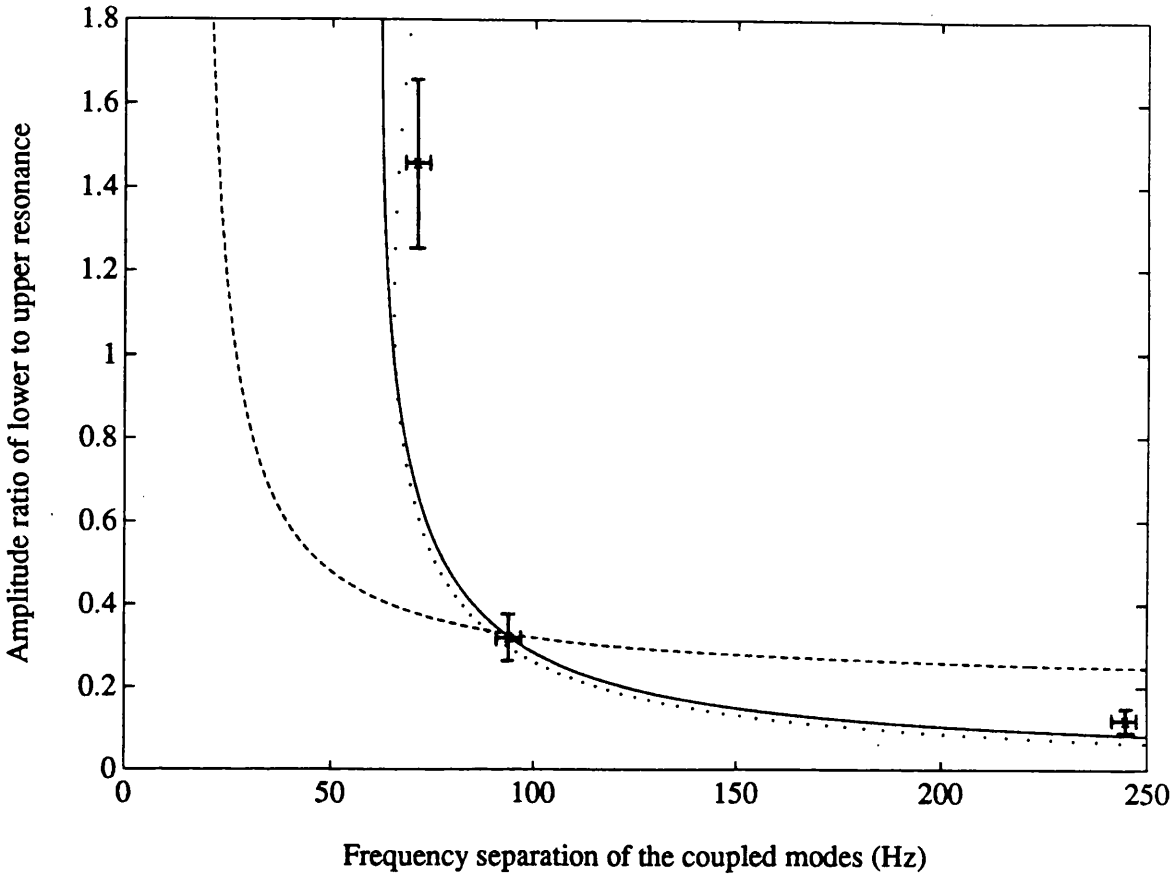

Figure 3.13: Comparison of the Predictions of the Equivalent Circuits with Experimental Data. *The dashed line shows the behaviour of the simple inductive coupling circuit, the dotted line the behaviour of the more complicated circuit involving capacitive coupling and the solid line the behaviour of the modified simple circuit. The crosses indicate experimental points.*

It is evident that for low coupling (i.e. a small frequency split between the resonances), the circuit does not model the experimental data well. The fit is better however for larger coupling.

3.5.2 A More Complicated Model

Several other models were investigated to see if a better fit to the experimental data could be found. These included capacitive rather than inductive coupling and combinations of capacitive and inductive coupling. It was thought that placing mass centrally on the sides of the bar would probably have different effects on the longitudinal and the radial contour

modes. This led to the development of a model, shown in figure 3.14, which could take account of this difference by using two separate, small inductors, L_1 and L_2, to represent the lugs. The capacitor C represents the compliance of the lugs.

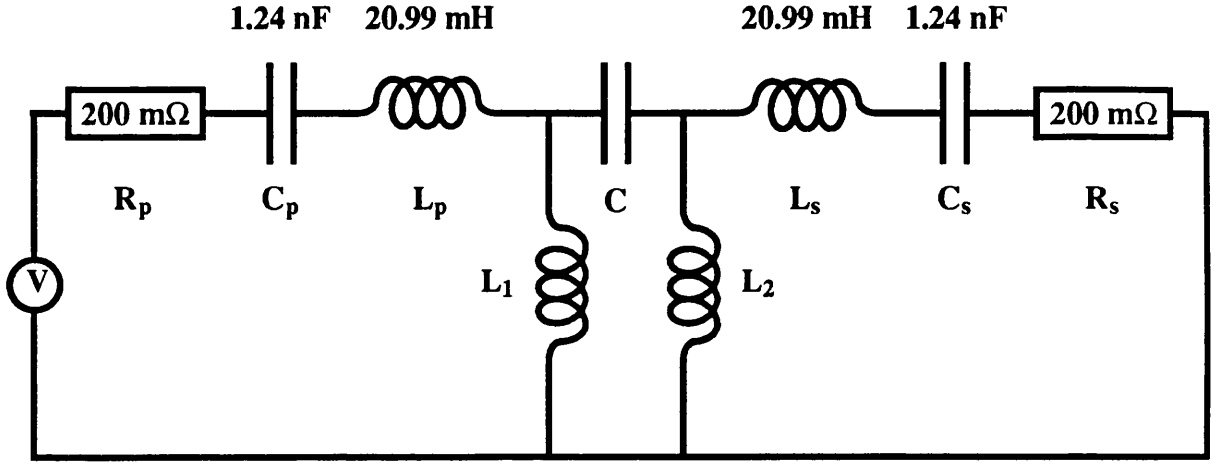

Figure 3.14: A More Complicated model which Uses a Mixture of Capacitive and Inductive Coupling. *L_1 was varied from 23.9 μH to 57 μH whilst L_2 was varied from 18.5 μH to 158 μH and C was varied from 494 nF to 81 nF to fit the whole curve shown in figure 3.13.*

It was decided to first try to choose circuit components to fit the experimental point that had the smallest frequency difference between the coupled resonances (71 Hz). The frequency of the fundamental longitudinal mode defined the product L_pC_p and the Q of the mode in air (~ 2 x 10^4) then defined R_p. The analysis which gave $C_s = 5C_p$ for the simple model is not valid for the circuit considered here, and it was decided to set $L_s = L_p$, $C_s = C_p$ and $R_s = R_p$. L_1 was initially chosen to be equal to L_2. For the experimental point of interest, the mass of the lugs used was ~ 0.2% of the mass of the aluminium bar. Thus the sum of L_1 and L_2 was chosen to be ~ 0.2% of L_p. The value of C was then increased from zero and the effect on the coupled resonances was noted. L_1, L_2 and C were varied in order to achieve the best fit to the experimental point The values of L_1, L_2 and C were then altered until the next experimental point, which had a frequency difference of 94 Hz between the coupled resonances, was fitted. It was found that to move from the first point fitted to the second point required the value of L_1 to be increased by 48%, the value of L_2 to be increased by 165% and the value of C to decrease by 44%. If the values of L_1, L_2 and C were altered in these ratios, the behaviour of the

circuit yielded a fit to the experimental data as shown in figure 3.13. It is observed that this equivalent circuit models the behaviour of the experimental data well.

Thus the above model implies that the effective mass of the lugs is very much higher for the radial contour mode than for the longitudinal mode for stronger coupling values. A possible reason for this difference may be due to the fact that the lug will be bent more by the movement of the radial contour mode than by the longitudinal mode. Larger diameter lugs will have a greater impedance to bending and thus they will appear to have a higher effective mass for the radial contour mode than for the longitudinal mode. The decrease in the value of C represents an increase in the stiffness of the lugs as the coupling increases.

The behaviour of this model agrees well with the experimental data. There are however, some drawbacks to it;

1) it is probable that the model could have been fitted to the experimental data in more than one way,

2) since there are now three resonant loops in the equivalent circuit there are in fact three resonances although one of these is in general outside the frequency band of interest for the coupled mode system,

3) there is also uncertainty in interpreting the physical meaning of the current in the middle loop of the circuit.

A model must provide predictions that can be tested in order to judge its validity. For the simpler model of the previous section, the VPI data was used to allow the values of the circuit components to be chosen and then the behaviour of the circuit was tested against the experimental data on differing lug sizes. For the more complicated model of this section, the experimental data was used to allow the values of the circuit components to be chosen. Thus the ratio of currents in the primary and secondary circuits for the lower and upper frequency coupled modes, must be compared to the ratio of the velocities $v_L : v_R$ obtained from the VPI pictures, figures 3.8(b) and (c). The same constant of proportionality should link these ratios for the two coupled modes (eq. (3.12)). It was

found that this was not the case and hence the values of the circuit components would need to be suitably altered in order to fit the model properly. Given the drawbacks to this model and the fact that this circuit is more difficult to analyse algebraically than the previous model, it was decided instead to try a new model.

3.5.3 The Final Model

The final model, shown in figure 3.15, retained the idea that the lugs may have a different effect on the two pure modes. The circuit is in fact an extension of the simple model of section 3.5.1. and thus the values of L_p, C_p, R_p, L_s, C_s and R_s are approximately the same as for the simple model. The effect of the lugs is modelled this time using three small inductors, L_1, L_2 and L_3.

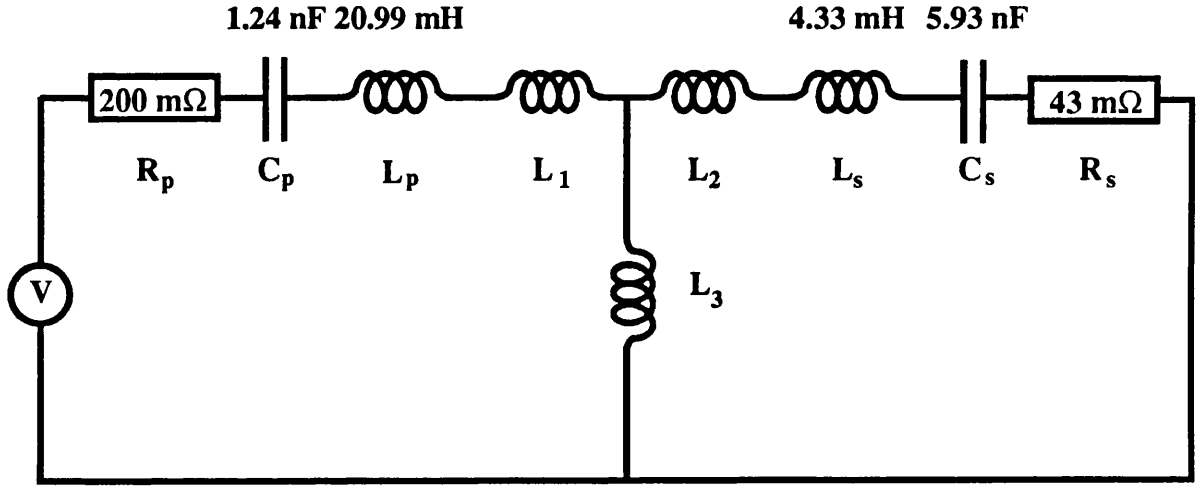

Figure 3.15: The Final Model. *L_3 was varied from 18.3 μH to 42 μH whilst L_1 was varied from 11.0 to 25 μH and L_2 from 38.4 to 88 μH to fit the whole curve shown in figure 3.13.*

The inductors L_1 and L_2 allow the frequency of the primary and secondary circuits to change with respect to each other as the mass of the lug is varied. To fit the model the requirement was made that the values of L_1, L_2 and L_3 were proportional to the mass of the lugs used. Thus movement from one experimental point to another required these inductors to be scaled by the same amount. From eqs. (3.16) and (3.17) the equation

$$\frac{L_3}{\sqrt{L_p L_s}} \approx \frac{\text{mass of lugs}}{\text{mass of aluminium}} \tag{3.18}$$

allows the value of L_3 to be chosen for a given set of lugs. In order to fit the first experimental point L_1 and L_2 must then be chosen to allow the model to account for the frequencies of the resonances and the ratio of the resonance heights. The relation between L_1, L_2 and L_3 is then defined.

Figure 3.13 shows a plot of this circuit's behaviour and the experimental points. It was found that the behaviour of this model gave a very good fit to the experimental data. This implies that the coupling of the modes was predominantly due to the mass of the lugs rather than, for example, their compliance. The quantity L_1+L_3 represents the effective mass of the lugs acting on the longitudinal mode, and L_2+L_3 that acting on the radial contour mode. It was found that in order to fit the experimental results L_2+L_3 had to be approximately twice as large as L_1+L_3 again implying that the lugs have a higher effective mass for the radial contour mode than the longitudinal mode.

3.5.4 Deductions from the Equivalent Circuit Concerning Thermal Motion

A consequence of having inductive coupling is that, at frequencies well below the resonances, the coupling decreases with decreasing frequency. At such frequencies, voltage generators placed on each side of the coupled circuit do not significantly affect the other side, since the impedance of L_3 is small. Thermal noise driving forces can be represented by such voltage generators and hence the thermal noise in each side of the coupled circuit at low frequency is essentially independent of that in the other side. Thus from this analogy it is deduced that for the loaded aluminium cylinder, the thermal motion at low frequency due to the fundamental longitudinal mode is essentially unaffected by damping of the mode's apparent Q due to coupling to the radial contour mode.

3.6 Conclusion

Degradation of the Q value of a pure mode due to coupling between modes has been observed. In the case of the aluminium sample this coupling would not be expected to increase the observed thermal motion at lower frequency. However this is due to the

particular coupling mechanism involved and need not be true for other mechanisms. It is believed that the coupling in columnar silicon may be due to the intrinsic anisotropic nature of the mass. An equivalent circuit to represent this may involve a common compliance and since its impedance will be larger at lower frequencies, for this case thermal motion may in fact be increased. Thus, as a general guideline, it is safer to avoid having resonances lying very close to each other in frequency; hence the aspect ratio for the test masses to be used in a gravitational wave detector must be carefully chosen.

Chapter 4

An Investigation of the Effect of Suspension Wire Resonances on the Measured Q of a Test Mass

4.1 Introduction

In chapter 3 it was stated that a columnar silicon mass, 4 inches in diameter by 2.9 inches long, had a Q value which was initially measured to be $(3.6 \pm 0.1) \times 10^6$ for its fundamental longitudinal mode, which occurred at a frequency of 47.791 kHz. However it was found that the measured Q of this sample varied, apparently randomly by a factor of approximately 30 when the mass was rehung, with 3.6×10^6 being the maximum measured value. This effect was thought to be due to resonances in the suspension wires. Similar effects have been observed elsewhere (Braginsky et al 1985, p. 28 and Michelson, 1992). In this chapter details are given of systematic investigations of the hypothesis that measured Q is a function of suspension wire length. Predictions are also made, with the use of electrical models, concerning the effect of the suspension wires on the thermal motion associated with the suspended test mass at frequencies of interest for the detection of gravitational waves. Details of some of this work are presented in a paper (Logan et al, 1992) which is contained in appendix E.

4.2 The Observed Variation in Q

When it was noted that the measured Q value for the fundamental mode of this columnar silicon mass was not experimentally repeatable, some time was spent determining the cause of the variation. The mass had one polished face and was excited magnetically. The following were investigated:

1) the coil / magnet distance was changed to test whether the mass was being magnetically damped by the excitation mechanism (appendix A).

2) following a suggestion of Braginsky (Braginsky et al, 1985, p.29), a thin layer of grease was applied between the mass and the wire at the breakaway points in order to decrease the coupling between them.

3) a thin layer of grease was applied between the mass and the wire along their line of contact to decrease coupling between them.

4) care was taken to ensure that the suspension wire was in contact with the mass at a nodal position, with respect to longitudinal motion. This was achieved by marking the central circumferential line of the mass and ensuring that the suspension wire was in contact with the mass along this line. Note that the angle the mass made with respect to the horizontal was kept constant by ensuring that the reflected laser beam travelled back along the path of the incident beam.

5) the sides of the mass felt slightly ridged and so in order to decrease any loss of energy due to friction between the mass and the wire, the sides of the mass were polished with a fine emery cloth.

After each of the above had been investigated it was found that the Q was still observed to vary, apparently randomly, and it was thought that the only variable not being controlled was the length of the suspension wire. It was therefore desirable to gain insight into the influence of the length of the suspension wire on the measured Q of the mass.

4.3 Suspension Wire Losses

The single loop suspension for the mass can be viewed as two separate wires between the breakaway points at the mass and those at the supporting plate. If the suspension loop is exactly round the centre of the mass, the motion of the longitudinal mode will drive the wires radially according to

$$r = r_o \sin\omega_o t \tag{4.1}$$

where r_o is the amplitude of motion of the side of the mass and

ω_o is the angular resonant frequency of the longitudinal mode of the mass.

At certain lengths these wires will become resonant and energy from the mass will be transferred to the wires and dissipated leading to a corresponding drop in the quality factor of the mass. In order to estimate what effect the suspension wires might have on the measured Q of the mass, an electrical analogue to the mechanical system was developed.

The suspension wires were modelled as electrical transmission lines which were open circuit at their far ends to represent a supporting plate of infinite impedance. The input impedance, Z, of such a transmission line is given by (e.g. Bleaney and Bleaney, 1959, p. 292)

$$Z = Z_o \frac{\sinh 2\alpha\ell - j \sin 2\beta\ell}{\cosh 2\alpha\ell - \cos 2\beta\ell} \tag{4.2}$$

where Z_o is the characteristic impedance of the line,

α is the loss per unit length in the line,

ℓ is the line length,

$\beta = \omega / c$,

ω is the angular frequency of the wave in the line and

c is the velocity of propagation in the line.

Energy is dissipated in the real part of the impedance which is given by

$$\mathrm{Re}[Z] = Z_o \frac{\sinh 2\alpha\ell}{\cosh 2\alpha\ell - \cos 2\beta\ell} \tag{4.3}$$

The energy dissipated in one transmission line per cycle is given by

$$E_L = \int_0^{2\pi/\omega_o} I^2 \, \mathrm{Re}[Z] \, dt \tag{4.4}$$

where I is the current flowing in the line.

From section 3.5, current is analogous to velocity and charge is analogous to displacement. Thus if the charge, q, at the input to the line is written as

$$q = q_o \sin\omega_o t \tag{4.5}$$

where the magnitude of q_o is equal to the magnitude of r_o given in eq. (4.1).

then

$$I = \omega_o q_o \cos\omega_o t \tag{4.6}$$

and hence the energy lost in both transmission lines

$$E_L = 2\omega_o q_o^2 \pi Z_o \frac{\sinh 2\alpha\ell}{\cosh 2\alpha\ell - \cos 2\beta\ell} \tag{4.7}$$

From eq. (2.11) the energy, E_T, stored in a right circular cylindrical mass is

$$E_T = \frac{1}{4} m\omega_o^2 A^2 \tag{4.8}$$

where A is the amplitude of motion of one face of the mass and
m is the mass.

Thus from the definition of the quality factor of a resonant system, eq. (2.1), the Q of the mass limited only by losses in the suspension wires is given, with the aid of the electrical analogue, by

$$Q_{sus} = \frac{m\omega_o A^2}{4r_o^2 Z_o}\left[\frac{\cosh 2\alpha\ell - \cos 2\beta\ell}{\sinh 2\alpha\ell}\right] \tag{4.9}$$

where r_o has been substituted for q_o.

The characteristic impedance of a wire, Z_o, is given by (e.g. Pain, 1983, pp. 109 - 110)

$$Z_o = c\mu \tag{4.10}$$

where μ is the linear density of the wire.

The loss per unit length in the line, α, is related to the quality factor of the line, Q_w, by (Bleaney and Bleaney, 1959, p. 292)

$$\alpha = \frac{\pi}{Q_w \lambda} \tag{4.11}$$

If $\alpha \ell << 1$, eq. (4.9) may be approximated to

$$Q_{sus} = \frac{mA^2 Q_w}{4r_o^2 \mu \ell}\left[1 + \frac{1}{2}\left(\frac{\omega_o \ell}{Q_w c}\right)^2 - \cos\left(\frac{2\omega_o \ell}{c}\right)\right] \tag{4.12}$$

This is in agreement with a calculation of Braginsky's (Braginsky et al, 1985, p. 28) which was carried out by consideration of the dynamics of the mechanical system.

The amplitude of motion of the end of the mass is related to that of the side by

$$\frac{r_o}{\mathcal{R}} = -\nu \frac{2A}{\mathcal{L}} \tag{4.13}$$

where $\mathcal{R}$ is the radius of the mass,

$\mathcal{L}$ is the length of the mass and

ν is Poisson's ratio for the material.

Thus using eq. (4.13), eq. (4.12) may be more usefully written as

$$Q_{sus} = \frac{m\mathcal{L}^2 Q_w}{16\, \mathcal{R}^2 \nu^2 \mu \ell}\left[1 + \frac{1}{2}\left(\frac{\omega_o \ell}{Q_w c}\right)^2 - \cos\left(\frac{2\omega_o \ell}{c}\right)\right] \tag{4.14}$$

It is evident that eq. (4.14) exhibits a periodic variation in Q_{sus} with varying suspension length. For the columnar silicon mass under consideration, which was suspended by 0.006 inch diameter wire:

$m = 1.39$ kg

$\mathcal{L}$ = 2.9 inches ≡ 0.07 m

$\mathcal{R}$ = 2 inches ≡ 0.05 m

$\mu = 1.44 \times 10^{-4}$ kg m^{-1}

ν = 0.1801 in the [111] direction

$\ell \sim 0.15$ m

c = 280 m s^{-1}

Plausible values for Q_w would be in the range of 10^3 to 10^5. Taking a value of $Q_w = 2 \times 10^4$ (Shoemaker, 1987, p. 34) together with the above values, eq. (4.14) would predict a variation in Q_{sus} from 2×10^5 to 1×10^{10} with a change in suspension length of 1.5 mm. Note that the upper value is extremely high. This is because only losses due to the suspension wires have been considered here; the intrinsic losses in the material of the mass have not. It is clear however that very small changes in the suspension length could have a large effect on the measured Q of the mass.

4.4 Systematic Measurement of Q as a Function of Suspension Length

4.4.1 Experimental Technique

To establish experimentally whether resonances in the suspension wires affected the measured Q of the fundamental longitudinal mode of the columnar silicon mass, the Q of this mode was measured as a function of change in suspension length.

Figure 4.1 shows the experimental method for changing the length of the suspension loop. A hook was placed under the suspension wire, positioned centrally between the suspension points at the supporting plate. This hook was attached via a cord to the shaft of a small electric motor so that when the shaft turned, the cord wound around it thereby pulling the hook and suspension loop up. A pointer was also attached to the shaft so that the angle through which the shaft turned could be measured on a scale mounted on the motor. This allowed the suspension loop to be shortened by a known amount and the Q at that length could be measured using the technique described in section 2.4. It was desirable that the experimental conditions were as close as possible to the original measurement conditions. However if the wire was pulled up from being initially parallel

to the supporting plate, as shown in figure 2.4, this would require a substantial change in the angle of the wire with respect to the horizontal, in order to effect a small change in the suspension length. This could lead to the conditions at the breakaway points of the supporting plate altering in the course of the experiment. In order to minimise this effect, the initial height of the hook was such that the wire passing over it made an angle of approximately 45° to the horizontal.

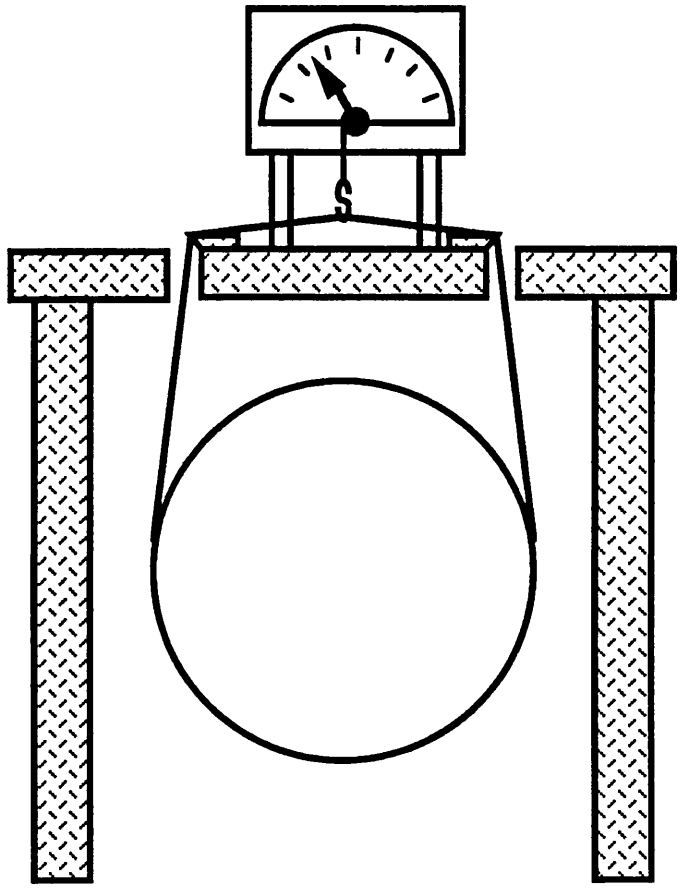

Figure 4.1: The Experimental Arrangement for Changing the Length of the Suspension Loop. *The circumference of the motor shaft was 20 mm.*

4.4.2 Results

Figure 4.2 shows the variation of Q as a function of change in suspension length. It is evident that the Q drops sharply at several points leading to a variation in the measured Q by a factor of about 30 with a change in suspension length of only 1.5 mm. From the

results shown in figure 4.2 it is evident that there are two sharp dips in the Q in one cycle of the pattern. This can be understood by postulating that the two wires were not exactly the same length, the lengths differing by 0.45 mm, leading to two dips being observed. In the second cycle of the variation it should be noted that there are in fact three dips present. It is believed that this may be due to either the mass shifting position slightly in the suspension loop or the wires settling in a slightly different way at the breakaway points at the supporting plate, causing the apparent length of the wires to change and one of them to become resonant again.

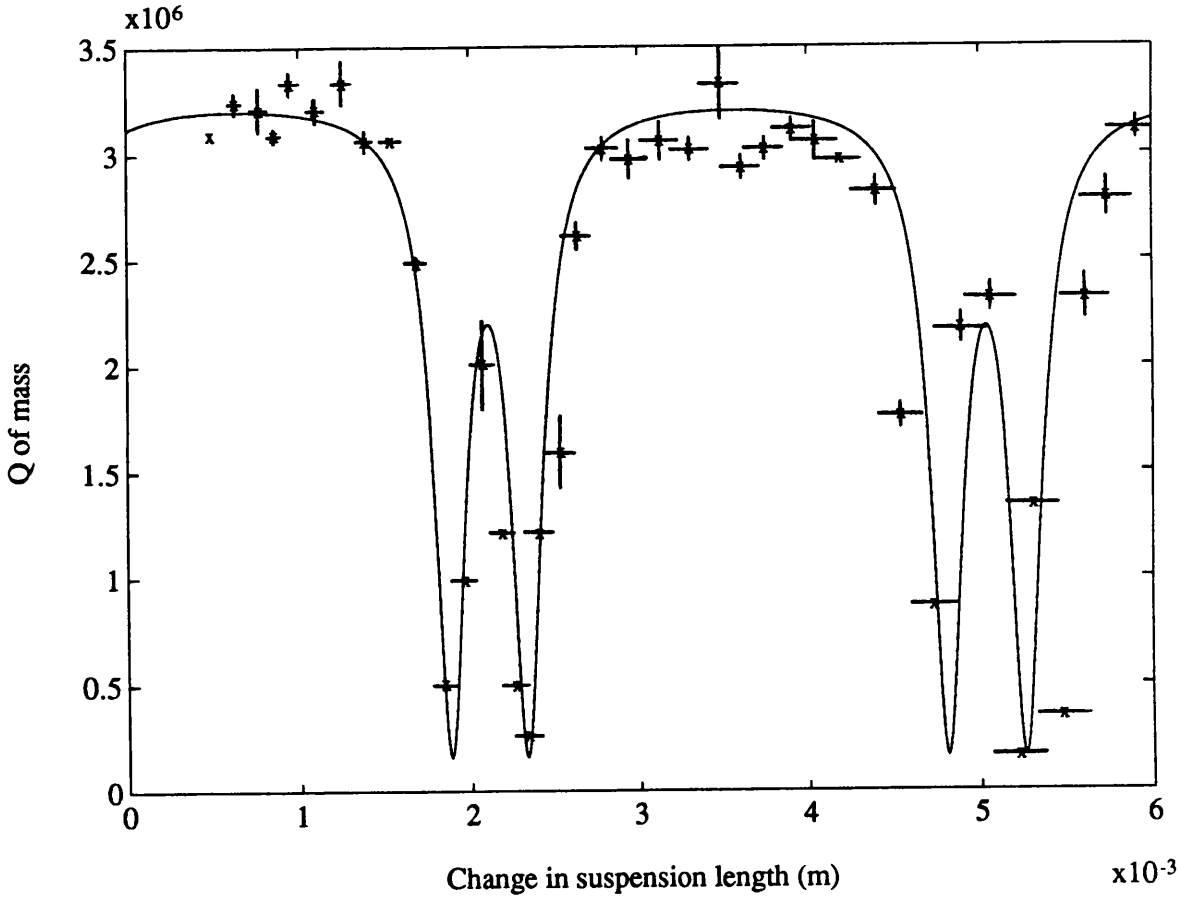

Figure 4.2: The Variation of Q with Changing Suspension Length. *The crosses indicate experimental points. The error shown for each point is the error in the mean value of Q, this being calculated from three separate decay curves. The solid line shows the behaviour of the equivalent circuit of section 4.5.1. It should be noted that there are in fact three minima in the second cycle of the pattern of the experimental data.*

It was found that when a magnetic drive was used the maximum Q value in such a series of measurements was not constant but varied by a factor of approximately 1.5. The highest Q value ever measured using a magnetic drive was $(3.6 \pm 0.1) \times 10^6$. To test whether the Q might be limited by the magnet glued to the mass, the magnet/coil drive was replaced by a capacitive drive. A variation in Q similar to that in figure 4.2 was observed and again some variation was found in the maximum measured Q, with the highest value once more being $(3.6 \pm 0.1) \times 10^6$. From these results there was no indication that the capacitive drive was superior to the magnetic drive. It was evident however that some factor, other than the variation of suspension length, was affecting the measured Q and this was thought to be the exact positioning of the breakaway points at the mass. If the wires were positioned exactly half-way along the length of the mass they would only be driven radially by the movement of the mass resonating in the fundamental longitudinal mode. If, however, the wires were slightly offset from the centre, the presence of friction ensures they would also be driven longitudinally. This could lead to greater loss of energy from the mass.

In order to investigate this idea a thin layer of grease was applied between the wire and the mass at the breakaway points in order to decrease the coupling between them (Braginsky, 1985, p.29). Again a similar variation in Q to that shown in figure 4.2 was observed but this time the minimum Q observed was $(0.61 \pm 0.01) \times 10^6$, compared to $(0.16 \pm 0.01) \times 10^6$ shown on figure 4.2, and the maximum Q, $(4.8 \pm 0.1) \times 10^6$, compared to $(3.3 \pm 0.1) \times 10^6$. It is believed that the increase in the minimum Q value is due to a smaller fraction of the mass's energy being transferred to the wire when the wire is on resonance, and that the increase in the maximum Q value is due to a decrease in friction effects at the breakaway points.

4.5 Electrical Modelling of Mass and Suspension Wire System

4.5.1 The Equivalent Circuit

In order to gain greater understanding of the mechanical system and to be able to predict the effect of the observed variation in Q on the thermal noise levels at lower frequencies,

an electrical analogue of the system was developed. As discussed in section 4.3, the suspension wires were modelled as lossy transmission lines which were open circuit at their far ends to represent a supporting plate of infinite impedance. The mass was modelled as a series resonant circuit. Figure 4.3 shows the equivalent circuit which was used.

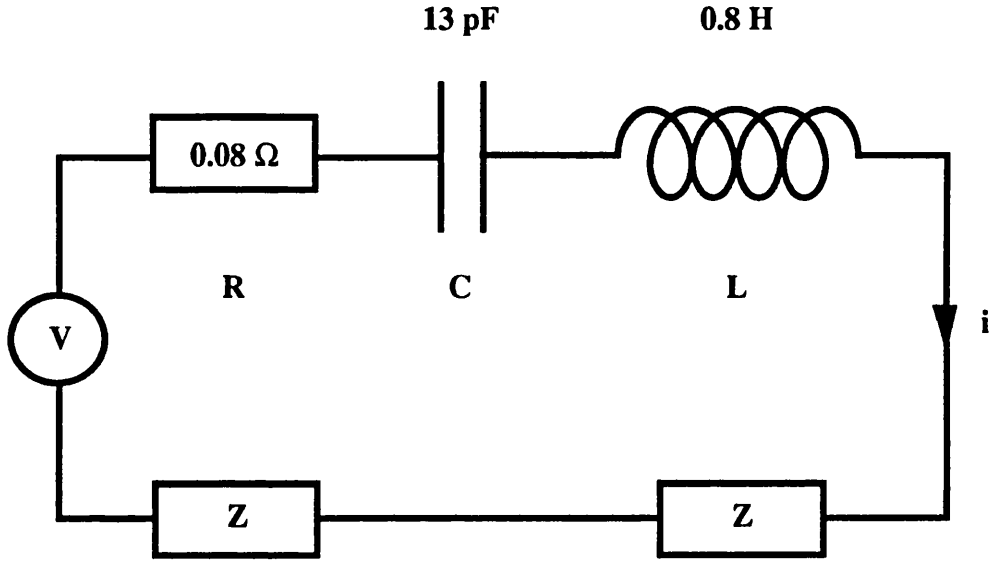

Figure 4.3: The Equivalent Circuit for the Mass and Suspension Wire System. *Z represents a transmission line. For a choice of* $Q_w = 3 \times 10^3$ *the values of L, C and R are as indicated (see section 4.5.3).*

Note that the inputs to the transmission lines are in series with the LCR circuit and thus the same current passes through all the components. This model was chosen since it represents the situation when the wires are driven by the same displacement and hence same velocities as the sides of the mass.

4.5.2 Resonant Circuit Representations of Transmission Lines

Series Circuit Representation

Consider a series resonant circuit such as that shown in figure 4.4.

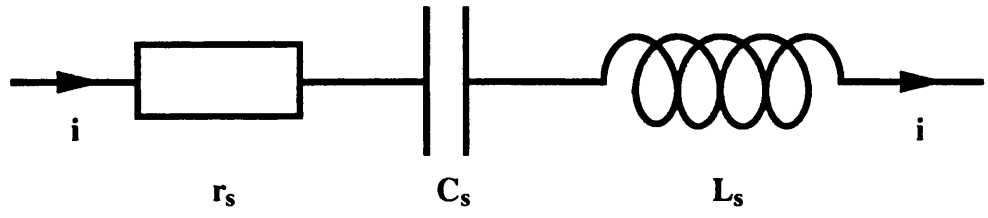

Figure 4.4: Series Resonant Circuit Representation of a Transmission Line. *The circuit is formed by an inductor, L_s, a capacitor, C_s, and a resistor, r_s. The angular resonant frequency of the circuit, ω_o, is given by $\omega_o = 1/\sqrt{L_s C_s}$ and the Q of the circuit by $Q_s = \omega_o L_s / r_s$.*

The impedance of the circuit

$$Z_s = j\left(\omega L_s - \frac{1}{\omega C_s}\right) + r_s \tag{4.15}$$

At frequencies close to the angular resonant frequency of the circuit, $\omega = \omega_0 + \Delta\omega$, $\Delta\omega << \omega_0$

$$Z_s \approx r_s + 2j\Delta\omega L_s$$

$$= r_s\left[1 + 2j\frac{\Delta\omega}{\omega_0} Q_s\right] \tag{4.16}$$

Now consider the input impedance of a lossy transmission line open circuit at its far end as described by eq. (4.2). Using complex notation this may be written as

$$Z = Z_0 \frac{1 + \exp\left(-j\frac{4\pi\ell}{\lambda} - 2\alpha\ell\right)}{1 - \exp\left(-j\frac{4\pi\ell}{\lambda} - 2\alpha\ell\right)} \tag{4.17}$$

Let the length of the line be $\ell = (2n+1)\lambda/4 + \Delta\ell$, where $n \geq 0$ is an integer and $\Delta\ell << (2n+1)\lambda/4$. Thus the exponential term of eq. (4.17) may be written as

$$\exp\left(-j\frac{4\pi\ell}{\lambda} - 2\alpha\ell\right) = -\exp\left(-j\frac{4\pi\Delta\ell}{\lambda} - 2\alpha\ell\right)$$

$$\approx -\left(1 - j\frac{4\pi\Delta\ell}{\lambda} - 2\alpha\ell\right) \qquad \alpha\ell << 1 \qquad (4.18)$$

Substitution of eq. (4.18) into eq. (4.17) yields

$$Z \approx Z_o\alpha\ell\left[1 + j\frac{2\pi}{\alpha\lambda}\frac{\Delta\ell}{\ell}\right] \qquad (4.19)$$

Now $\frac{\Delta\ell}{\ell} = -\frac{\Delta\lambda}{\lambda} = \frac{\Delta\omega}{\omega_o}$ and thus eq. (4.19) may be rewritten as

$$Z = Z_o\alpha\ell\left[1 + 2j\frac{\Delta\omega}{\omega_o}\frac{\pi}{\alpha\lambda}\right] \qquad (4.20)$$

Thus comparing eq. (4.20) with eq. (4.16) it is observed that when the $\ell = (2n+1)\lambda/4$, the transmission line behaves like a series resonant circuit with (Bleaney and Bleaney , 1959, p. 292)

$$r_s = Z_o\alpha\ell \qquad \alpha\ell << 1 \qquad (4.21)$$

and

$$Q_w = \frac{\pi}{\alpha\lambda} \qquad \alpha\ell << 1 \qquad (4.22)$$

Parallel Circuit Representation

Consider the parallel resonant circuit of figure 4.5. The admittance of this circuit, Y_p is given by

$$Y_p = j\left[\omega C_p - \frac{1}{\omega L_p}\right] + \frac{1}{r_p} \qquad (4.23)$$

Thus at frequencies close to the angular resonant frequency of the circuit, $\omega = \omega_o + \Delta\omega$, $\Delta\omega << \omega_o$,

$$Y_p \approx \frac{1}{r_p} + 2j\Delta\omega C_p$$

$$= \frac{1}{r_p}\left[1 + 2j\frac{\Delta\omega}{\omega_o}Q_p\right] \qquad (4.24)$$

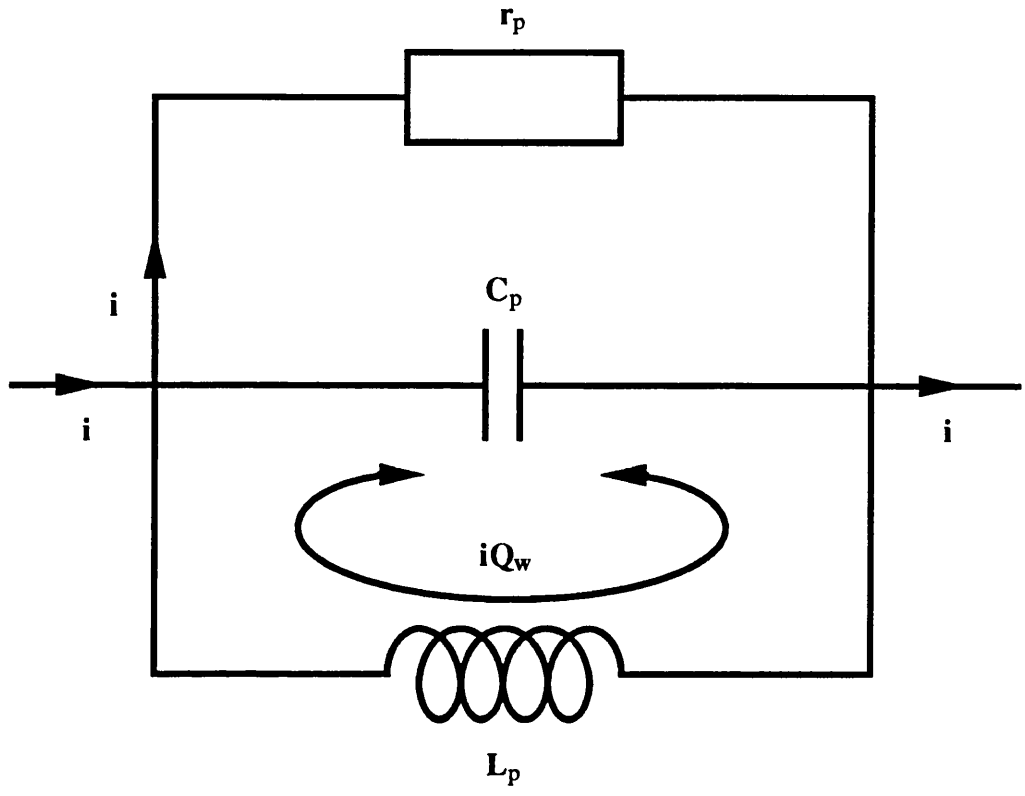

Figure 4.5: Parallel Resonant Circuit Representation of a Transmission Line. *The circuit is formed by an inductor, L_p, a capacitor, C_p, and a resistor, r_p. The angular resonant frequency of the circuit, ω_o, is given by $\omega_o = 1/\sqrt{L_pC_p}$ and the Q of the circuit by $Q_p = \omega_o C_p r_p$.*

Now consider the input impedance of a lossy transmission line open circuit at its far end as described by eq. (4.17). Let the length of the line $\ell = n\lambda/2 + \Delta\ell$ where $n \geq 1$ and $\Delta\ell << n\lambda/2$. The exponential term in eq. (4.17) is thus written as

$$\exp\left(-j\frac{4\pi\ell}{\lambda} - 2\alpha\ell\right) = \exp\left(-j\frac{4\pi\Delta\ell}{\lambda} - 2\alpha\ell\right)$$

$$\approx 1 - j\frac{4\pi\Delta\ell}{\lambda} - 2\alpha\ell \qquad \alpha\ell << 1 \qquad (4.25)$$

Substitution of eq. (4.25) into eq.(4.17) gives the admittance of the transmission line, $Y = Z^{-1}$

$$Y \approx \frac{1}{Z_o}\left[\alpha\ell + j\frac{2\pi\Delta\ell}{\lambda}\right]$$

$$= \frac{\alpha\ell}{Z_o}\left[1 + 2j\frac{\Delta\omega}{\omega_o}\frac{\pi}{\alpha\lambda}\right] \qquad (4.26)$$

Thus comparing eq. (4.26) with eq. (4.24) it is observed that when $\ell = n\lambda/2$, the transmission line behaves like a parallel resonant circuit with

$$r_p = \frac{Z_o}{\alpha\ell} \qquad \alpha\ell << 1 \qquad (4.27)$$

and Q_w as defined by eq. (4.22).

Note that for low losses in the line $r_p >> r_s$.

4.5.3 Choice of Circuit Parameters

It is assumed that the fraction of energy stored in the transmission lines is very small compared to that stored in the main LCR circuit of figure 4.3, and thus the resonant frequency of the system is essentially unaffected by the presence of the transmission lines. Hence when both transmission lines have $\ell = (2n+1)\lambda/4$, the whole circuit looks like a series resonant circuit with quality factor

$$Q_s = \frac{1}{2r_s + R}\sqrt{\frac{L}{C}} \qquad (4.28)$$

where R represents the damping in the mass,

L represents the mass and

C represents the compliance of the mass.

When both transmission lines have $\ell = n\lambda/2$ the circuit has quality factor

$$Q_p = \frac{1}{2r_p + R}\sqrt{\frac{L}{C}} \tag{4.29}$$

If the suspension wires are not exactly the same length, eqs. (4.28) and (4.29) must be modified. Because of the difference in length, the transmission lines do not resonate together. The highest and lowest Q values of the circuit occur when the sums of the real parts of the impedances of the two transmission lines are at a minimum, r_{min}, and maximum, r_{max}, respectively. r_{min} and r_{max} can be calculated using eq. (4.3). The term $2r_s$ is replaced by r_{min} in eq. (4.28) and $2r_p$ is replaced by r_{max} in eq. (4.29).

An experimentally plausible value for Q_w was initially chosen and α was calculated using eq. (4.22). Z_0 was calculated for the suspension wire from eq. (4.10) and this value, together with the experimentally determined difference in suspension wire lengths, was used to calculate r_{min} and r_{max}. This was done numerically using a computer package (Matlab, The MathsWork Inc.). From figure 4.2, $Q_p = 0.16 \times 10^6$ and the average value of $Q_s = 3.2 \times 10^6$, and thus the ratio of eqs. (4.28) and (4.29), modified as described above for unequal line lengths, allowed calculation of R. This value combined with the resonant frequency of the mass which is represented in the circuit as

$$f_o = \frac{1}{2\pi\sqrt{LC}} \tag{4.30}$$

allowed the values of L and C to be calculated. Thus all the parameters of the circuit were defined for a given Q_w which was varied in order to provide the best experimental fit.

4.5.4 Circuit Analysis

The circuit was analysed using a computer package (Matlab, The MathsWork Inc.). Figure. 4.2 shows the response of the circuit which closely matched the experimental data, the transmission lines having $Q_w = 3 \times 10^3$ and differing in length by 0.45 mm.

As stated above, when $\ell = (2n+1)\lambda/4$ the transmission lines look like series circuits with low resistance. The same current, i, that flows round the main circuit passes through all components of the series representations of the transmission lines. This allows

understanding of what is happening between the mass and suspension wire. When $\ell = (2n+1)\lambda/4$ the suspension wire is at an anti-nodal position at the mass, the other end being fixed at the supporting plate, and hence the wire moves easily with the mass and appears to have low impedance. Thus the maximum amplitude of motion of the wire is just that of the mass. Since the impedance of the wire is small there is little energy dissipated in it, and hence the Q of the mass is high.

The opposite case occurs when $\ell = n\lambda/2$ and the transmission lines behave like parallel circuits with high resistance. As indicated in figure 4.5 the current, i, which circulates round the rest of the main circuit only flows through the resistive part of the parallel circuit. The L_pC_p loop of the parallel circuit has a current which is a factor of Q_w higher than this flowing in it. It is thus possible to build up high velocity and hence amplitude on the wire, as indicated in the model by the current iQ_w, and so the wire is on resonance. When the suspension wire has $\ell \approx n\lambda/2$ the wire is close to a nodal position at the mass and the wire presents a high mechanical impedance to the mass. Thus for a given amplitude of motion, the mass transfers and dissipates much more energy in resonating the wire and the measured Q of the mass is low. Note that the power dissipated in the transmission line is i^2r_p which is proportional to Q_w for a given current i. Thus the greater Q_w is, the greater is the power dissipated in the line and hence the lower the dip in the Q of the circuit.

Thus this electrical analogue provides an understandable model for the variation of the measured Q of the suspended mass and fits the experimental data well.

4.5.5 A Variation of the Equivalent Circuit

The equivalent circuit described above was modelled using lossy transmission lines which were open circuit at their far ends to represent lossy suspension wires attached to a supporting plate of infinite impedance. An alternative to this would be to model the suspension wires as lossless with all losses occurring at the supporting plate. The electrical equivalent of this would be lossless transmission lines terminated by an impedance R_T. The input impedance, Z_T, of such a line is given by (e.g. Duffin, 1980, p. 295)

$$Z_T = Z_o \frac{Z_o R_T + j\frac{1}{2}\left(Z_o^2 - R_T^2\right)\sin 2\beta\ell}{Z_o^2 \cos^2 \beta\ell + R_T^2 \sin^2 \beta\ell} \tag{4.31}$$

Following similar analysis to that in section 4.5.2, it is found that when $\ell = (2n+1)\lambda/4$ the transmission line behaves like a series resonant circuit with resistance

$$r_{Ts} = \frac{Z_o^2}{R_T} \qquad R_T >> Z_o \tag{4.32}$$

and when $\ell = n\lambda/2$ the line resembles a parallel resonant circuit with resistance

$$r_{Tp} = R_T \qquad R_T >> Z_o \tag{4.33}$$

The quality factor of the line, Q_{wT}, is given by

$$Q_{wT} = \frac{R_T \pi \ell}{Z_o \lambda} \qquad R_T >> Z_o \tag{4.34}$$

Assuming R_T is independent of the length of the transmission line i.e. that the damping coefficient of the supporting plate is not dependent on the length of the suspension wire, it is evident that Q_{wT} is proportional to the length of line.

Note that if a fixed line length is considered then substitution of eq. (4.34) into eq. (4.32) yields

$$r_{Ts} = \frac{Z_o \pi \ell}{Q_w \lambda} = r_s \tag{4.35}$$

The above expression for r_s can be obtained by using eqs. (4.21) and (4.22). Similarly substituting eq. (4.34) into eq. (4.33) yields the following expression for r_{Tp}.

$$r_{Tp} = \frac{Z_o Q_w \lambda}{\pi \ell} = r_p \tag{4.36}$$

The expression for r_p is obtained using eqs. (4.27) and (4.22).

Thus for a fixed line length this model is identical to the one considered in the previous section.

From the former model Q_w was found to be 3 x 10^3. This value was substituted into eq. (4.34) for Qw_T, allowing calculation of R_T. For a fixed line length of 0.15 m, R_T was found to be 1.5 Ω. L,C and R retain the same values as the previous model since $r_{Tp} = r_p$ and $r_{Ts} = r_s$.

The behaviour of this circuit was analysed in the same manner as the previous circuit and yielded a similar theoretical fit to the data as shown in figure 4.2. Thus this circuit is also a valid model for the mechanical system.

4.5.6 Comparison of the Two Models

Although both models can provide the same fit to the experimental data, over a larger change in the length of the line than is considered in figure 4.2, the models behave differently. For simplicity the transmission lines will be considered as having equal lengths.

For the first equivalent circuit, where the losses occur in the transmission lines themselves, the Q_w of the line is given by eq. (4.22) and this is clearly independent of the length of the line. Given that L, C and R are fixed values in the circuit, the upper limit to the Q of the equivalent circuit, given by eq. (4.28), is determined by r_s, which from eqs. (4.21) and (4.22)

$$r_s = \frac{Z_o \pi \ell}{Q_w \lambda} \propto \ell \qquad \alpha\ell << 1 \qquad (4.37)$$

The lower limit to the Q of the circuit, given by eq. (4.29), is determined by r_p which using eqs. (4.27) and (4.22) may be written

$$r_p = \frac{Z_o Q_w \lambda}{\pi \ell} \propto \frac{1}{\ell} \qquad \alpha\ell << 1 \qquad (4.38)$$

Thus it may be observed, with reference to eq. (4.28) that the upper limit to the Q of the

circuit decreases as the length of the suspension wire increases, whilst from eq. (4.29) it is observed that as this happens the lower limit to the Q of the circuit increases. Note however that since $R >> r_s$, the change in the upper limit to the Q of the circuit is very small.

From this equivalent circuit, for a mechanical system where the suspension wires supporting the mass are lossy and there is no loss at the supporting plate, it is deduced that if the Q of the mass was measured over several cycles as the length of the suspension wires is increased, in principle the minimum Q should increase whilst the maximum Q should remain essentially constant.

For the second model where the lossless transmission lines are terminated by resistors of a defined value, eqs. (4.32) and (4.33) for r_{Ts} and r_{Tp} are clearly independent of the length of the transmission line. Thus from eqs. (4.28) and (4.29), where r_s is replaced by r_{Ts} and r_p by r_{Tp}, the upper and lower limits to the Q of the equivalent circuit are also independent of the length of the transmission line.

Thus from this analogy, for a mechanical system where the suspension wires are lossless and are connected to a lossy supporting plate, the variation of the measured Q of the mass, over several cycles as the length of the suspension wires is increased, should in principle show no variation in the maximum and minimum Q values.

Therefore in principle by measuring the Q of the mass over several cycles, it should be possible to determine whether the dominant loss mechanism is in the suspension wire or at the supporting plate. This was not experimentally tested since changing the length of the suspension wires by a relatively large amount is not straightforward. If the technique described in section 4.4.1 is used to alter the length of the wire, this will cause the angle at which the wire breaks away over the sharp edges to change markedly. This may cause the level of damping at these points to alter. A possible way of overcoming this effect would be to pass the suspension wire, at the top of the supporting plate between the breakaway points, through a horizontal tube of length slightly shorter than the distance between the breakaway points. Raising the height of such a tube whilst keeping it horizontal, should not cause such a significant change in the angle of the wires at the breakaway points. However, since the wires will breakaway almost vertically from the

supporting plate, this may create different conditions at the suspension points from the original experiment.

4.6 Predictions of the Level of Thermal Motion of the Mass at Lower Frequencies

In sections 4.4 and 4.5, observation and modelling of the variation in the measured Q of the fundamental longitudinal mode of a columnar silicon mass has been discussed. The following question is then raised: if a test mass in a laser interferometric gravitational wave detector is suspended such that its measured Q is low, is the thermal motion of the test mass increased in the frequency band of interest for the detection of gravitational waves?

Using the models of section 4.5, it is possible to calculate the effect of thermal excitation on the displacements of the ends of the bar with respect to its centre of mass. This allows determination of the possible effect, if any, of the observed variation in Q with suspension length on the level of this motion. Thermal displacement in the mechanical system is represented by the fluctuating charge across the capacitor in the equivalent circuit shown in figure 4.3. The equivalent circuits in fact provide many possible models for the magnitude of this fluctuating charge since this will depend on the assumed frequency dependence of the Q of the suspension wires and of the Q of the mass. As noted in section 2.2.3, it is conventionally assumed that the Q of a material is inversely proportional to frequency. However for some materials there is evidence that Q is constant over a wide frequency range. These two cases will be considered in this section. The way in which Q varies as a function of frequency and how this affects the loss of energy in a system is dealt with more rigorously in chapter 5.

Thermal noise forces in a mechanical system are represented in an equivalent circuit by a voltage generator which has a fluctuating voltage power spectral density which is given by (section 2.2.2)

$$\langle v_{th}^2 \rangle = 4k_B T R_o(f) \tag{4.39}$$

where $R_o(f)$ is the real part of the impedance in an equivalent circuit. This represents the damping in the mechanical system[1].

The fundamental longitudinal mode of the mass contains k_BT energy, most of which appears in the longitudinal motion of the mass. A small fraction will however appear in the radial motion of the mass. The equivalent circuit under consideration here models this radial movement and hence the thermal noise forces are represented in the circuit by

$$\langle v_{th}^2 \rangle = 4\varepsilon k_B T R'(f) \tag{4.40}$$

where $R'(f)$ is the real part of the impedance in the equivalent circuit modelling radial motion of the longitudinal mode of the mass and

ε is a constant with $\varepsilon < 1$.

Writing the impedance of the transmission line as $Z(f) = r(f) + jX(f)$, then $R'(f) = R(f) + 2r(f)$. If it is assumed for simplicity, that both lines are the same length, the fluctuating charge across the capacitor, q_c, can be shown to have a power spectral density given by

$$\langle q_c^2 \rangle = \frac{4\varepsilon k_B \eta T C^2}{s^4C^2\gamma^2 + 2s^3C^2\gamma\eta + s^2C^2\eta^2 + 2s^2C\gamma + 2sC\eta + 1} \tag{4.41}$$

where $\gamma = \left(L + \frac{2X(f)}{\omega}\right)$,

$\eta = [R(f) + 2r(f)]$ and

$s = j\,2\pi f$.

When $f = (2n+1)c/4\ell$ or $f = nc/2\ell$, $Z(f)$ is purely resistive and eq. (4.41) may be simplified to

[1]The inductor in such a circuit is used to represent the distributed mass of the system as a single point or effective mass. The effective mass of a bar resonating in its fundamental longitudinal mode is equal to half of the actual mass of the bar (Paik, 1974). Thus an equivalent circuit which models the longitudinal motion of a bar would use an inductor with a value equivalent to half the mass of the bar.

$$\langle q_c^2 \rangle = \frac{4\varepsilon k_B T \eta C^2}{s^4 C^2 L^2 + 2s^3 C^2 L\eta + s^2 C^2 \eta^2 + 2s^2 CL + 2sC\eta + 1} \qquad (4.42)$$

Consider the transmission lines to be of a fixed length, ℓ. Then the two equivalent circuits described in sections 4.5.1 and 4.5.5 have, from eqs. (4.35) and (4.36), $r_{Ts}(f) = r_s(f)$ and $r_{Tp}(f) = r_p(f)$ when $Q_w = Q_{wT}$. Hence these two models have the same frequency behaviour. For frequencies very much less than the resonant frequency, f_o, of the series LCR circuit, it is possible to further simplify eq. (4.42) as will be shown below for frequencies between the normal modes of the wire and for frequencies at the normal modes of the wire.

Transmission Lines at Frequencies Midway Between the Normal Modes Frequencies [i.e. f = (2n+1)c/4ℓ]

For this case

$$\langle q_c^2 \rangle \approx 4\varepsilon k_B T [R(f) + 2r_s(f)] C^2 \qquad f << f_o \qquad (4.43)$$

For realistic values of $Q_w >> 1$, $r_s(f) = \frac{Z_o \pi \ell f}{Q_w c} << R(f)$ in the frequency band of interest for the detection of gravitational waves. Hence when the frequency is exactly between the normal mode frequencies, from eq. (4.43)

$$\langle q_c^2 \rangle \approx 4\varepsilon k_B T R(f) C^2 \qquad (4.44)$$

This is independent of line length and is equal to the thermal noise of the mass alone.

Hence from this electrical analogy it can be seen that away from any resonances in the wires the thermal noise of the system remains essentially unchanged by the presence of the wires. This level of thermal motion remains unaltered, even if the suspension length is such that at the resonant frequency of the mass, the wires are on resonance with the mass and the measured Q of the mass is low.

To evaluate eq. (4.44) first requires evaluation of the constant ε and also knowledge of

the form of R(f). From eq. (4.13)

$$\langle x^2_{radial} \rangle = \left(\frac{2v\mathcal{R}}{\mathcal{L}}\right)^2 \langle x^2_{long.} \rangle \tag{4.45}$$

where from eq (2.31), $\langle x^2_{long.} \rangle \approx \frac{8k_BT}{Qm\omega_o^3}$.

Thus combining eqs. (4.44), (4.45) and (2.31)

$$4\varepsilon k_B T R(f) C^2 \equiv \left(\frac{2v\mathcal{R}}{\mathcal{L}}\right)^2 \frac{8k_BT}{Qm\omega_o^3}$$

and since $C = (\omega_o QR)^{-1}$ and $R = (\omega_o L)/Q$ this may be expressed as

$$\left|\frac{\varepsilon}{L}\right| \equiv \left|\frac{2}{m}\left(\frac{2v\mathcal{R}}{\mathcal{L}}\right)^2\right| \tag{4.46}$$

Thus $\varepsilon = 0.074$.

The appropriate form for the Q of a series resonant circuit, of resonant frequency f, when the losses are associated with the spring constant in the mechanical analogy, and the inverse of capacitance in the electrical analogy, is

$$Q(f) = \frac{1}{2\pi f C R(f)} \tag{4.47}$$

Two possible cases will be considered. The first corresponds to the conventional assumption that Q is inversely proportional to frequency, the second case, which is often found in practice, that Q is frequency independent. Which model is applicable will depend on the material and the frequency band under consideration. (See chapter 5 for a fuller discussion of this topic.)

1a) Q inversely proportional to frequency (i.e.$Q = 3.2 \times 10^6 \times \frac{48kHz}{f}$)
This implies that R(f) is independent of frequency. Hence, from eq. (4.44), from this electrical analogue it is observed that at frequencies very much less than its resonant frequencies, the thermal motion of the mass is essentially independent of frequency.

1b) Q frequency independent (i.e. $Q = 3.2 \times 10^6$)

This implies that $R(f) \propto f^{-1}$.and hence from eq. (4.44)

$$\langle q_\varepsilon^2 \rangle \approx \frac{4\varepsilon k_B T C}{2\pi f Q} \tag{4.48}$$

Thus for this case, the thermal motion of the mass is inversely proportional to frequency leading to increased motion at lower frequencies compared to (a)

Transmission Lines at the Normal Mode Frequencies [i.e. $f = nc/2\ell$]

Now consider the normal mode frequencies of the suspension wires. From eq. (4.42)

$$\langle q_\varepsilon^2 \rangle \approx 4\varepsilon k_B T [R(f) + 2r_p(f)] C^2 \qquad f << f_o \tag{4.49}$$

Using eq. (4.36), r_p may be expressed as

$$r_p(f) = \frac{Z_o Q_w c}{\pi f \ell} \tag{4.50}$$

and for high Q transmission lines $r_p(f) >> R(f)$ for the frequency band of interest. Thus when the frequency is such that the lines are on resonance from eqs. (4.49) and (4.50)

$$\langle q_\varepsilon^2 \rangle \approx 8\varepsilon k_B T r_p(f) C^2 = \frac{8\varepsilon k_B T C^2 Z_o c Q_w}{\pi f \ell} \tag{4.51}$$

Two possible models for the frequency dependence of Q_w of transmission lines are considered. These correspond again to the case which is conventionally assumed and the case often found in practice. Again which model is applicable to a given suspension wire will depend on the material and frequency band considered

2a) Q_w inversely proportional to frequency (i.e. $Q_w = 3 \times 10^3 \times \frac{48\text{kHz}}{f}$). This is equivalent to α proportional to frequency squared and implies that $\langle q_\varepsilon^2 \rangle \propto \frac{1}{f^2}$

Since $r_p >> R$, it is observed that the level given by eq. (4.51) is higher than that given by eq. (4.44). This leads to a spectrum of thermal noise spikes due to the suspension wires resonating, being superimposed on the fundamental level of thermal noise from the mass.

The peak heights of these spikes are inversely proportional to frequency squared.

2b) Q_w frequency independent (i.e. $Q_w = 3 \times 10^3$). This is equivalent to α proportional to frequency and implies that $\langle q_e^2 \rangle \propto \frac{1}{f}$

For this case, the spectrum of thermal noise spikes, which is superimposed on the fundamental level of thermal noise given by eq. (4.44), has peak heights which are inversely proportional to frequency.

The Form of the Thermal Motion Power Spectrum

Figure 4.6(a) shows the case when both the Q values of the test mass and the suspension wires are inversely proportional to frequency, as described in 1(a) and 2(a). The graph is drawn for suspension wires 0.15 m in length leading to the first wire resonance occurring at 930 Hz. Figure 4.6(b) shows the case when both of these Qs are frequency independent, as described in 1(b) and 2(b). $\langle q_e^2 \rangle$ is approximately 50 times less than for (a) for the first resonance of the suspension wires. On comparison of the two graphs it is observed that the fundamental level of thermal motion from the test mass is much higher when the Q of the mass is frequency independent.

The models described above predict that the fundamental level of thermal motion of a suspended mass with respect to its centre, is not affected by the degradation of the measured Q caused by the suspension wires being on resonance with the mass. The exact form of the thermal motion will depend on how the Q of the material of the mass and suspension wires vary as a function of frequency.

4.7 The Thermal Motion of A Pendulum

The overall thermal motion for a test mass in a laser interferometric gravitational wave detector is more complicated than that described so far, since thermal energy in the resonant modes of the suspension wires will cause further movement of the ends of the bar through their effect on motion of the centre of mass. Similarly, thermal energy in the pendulum mode of the suspension will also produce movement of the ends of the bar.

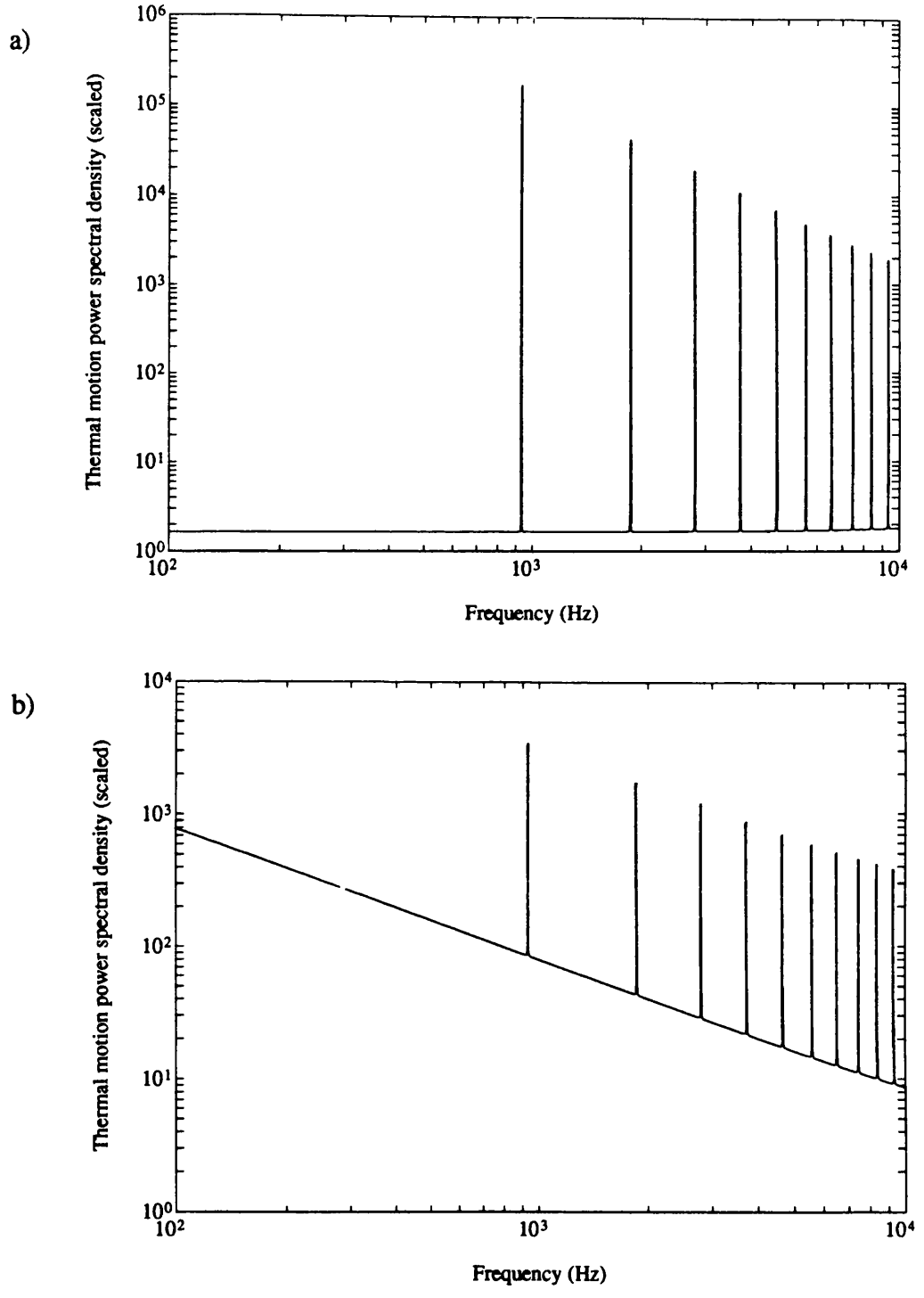

Figure 4.6: The Predicted Form for the Thermal Motion Power Spectral Density Associated with the Radial Motion of the Fundamental Longitudinal Mode of a Test Mass. *a) shows the case when the materials of the both the test mass and the suspension wire have Q values which are inversely proportional to frequency b) shows the case when the materials of both the test mass and the suspension wire have a frequency independent Q. Both graphs have been scaled up by a factor of 10^{44}.*

In order to calculate the total level of thermal motion of the suspended columnar silicon mass, it is necessary to first model and calculate the thermal motion of the pendulum which the suspended mass forms. Before investigating the possible structure of such a model, consideration is first given to the relation between the Q_w of the suspension wire and the Q of the pendulum, Q_{pen}.

4.7.1 The Quality Factor of a Pendulum

The restoring force for a pendulum comes primarily from the gravitational field with only a small fraction due to the flexing of the suspension wires which support the mass. The gravitational field is non-lossy and thus energy is only dissipated in the suspension wires, assuming that no other losses are present in the system. From the definition of the Q of a resonant system, eq. (2.1), the Q of the suspension wires is given by

$$Q_w = \frac{2\pi E_w}{E_{lost}} \tag{4.52}$$

where E_w is the energy stored in the suspension wires and

E_{lost} is the energy lost in the suspension wires per cycle.

Hence the Q of the pendulum

$$Q_{pen} = 2\pi \frac{E_w + E_g}{(2\pi E_w)/Q_w}$$

$$\approx Q_w \frac{E_g}{E_w} \tag{4.53}$$

where E_g is the energy stored in the gravitational field.

Thus it is possible for the pendulum to have a higher Q than the suspension wire material.

Now

$$\frac{E_g}{E_w} = \frac{k_g}{k_w} \tag{4.54}$$

where k_g is the gravitational spring constant given by

$$k_g = \frac{mg}{\ell} \tag{4.55}$$

and k_w is the elastic spring constant for the pendulum given by (Saulson, 1990)

$$k_w = \frac{n\sqrt{TEI}}{2\ell^2} \tag{4.56}$$

where n is the number of wires supporting the mass,

T is the tension in each wire,

E is Young's modulus and

I is the moment of inertia of the wire cross section. For a wire of circular cross section and radius r, $I = \frac{\pi r^4}{2}$.

Substituting eqs. (4.54) and (4.56) into eq. (4.53) gives the Q_{pen} of the pendulum to be

$$Q_{pen} = Q_w \frac{2mg\ell}{n\sqrt{TEI}} \tag{4.57}$$

4.7.2 Discussion of the Losses in the Pendulum Mode of a Suspended Mass Compared with Those of the Normal Modes of the Suspension Wires

One of the fundamental assumptions in considering the energy stored in a simple pendulum is that the suspension wire is inextensible. This implies that the energy is stored in the gravitational field and not in the suspension wire. Thus assuming no other losses are present, the Q of a simple pendulum would be predicted to be infinite. In reality the pendulum wire must bend slightly in order to allow the pendulum bob to swing. Energy is required for this and, since there will be some loss in the material of the wire, some energy will be lost from the pendulum resulting in a finite value for Q_{pen}. As shown in the previous section , Q_{pen} may be significantly larger than the Q of the suspension wire.

Now consider the suspension wires resonating in one of their normal modes. For this to happen it is necessary for the wire to be slightly extensible. Potential energy is thus stored, and hence also dissipated, in the wire as a result of the change of length. Thus the value of Q_w, which was inferred from the experimental data for Q of a columnar silicon mass, as a function of suspension wire length, is a measure of the losses in the violin modes of the wires.

Hence at the pendulum frequency, the suspension wires are assumed to be inextensible whereas at their resonant modes the wires are extensible and the Q of the system changes from being limited by Q_{pen} to being limited by Q_w. In order to see how this changeover takes place, consider the extension of a wire as characterised by the vertical oscillations of a simple pendulum indicated in figure 4.7.

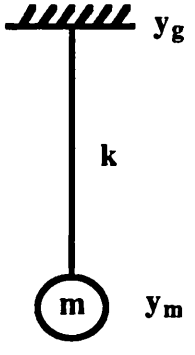

Figure 4.7: A Simple Pendulum. *y_g and y_m denote the vertical displacement of the point of suspension and the mass respectively. The suspension wire has stiffness k.*

The equation of motion for vertical oscillations of the system, assuming no damping, is given by

$$m\frac{d^2y_m}{dt^2} = -k\,(y_m - y_g) \tag{4.58}$$

From this it may be shown that

$$\Delta\ell = y_g - y_m = \frac{-\omega^2 y_g}{\omega_v^2 - \omega^2} \tag{4.59}$$

where $\Delta\ell$ is the change in the length of the suspension wire and

ω_v is the angular resonant frequency of the vertical mode of the pendulum.

From eq. (4.59) it may be observed that for $\omega << \omega_v$, $\Delta\ell \approx 0$. Thus for frequencies less than the resonant vertical frequency of the system the suspension wire appears to be inextensible and the mass moves with the same vertical displacement as the suspension point. For $\omega >> \omega_v$, $\Delta\ell \approx y_g$, and hence for frequencies greater than the resonant vertical frequency of the system, the suspension wire appears to be extensible with the change in length of the suspension wire being equal to the displacement of the suspension point. This implies that for such frequencies the mass remains stationary.

It may be shown that the resonant vertical frequency of the pendulum which is formed by the columnar silicon mass and suspension wire is given by

$$f_v = \frac{1}{2\pi}\sqrt{\frac{2ES}{m\ell}} = 31 \text{ Hz} \qquad (4.60)$$

where E is Young's modulus for the suspension wire (2.15×10^{11} N m^{-2}),

S is the cross-sectional area of the wire (1.8×10^{-8} m^2),

m is the mass (1.39 kg) and

ℓ is the length of the suspension wire (0.15 m).

Thus at frequencies below f_v =31 Hz, the Q of the system appears to be enhanced above Q_w since most of the energy is stored in the gravitational field and only a small fraction is lost in the wire. At frequencies above 31 Hz, the energy in the system is mainly stored in the suspension wires and hence the Q of the system is limited by Q_w.

4.7.3 Choice of Circuit Parameters

From the experimental data on the Q of the columnar silicon mass as a function of suspension length, the Q_w of the suspension wire was inferred to be 3×10^3 at a frequency of 48 kHz. The velocity of sound in the suspension wires is given by $c = \sqrt{T/\mu}$ where T is the tension in one wire and μ is the linear density of the wire. This expression may be compared with that for the phase velocity for waves in the transmission line analogy, $c_{pW} = 1/\sqrt{L_w C_w}$, ($\alpha << 1$), where L_w is the inductance per unit

length of the line and C_w is the capacitance per unit length. (For lines with negligible loss the group velocity is also given by $1/\sqrt{L_w C_w}$ and thus the waves are non-dispersive.) Since L_w is analogous to mass per unit length, i.e. linear density, μ, it is observed that C_w is equivalent to (tension)$^{-1}$. Thus the total capacitance of each line $C_{wt} \equiv 2\ell/mg$. Hence in order to model the pendulum motion of the suspended mass, an inductor equivalent to the mass of the pendulum bob is placed in series with two transmission lines as indicated in figure 4.8. The angular resonant frequency of the circuit is given by

$$f_{pen} = \frac{1}{2\pi\sqrt{L_{pen}\frac{C_{wt}}{2}}} \equiv \frac{1}{2\pi}\sqrt{\frac{g}{\ell}} \qquad L_w \ell << L_{pen} \quad (4.61)$$

Thus the circuit resonates with the same frequency as the pendulum formed by the suspended mass.

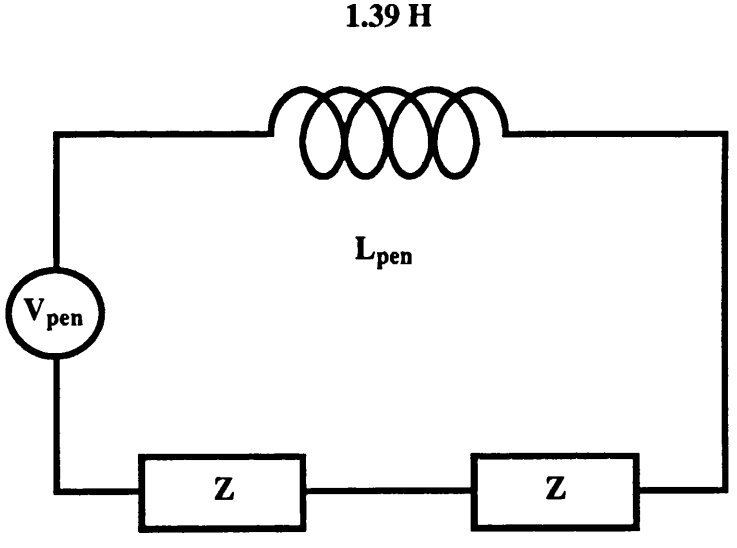

Figure 4.8: The Equivalent Circuit for the Pendulum Mode of the Suspended Test Mass. *The resonant frequency of the circuit is 1.3 Hz. The transmission lines have $Q_w = 3 \times 10^3$ at 48 kHz. Z represents the impedance of a transmission line which may be written as $Z(f) = r(f) + X(f)$.*

This circuit corresponds to the situation where the suspension wires move with the same displacement and hence velocity as the centre of mass of the pendulum bob. Note that other pendulum modes such as rocking and tilting of the pendulum bob will not be

considered here. The transmission lines can be modelled either as being lossy with their far ends terminated by an infinite impedance (section 4.5.1), or lossless with their far ends terminated by a resistor (section 4.5.5), these two cases being equivalent to each other for a fixed line length (section 4.5.5).

It is important to realise that this model will only correctly predict the level of the thermal motion power spectral density at frequencies greater than the vertical resonant frequency of the pendulum, f_v. Below f_v, the circuit will yield an overestimate of this level since the circuit models the situation where all the energy is stored in the suspension wires and hence some energy is dissipated there. As discussed in the previous section, this is not the case for the pendulum frequency where the majority of the energy is stored in the gravitational field which is non-lossy with only a small fraction of the energy being dissipated in the wires.

4.7.4 Prediction of the Level of Thermal Motion of a Pendulum at Frequencies above its Vertical Resonant Frequency

Thermal displacement of the pendulum is represented in the equivalent circuit of figure 4.8, by the fluctuating charge, q_{Lpen}, in the inductor L_{pen}.where

$$\langle q^2_{Lpen} \rangle = \frac{8k_B Tr(f)}{s^4\left(L + \frac{2X(f)}{\omega}\right)^2 + 4s^3 r(f)\left(L + \frac{2X(f)}{\omega}\right) + 4s^2 r^2(f)} \tag{4.62}$$

The resonant frequency of the pendulum lies well below the frequency bandwidth of interest for the detection of gravitational waves. Thus in order to calculate the thermal noise in this bandwidth, the level of thermal motion of the pendulum at frequencies much greater than its resonant frequency must be considered. For this case eq. (4.62) may be further simplified to

$$\langle q^2_{Lpen} \rangle = \frac{k_B Tr(f)}{2\pi^4 f^4\left(L + \frac{X(f)}{\pi f}\right)^2} \tag{4.63}$$

Three cases will be considered: frequencies below the resonant modes of the suspension

wires, frequencies at which the suspension wires are resonant at their normal modes and frequencies mid-way between the normal modes of the suspension wires.

Transmission Lines at Frequencies Below their Normal Mode Frequencies [i.e $f < c/4\ell$]

Below the normal mode frequencies of the transmission lines, the real part of the impedance of the line is, from eq. (4.3)

$$r(f) = Z_o \frac{\sinh 2\alpha\ell}{\cosh 2\alpha\ell - \cos 2\beta\ell}$$

By expanding in terms of exponential functions it may be shown that

$$r(f) \approx \frac{Z_o c}{4\pi\ell f\, Q_w(f)} \qquad f < c/4\ell \qquad (4.64)$$

The imaginary term of the impedance of the line is, from eq. (4.2)

$$X(f) = -Z_o \frac{\sin 2\beta\ell}{\cosh 2\alpha\ell - \cos 2\beta\ell}$$

this may, in a similar manner, be shown to be

$$X(f) \approx -\frac{Z_o c}{2\pi\ell f} \qquad f < c/4\ell \qquad (4.65)$$

Now $L + X(f)/(\pi f) \approx L$ for $f_v < f < c/4\ell$ and hence eq. (4.63) may be written with the aid of eq. (4.64) as

$$\langle q^2_{Lpen} \rangle \approx \frac{Z_o k_B T c}{8\pi^5 f^5 L^2 Q_w(f)\ell} \qquad f_v < f < c/4\ell \qquad (4.66)$$

As before, two cases are considered concerning the frequency dependence of $Q_w(f)$:

a) Q_w inversely proportional to frequency.

For this case it is observed from eq. (4.66) that the fundamental level of the thermal motion power spectral density of the pendulum $\langle q^2_{Lpen} \rangle \propto \frac{1}{f^4}$ for frequencies greater than f_v and less than $c/4\ell$.

b) Q_w frequency independent.

In this case the fundamental level of the thermal motion power spectral density $\langle q^2_{Lpen} \rangle \propto \frac{1}{f^5}$ for frequencies between f_v and $c/4\ell$.

Transmission Lines at Frequencies Midway Between their Normal Mode Frequencies [i.e. f = (2n+1)c/4ℓ]

When the line is at a frequency exactly midway between its normal modes i.e. $f = (2n+1)c/4\ell$, eq. (4.63) may be written as

$$\langle q^2_{Lpen} \rangle \approx \frac{k_B T r_s(f)}{2\pi^4 f^4 L^2} \tag{4.67}$$

since $X(f) = 0$ and where, from eq. (4.37), $r_s(f) = \frac{Z_o \pi \ell f}{Q_w(f)\, c}$. Thus

$$\langle q^2_{Lpen} \rangle \approx \frac{k_B T Z_o \ell}{2\pi^3 f^3 L^2 Q_w(f) c} \tag{4.68}$$

Again two cases are considered:

a) Q_w inversely proportional to frequency.

From eqs. (4.66) and (4.68) the fundamental level of the thermal motion power spectral density for a pendulum changes slope from $\langle q^2_{Lpen} \rangle \propto \frac{1}{f^4}$ for frequencies $f_v < f < c/4\ell$ to $\langle q^2_{Lpen} \rangle \propto \frac{1}{f^2}$ for frequencies $f = (2n+1)c/4\ell$.

b) Q_w independent of frequency.

For this case the fundamental level of the pendulum thermal motion power spectral density changes slope from $\langle q^2_{Lpen} \rangle \propto \frac{1}{f^5}$ at frequencies $f_v < f < c/4\ell$, to $\langle q^2_{Lpen} \rangle \propto \frac{1}{f^3}$ for frequencies $f = (2n+1)c/4\ell$.

Transmission Lines at their Normal Mode Frequencies [i.e. f = nc/2ℓ]

When the frequency is such that the lines are at one of their normal mode frequencies i.e. f = nc/2ℓ, eq. (4.63) may be written as

$$\langle q^2_{Lpen} \rangle \approx \frac{k_B T r_p(f)}{2\pi^4 f^4 L^2} \tag{4.69}$$

since X(f) = 0, and where from eq. (4.38) $r_p(f) = \frac{Z_o Q_w(f) c}{\pi f \ell}$ and thus

$$\langle q^2_{Lpen} \rangle \approx \frac{k_B T Z_o c Q_w(f)}{2\pi^5 f^5 L^2 \ell} \tag{4.70}$$

Since $r_p(f) >> r_s(f)$ the level of thermal motion predicted by eq. (4.70) is much greater than that predicted by eq.(4.68). This leads to a spectrum of thermal noise spikes, due to the suspension wires resonating, being superimposed on the fundamental level of thermal motion from the pendulum. Again two cases are considered:

a) Q_w inversely proportional to frequency.
When the transmission lines are on resonance, the thermal motion power spectral density of the pendulum increases from its fundamental level to the level given by eq. (4.70). The peak heights of these spikes falls off as $\langle q^2_{Lpen} \rangle \propto \frac{1}{f^6}$.

b) Q_w frequency independent.
For this case the peak heights of the thermal noise spikes falls off as $\langle q^2_{Lpen} \rangle \propto \frac{1}{f^5}$.

Conclusion

Consider a pendulum of resonant frequency f_{pen}, and quality factor Q_{pen} and hence Q_w, at the pendulum frequency f_{pen}. In order to minimise the fundamental level of thermal motion of the pendulum it is better to have suspension wire material with a Q_w which is independent of frequency. This is because the level of the thermal motion power spectral density falls off faster at frequencies greater than f_{pen} than for a material with a Q_w inversely proportional to frequency. Note that this is different to the case of minimising thermal motion of the test mass where, given a mass with a Q at a resonant frequency f_o,

it is preferable to have a material with a Q which is inversely proportional to frequency.

For the case considered here of the pendulum formed by the columnar silicon mass, the situation is somewhat different. From the analysis of the experimental data of Q of the mass as a function of suspension length it was inferred that Q_w was 3×10^3 at the resonant frequency of the mass (48 kHz). If Q_w is assumed to be inversely proportional to frequency, from eq. (4.57) this would imply that $Q_{pen} = 2.5 \times 10^{10}$ at f_{pen}, where $\ell = 0.15$ m, $r = 3 \times 10^{-3}$ inch and $E = 2.15 \times 10^{11}$ N m^{-2}. If, on the other hand, Q_w is assumed to be frequency independent, this would imply that $Q_{pen} = 7 \times 10^5$ at f_{pen}. Thus there are several orders of magnitude difference, predicted by the two laws, in the Q_{pen} of the pendulum at the pendulum frequency. Figure 4.9 shows a comparison of the predicted forms of the thermal noise power spectral density for the pendulum for the two cases considered i.e. for Q_w inversely proportional to frequency and for Q_w frequency independent. Both graphs have $Q_w = 3 \times 10^3$ at 48 kHz. From these graphs it is evident that, for this pendulum, the fundamental level of the thermal motion power spectral density is lower when Q_w is inversely proportional to frequency. This arises since, even though the fall off is less steep, the Q_{pen} of the pendulum at f_{pen} is much larger. It is noted, however,that caution must be exercised when extrapolating the behaviour of Q_w over such a large frequency range. Neither law may hold over the entire frequency band as has been assumed here. The graphs do however illustrate the general shape of the spectrum in these two 'extreme' cases.

4.8 The Total Thermal Motion of a Suspended Mass

The total thermal motion of a suspended test mass is due to a summation of four effects:

1) thermal energy in the mass itself, causing movement of the ends of the mass with respect to its centre,

2) thermal energy in the resonant modes of the wires in the radial direction causing further movement of the ends of the mass with respect to its centre,

a)

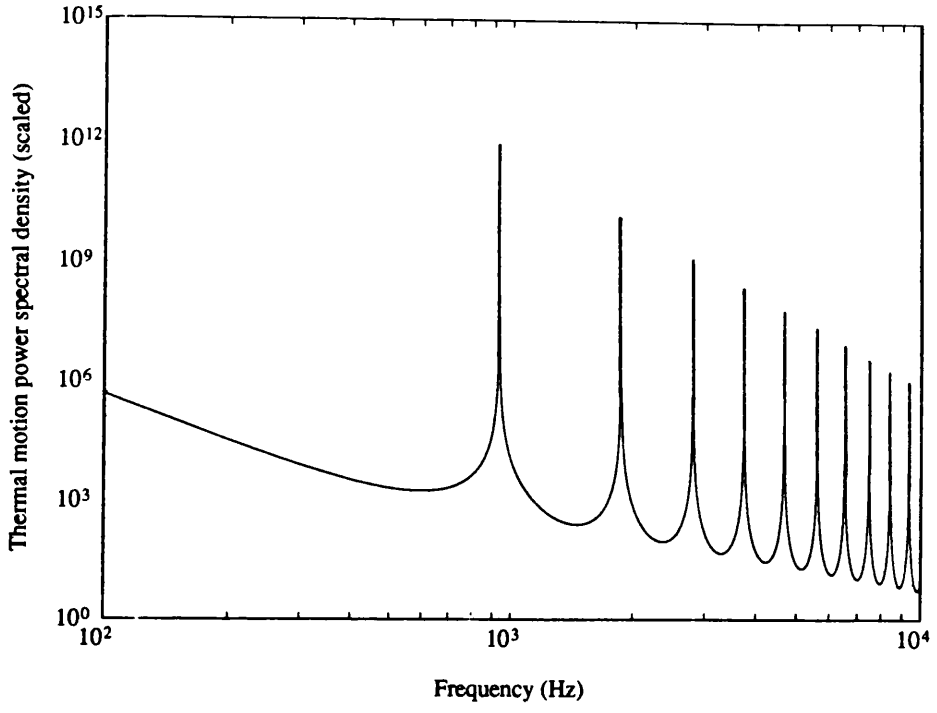

b)

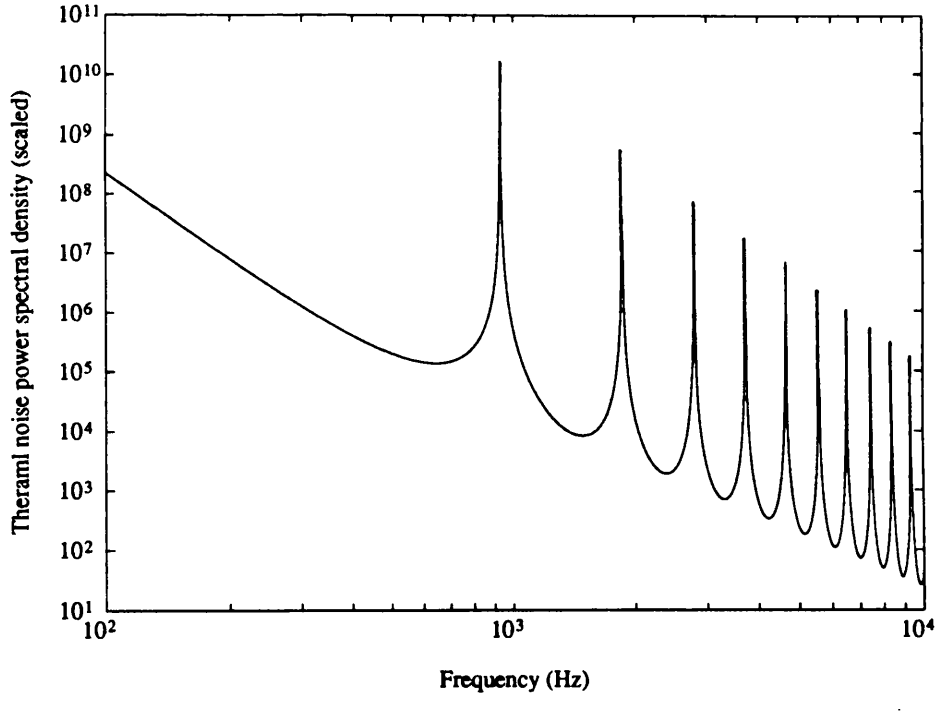

Figure 4.9: The Predicted Form for the Thermal Motion Power Spectral Density of the Pendulum formed from the Columnar Silicon Mass. *a) shows the case when the Q of the pendulum is inversely proportional to frequency. b) shows the case when the pendulum Q is frequency independent. Both graphs have been scaled up by a factor of* 10^{44}.

the mass as a whole, and

4) thermal energy in the resonant modes of the wires in the longitudinal direction causing further movements of the mass as a whole, through the effect of the wire modes on the centre of mass.

The equivalent circuit of figure 4.3, as discussed in section 4.6, is used to predict the total level of thermal motion due to (1) and (2). It was noted however that this equivalent circuit actually predicts the level of radial motion of the mass. Since in a laser interferometric gravitational wave detector, it is the thermal motion of the front face of the mass that is of concern, the predicted level of radial motion must be converted to longitudinal motion of the mass as indicated by eq. (4.45).

The equivalent circuit of figure 4.8, discussed in section 4.7, is used to predict the total level of thermal motion due to (3) and (4). Thus the predicted total thermal motion of a suspended mass is obtained by combining the results from the two equivalent circuits

$$\langle q_{total}^2 \rangle = \langle q_{Lpen}^2 \rangle + \frac{\mathcal{L}^2}{4\nu^2\mathcal{R}^2} \langle q_C^2 \rangle \tag{4.71}$$

where $\langle q_C^2 \rangle$ and $\langle q_{Lpen}^2 \rangle$ are defined by eqs. (4.41) and (4.62)

4.8.1 The Effect of Thermal Motion of the Suspended Test Masses on the Sensitivity of a 3 km Baseline Detector

Using the results of sections 4.6 and 4.7 it is possible to calculate the sensitivity of a laser interferometric gravitational wave detector which is limited by thermal motion of the internal modes of the test masses. Note that the effect of thermal motion of the beamsplitter is small compared to that of the test masses since the sensing light is reflected many times from the test masses in each arm leading to amplification of thermal motion of the test masses. Since the thermal motion of the four test masses in the detector will not be coherent, the power spectral density of the apparent gravitational wave amplitude due to their thermal motion is given by

$$\langle h^2 \rangle = \frac{4\langle x^2 \rangle}{L_D^2} \tag{4.72}$$

where $\langle x^2 \rangle$ is the total thermal motion power spectral density of the suspended mass and

L_D is the arm length of the interferometer.

The largest columnar silicon masses presently available are approximately 15 inches in diameter by 8 inches long. Consider using four such masses to form the mirrors for a 3 km baseline interferometer. The fundamental longitudinal mode of such a mass occurs at a resonant frequency, f_o, of about 15 kHz with 6 normal modes lying in frequency below this (McMahon, 1964). Five of these modes will introduce only second order effects since the average motion of a circle concentric with the face of the mass is zero. The antisymmetric drum mode, illustrated in figure 3.10, occurs at about 11 kHz and clearly does not fall into this class. However, by suitably arranging the laser spots to fall on the nodal line of this mode, assuming a delay line system is used in the arms of the interferometer, this mode will also give rise to only second order effects. Thus only motion of the fundamental longitudinal mode will be considered here.

A piece of columnar silicon 15 inches in diameter by 8 inches long has a mass of 53 kg. To support this using a single loop suspension of stainless steel wire would require wire of diameter 0.75 mm. Pendulum Qs of the order of 10^7 have been experimentally demonstrated (Martin, 1978). From eq. (4.57), assuming a pendulum frequency of 1 Hz, this would imply a Q_w of 10^5 at 1 Hz if these experiments were limited solely by the Q of the wire. Thus the equivalent circuit to represent the pendulum which the suspended mass forms, has L_m = 53 H, Z_o = 0.98 Ω, $Q_{pen}(f_{pen}) = 10^7$ and $Q_w(f_{pen}) = 10^5$.

Consider the mass resonating in its fundamental longitudinal mode. Eq. (4.46) allows evaluation of the value of the inductor, L, used to model the effect radial motion of the mass. Thus the equivalent circuit for the mass has L = 17 H and C = 6.6 pF. If the Q of the columnar silicon is frequency independent, using the highest measured value, $Q = 5 \times 10^6$ at 48 kHz and at f_o = 15 kHz and thus $R(f_o)$ = 0.32 Ω. If the Q of the columnar silicon is inversely proportional to frequency $Q(f_o) = 1.6 \times 10^7$ and

$R = 0.10\ \Omega$.

Note that this approach models two pendulums which both have the same Q_{pen} at the pendulum frequency, but have test masses of different Q values at their resonant frequency. This is since the Q values of the mass are obtained using two different laws, from an experimental measurement made at 48 kHz. The mass which has an assumed Q inversely proportional to frequency has a Q three times higher at 15 kHz, than the test mass which is assumed to have a frequency independent Q.

The equivalent circuits of sections 4.6 and 4.7 were used to consider two cases, with their results combined as described by eq. (4.71) and converted to an apparent gravitational wave amplitude using eq. (4.72).

1) A 'worst case' i.e. combining the worst case for thermal motion of the pendulum with that of the test mass. This corresponds to Q_w (and thus Q_{pen}) being inversely proportional to frequency and the Q of the mass being frequency independent. This case is illustrated in figure 4.10(a)

2) A 'best case' i.e. combining the best case for thermal motion of the pendulum with that of the test mass. This corresponds to Q_w (and thus Q_{pen}) being frequency independent and the Q of the mass being inversely proportional to frequency. This is illustrated in figure 4.10(b).

Below the frequency of the first wire resonance, case 2 is clearly superior to case 1. Since the wire resonances are very high Q in the best case, it should be possible to filter these out of the detector output. This would not be so easy in the worst case where the resonances are lower Q and thus occupy a greater bandwidth. Note however that the worst case shown in figure 4.10(a) is probably unrealistically bad. This is since Q_w for the highest frequency wire resonance shown, which occurs at 9.5 kHz, is approximately 10, while from the model of the experimental system discussed in section 4.5, it was inferred that Q_w was ~ 3×10^3 at a frequency of 48 kHz. This implies that the form of Q_w inversely proportional to frequency over the whole frequency range of 1 to 48 kHz, with $Q_w = 10^5$ at 1 Hz, is not a realistic model of the experimental situation.

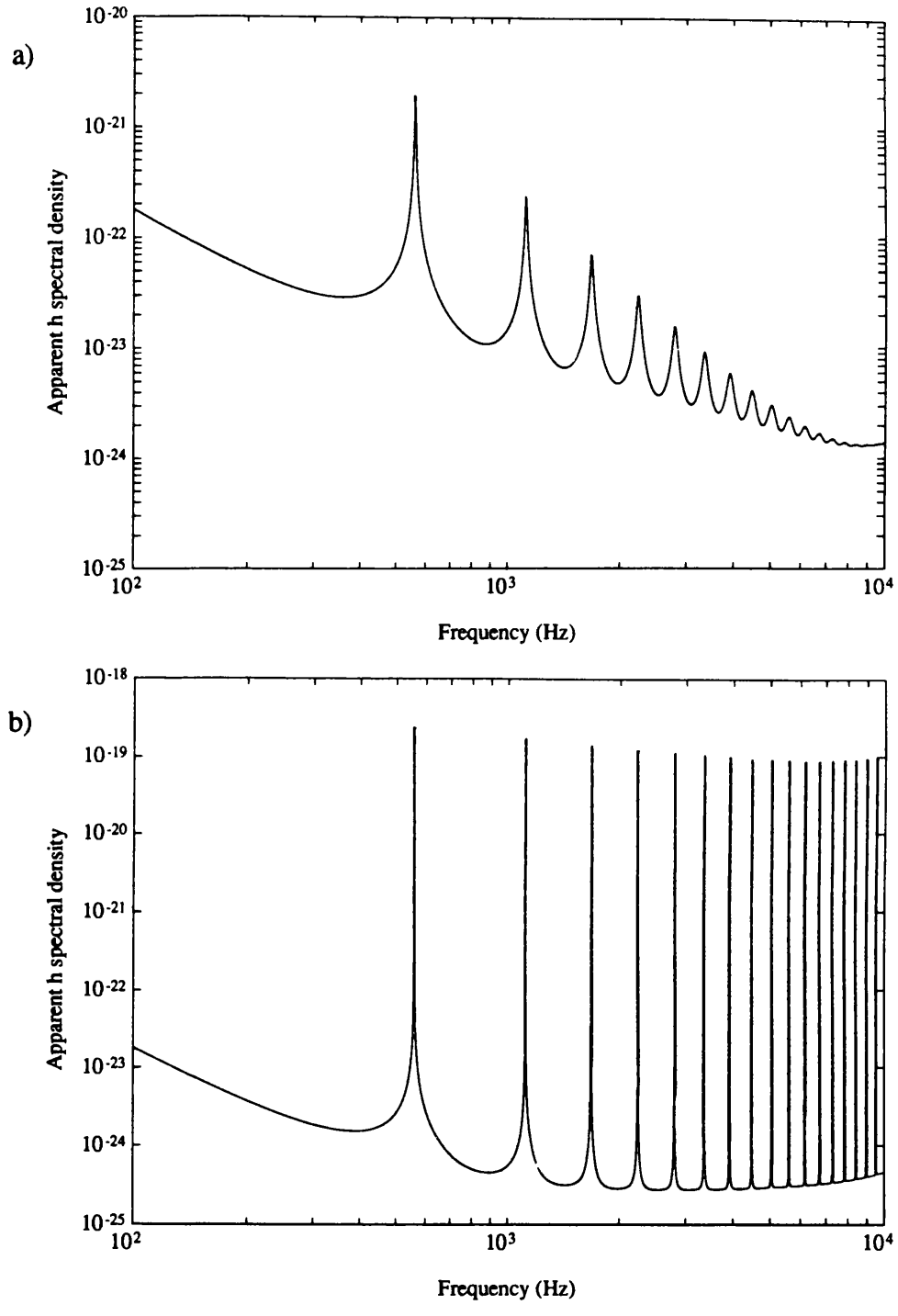

Figure 4.10: The Limit to Sensitivity of a 3 km Baseline Interferometer due to the Effect of Thermal Motion of the Suspended Test Masses. *The graphs shows plots of the spectral density of the apparent gravitational wave amplitude caused by thermal motion of the test masses. a) shows the worst case with the Q of the pendulums inversely proportional to frequency and the Q of the test masses frequency independent. b) shows the best case with the Q of the pendulums frequency independent and with the Q of the test masses inversely proportional to frequency.*

4.9 Conclusion

Based on an equivalent circuit it is concluded that the fundamental level of thermal noise from a test mass is not affected by the apparent degradation in the measured Q of the mass, due to resonances in the suspension wires. It has also been demonstrated that the spectrum of thermal motion of suspended test masses in a laser interferometric gravitational wave detector depends on how the Q of the test mass and of the suspension wires vary with frequency. Thus in order to predict the effect of thermal motion of the suspended test masses on the sensitivity of a laser interferometric gravitational wave detector, it is necessary to first know how the quality factors of the materials involved vary as a function of frequency over the frequency band of interest for the detection of gravitational waves. This will be the subject of chapter 5.

Chapter 5

An Investigation of Q as a Function of Frequency

5.1 Introduction

In chapter 4, figure 4.10, two cases were presented for the limit to the sensitivity of a laser interferometric gravitational wave detector due to the thermal motion of the suspended test masses. The difference between the two cases was due to different assumptions concerning the frequency dependence of the quality factor of the suspension wire and test mass materials. In this chapter a model of damping, and hence Q as a function of frequency, is discussed for anelastic materials with a brief review of the formal theory of anelasticity being presented. Experimental measurements of Q as a function of frequency for aluminium and fused silica are detailed and reviewed in the light of this theory.

5.2 A Brief Review of the Formal Theory of Anelasticity

A more comprehensive analysis of this topic is given by e.g. Zener (Zener, 1948) and Nowick and Berry (Nowick and Berry, 1972)

5.2.1 The Definition of an Anelastic Solid

Consider first an ideal elastic solid for which Hooke's law defines the relation between stress, σ, and strain, ε, as

$$\sigma = M\varepsilon \tag{5.1}$$

or

$$\varepsilon = J\sigma \tag{5.2}$$

where M is the appropriate modulus of elasticity for the deformation

J = 1/M is the modulus of compliance

Eqs. (5.1) and (5.2) imply the following three conditions which define ideal elastic behaviour:

1) For every applied stress there is a unique equilibrium value of strain, and vice versa.
2) Equilibrium is reached instantaneously, i.e. eqs. (5.1) and (5.2) contain no time dependence. (Note that since the velocity of sound in a material is finite, instantaneous equilibrium is only truly reached in an infinitesimally small sample of the the material)
3) The stress - strain relationship is linear.

Note that condition (1) implies that upon removal of the applied stress or strain the ideal elastic solid recovers to its initial starting conditions.

If condition (2) is altered to allow a time dependent response, the material is said to be anelastic. Thus an anelastic solid is defined by:

1) For every applied stress there is a unique equilibrium value of strain, and vice versa.
2) The equilibrium response is attained only after a 'sufficient' period of time has elapsed. The time required to reach equilibrium may be anything from fractions of a second to very long periods of time.
3) The stress - strain relationship is linear.

Note that condition (2) does not imply the absence of an instantaneous response to an applied stress or strain. The term 'anelasticity' signifies that in addition to an elastic (instantaneous) response there is a time dependent nonelastic response.

5.2.2 The Quasi-static Response Functions

Strain Relaxation

Consider applying a constant stress, σ_0, at time t = 0, to a sample of material and observing the resulting strain as a function of time, $\varepsilon(t)$. Generalising eq. (5.2) to include time dependency, the strain relaxation or creep function, J(t), is defined as

$$J(t) = \frac{\varepsilon(t)}{\sigma_0} \qquad t \geq 0 \qquad (5.3)$$

Figure 5.1 shows a comparison of the behaviour of a perfectly elastic solid with that of an anelastic solid.

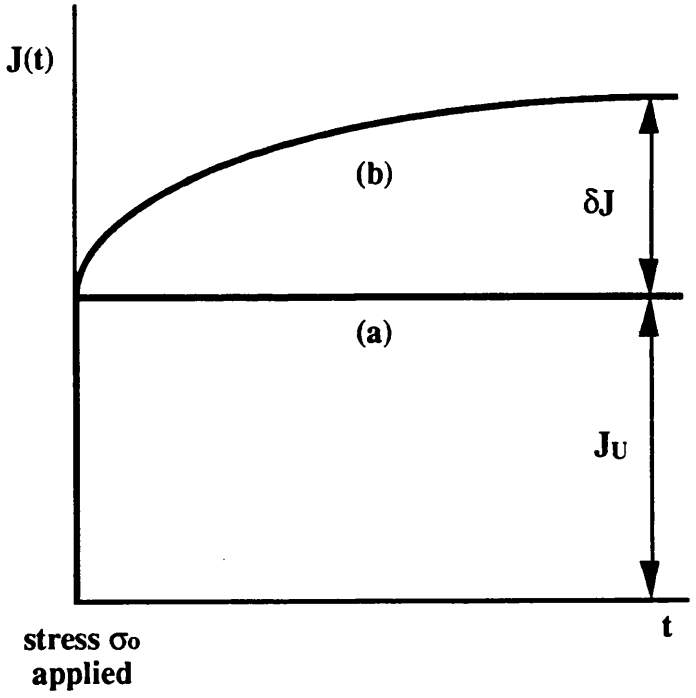

Figure 5.1: The Strain Relaxation Function. *Curve a) shows the response of a perfectly elastic material, curve b) the response of an anelastic material.*

The initial value of J(t) is called the unrelaxed compliance i.e. $J(0) \equiv J_U$, since the sample has not had time to relax to its equilibrium value, which is called the relaxed compliance,

i.e. $J(\infty) \equiv J_R$. The relaxation of the compliance is defined as

$$\delta J = J_R - J_U \tag{5.4}$$

Stress Relaxation

Consider instead applying a constant strain, ε_o, to the sample and observing the resulting stress as a function of time, $\sigma(t)$. Eq. (5.1) may be generalised to include time dependency and thus the stress relaxation function, M(t) is defined as

$$M(t) = \frac{\sigma(t)}{\varepsilon_o} \qquad t \geq 0 \tag{5.5}$$

The initial value of M(t) is termed the unrelaxed modulus i.e. $M(0) \equiv M_U$ and the equilibrium value, the relaxed modulus i.e. $M(\infty) = M_R$. Since for each value of applied strain there is a unique equilibrium value of stress

$$M_R = \frac{1}{J_R} \tag{5.6}$$

For $t \approx 0$ the material exhibits ideal elasticity and thus from eq. (5.1) and (5.2)

$$M_U = \frac{1}{J_U} \tag{5.7}$$

Since $J_R > J_U$, $M_R < M_U$. Figure 5.2 shows a comparison of the response of a perfectly elastic solid to an applied strain, with that of an anelastic solid.

The relaxation of the modulus M is defined as

$$\delta M = M_U - M_R \tag{5.8}$$

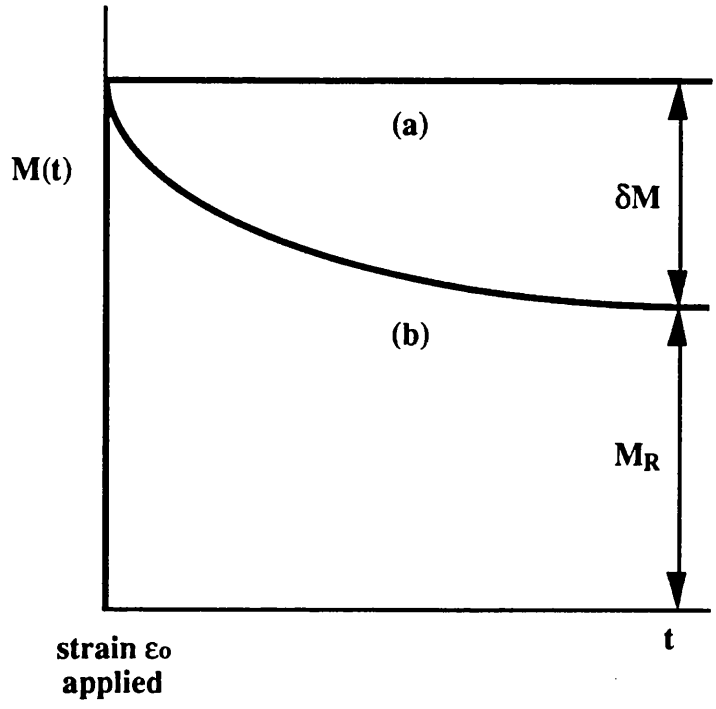

Figure 5.2: The Stress Relaxation function. *Curve a) shows the response of a perfectly elastic material, curve b) the response of an anelastic material.*

5.2.3 The Quality Factor of an Anelastic Material

Consider now applying a periodic stress to a sample of anelastic material

$$\sigma = \sigma_0 e^{j\omega t} \tag{5.9}$$

where σ_0 is the amplitude of the stress

ω is the angular frequency of the applied stress

Since the stress-strain relationship is linear, the strain must also be periodic with the same angular frequency and may be written as

$$\varepsilon = \varepsilon_0 e^{j(\omega t - \phi(\omega))} \tag{5.10}$$

where ε_0 is the amplitude of the strain

$\phi(\omega)$ is the angle by which the strain lags behind the stress. This is known as the loss angle.

The energy per unit volume of the sample, at any phase in the cycle, is given by

$$E = \int \sigma d\varepsilon \tag{5.11}$$

Thus the energy lost, E_L, per cycle per unit volume is

$$E_L = \int_0^{2\pi/\omega} -\omega\sigma_o\varepsilon_o \cos\omega t \sin(\omega t - \phi(\omega))\, dt$$

$$= \pi\varepsilon_o\sigma_o \sin\phi(\omega) \tag{5.12}$$

The maximum energy stored per unit volume, E_s, is attained when the strain goes from a minimum to a maximum and is thus given by

$$E_s = \int_{(\phi - \pi/2)/\omega}^{\phi/\omega} -\omega\sigma_o\varepsilon_o \cos\omega t \sin(\omega t - \phi(\omega))\, dt$$

$$= \frac{1}{2}\sigma_o\varepsilon_o \cos\phi(\omega) + \frac{\pi}{4}\sigma_o\varepsilon_o \sin\phi(\omega) \tag{5.13}$$

For materials of interest for test masses in gravitational wave detectors, in general $\phi(\omega) << 1$ and hence eq. (5.13) reduces to

$$E_s = \frac{1}{2}\sigma_o\varepsilon_o \cos\phi(\omega) \tag{5.14}$$

Thus from the definition of the quality factor of a resonant system, eq. (2.1), eqs. (5.12) and (5.14) yield the following expression for the Q of an anelastic material with angular resonant frequency ω_o

$$Q = \frac{1}{\tan\phi(\omega_o)} \qquad \phi(\omega) << 1 \tag{5.15}$$

$\tan\phi(\omega)$ is known as the internal friction of a material. Since $\phi(\omega)$ is assumed small eq. (5.15) may be written as

$$Q = \frac{1}{\phi(\omega_o)} \tag{5.16}$$

Thus a fraction $2\pi\phi(\omega_o)$ of the stored energy is dissipated per cycle. It is observed from eq. (5.16) that the frequency dependence of Q for a material may be ascertained by first considering the frequency dependence of the loss angle for the material.

5.2.4 The Functional Form of Internal Friction

An anelastic solid may be represented by a suitable combination of springs and dashpots. One such model is shown in figure 5.3. When a strain, ε_o, is applied to the system both springs extend. As time passes, the dashpot will yield until the stress on spring 1 is zero. At this time all the stress in the system will appear across spring 2.

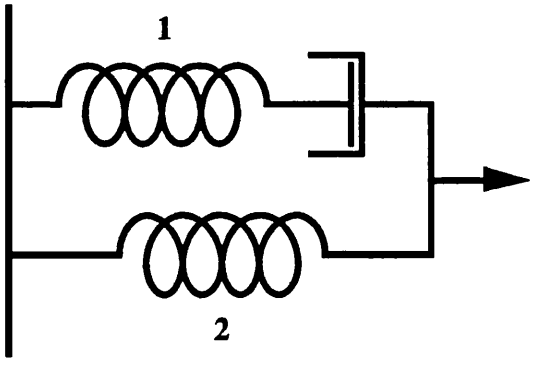

Figure 5.3: Representation of the Standard Anelastic Solid. *This is formed by a spring and a dashpot in series, a combination known as a Maxwell unit, with a second spring in parallel with these.*

It is noted that this model is not unique. Another possible representation is a spring and dashpot in parallel, a combination termed a Voigt unit, with a second spring in series.

The stress-strain equation for the model of figure 5.3 can be shown to be of the form

$$\sigma + a_1\dot{\sigma} = b_o\varepsilon + b_1\dot{\varepsilon} \tag{5.17}$$

where the dot notation represents differentiation with respect to time and a_1, b_o and b_1 are constants which remain to be determined.

Consider the case when both ε and $\dot{\varepsilon}$ are zero. Under these conditions eq. (5.17) has solution

$$\sigma(t) = \sigma_o e^{-t/a_1} \tag{5.18}$$

where σ_o is the value of the stress at $t = 0$.

Thus the constant a_1 is set equal to τ_ε, the stress relaxation time under conditions of constant strain.

Now consider a strain, ε_o, being applied at $t = 0$. The solution to eq. (5.17) is then

$$\sigma(t) = b_o\varepsilon_o + (\sigma_o - b_o\varepsilon_o)e^{-t/\tau_\varepsilon} \tag{5.19}$$

The stress in the sample relaxes, with relaxation time τ_ε, to its equilibrium value which with the aid of eq. (5.5), is given by $M_R\varepsilon_o$. Thus b_o is set equal to M_R, the relaxed elastic modulus. Hence eqs.(5.8) and (5.19) gives the stress relaxation function, as defined by eq. (5.5), to be

$$\begin{aligned} M(t) &= M_R + (M_U - M_R)e^{-t/\tau_\varepsilon} \\ &= M_R + \delta M e^{-t/\tau_\varepsilon} \end{aligned} \tag{5.20}$$

This describes the stress relaxation function depicted in figure 5.2.

Consider now the case when both σ and $\dot{\sigma}$ are zero. For this case eq. (5.17) has solution

$$\varepsilon(t) = \varepsilon_o e^{-M_R t/b_1} \tag{5.21}$$

where ε_o is the value of the strain at t = 0.

Thus b_1 is set equal to $M_R\tau_\sigma$ where τ_σ is the strain relaxation time under conditions of constant stress. Hence eq. (5.17) becomes

$$\sigma + \tau_\varepsilon\dot{\sigma} = M_R(\varepsilon + \tau_\sigma\dot{\varepsilon}) \tag{5.22}$$

If a stress σ_o is now applied at time t = 0 with $\dot{\sigma} = 0$, eq. (5.22) has solution

$$\varepsilon(t) = J_R\sigma_o + (\varepsilon_o - J_R\sigma_o)e^{-t/\tau_\sigma} \tag{5.23}$$

and hence the strain relaxation function, from eqs. (5.3) and (5.4), is given by

$$\begin{aligned} J(t) &= J_R + (J_U - J_R)e^{-t/\tau_\sigma} \\ &= J_R - \delta J e^{-t/\tau_\sigma} \end{aligned} \tag{5.24}$$

This equation describes the graph of J(t) depicted in figure 5.1. Thus it has been demonstrated that this model describes the characteristics of an anelastic solid, as noted in section 5.2.1.

Now consider a very short time interval Δt during which the stress σ becomes $\sigma + \Delta\sigma$. Integrating eq. (5.22) with respect to time and taking the limit of Δt tending to zero yields

$$\tau_\varepsilon \Delta\sigma = M_R\tau_\sigma \Delta\varepsilon \tag{5.25}$$

The ratio of $\Delta\sigma$ to $\Delta\varepsilon$ is equal to the unrelaxed elastic modulus since, in such a short timescale, the sample has not had time to relax to equilibrium. Thus eq. (5.25) may be rewritten as

$$\frac{M_U}{M_R} = \frac{\tau_\sigma}{\tau_\varepsilon} \tag{5.26}$$

Now consider substituting the stress and strain functions given by eqs. (5.9) and (5.10) into eq. (5.22). This gives the angle by which the strain lags behind the stress as

$$\tan\phi(\omega) = \frac{M_U - M_R}{\overline{M}} \cdot \frac{\omega\bar{\tau}}{1 + (\omega\bar{\tau})^2} \tag{5.27}$$

where $\overline{M} = \sqrt{M_R M_U}$ and $\bar{\tau} = \sqrt{\tau_\sigma \tau_\varepsilon}$.

For $\phi(\omega) << 1$, $M_U \approx M_R$ and thus, from eq. (5.26), $\tau_\sigma \approx \tau_\varepsilon = \tau$. Hence $\phi(\omega) \approx \tan\phi(\omega)$ for $\phi(\omega) << 1$, may be written as

$$\phi(\omega) = \Delta \frac{\omega\tau}{1 + \omega^2\tau^2} \tag{5.28}$$

where $\Delta = \delta M/M_R$ is the relaxation strength of the material.

The form of $\phi(\omega)$ is thus a Deybe peak with a maximum value of $\Delta/2$ centred on $\omega = 1/\tau$ as shown in figure 5.4. Note that $\phi(\omega) << 1$ implies that $\Delta << 1$.

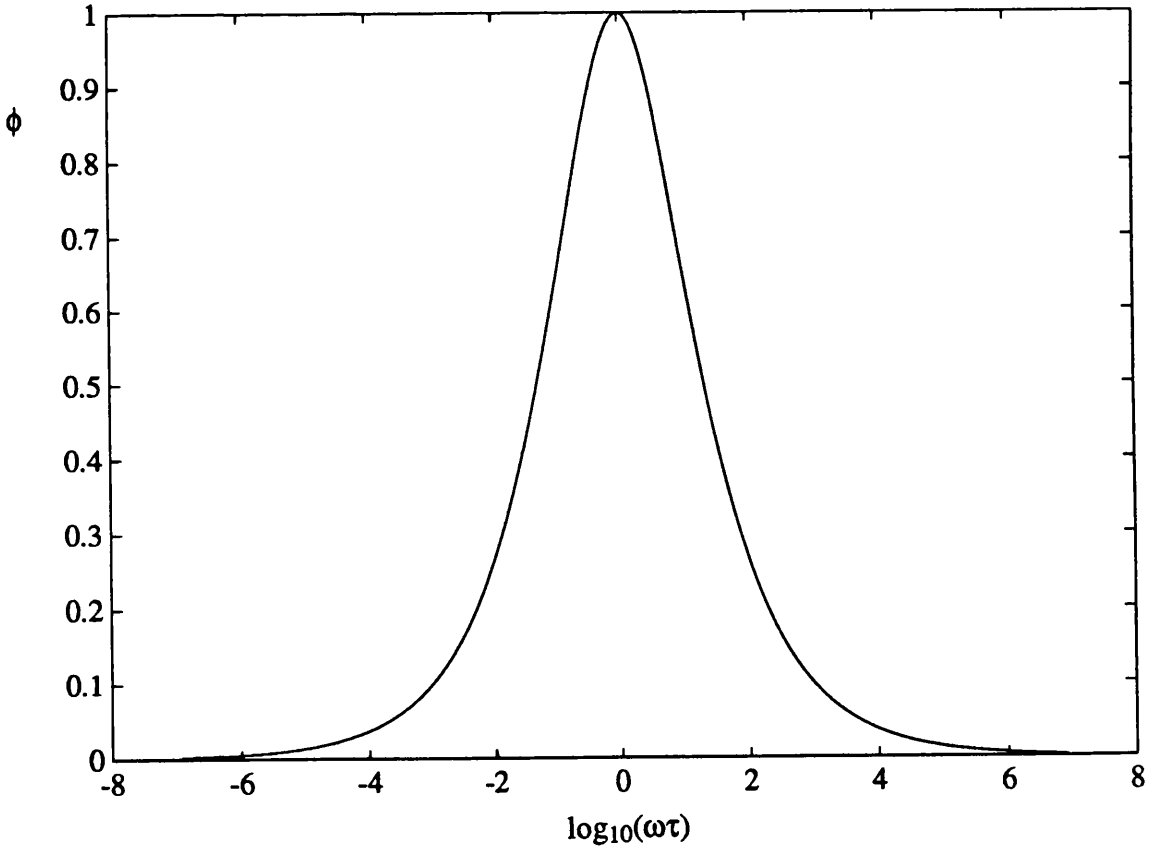

Figure 5.4: The Form of $\phi(\omega)$. This shows the symmetrical Debye peak. The curve is normalised such that the maximum value of $\phi(\omega)$ is 1.

5.2.5 Multiple Relaxation Mechanisms

So far consideration has been given to the case when there is only one relaxation process present in an anelastic solid. When there is more than one such process, the model of figure 5.3 may be extended as indicated in figure 5.5.

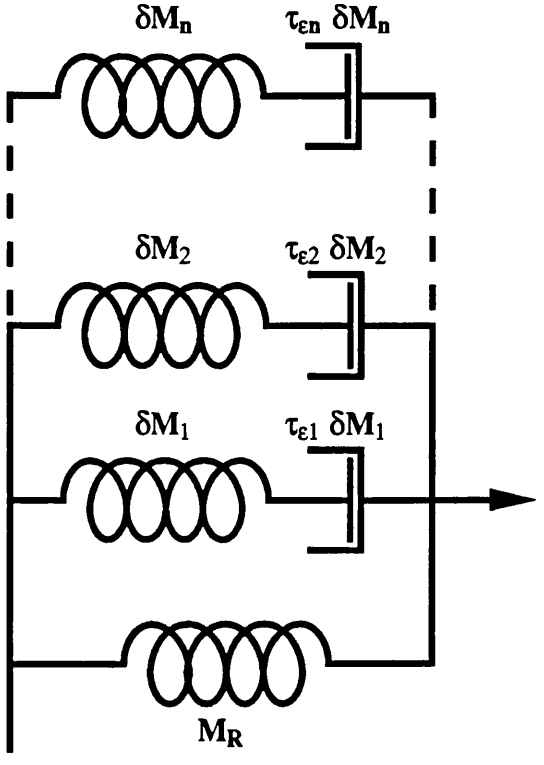

Figure 5.5: ***Model of an Anelastic Solid with n Relaxation Mechanisms.*** *This is formed by placing n Maxwell units in parallel with a spring of spring constant* M_R. *The viscosity of the nth dashpot is given by* $\tau_{\varepsilon n}\delta M_n$.

It may be shown that the internal friction, $\tan\phi(\omega)$, is only expressible as a sum of Debye peaks when either all of the relaxation strengths are very much smaller than 1 or when the relaxation times differ by several orders of magnitude. A small relaxation strength implies that $\phi(\omega) << 1$ and for this case $\tan\phi(\omega) \approx \phi(\omega)$ which may then be written as

$$\phi(\omega) = \sum_{i=1}^{n} \Delta_i \frac{\omega\tau_i}{\left[1 + \omega^2\tau_i^2\right]} \qquad \Delta_i << 1 \qquad (5.29)$$

5.2.6 Application of the Concept of Internal Friction to a Simple Harmonic Oscillator

Returning to the simpler case of a single relaxation mechanism with $\phi(\omega) << 1$, eq. (5.22) may be rewritten with the aid of eq. (5.26) as

$$\sigma + \tau_\varepsilon \dot{\sigma} = M_R \varepsilon + M_U \tau_\varepsilon \dot{\varepsilon} \tag{5.30}$$

On substitution of the stress and strain functions given by eqs. (5.9) and (5.10) into eq. (5.22) and defining a complex modulus $M^*(\omega)$ as

$$M^*(\omega) = \frac{\sigma_o e^{j\phi}}{\varepsilon_o}$$

it is found that

$$M^*(\omega) = M_R\left[1 + \Delta\frac{\omega^2\tau^2}{1+\omega^2\tau^2} + j\Delta\frac{\omega\tau}{1+\omega^2\tau^2}\right]$$

$$\approx M_R[1 + j\phi(\omega)] \qquad \text{for } \Delta << 1 \tag{5.31}$$

Consider now the harmonic oscillator of figure 5.6

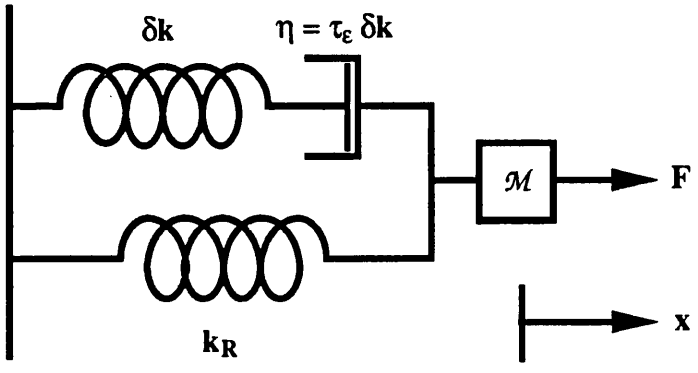

Figure 5.6: A Harmonic Oscillator formed from a Mass Attached to an Anelastic Spring. *The spring is represented by a Maxwell unit in parallel with a second spring. η is the viscosity of the dashpot.*

The stress-strain equation for the anelastic spring is given by eq. (5.30). Thus the complex spring constant may be written, with the aid of eq. (5.31) as

$$k^*(\omega) = k_R\left[1 + j\phi(\omega)\right] \tag{5.32}$$

where k_R is the relaxed spring constant.

The equation of motion of the oscillator is then given by

$$\mathcal{M}\ddot{x} + k_R\left[1 + j\phi(\omega)\right] x = F \tag{5.33}$$

Following similar analysis to that in section 2.2.3 it is found that if the driving force is thermal in origin, the thermal motion power spectral density of the mass is given by (Saulson, 1990)

$$< x^2(\omega) > = \frac{4k_B T k_R \phi(\omega)}{\omega\left[(k_R - \mathcal{M}\omega^2)^2 + \phi(\omega)^2 k_R^2\right]} \tag{5.34}$$

By comparing eqs. (2.26) and (5.34) it is observed that the conventionally assumed case of velocity damping corresponds to $\phi(\omega) \propto \omega$ and hence, from eq. (5.16,) it is demonstrated that for this case, $Q \propto 1/\omega$. From eq. (5.28), $\phi(\omega) \propto \omega$ occurs when $\omega\tau << 1$. Also from eq. (5.28) it is observed that for $\phi(\omega)$ to be frequency independent, corresponding to a frequency independent Q, $\omega\tau = 1$. Note that if there is a distribution of values of τ, this may lead to $\phi(\omega)$ being frequency independent over a large frequency band. Figure 5.7 shows a comparison of the predicted thermal motion power spectral density of two materials, one with $\phi(\omega) \propto \omega$ i.e. Q inversely proportional to frequency, and one with $\phi(\omega)$ frequency independent i.e. Q frequency independent. It is clear from the figure that if the latter model proves to be correct, this will lead to increased thermal motion of the test masses as compared to the level given by curve 1. As should be clear from discussions in the previous chapter, this could have serious implications for gravitational wave detectors operating at low frequencies.

It is evident from eq. (5.34) that in order to predict the level of thermal motion of a material, the form of $\phi(\omega)$ must be known. However it is very difficult to measure

directly the loss angle of very low loss materials in the frequency range of interest for the detection of gravitational waves. An alternative to this is to measure Q(ω) at the resonant frequencies of samples of such materials. The following two sections detail work which was carried out to try to establish the form of Q(ω) for aluminium and for fused silica.

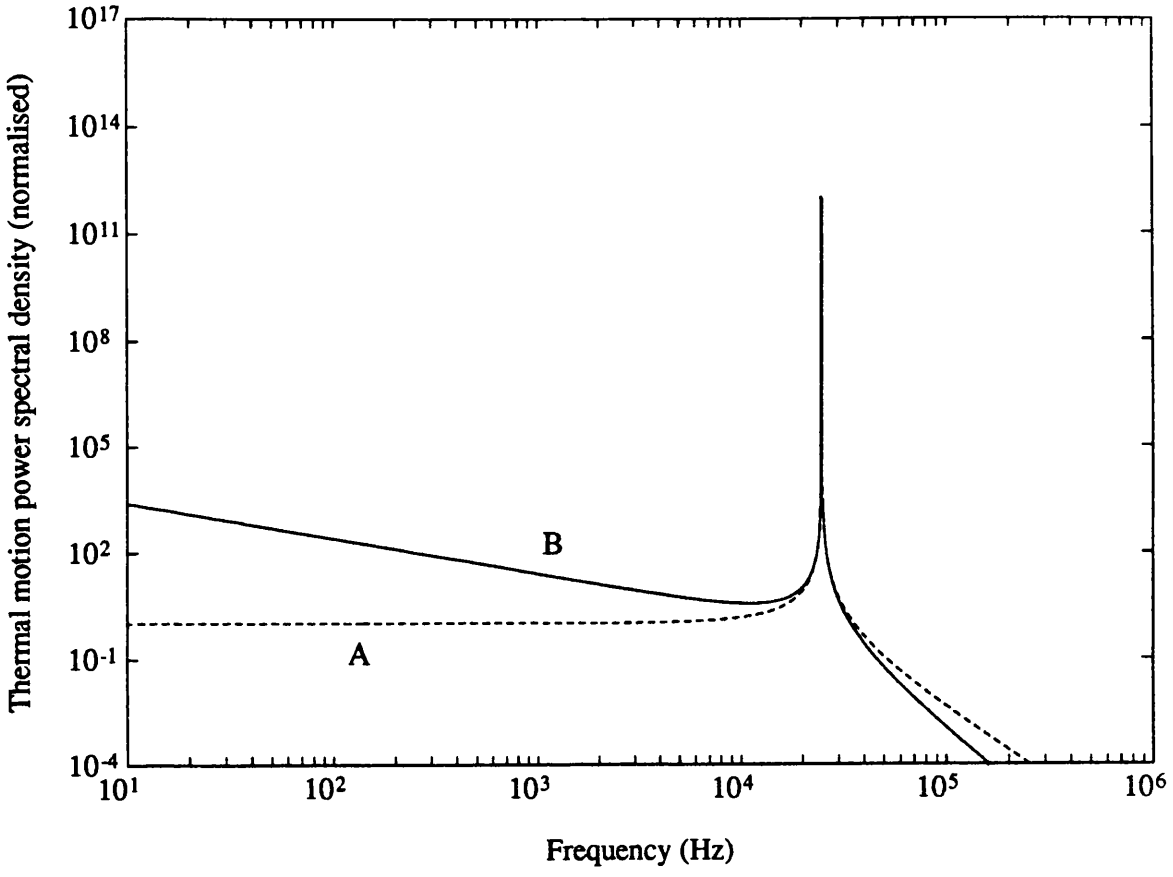

Figure 5.7: Comparison of Models with Different Frequency Dependent Q values. *Curve A shows a material with a Q which is inversely proportional to frequency (this is the conventionally assumed case). Curve B shows a material with a frequency independent Q. Both graphs have been drawn for an oscillator with a Q of 3 x 10^6 at a resonant frequency of 25 kHz. The graph has been normalised such that curve A is equal to 1 at low frequencies. (following Saulson, 1990)*

5.3 Measurement of Q as a Function of Frequency in Aluminium

It is desirable to measure the Q of materials of interest for use as test masses, at frequencies of interest for the detection of gravitational waves (~ a few hundred Hz to ~ several kHz). It is also desirable to consider only one mode of oscillation at a time since some loss mechanisms may be more strongly associated with some modes than with others. The fundamental longitudinal mode was chosen for study in these measurements since this mode is one of the most important for introducing thermal noise into a gravitational wave detector (section 2.5). Hence in order to satisfy these criteria, several samples of a material are needed in order to cover the frequency range. To make measurements at the lower frequencies requires long samples together with suitable vacuum housing. In order to ascertain whether this experimental limitation could be circumvented, it was decided to study the effect of suitably shaping samples, as described later, in order to lower the resonant frequency of the fundamental longitudinal mode. Thus aluminium was initially chosen for these tests since it was readily available and relatively inexpensive.

5.3.1 Solid Aluminium Masses

Three solid, right circular, cylindrical masses of aluminium alloy 6082, 2 inches in diameter by 1, 2.5 and 6 inches long were studied initially. All of the masses were cut from the same stock and had a polished finish. McMahon's work on resonant frequencies of aluminium bars (McMahon, 1964) was used to predict the resonant frequency of the longitudinal mode of each sample. Their Q values were measured using an inductive excitation mechanism, as described in section 2.4, and laser light reflected directly from the front face of the mass under study. Note that since Q values ~ 10^4 were anticipated, wire resonances were not expected to affect the measured Q and thus the mechanism used to alter the length of the suspension loop, section 4.4.1, was not employed.

An initial measurement of the Q of each sample was made. The mass was then resuspended and the Q remeasured to check that consistent results were obtained. The front face of each mass was then polished further in order to increase the surface

reflectivity. This made little difference to the measured Q value. Figure 5.8 shows the experimental results.

It was found that for the highest frequency mass, the decay time of the fundamental longitudinal mode was about the same as the period of one of the modes of the pendulum which the suspended mass formed. Because the mass was so light, the pendulum modes were easily excited and thus it proved difficult to obtain decay traces for the mass which were uncorrupted by the pendulum oscillation. Note that the feedback technique described in section 2.4 minimises the effect of the longitudinal pendulum mode in the output signal of the interferometer. It cannot however compensate for any tilting or rotational modes.

The masses were heat treated to see if their Q could be improved. Following McCourt's findings (McCourt, 1976) the procedure outlined below was carried out:

1) The masses were heated at 280°C for four and a quarter hours.
2) They were then quenched in cold water and left at room temperature whilst the oven cooled.
3) The masses were then placed back in the oven and heated at 110°C for a further hour.
4) The oven was then switched off and the masses were left to cool overnight.

Materials contain both point and line defects, or dislocations, in their structure. These defects cause internal stresses to be established within the material. Heat treatment, such as that outlined above, is intended to minimise the number of these defects and hence minimise the internal stresses in the sample. A material will in general have more point defects and dislocations than would be expected from calculations of the thermal equilibrium value at room temperature. This arises due to working of the material. Heating the material has the effect of reducing the number of point defects to the equilibrium number at the elevated temperature. Quenching then 'freezes in' this number of point defects. Subsequent annealing (i.e. steps 3 and 4) allows the movement of dislocations. Dislocations of opposite sign will annihilate each other whilst dislocations of the same sign will tend to form low angle grain boundaries. This process may be followed by recrystallisation of the material (e.g. Reed-Hill, 1973). Thus quenching followed by annealing should decrease the internal elastic strain of the material and thus

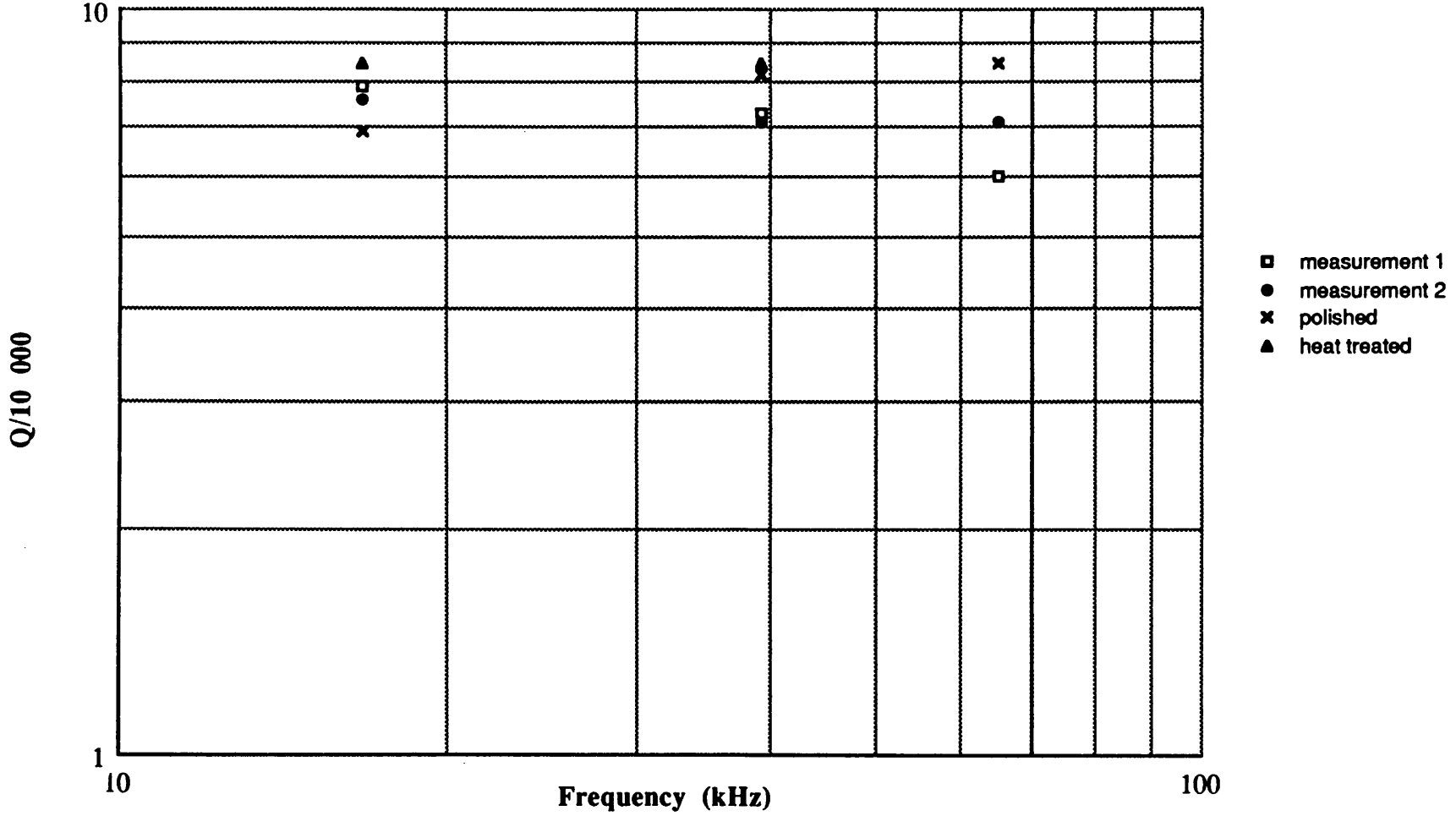

Figure 5.8: Q as a Function of Frequency for the Fundamental Longitudinal Mode of Solid Aluminum Masses. *The graph shows the initial measured Q value of each sample. Each sample was then rehung and a second measurement made. One end face of each mass was then further polished in order to increase its reflectivity. Finally the masses were heat-treated as detailed in the text. The resonant frequencies of the masses were 16.730k Hz, 39.120 kHz and 65.012 kHz. Note that error bars have been omitted for clarity. The error on each Q measurement is ± 1000.*

decrease internal friction. However the choice of temperatures and heating times are very important and vary from alloy to alloy. The exact heat treatment requirements were not known for this alloy and so, based on McCourt's work, the above recipe was tried. It is evident however that this made little difference to the Q of the samples.

Note that no measurement of Q for the highest frequency mass was obtained after it was heat treated due to the difficulty of obtaining decay traces. It is assumed that since such treatment had little effect on the other two samples, this would also be the case for this mass.

5.3.2 Q Measurements at Lower Frequencies

The longest mass which could be suspended inside the vacuum jar was 7 inches long, this length corresponding to a resonant frequency for the fundamental longitudinal mode of approximately 14 kHz. The problem was then raised as to how the resonant frequency of such a mass could be lowered. Two approaches to this problem were tried, as outlined below

Bars with holes

One way of lowering the frequency of a right circular cylindrical mass is to cut a section out of its middle as indicated in figure 5.9.

Three masses, of the same alloy as the solid bars, were machined in this manner. The masses were again 2 inches in diameter with lengths 7, 5 and 3 inches. The ratio of the length of the hole to the length of the bar was kept constant at 1/3, and the width of each shaft was 1/4 inch at its widest. The outer surface of the mass had a polished finish similar to that of the solid masses whilst the inner surface of the hole, although smooth, was not highly polished. Note that these masses were suspended in such a way that the suspension wires broke free from the mass in the same manner as for the solid bars. However the wire did have to pass over sharp edges below the mass.

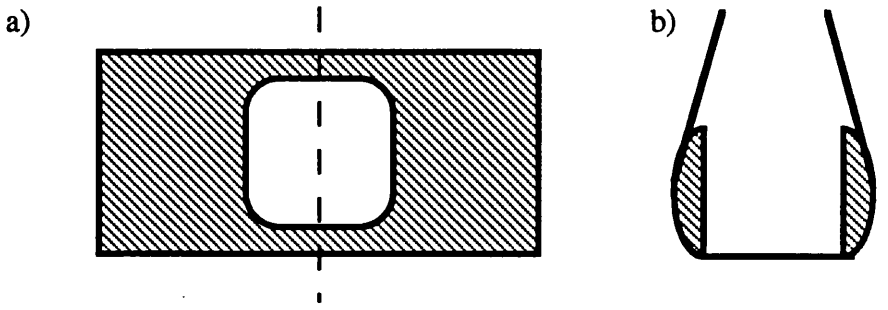

Figure 5.9: Diagram of an Aluminium Mass Machined in order to Lower its Resonant Frequency. *a) The top view of the mass shows the rectangular hole that was cut. As indicated, the corners of the rectangle were slightly rounded, all other edges however were sharp. b) Cross section through the two shafts of the bar as indicated by the dotted line. The diagram also indicates the positioning of the suspension wire round the mass.*

In order to calculate the expected frequency of the longitudinal mode of such a mass, the bar was modelled as two masses joined by two springs each of spring constant

$$k = \frac{AE}{L_s} \tag{5.35}$$

where A is the cross sectional area of one shaft,
E is Young's modulus for the material and
L_s is the length of the shaft.

The angular resonant frequency of the longitudinal mode of such a system is given by

$$\omega_o = \sqrt{\frac{4k}{m}} \tag{5.36}$$

where m is the mass of one solid end of the bar.

It is noted that in this model two assumptions are made. Firstly, the mass of the shafts is negligible compared to that of the ends. For the bar dimensions outlined above, the mass of the shafts is 1/14 that of the ends and thus this approximation is reasonable. The second approximation is that all the movement of the bar is due to that of the shafts.

From eq. (5.35), $k \propto A$ and thus the spring constant of the ends is much higher than that of the shafts, in the ratio of 1:7 for the bars described above. Thus the shafts will indeed move more than the ends for a given applied force, since they are more compliant, and hence assumption two is also seen to be reasonable.

Table 5.1 gives a comparison of the theoretical values of the fundamental longitudinal frequency of the bars, f_{th}, calculated with the aid of eq. (5.36), with the nearest frequencies found experimentally, f_{ex}. It was found that for the longest mass, good agreement was attained between the theoretically predicted and the experimental frequencies. For the two shorter masses however there was a larger discrepancy.

When the Q of these samples were measured, the scatter in the results for a given mass was found to be similar to the scatter found for the solid masses. These bars were also heat treated as described in section 5.3.1. However once more, no appreciable improvement in Q was found. The highest Q values are shown in figure 5.10. It is observed that the Q increases with increasing frequency.

Length of mass (inches)	**f_{th} (kHz)**	**f_{ex} (kHz)**	**Q (x 10^4)**
3	16.8	13.286	7.1 ± 0.1
5	10.1	7.962	4.0 ± 0.1
7	7.2	6.982	2.5 ± 0.1

Table 5.1: Q values and Comparison of Theoretical and Experimental Frequencies for the Fundamental Longitudinal Mode of the Bars with Holes. *The Q value shown for each sample was the highest measured value. The error shown is the standard error in the mean calculated from three decay traces taken when the Q value shown was measured.*

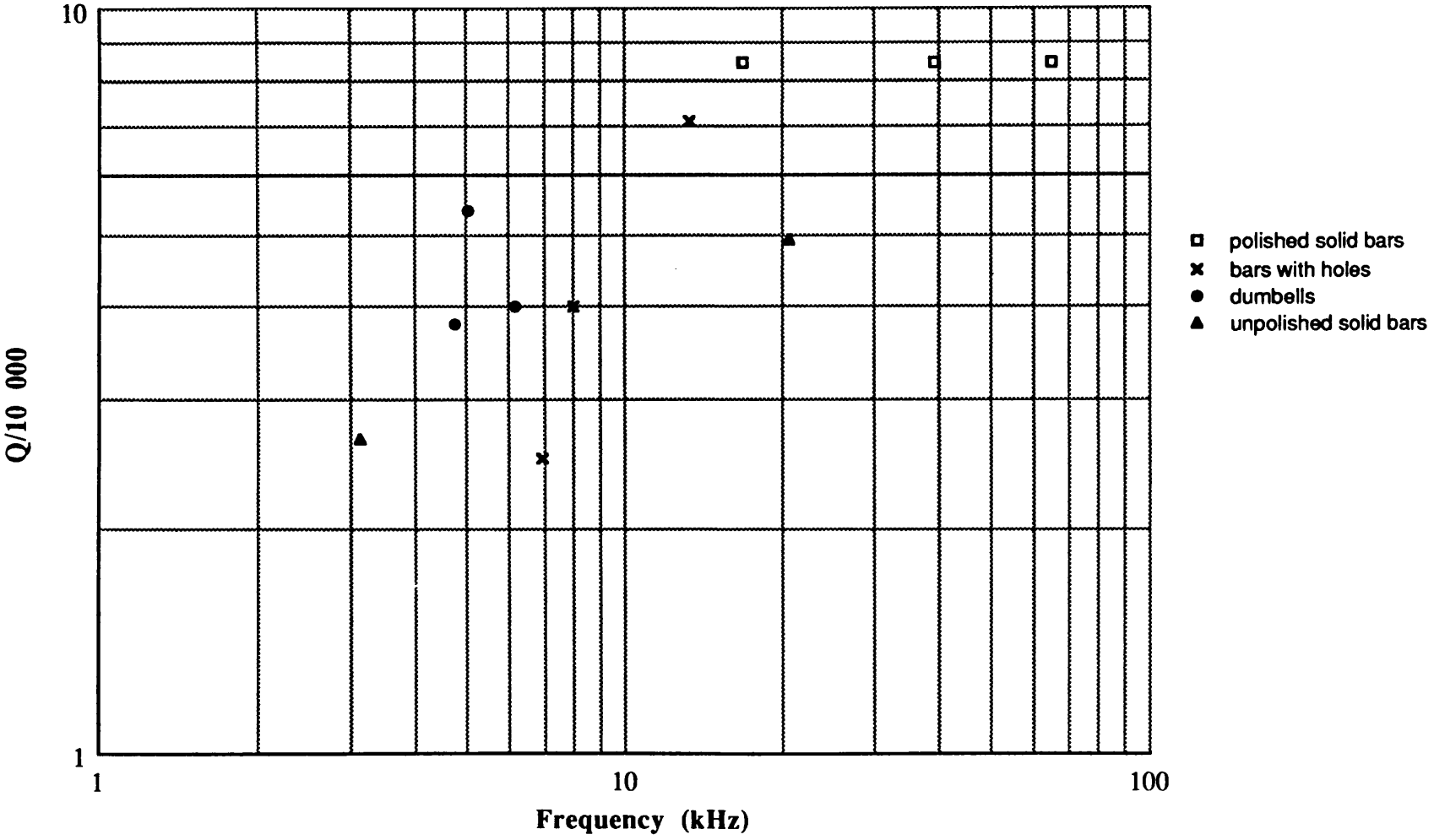

Figure 5.10: Q as a Function of Frequency for the Fundamental Longitudinal Mode of all the Aluminium Samples Tested. *Error bars have been omitted for the sake of clarity. The error on each Q measurement is as detailed in the text.*

Dumbbells

The second approach to lowering the frequency of a solid right circular cylindrical mass was to machine it into a dumbbell as shown in figure 5.11.

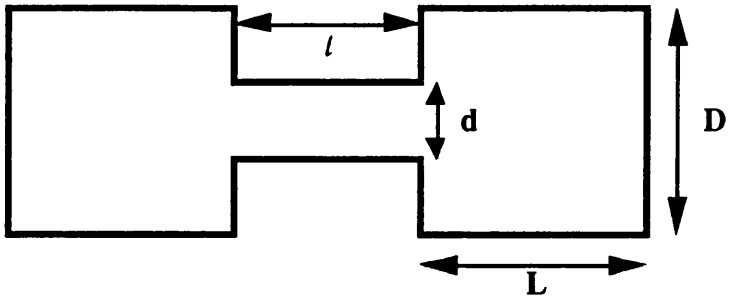

Figure 5.11: Diagram of a Dumbbell. *This was used to lower the frequency of the fundamental longitudinal mode of the mass from which the dumbbell was cut.*

Such a dumbbell may be modelled as two masses joined by a spring of spring constant k as defined by eq. (5.35). The angular resonant frequency of the fundamental longitudinal mode is then given by

$$\omega_o = \sqrt{\frac{2k}{m}} \tag{5.37}$$

Table 5.2 shows a comparison of the theoretically predicted frequencies with those found experimentally. Again it is noted that the frequency predictions are more accurate for longer bars. Note that two of the theoretically predicted frequencies were chosen to be the same. This was so that a comparison of the Q values of dumbbells with different dimensions but the same resonant frequency could be made.

The dumbbells proved more difficult to suspend, due to the narrowness of the stalk, and thus an alternative suspension technique had to be designed. This involved passing the suspension loop through a narrow vertical tube, as indicated in figure 5.12, in order to ensure that the wires broke free above the centre of mass of the dumbbell thereby providing a stable configuration. It is noted that such an arrangement differs from the way in which both the solid masses and those with holes were suspended.

L (inches)	l (inches)	d (inches)	f_{th} (kHz)	f_{ex} (kHz)	Q (x 10^4)
1.75	0.9	0.3	5.3	4.732	3.8 ± 0.1
1.75	0.4	0.3	7.8	6.190	4.0 ± 0.1
1.75	3.5	0.6	5.3	5.022	5.4 ± 0.1

Table 5.2: ***Q values and Comparison of Theoretical and Experimental Frequencies for the Fundamental Longitudinal Mode of the Dumbbells.*** *The Q value shown for each sample was the highest measured value. The error shown is the standard error in the mean calculated from three decay traces taken when the Q value shown was measured. The diameter, D, of each mass was 2 inches.*

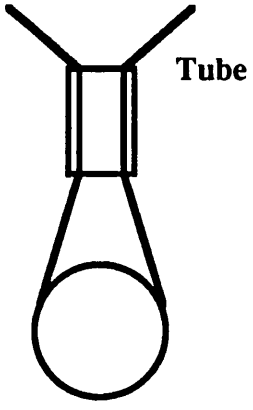

Figure 5.12: ***Suspension Method for the Dumbbells.*** *The diagram shows a cross-section through the narrow stalk of the dumbbell. The size of the tube compared to that of the stalk has been greatly exaggerated for clarity.*

5.3.3 Discussion of Results

Fuller discussions of relaxation processes in materials are given by e.g. Zener (Zener, 1948), Nowick and Berry (Nowick and Berry, 1972) and Ferreirinho (Ferreirinho, 1991).

Frequency Independence of Q for Solid Bars

From the graph of figure 5.10 it is observed that for the solid aluminium bars, Q is independent of frequency. There is good evidence that this is in fact the case for metals in the kilohertz frequency range (Nowick and Berry, 1972, Ch 14 and references therein). It is believed that such behaviour is due to the motion of dislocations; the exact mechanism, however, is not well understood at present. The so called vibrating string model, first suggested by Koehler (Koehler, 1952) and further developed by Granato and Lücke (Granato and Lücke, 1956), is commonly used as the basis of a model for dislocation damping. This will be briefly outlined below.

The Vibrating String Model

Consider applying an alternating stress to a sample of material. If the frequency of this stress is of the order of kilohertz, impurity atoms in the material will be unable to follow the applied stress since diffusion at room temperature is extremely slow (Koehler, 1952). However due to the long range stress fields which surround both impurity atoms and dislocations, such atoms are attracted to dislocations in order to reduce the stress in the material (e.g. Hull, 1975, section 10.3). This leads to dislocations being pinned in place by impurities. Consider a dislocation loop of length ℓ which is pinned at its ends in this manner. The applied stress then forces the dislocation loop to oscillate in its slip plane like a stretched string. This motion will be damped due to interactions of the dislocation with phonons and thus the equation of motion for the dislocation may be written as

$$m_\ell \ddot{u} + B\dot{u} - \gamma\left(\frac{\partial^2 u}{\partial y^2}\right) = \sigma_o b e^{i\omega t} \qquad (5.38)$$

with boundary conditions $u(0,t) = u(l,t) = 0$,

where m_ℓ is the effective mass per unit length of the dislocation,

- u is the displacement of the dislocation from its equilibrium,
- y is the distance along the length of the dislocation,
- B is the damping constant per unit length
- γ is the tension in the dislocation line per unit length

σ_o is the amplitude of the applied stress resolved in the slip plane and

b is the magnitude of the Burgers vector.

It may be shown that such a system has internal friction given by (Nowick and Berry, 1972)

$$\tan\phi(\omega) = \frac{\Lambda \ell^2 b^2 G}{12\gamma} \frac{\omega\tau}{\left[\left(1 - \frac{\omega^2}{\omega_o^2}\right)^2 + \omega^2\tau^2\right]} \tag{5.39}$$

where Λ is the density of dislocations of length ℓ,

G is the shear modulus of the material

$$\omega_o^2 = \frac{12\gamma}{m_\ell \ell^2} \quad \text{and} \tag{5.40}$$

$$\tau = \frac{B\ell^2}{12\gamma} \tag{5.41}$$

For a material of density ρ and Poissons ratio ν, the effective mass per unit length of a dislocation is given by (Granato and Lücke, 1956)

$$m_\ell = \pi\rho b^2 \tag{5.42}$$

and the tension in the dislocation line per unit length is given by (Granato and Lücke, 1956)

$$\gamma = \frac{2Gb^2}{\pi(1-\nu)} \tag{5.43}$$

For aluminium which has G = 2.6 x 10^{10} N m^{-2} and ν = 0.345 (Kaye and Laby, 1986) and taking a dislocation length of $\ell \sim 10^{-6}$ m (Routbort and Sack, 1966) eqs. (5.40), (5.42) and (5.43) give $\omega_o \sim 10$ GHz. Thus it is the low frequency case that is of concern i.e. where both $\omega << \omega_o$ and $\omega^2\tau^2 << 1$. For this case eq.(5.39) reduces to

$$\tan\phi(\omega) = \frac{\Lambda \ell^4 B\pi^2(1-\nu)^2\omega}{576\, Gb^2} \tag{5.44}$$

Hikata et al have experimentally determined the value of B for aluminium to be 5 kg s^{-1}

(Hikata et al, 1970). However calculation of values for $\tan\phi(\omega)$ requires knowledge of the dislocation density and loop length in the sample. Values for these can vary greatly depending on the previous history of the sample and on the concentration of impurities. Friedel quotes values for the dislocation densities in crystals ranging from 10^2 to 10^{12} dislocations per square centimetre (Friedel, 1964, p 211) depending on the condition of the sample. Thus it is not possible to quantitatively calculate the level of internal friction for the samples of aluminium considered here. However, it is evident that the vibrating string model predicts that:

1) from eq. (5.39) at higher frequencies, $\tan\phi(\omega)$ should exhibit either a sharp resonance type peak if the damping coefficient, B, is small, or a relaxation type peak if B is large.
2) from eq. (5.44) at low frequencies (i.e. in the kilohertz range) the internal friction is proportional to Λl^4 and to ω. Thus for this case Q would be inversely proportional to frequency.

Note that only dislocation loops of the same length, l, have so far been considered. In reality, of course, there is a distribution of loop lengths. Koehler has shown that if the impurity atoms are considered to be randomly distributed along the length of a dislocation line this situation can be described by a distribution function which exponentially decreases with increasing loop length (Koehler, 1952). Using this distribution function Granato and Lücke introduced an effective loop length, l_e, in place of l, where l_e is approximately three times the average loop length. (Note that since $\tan\phi(\omega) \propto l^4$, longer loops contribute more to the level of internal friction than small ones and hence l_e is expected to be greater than the average loop length.)

Note also that the oscillating dislocations will exert a force on the pinning points which, when a certain critical value is reached, will overcome the force which binds the impurities to the dislocation. At this point the dislocation loops will break free and the internal friction in the sample will depend on the amplitude of the applied stress. In the measurements made on the aluminium samples under consideration here, only exponential decay curves were recorded. It is thus concluded that the applied stress was not high enough for such behaviour was to be observed.

There is experimental evidence in the megahertz frequency range for the high frequency

behaviour predicted by the vibrating string model (e.g. Alers and Thompson, 1961). However in the low frequency regime, i.e. in the kilohertz range, the predicted proportionality of internal friction with frequency is not observed and thus there is reason to doubt the validity of the vibrating string model over the entire frequency range.

Extensions to the Vibrating String Theory

Routbort and Sack found that internal friction in aluminium is independent of frequency from 1 Hz to 40 kHz with a $Q \sim 3 \times 10^4$ (Routbort and Sack, 1966). By irradiating samples of various metals including aluminium, a process which introduces point defects and thus leads to more pinning points for dislocations in a material, they concluded that the observed internal friction was indeed due to dislocations but that the vibrating string model did not adequately explain their results at frequencies in the kilohertz range. They propose that there is an additional source of dissipation from dislocations which involves some hysteresis, rather than anelastic mechanism leading to frequency independent internal friction.

Mason and Wher have proposed an extension to the vibrating string model which has such a hysteresis mechanism (Mason and Wher, 1970). This takes account of the so called Peierls valleys which the vibrating string model neglects. Consider an edge dislocation in an otherwise perfect crystal, as shown in figure 5.13.

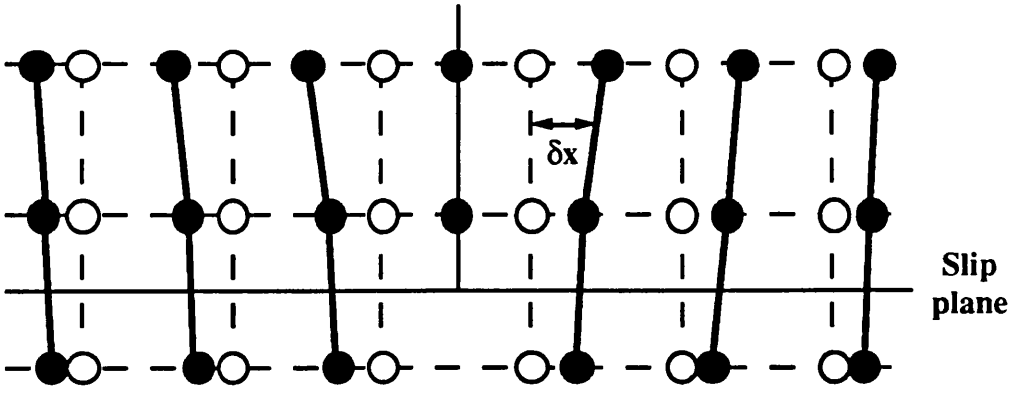

Figure 5.13: The Displacement of Atoms due to an Edge Dislocation. *White circles represent the position of atoms in a perfect crystal, black circles represent the position of atoms after an extra half plane of atoms has been inserted.*

Any plane of atoms parallel to the dislocation is subject to two forces; (1) the stress field resulting from the introduction of the extra half plane of atoms, which tends to increase the plane's displacement, δx, from its equilibrium position, and (2) the displacement of the plane of atoms from its equilibrium position relative to the surrounding atoms which tends to decrease δx. Since there will be another plane of atoms on the other side of the dislocation which is subject to equal and opposite forces, the dislocation is in an equilibrium position. When the dislocation is displaced slightly, the forces become unbalanced and a stress is required to maintain the dislocation in the new position. Thus the potential energy of the dislocation as a function of position in the crystal exhibits a periodic variation (e.g. Hull, 1975, section 10.2).

Consider now a dislocation lying in a position of minimum energy i.e. lying in what is termed as a Peierls valley. At finite temperatures the dislocation will no longer lie in one valley but will contain kinks as indicated in figure 5.14. The energy required to form a kink is approximately the thermal energy, kT, at room temperature and thus a dislocation line will in general have a number of kinks (Schockley, 1952).

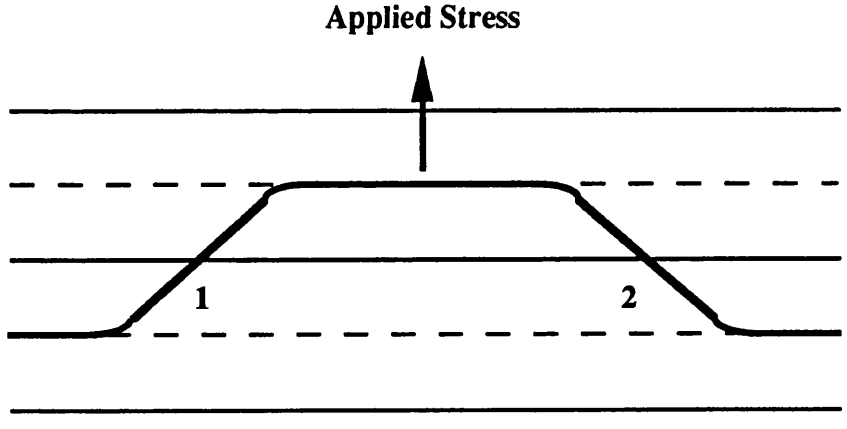

Figure 5.14: Two Kinks in a Dislocation Line. *The solid lines show maxima of potential energy and the dashed line, minima.*

Consider applying a stress to a dislocation line as indicated in figure 5.14. This will tend to move the dislocation line into the next Peierls valley i.e. the applied stress will tend to push the kinks out laterally. However there is an attractive force between the two kinks, labelled 1 and 2 in figure 5.14, which endeavours to annihilate them in order to reduce the dislocation length. Hence it may be seen that there is an energy barrier to sideways

motion of the kinks (Van Bueren, 1960, pp. 205 - 206).

Mason and Wher have proposed a mechanism whereby interactions between lattice phonons and kinks provide additional damping at low frequencies (i.e. the kilohertz range) which is independent of frequency, whilst the vibrating string model still dominates at higher frequencies; this arises since kinks can only follow an applied stress up to frequencies of a few megahertz (Mason and Wher, 1970). As noted above, kinks can move sideways relatively easily, but they do still have a potential barrier to overcome. Some of the energy which the kink gains as it travels down the side of its potential valley is lost in interactions with phonons and thus a stress is needed in order to keep the dislocation moving, thus providing a hysteresis mechanism for energy loss in the material.

More recently Baur and Benoit have suggested that frequency independent internal friction in metals is due to interactions of dislocations with stationary point defects (Baur and Benoit, 1987). They propose that dislocation motion is hindered by interactions with point defects that do not lie on straight dislocations and thus the dislocations in effect zig-zag through a cloud of point defects. For some dislocations there may be several stable positions in the point defect cloud very close to each other. Thus under the application of an external stress, such a dislocation may leave its initial equilibrium position and move to another. On the removal of the applied stress the dislocations remain at their new positions thus providing a hysteric loss mechanism which leads to the internal friction of the material being frequency independent.

Conclusion for the Solid Bars

Whilst the exact mechanism or mechanisms for damping in materials due to the motion of dislocations are still not well understood, it is likely that the measurements of Q presented here, for the solid aluminium samples, are limited by such a loss.

It is evident from figure 5.10 that the Q values for the bars which were machined are lower than the values for the solid bars and are frequency dependent. The results obtained for the dumbbells are more readily understandable than those obtained for the bars with holes and thus the dumbbells will be considered first.

Dumbbells

From the results presented in figure 5.10, it is noted that the dumbbells have lower Q values than those measured for the solid bars. This decrease in Q may be due to surface damage caused by machining the masses.

From table 5.2 it is observed that two of the dumbbells had almost the same frequency and yet had different Q values. The ends of the dumbbells are approximately 30 times stiffer than the stalks and thus most of the movement of the dumbbells will be confined to the stalks. The difference between the Q values for the two dumbbells must therefore be due to the difference in dimensions of the stalks, one being 0.15 inches in radius and 0.9 inches long, and the other being 0.3 inches in radius and 3.5 inches long.

A certain depth of surface damage will have occurred when the dumbbell shape was cut from a solid cylindrical aluminium mass. If it is assumed that the depth of surface damage is the same for both dumbbells, then the dumbbell with the thicker stalk will have a smaller ratio of volume of 'damaged' to 'good' material and would thus be expected to have a higher Q, as indeed is the case. The total loss in a dumbbell may be taken as the sum of the losses in the damaged section of the material, L_d, plus the loss in the section of good material, L_g. A system of simultaneous equations may then be set up with reference to figure 5.15.

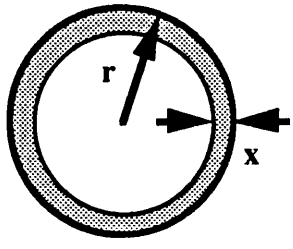

Figure 5.15: Cross Section through the Stalk of a Dumbbell. *The shaded region shows the depth, x, of surface damage.*

$$L_1 = L_g \frac{(r_1 - x)^2}{r_1^2} + L_b \left[1 - \frac{(r_1 - x)^2}{r_1^2} \right]$$

$$L_2 = L_g \frac{(r_2 - x)^2}{r_2^2} + L_b \left[1 - \frac{(r_2 - x)^2}{r_2^2} \right] \qquad (5.45)$$

$$L_s = L_g \frac{(r_s - x)^2}{r_s^2} + L_b \left[1 - \frac{(r_s - x)^2}{r_s^2} \right]$$

where L_1 is the total loss in dumbbell of stalk radius r_1,

L_2 is the total loss in dumbbell of stalk radius r_2 and

L_s is the total loss in a solid aluminum cylinder or radius r_s.

This system of equations may then be solved for the unknowns, L_g, L_b and x. This was done with the aid of a computer package (Mathematica, Wolfram Research, Inc). It was found that

$L_g = 8.6 \times 10^{-6}$ (≡ good material having a Q of 1.2×10^5),

$L_b = 3.7 \times 10^{-5}$ (≡ damaged material having a Q of 2.7×10^4) and

x = 0.06 inch (≡ 1.4 mm)

In this calculation it is assumed that the boundary between the good and the damaged material is well defined and that the loss in the damaged material is of constant value up to this boundary. This is clearly an approximation. It is also probable that the surface damage layer is not so deep for the solid bars, which were polished, compared to that for the dumbbells, which were machined and not so a highly polished on the stalks. The analysis would however suggest that the basic idea can explain the observed results since reasonable numbers for L_g, L_b and x are obtained. The fact that the two dumbbells which have different lengths of stalks but the same stalk diameters, and hence the same ratio of damaged material to good material, have been measured to have the same Q values, within the accuracy of the measurement, lends further credence to this argument.

Bars with Holes

From the results presented in figure 5.10, the Q values of the bars with holes are lower

than that of the solid bars. It is noted that the Q of these bars increases with increasing frequency. These Q results cannot be so simply understood as for the dumbbells. Applying the same idea about the presence of a damage layer as in the previous section would lead to the prediction that all three bars would have a Q which was independent of frequency with a value of about 4×10^4. Clearly this is not the case.

It is noted that the dumbbells had stalks which were approximately 30 times more compliant than the ends, and thus when the dumbbell resonated most of the motion would be confined to the stalks. However the struts for the bars with holes had a combined compliance which was a factor of only 7 more than the ends. Thus when these bars resonate there is more motion distributed throughout the whole bar. Due to the form of the samples, the mode structure will be very distorted and it is possible that instead of moving longitudinally, the struts may have had some tendency to bend. It is also possible that due to the distortions of the normal modes and the accompanying change in the resonant frequencies, that it was not in fact the longitudinal mode that was studied for each bar. It is also noted that in the suspension of these samples the weight of the bar is supported at only two sharp points rather than being cradled by the wire. This may cause increased strain in the samples. Taking into account all of these factors the interpretation of these results is not straightforward. It is not surprising however that Q as a function of frequency for these bars is not the same as for the solid bars.

Unpolished Solid Bars

In order to try to ascertain whether there is a real decrease in the Q of aluminium as the resonant frequency of the sample is decreased, rather than one artificially produced by machining, the Q of a bar of the same alloy as the other samples studied, 31.5 inch long by 2 inches in diameter, was measured. The sample was suspended in a large vacuum tank as described in section 5.4. Unfortunately it was not possible to have this bar polished at the time these experiments were being carried out, and so it was expected that the measured Q for this sample would be lower than for the polished solid bars. Thus a second sample of aluminium, 2.25 inches long, was obtained which was in a similar unpolished condition in order that the results of the two samples could be compared. The resonant frequency of the fundamental longitudinal mode of the long bar was 3.122 kHz and the Q of this mode was measured to be $(2.7 \pm 0.2) \times 10^4$. The fundamental

longitudinal mode of the shorter sample occurred at a frequency of 41.140 kHz and the Q of this mode was measured to be $(4.9 \pm 0.1) \times 10^4$. These results are shown on figure 5.10. It is evident that the surface condition of the material has a large effect on the Q. In order to check whether friction, due to the surface condition of the mass along the line of contact with the suspension wire, was dissipating energy, a layer of grease was applied to the smaller mass along the line of contact between the mass and the wire. The Q was then remeasured and found to be unchanged. This indicates that the level of surface damage, rather than friction effects, is more important in determining the measured Q value. Thus the results would, if anything, suggest a tendency for the Q of aluminium, limited by surface effects, to decrease towards lower frequencies.

Conclusion

To reach lower frequencies it is probably not a good idea to machine out parts of the sample since it is difficult to assess the effect of this. It is also evident that the surface condition of the material has a very strong effect on the level of losses in the material. Samples should therefore be treated identically and have as good a surface finish as possible. It is concluded that the Q for aluminium is frequency independent from 16 to 65 kHz and that this is probably due to the movement of dislocations in the material.

5.4 Measurements of Q as a Function of Frequency in Fused Silica

Fused silica is a possible material for use as test masses in an interferometric gravitational wave detector. Thus the measurement of Q as a function of frequency of this material is of interest.

With the experience gained from working with the aluminium samples, it was decided that it would be preferable to try to measure the quality factor of fused silica using right circular cylindrical samples only. To be certain that all the samples to be tested had been treated in the same manner, it was desirable that they all came originally from the same piece of silica. It was found however that in order to obtain a long enough piece of silica with a large enough diameter so that the samples could be suspended easily, hollow

tubing rather than solid bars had to be used. The silica was 'off the shelf' stock from Heraeus (Heraeus). The original piece obtained was 2.7 m long with outer diameter 13.8 cm and wall thickness 6 mm. This was cut into five pieces with lengths ranging from 10 cm to 1.5 m. It was noted that there were slight variations in the wall thickness of the samples leading to their surfaces having a slightly rippled effect.

5.4.1 Measurement Technique

The silica samples were suspended in turn inside a large vacuum tank, originally used to house a prototype bar detector for gravitational waves. The masses were suspended from a large aluminium plate which itself was supported by lead and rubber stacks as illustrated in figure 5.16 which shows the suspension of the longest silica sample. The top breakaway points were as used previously (section 2.4) and a thin film of grease was applied at the breakaway points at the mass, as described in section 4.4.2, in order to try to reduce friction effects. Since Q values of the order of 10^5 were expected, the device for altering the length of the suspension wires was used. It was found however that there was no indication that the measured Q was a function of suspension length. The samples were excited magnetically using two coil and magnet drivers placed at the top and bottom of the end face of the suspended mass, as shown in figure 5.16. Excitation was provided in two places in order to try to excite selectively the longitudinal mode of the sample. The Q of each cylinder was measured using the technique described in section 2.4. The optics for the interferometer were mounted on an aluminium plate, which was supported by lead and rubber stacks, placed outside the vacuum tank. Laser light was then shone onto a mirror attached to the sample under test, through a port hole in the tank door.

5.4.2 Experimental Results

Gladwell and Vijay's work on finite element analysis of cylinders (Gladwell and Vijay, 1975) was used to predict the frequency of the longitudinal mode of the cylinders. Table 5.3 shows a comparison of the theoretically predicted frequencies, f_{th}, with those found experimentally, f_{ex}, and the Q measured for the fundamental longitudinal mode of each sample.

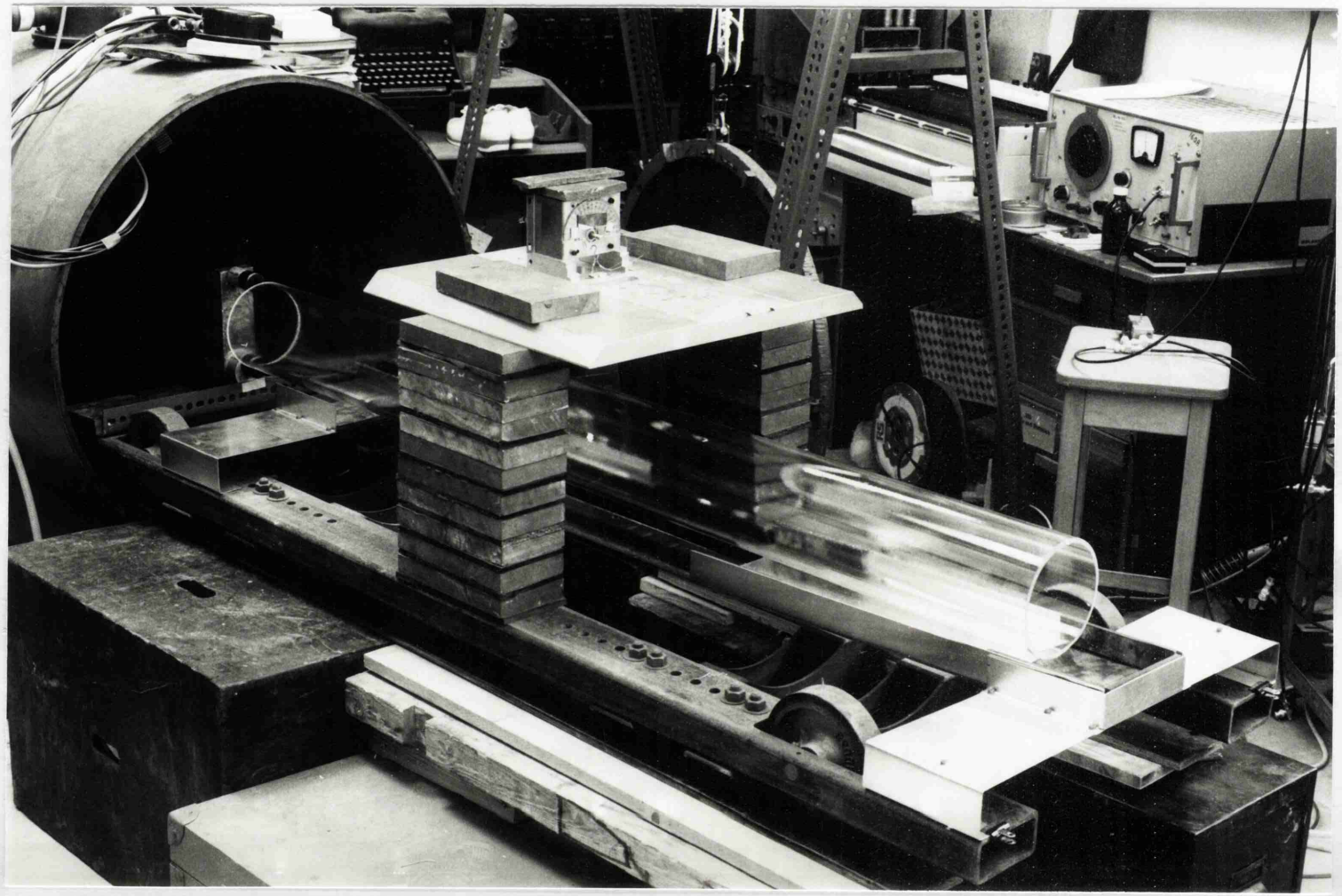

Figure 5.16: Photograph of the 1.5 m Long Fused Silica Cylinder Suspended Outside the Vacuum Tank. *Also shown, on top of the supporting plate, is the mechanism for altering the length of the suspension loop.*

Length (m)	f_{th} (kHz)	f_{ex} (kHz)	Q (x 10^5)
0.1	14	14.90	1.56 ± 0.05
0.165	13.2	13.551	1.63 ± 0.05
0.3	9.7	9.456	2.99 ± 0.05
0.6	5.0	4.775	2.90 ± 0.05
1.5	~ 2.0	1.919	3.4 ± 0.1

Table 5.3: Q Values and Comparison of Theoretical and Experimental Frequencies for the Fundamental Longitudinal Mode of Fused Silica Samples. *The theoretical frequency of the longest tube is shown as being approximate since its dimensions lay outside the scope of Gladwell and Vijay's paper. This was estimated using eq. (2.7) for the frequency of a solid bar since Gladwell and Vijay's results indicated that as the aspect ratio of a sample increases, there is virtually no difference between the predicted frequency of the longitudinal mode of a hollow cylinder as compared to a solid bar.*

It was found that for the 1.5 m long cylinder there were two resonances occurring at frequencies close to that expected for the longitudinal mode, at 1.919 and 1.848 kHz. In order to decide which mode was in fact the longitudinal mode, an asymmetric excitation was used in which one magnet was attached to the suspended mass at the top of the rear face and the other was placed approximately 140° round from it. When this was done, only the resonance at 1.919 kHz was strongly excited and it was thus concluded that this was the longitudinal mode.

Figure 5.17 shows the variation of Q with frequency. The results were repeatable for most of the samples. It was found however that the Q for the longitudinal mode of the 1.5 m long mass, varied by a factor of 2.5 between two separate measurements, the mass being resuspended for the second measurement. The higher of these values is plotted in figure 5.17. Since this mass was so long, there was a relatively large range of positions

for the suspension wire over which the mass would balance. It is thus likely that the suspension wire was in a slightly different position on the mass for the two measurements. Due to the slight variation in the surface smoothness of the sample it is probable that for one measurement, friction between the wire and the mass was higher than for the other measurement. Note that grease was only applied between the mass and the wire at the breakaway points and not along the entire line of contact.

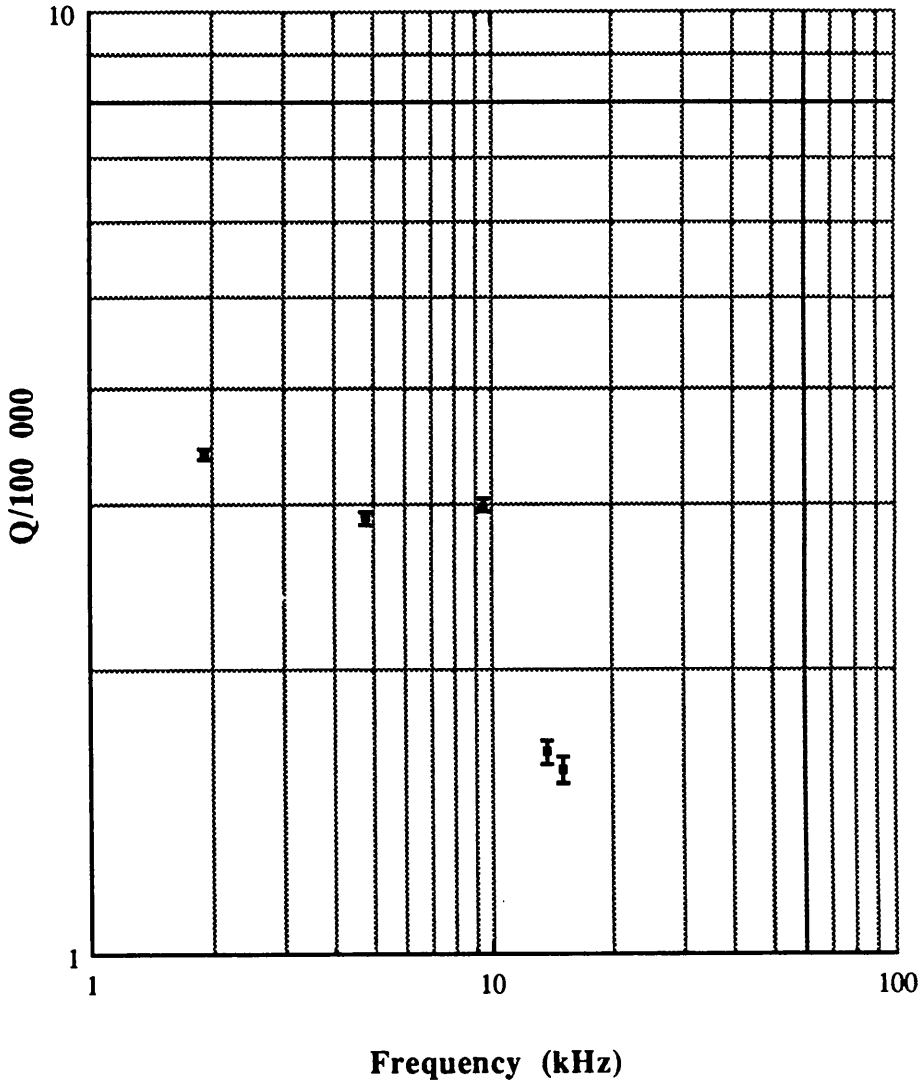

Figure 5.17: Q of the Longitudinal Mode of Fused Silica as a Function of Frequency.

5.4.3 Discussion

There is very little information in the literature about loss mechanisms in fused silica at room temperature and in the kilohertz frequency range. Brillet et al originally measured the Q of the lowest frequency resonant mode of a fused silica mass 50 cm in diameter by 20 cm thick to be ~ 4×10^5 (Brillet et al, 1990) This mode occurred at a frequency of 3.4 kHz and is believed to be some sort of bending mode (Dialinas, 1991). The two flat faces of the mass were subsequently polished and the Q increased in value to 9×10^5. Braginsky et al have suggested that the presence of a surface layer of crystallites of random size and orientation may give rise to a significant contribution to the damping of resonant modes in fused silica (Braginsky et al, 1985, pp. 21 - 23). For a non-cubic crystal, such as quartz, the coefficient of thermal expansion is a function of orientation (Nowick and Berry, 1972, section 17.5). Thus when a longitudinal stress is applied to a sample, anelastic relaxation may occur by the flow of thermal currents which are induced between the crystallites on the surface of the fused quartz sample. Thus surface effects may be an important loss mechanism in the fused silica samples under consideration here. Whilst caution must be exercised in interpreting the experimental data shown in figure 5.17, due to the small number of experimental points, the results would not be inconsistent with the Q of the material being frequency independent between 2 and 10 kHz and then being proportional to f^{-1} between 10 and 15 kHz. The results at the higher frequencies may depend on the aspect ratio of the samples as described below.

The ratio of the amplitude of motion of the end face of a solid bar to that of the radial motion is given by

$$\frac{A}{r_o} = -\frac{\mathcal{L}}{2\mathcal{R}\nu} \tag{5.46}$$

where $\mathcal{L}$ is the length of the bar,

$\mathcal{R}$ is the radius of the bar,

A is the amplitude of motion of one end face of the bar,

r_o is the amplitude of motion of the side of the bar and

ν is Poisson's ratio for the material ($\nu = 0.17$ for fused silica (Heraeus)).

From this it is observed that as the length of the bar is decreased whilst its radius remains

constant, the ratio of the amplitude of motion of the end of the bar to that of the side also decreases. This implies that the level of radial motion must become increasingly important. Thus instead of executing predominantly longitudinal extension and contraction, the sides of the sample will instead begin to bow out and in to a greater degree. A similar effect must also occur in hollow cylinders where the thinner wall thickness provides less impedance to flexing in this manner. For the two shortest silica cylinders $\mathcal{L} \sim \mathcal{R}$ compared to the longest cylinder where $\mathcal{L} \sim 10\mathcal{R}$. Thus for these short samples radial movement will be more important than for the longer samples. It is possible that bending of the cylinder's wall may introduce a new relaxation mechanism or may increase intercrystalline thermal damping due to the inhomogeneity of the applied stress, thus resulting in lower Q values for these samples as compared to the longer samples.

5.5 Conclusion

Most experimental designs for laser interferometric gravitational wave detectors assume that the Q of the test mass material is inversely proportional to frequency, leading to a thermal noise power spectrum that is frequency independent below the lowest frequency resonance. In this chapter experimental data have been presented as to how the Q of the fundamental longitudinal mode varies as a function of frequency for samples of both aluminium and fused silica. It would appear from these results that the measured Q of these materials is in fact frequency independent over large frequency bandwidths. (Note that although there is some indication that Q may be inversely proportional to frequency for fused silica at frequencies greater than ~ 10 kHz, this is outside the frequency range of interest for the detection of gravitational waves.) If the results discussed in this chapter can be extrapolated down to low frequencies such that Q is frequency independent down to a few hundred hertz, this will mean that the thermal noise power spectrum from test masses made of such material will be inversely proportional to frequency. This will have potentially serious consequences for the sensitivity of gravitational wave detectors working at low frequency. It is thus very important that more data are accumulated, at lower frequencies and for a wider range of materials, in order to conclude with more certainty what the form of the thermal motion power spectral density of a test mass for a particular material will be.

Chapter 6

An Investigation of the Level of Birefringence in Fused Silica

6.1 Introduction

In section 2.3 the constraints placed on the choice of test mass material, due to mechanical considerations, were outlined. An additional constraint is placed upon the choice of material used for the beamsplitter: in order that the laser beam suffers minimum distortion as it travels through the beamsplitter, the material must be optically homogeneous. Note that if Fabry-Perot cavities are employed in the arms of a laser interferometric gravitational wave detector, this constraint also applies to the material chosen for the test masses. One of the limiting factors to optical homogeneity is the level of birefringence present in the mass. In this chapter details of measurements of stress induced birefringence in a fused silica mass, similar to the mirror substrates currently used in the 10 m Glasgow prototype detector, will be given. The effect of birefringence on the fringe contrast and thus sensitivity of a detector will then be discussed.

6.2 The Nature of Birefringence

Birefringence is a form of optical anisotropy which is naturally possessed by some crystals, and in some other materials may be induced by the application of a mechanical or thermal stress, or an electrical voltage. Birefringent crystals display the phenomenon of double refraction i.e. the formation of two refracted rays from one incident ray. One of these, the ordinary ray, obeys Snell's law of refraction, the other, the extraordinary ray, does not. These two rays are polarised perpendicular to each other. The refractive index for the extraordinary ray varies according to the direction it passes through the crystal; it varies from n_o, the value of the refractive index for the ordinary ray, to n_e where n_e may

be either greater or less than n_o depending on the material. The optic axis of the crystal is defined to be the direction through the crystal for which $n_e = n_o$. The birefringence of the crystal is given by (e.g. Hecht, 1987, p. 289)

$$\Delta n = n_o - n_e \tag{6.1}$$

Crystalline quartz is naturally both birefringent and optically active (i.e. it rotates the plane of polarisation of an incident wave, even when the incident wave propagates along the optic axis). Fused silica possesses neither of these properties (e.g. Hecht, 1987, p. 288 and p. 310). Birefringence may however be induced by the application of a mechanical stress. The effective optic axis is in the direction of the applied stress and the resulting induced birefringence is proportional to the magnitude of the stress. Note that for the special case of the incident ray being perpendicular to the optic axis, the ordinary and extraordinary rays are in fact coincident with each other, but still travel at different velocities. (The extraordinary ray is polarised parallel to the optic axis and the ordinary ray is polarised perpendicular to the optic axis.) This leads to a phase shift between the two rays and hence results in elliptically polarised light. Thus if light of wavelength λ passes through a distance d of a birefringent medium, the resulting phase shift, δ, between the two rays is given by

$$|\delta| = \frac{2\pi}{\lambda} (|n_o - n_e|)\, d \tag{6.2}$$

The following sections detail experiments aimed at measuring the level of birefringence in a fused silica sample where the sample was either suspended on two loops of wire or was held in a cradle as illustrated in figure 6.1. Stress is only applied normal to the wall of the cylinder and hence input light will propagate perpendicular to the plane of the effective optic axis. Thus, as noted in the paragraph above, only one resultant beam is expected to exit the mass.

6.3 Estimation of the Level of Birefringence Caused by Gravity

An order of magnitude calculation was first carried out to try to estimate the predicted

level of birefringence that might be caused by gravity acting on a suspended beamsplitter. The sample of material studied experimentally (section 6.4) was a solid cylinder of Corning 7940, grade A, fused silica (Corning). This is a high grade optical material. The mass was 5 inches in diameter by 4 inches long with one face deviating from the normal by 1 arc minute.

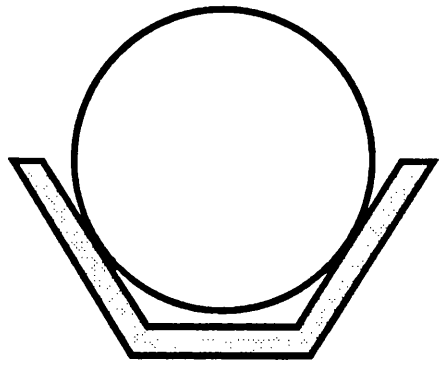

Figure 6.1: End View of Fused Silica Mass held by a Cradle. *The walls of the cradle extend along the full length of the mass. There are however three strips of rubber spaced equally along the length of each wall of the cradle and thus the mass is only supported at six points. Note that the mass is not supported at the bottom.*

The retardation, Γ, in an isotropic material due to an applied stress is given by (Gray, 1972)

$$\Gamma = \frac{C\sigma\ell}{\lambda} \tag{6.3}$$

where Γ is the retardation expressed as a fraction of a wavelength,

C is the stress-optical coefficient for the material. $C = -3.36 \times 10^{-12}\ m^2\ N^{-1}$ at 633 nm for the fused silica under study (Gray, 1972).

σ is the applied tensile stress,

ℓ is the distance through the mass which the light traverses and

λ is the wavelength of the light.

A negative stress-optical coefficient means that light polarised parallel to an applied

compressive stress (i.e the extraordinary component of incident light) has a higher refractive index than that polarised perpendicular to the stress (i.e. the ordinary component of the incident light).

Consider the stress to be force due to the weight, W, of the mass (28 N) applied across the widest diametrical cross-section as indicated in figure 6.2.

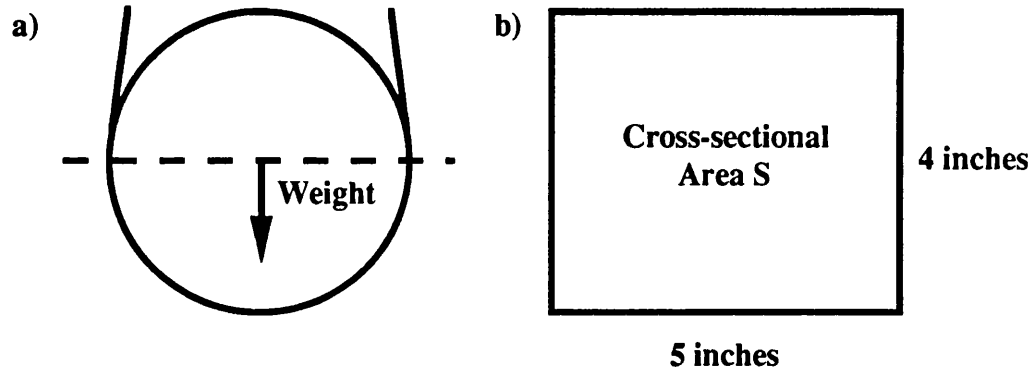

Figure 6.2: Front and Plan View of the Fused Silica Mass.
a) indicates the weight of the mass acting across the widest diametrical cross-section of the mass, indicated by (b).

The applied stress may then be written as

$$\sigma = \frac{W}{S} \tag{6.4}$$

Thus eq. (6.3) may be rewritten with the aid of eq. (6.4) as

$$|\Gamma| = \left|\frac{CW\ell}{S\lambda}\right| \tag{6.5}$$
$$= 10^{-3} \text{ of a wavelength}$$
$$\equiv 0.4^{\circ}$$

Thus a phase shift of the order of half a degree might be expected due to birefringence induced in the mass by gravity alone.

6.4 Experimental Technique

6.4.1 Initial Investigations

The fused silica mass described in the previous section was first examined using a plane polariscope. This is a well known method of analysing stress birefringence, or photoelasticity (e.g. Kuske and Robertson, 1974, pp. 91- 96). The polariscope consists of two crossed polarisers illuminated from the rear, generally by a diffuse white light source. Consider a sample of material subject to stress birefringence placed between the two polarisers. Since refractive index is a function of wavelength, different wavelengths will be retarded by different amounts as they pass through the mass. Consider a point on the mass such that the phase shift induced, between the ordinary and extraordinary rays of the incident light, for one wavelength is a multiple of 2π. This wavelength will then not be transmitted by the second polariser. Components of all other wavelengths will however be transmitted, resulting in coloured light. Thus the resulting output from the polariscope is a pattern of coloured fringes. Each coloured fringe corresponds to a line of constant birefringence and thus of constant stress and hence the fringe pattern is in fact a map of the stress pattern.

The fused silica mass was examined in this way, both when placed in its cradle and when suspended on two loops of wire. Note that although the cradle extended along the full length of the mass, the mass was in fact in contact with the cradle, via strips of rubber, at only three points on each side along its length. When the mass was suspended the two loops of wire were approximately 1 cm apart. No fringes were observed with the polariscope. However there were signs of cloudy white light in each of the four quadrants of the mass. This indicated that there was possibly a low level of birefringence in these quadrants, the phase shift induced between the ordinary and extraordinary rays being too small to result in the removal of any one wavelength. It was desirable to make make more quantative measurements of the effect and two techniques to accomplish this were tried. These are outlined in the following two sections.

6.4.2 Method 1: Matched Photodiodes

Figure 6.3 shows a schematic of the experimental arrangement. The light source used was an argon ion laser operating at 514 nm. The laser light was intensity stabilised using a commercial electro-optic stabiliser (Coherent Associates), after which it was passed through a polarising beamsplitter to ensure that the light was initially vertically polarized. The laser beam then passed through a half wave plate which was orientated such that light was transmitted at a polarisation angle of 45° to the horizontal. The light traversed the mass and was then split into horizontal and vertical components by a second polarising beamsplitter which was orientated such that in the absence of the mass, equal intensities of light were sent to photodiodes. These photodiodes were matched so that they both produced the same output current for a given intensity of incident light. They were connected to a differential amplifier and thus in the absence of any birefringence, the output voltage from this amplifier would be zero.

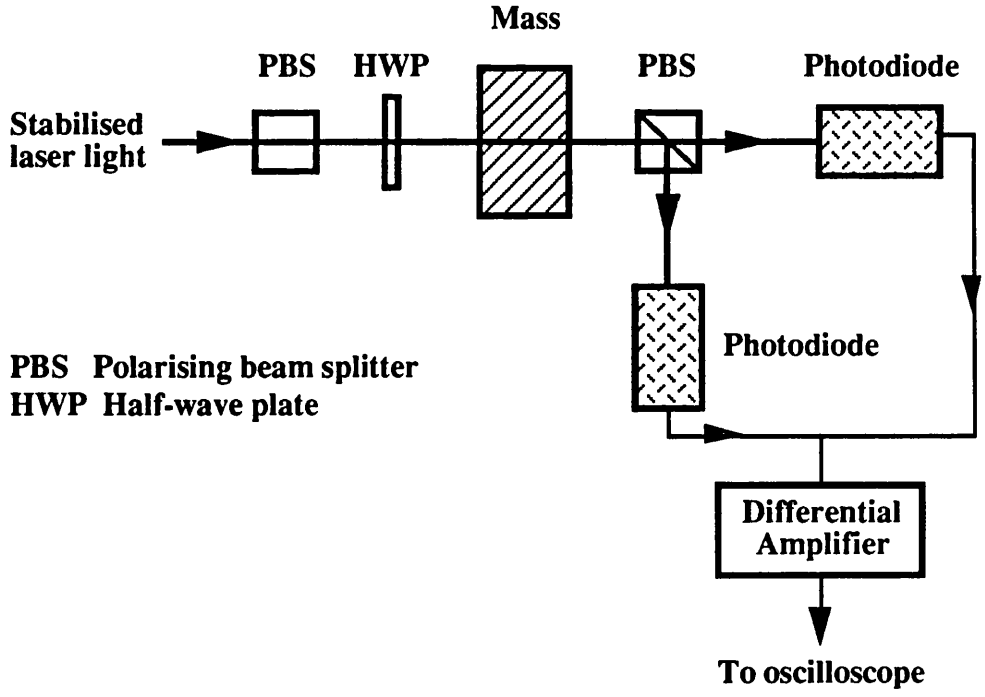

Figure 6.3: Experimental Arrangement, as Viewed from Above, for Measuring Birefringence Using Matched Photodiodes. *The cradle for the mass was attached to an adjustable mount.*

If any birefringence was present in the mass, it may be shown that the difference in the

intensity of light at the two photodiodes, ΔI, is given by

$$\Delta I = \frac{I}{2}(1 - \cos\delta)\sin 4\theta \qquad (6.6)$$

where I is the intensity of light incident on the mass,

θ is the angle at a point in the mass between the induced optic axis and the angle of polarisation of the input light and

δ is the relative phase shift between the ordinary and extra-ordinary rays.

A 'map' of the level of birefringence may then be built up by aligning the laser onto different points on the face of the mass and measuring ΔI.

6.4.3 Results from the Matched Photodiodes

The map of the output voltages from the differential amplifier, at points across the face of the mass, showed that adjacent quadrants of the mass gave rise to signals of opposite sign. Evaluation of δ at a point on the mass, from eq. (6.6), requires a knowledge of the angle θ at the point in question. It is not possible from one set of measurements to determine this angle; to do this would require varying input polarisations to be used until the positions of the optic axes were found for the points under study. Thus as a first approximation, the root mean squared value of $\sin 4\theta$ was used in order to gain an estimate of δ.

When only one photodiode was connected to the differential amplifier, the other input being earthed, the intensity of the light incident on the mass gave rise to a signal of 16 V, i.e $I / 2 = 16$ V. The minimum observed value of ΔI (excepting the central point which gave a reading of 0 V) was found to be 0.05 V and the maximum value, 1.15 V. Since $\sqrt{(\sin^2 4\theta)} = 1/\sqrt{2}$, eq. (6.6) gives the estimated value of δ to vary between 5° and 26°. From the preliminary measurements made using the polariscope (section 6.4.1), it was known that δ must be small. Thus the results obtained by the method used here were rather surprising. The implication was that either using a root mean square value for $\sin 4\theta$ was not valid, or that the experimental set-up was not functioning as expected. On investigation of the experimental technique it was found that the voltages produced by the

differential amplifier were very dependent on the angle that the laser beam made with the photodiode. It was possible to change the value and, if the angular misalignment was large enough, the sign of the output voltage by altering the angle of one of the photodiodes. It was believed that this effect was due to the properties of the interference filters which were placed directly in front of each photodiode. This method of measuring birefringence was thus found to be unreliable and hence a second method was investigated.

6.4.4 Method 2: The Soleil Compensator

The Soleil compensator is an optical device which is used to provide controllable retardation between the components of an incident polarised beam of light. Consider three plates of quartz cut parallel to the optic axis, two of which are wedged shaped, stacked in the manner shown in figure 6.4.

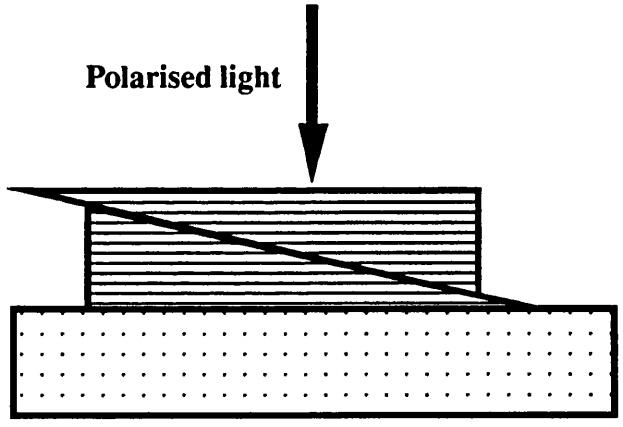

Figure 6.4: Cross Section through a Soleil Compensator. *The wedges are stacked on the flat plate such that their optic axes are perpendicular to those of the plate, as indicated by the lines and dots.*

If a beam of light polarised at some arbitrary angle is incident on the stack, the light will be split into the ordinary and extraordinary components. Note that the wedge angles are small enough that the spatial separation of these rays is negligible. As the light passes from the wedges to the flat plate, the ordinary and extraordinary rays interchange roles and thus the slower component in the wedges becomes the faster component in the flat plate. If the light passes through the same distance in the wedged material as in the flat

plate, the phase shift introduced by the wedged plates is exactly cancelled by that introduced by the flat plate and thus there is no net relative retardation. By sliding the wedges past each other their combined thickness may be altered resulting in a controllable relative retardation of the component polarisations of the incident light.

Figure 6.5 indicates the manner in which the compensator was used. A helium-neon laser (wavelength 633 nm) was used as a light source. The compensator was placed between crossed polarisers, with its axes set at 45° to the input polarisation, and adjusted so that in the absence of the mass, the light reaching the photodiode was minimised i.e. the positions at which the compensator acted as a full wave plate were found. The mass was then placed between the first polariser and the compensator which was then once again adjusted in order to minimise the light on the photodiode. A micrometer attached to the compensator allowed the level of adjustment required to be noted and this reading could then be converted into an angle. Both vertically polarised light and light polarised at 45° to the horizontal have been employed in the prototype detector at Glasgow and thus both of these polarisations are of interest to investigate.

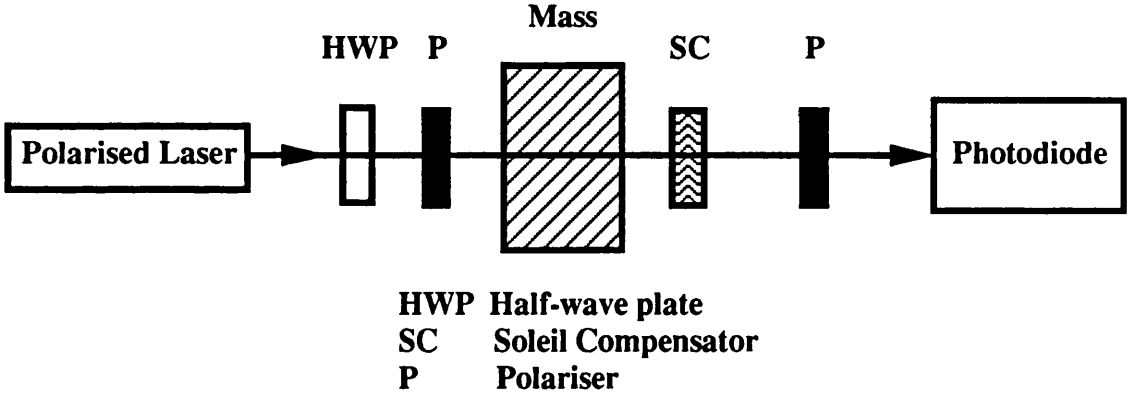

Figure 6.5: Experimental Arrangement for Measuring Birefringence Using a Soleil Compensator. *The polarised light from the laser is passed through the half-wave plate to define the direction of the input polarisation to the mass. The first polariser is aligned such that the input polarisation is transmitted . The second polariser is aligned such that it is perpendicular to the first and so in the absence of the mass and compensator, minimum light reaches the photodiode.*

6.4.5 Results from the Soleil Compensator

Figure 6.6 shows a map of spot measurements which were made across the face of the silica mass using light which was polarised at 45° to the horizontal. It is noted that the general magnitude of these results is in accordance with the rough calculation of the level of birefringence that might be expected due to the effect of gravity (section 6.3).

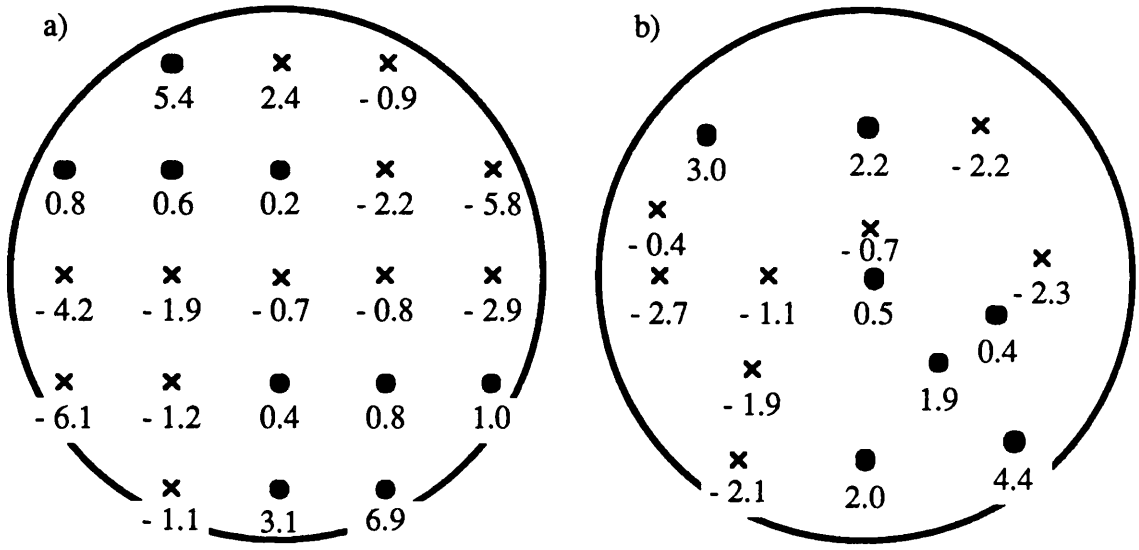

Figure 6.6: Birefringence Levels across the Face of the Five Inch Silica Mass. *The crosses and circles indicate the approximate position of the input light (±0.5 cm in x and y directions). Crosses mark phase shifts of a negative sign, circles mark phase shifts of a positive sign. The numbers indicate the phase difference, measured in degrees, each with an error of ± 0.2°. The input light was polarised at an angle of 45° to the horizontal. a) shows the results when the mass was sitting in its cradle, b) when the mass was suspended on two loops of wire with the loops approximately 1 cm apart.*

It is observed from figure 6.6 that the largest effect was round the outside of the mass whilst the centre of the mass showed a relatively small effect. Adjacent quarters of the mass displayed phase retardations of opposite signs. There is an indication that these quarters are divided by a cross which, particularly towards the centre of the mass, exhibits low birefringence. Minimal or zero birefringence may be due to one of two things; either the point in question is subject to only minimal or zero net stress or the input

light is polarised either parallel or perpendicular to the optic axis so that the light propagates through the mass purely as either the ordinary or extraordinary ray. Note from figure 6.6 that the same general pattern and magnitude of effect were observed irrespective of whether the mass was placed in its cradle or suspended on two loops of wire.

The Production of the Cross

After the results shown in figure 6.6(a) were taken, the mass was rotated, in its cradle, approximately 50° clockwise looking against the direction of the light. This was done in order to see if the pattern would rotate with the mass, in which case the observed birefringence would be due to residual stresses i.e. stresses which were frozen in during the formation of the mass. It was however found that the same general pattern, in the orientation shown in figure 6.6(a), was observed and thus the pattern seemed to be independent of the rotation of the mass. Note that only if the residual stress is purely a function of radius would the residual stress pattern be independent of the rotation of the mass. Thus it seems unlikely that the cross which divides the face of the mass into quarters showing either positive or negative phase shifts, could be due to residual stress alone.

The same pattern, with the orientation and magnitude shown in figure 6.6, was also observed when vertically polarised light was incident on the mass, rather than light polarised at 45° to the horizontal. Since vertically polarised light showed the same cross with small birefringent effect, it is concluded that this cross must be an area of minimum net stress since vertically polarised light and light polarised at 45° to the horizontal cannot both be parallel or perpendicular to the induced optic axes in the area of the cross. This is further verified by the fact that several different polarisations of light were passed through the central point of the mass and only minimal birefringence effects were observed; the greatest phase shift being of the order of $0.7 \pm 0.2°$.

The Effect at the Bottom of the Mass

Compression due to the inward forces produced by either the suspension wires or the cradle, as shown schematically in figure 6.7, could produce the higher levels of

birefringence observed around the bottom of the mass. (Recall from section 6.2 that induced optic axis at a point in the mass is in the direction of the effective stress and that resulting induced birefringence is proportional to the magnitude of the stress.) In the region where horizontal compressive stresses from the quarters add together, and may be of similar magnitude to those in the vertical direction, the differential stresses will be small and thus may lead to a central vertical strip of low birefringence as in figure 6.6.

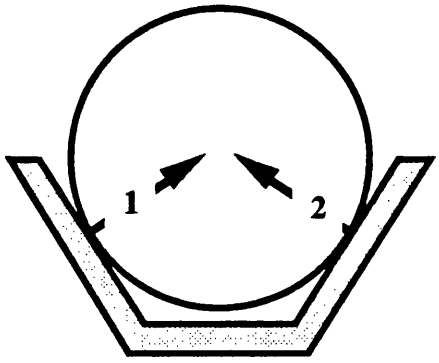

Figure 6.7: Schematic Indicating the Direction of Stresses Applied to the Mass when Placed in the Cradle.

The Effect at the Top of the Mass

It is however less clear why there should be areas of high birefringence towards the top of the mass. It may be that due to compression at the bottom, the top tends to bulge out slightly leading to areas of tension. It is also possible that the observed high birefringence at certain points round the edge, is due to residual rather than applied stress or to a combination of the two. The central horizontal and vertical lines of minimum stress may be due, at least in part, to some cancellation of applied and residual stresses. Thus the total pattern is probably due to a mixture of these effects.

The Change of Sign of the Effect in Adjacent Quarters of the Mass

The sign changes which are observed in adjacent quarters may be due to a combination of effects. When fused silica is placed under conditions of compression, the index of refraction for the extraordinary ray, n_e, is greater than the index of refraction for the ordinary ray, n_o ($n_e > n_o$). Under conditions of tension, $n_o > n_e$ (Gray, 1972). Whilst n_o

will be of constant value throughout the mass, if there are areas of compression and tension, n_e will be respectively greater or less than n_o. Now if the phase shift between the ordinary and extraordinary rays is between zero and π, the incident light will rotate in the direction of the slower axis (Longhurst, 1973, pp. 549 - 550) producing either left or right elliptically polarised light as illustrated in figure 6.8.

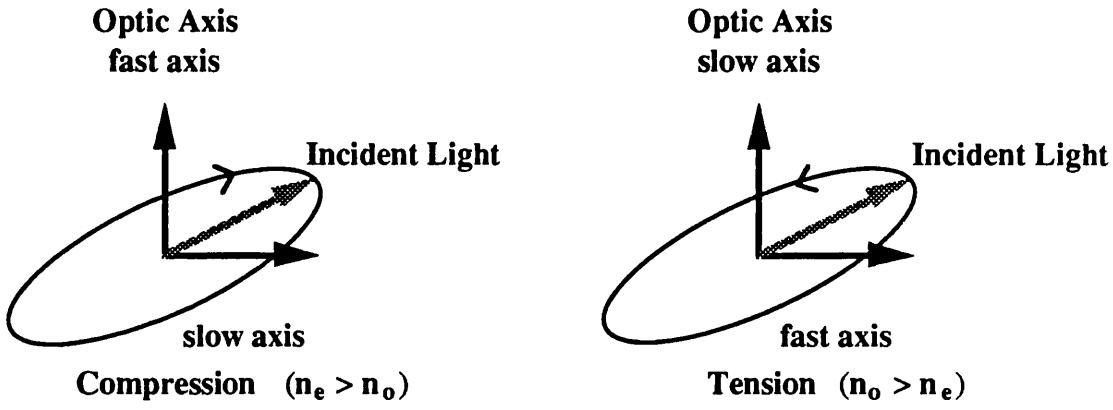

Figure 6.8: The Production of Right and Left Handed Elliptically Polarised Light. *The extraordinary component of the incident light lies parallel to the optic axis and the ordinary component lies perpendicular to it. It is assumed that the phase shift, δ, produced between the two axes is such that $0 < \delta < \pi$. Looking against the light it is observed that if $n_e > n_o$, right-hand elliptically polarised light is produced, if $n_o > n_e$ then left-hand elliptically polarised light is produced.*

It might therefore at first be thought that since both lower quarters of the mass are subject to compressive forces, the results from the two quarters should be identical. To see why this is not so consider for example, vertically polarised light incident on points 1 and 2 in figure 6.7. Since both of these points are subject to compressive forces, the optic axes, which are in the direction of the applied stress as indicated in the figure by the arrows, are the fast axes. Thus the incident light will rotate towards the slow axis which lies perpendicular to the optic axis, i.e. the light rotates away from the optic axis. Thus light emerging from point 1 on the mass will be left-hand elliptically polarised, looking against the direction of the light, and light emerging from point two will be right-hand elliptically polarised. It is thus evident that the angle between the input polarisation and the induced optic axis at a point on the mass also determines the form of the output light.

Concluding Remarks

The actual stress distribution in the mass will be far more complex than has been considered so far. Further experimental information would be required to more fully interpret the pattern of the experimental results as displayed in figure 6.6. The important information, from the point of view of designing a gravitational wave detector is, however, the magnitude of the birefringence and the fact that, from the results presented in this chapter, the level of birefringence in the central area of the mass, where laser light is mostly likely to pass through, is small. In the following section the effect of birefringence on the sensitivity of a detector will be considered.

6.5 The Effect of Birefringence in the Beamsplitter on the Fringe Contrast of a Gravitational Wave Detector

Proposals for long baseline interferometric gravitational wave detectors incorporate light recycling techniques in the detector design. This is a method of increasing the detector sensitivity by recycling light which is normally unused (section 1.5.2). Loss of light in the interferometer will impair the sensitivity of a gravitational wave detector since the amount of light available for recycling is decreased (Meers, 1988). It is will be shown below that the greater the level of birefringence in the beamsplitter of the interferometer the greater is the degradation in the fringe contrast of the interferometer. Thus it is important to choose material for the transparent optical components which exhibits low birefringence.

Gravitational wave detectors operate with polarised light. Consider such a beam of laser light incident on the beamsplitter. Figure 6.9 shows the optical paths in a simple Michelson interferometer. One beam is reflected from the front face of the beamsplitter, whereas the other beam must traverse the beamsplitter twice in order to recombine with the first beam. The output of the interferometer then passes once through the beamsplitter in order to exit the interferometer. Thus, assuming that the arms of the interferometer are of equal length, there is a path difference between the two interfering beams of two passes

through the beamsplitter.

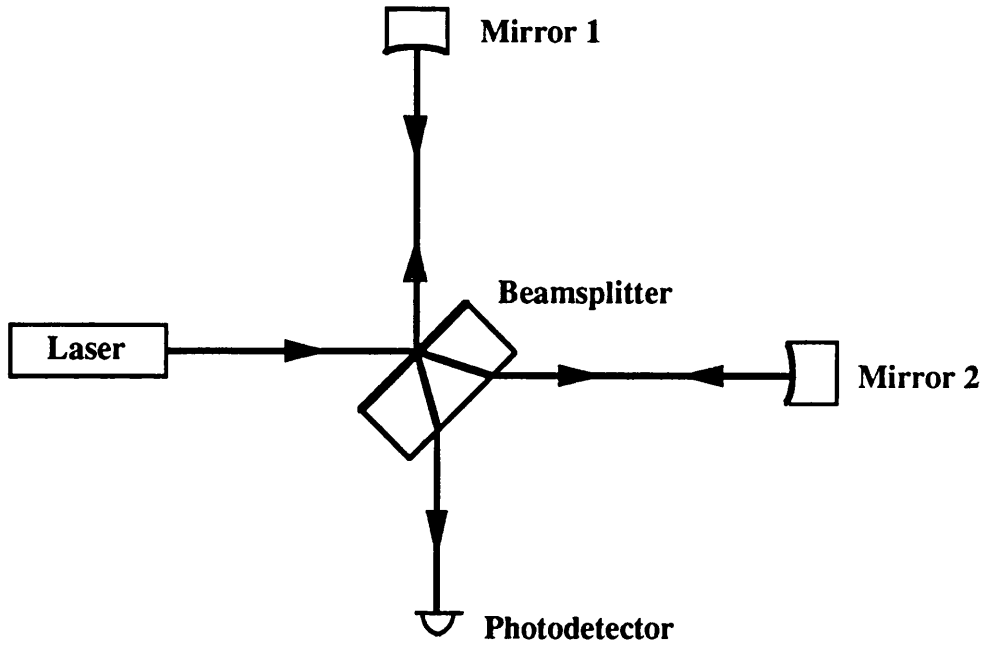

Figure 6.9: The Optical Paths of Beams in a Michelson Interferometer. *The size of the beamsplitter with respect to the end mirrors has been exaggerated in order to show the paths taken by the two interfering beams. Reflective surfaces of the optical components are indicated by bolder lines.*

It is noted that the incident beam is no longer perpendicular to the effective optic axis, induced by stress due to the suspension of the mass, and thus strictly speaking the ordinary and extraordinary beams should emerge separately from the mass. If however $\Delta n << 1$, the separation of these beams will be negligible.

Consider the input light to the interferometer to be initially linearly polarised. It may therefore be considered to consist of two components, one parallel and one perpendicular to the optic axis at the point at which it is incident on the mass, e.g. suppose the input polarisation is at 45° to the optic axis, since this is the situation where induced birefringence has most effect on the fringe contrast of the interferometer. Half of the intensity of the incident beam passes through the beamsplitter. If this medium is birefringent a phase difference of δ will be introduced in one component with respect to the other. After reflection at mirror 2, as indicated in figure 6.9, this beam then passes

back through the beamsplitter where a second phase shift of δ is introduced. Interferometric gravitational wave detectors operate on a dark fringe, for reasons outlined in section 1.5.1, and hence the recombination of beams 1 and 2, for $\delta << 1$, may be represented vectorially as shown in figure 6.10.

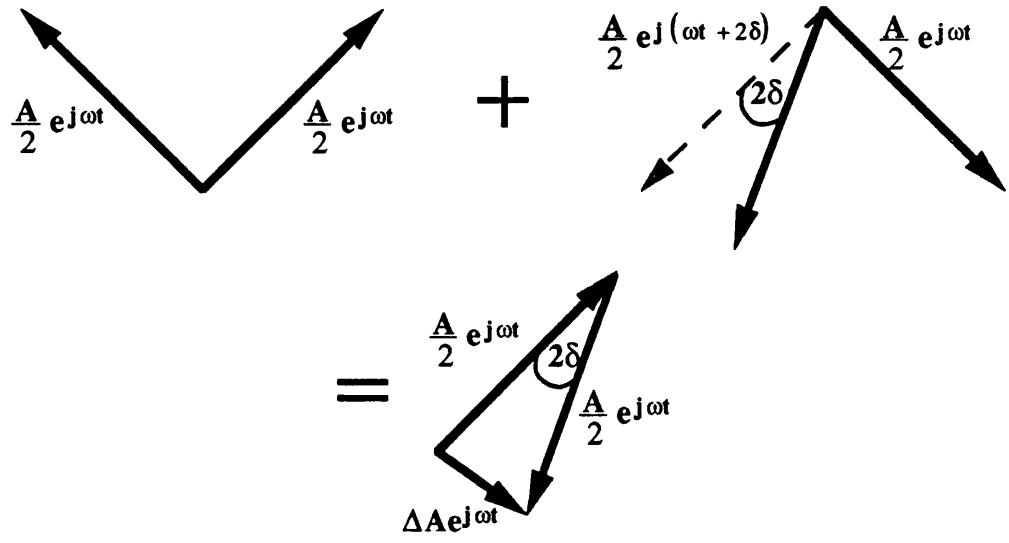

Figure 6.10: Vectorial Representation of the Recombination of the Two Beams in the Interferometer for $\delta << 1$.

Note that if the beamsplitter shows no birefringence, i.e. $\delta = 0$, then the two interfering beams completely cancel each other. It may be shown from figure 6.10 that when δ is small, the resultant degradation in the fringe contrast

$$\frac{\Delta I}{I} = \delta^2 \tag{6.7}$$

where I is the intensity of the input light ($I \propto A^2$).

Using the results of figure 6.6(a), if δ^2 is averaged over the entire face of the mass $\Delta I / I \sim 3 \times 10^{-3}$. If the averaging is done over the central nine points, the area through which it is more probable that light will traverse, then $\Delta I / I \sim 4 \times 10^{-4}$. These values may be compared with the loss of light at the mirrors. Strain has measured the average loss in the mirrors currently used in the Glasgow prototype to be 6×10^{-5} per mirror (Strain, 1990). Thus for a 3 km detector with 30 bounces in each arm, the total loss = 3.6×10^{-3}

due to mirror losses alone. Thus losses due to birefringence at the beamsplitter are, at present, an order of magnitude smaller than those due to the mirrors as long as the beam passes through the central area of the beamsplitter. Note however that as the technology for manufacturing low loss mirrors improves, stress induced birefringence could become increasingly more important. Note also that the measurements presented in this chapter were obtained using low laser power. High laser powers could result in appreciable temperature gradients being established within the substrate. This would produce thermal stresses within the material giving rise to thermally induced birefringence. Winkler has estimated that a temperature drop across the radius of the laser beam of 0.2 K (which could be caused by laser power of the order of 1 kW) would produce a degradation in fringe contrast of 10^{-4} (Winkler, 1993). This is of the same order of magnitude as that produced by birefringence due to mechanical stress.

6.6 Conclusion

From the results presented here it is clear that birefringence may degrade the sensitivity of a gravitational wave detector. Thus care must be taken in choosing the material and thickness of the beamsplitter and, if Fabry-Perot cavities are used in the arms of the interferometer, the inboard mirrors. It is evident from the results presented in figure 6.6 that, in order to minimise the effect of degradation of the fringes by stress birefringence, the laser beam should be incident on the central region of the mass. With this consideration in mind it is also noted that the results would tend to indicate that the diameter of the beamsplitter should be much larger than the laser beam diameter.

It is noted that thermal gradients produced by heating in the beamsplitter and mirror substrates will, in addition to producing thermal stress, produce a gradient in the refractive index of the material since refractive index is a function of temperature. Such an effect produces distortion of the wavefront of an incident beam, an effect known as thermal lensing. Winkler (Winkler, 1993) has estimated that this effect will be more significant than birefringence induced by thermal stress or, from the author's results, than birefringence induced by mechanical stress. However it may be that thermal lensing could be compensated for by the fabrication of specially ground compensating plates and thus both mechanically and thermally induced birefringence may still be significant.

Chapter 7

Conclusions and Future Prospects

In chapter 1 it was shown that the thermal motion of the test masses will be one of the limits to the ultimate sensitivity of a long-baseline laser interferometric gravitational wave detector. The criteria for choosing the material from which the test masses are formed, have been discussed. In particular it has been shown that in order to minimise their thermal motion, the test masses should have a high Q. The majority of the work contained in this thesis has been concerned with the investigation of the Q of materials.

The effect of coupling between normal modes in samples of materials has been studied. It was noted that the Q values of the coupled system were degraded by that of the more lossy mode. An equivalent circuit was used to try to determine whether or not the thermal motion of a test mass would be increased, at frequencies very much lower than the coupled mode frequencies, by this apparent degradation in Q. The answer to this question depends upon the nature of the coupling. For a system where the coupling is through common mass, thermal motion of the mass should not be increased over that for the uncoupled system. In the case of coupling through a common compliance, such as may be the case for the columnar silicon mass studied, thermal motion of the test mass may in fact be increased. It is thus concluded that, as a general guideline, it is safer to choose the aspect ratio of the test masses for an interferometric gravitational wave detector such that the normal mode frequencies do not lie close to each other.

It was found that the measured Q of the fundamental longitudinal mode of a columnar silicon mass was suitably high, at least at high frequencies, for the material to be considered for the test masses for a long baseline interferometer. It was however found that by systematically altering the length of the suspension wires, the measured Q for this mode varied periodically between maximum and minimum values. This was shown to be due to resonances in the suspension wires. It was found that the application of grease at

the points where the wire broke free from the mass increased both the maximum and minimum measured Q values. The maximum measured Q value for the longitudinal mode of a columnar silicon mass, which resonated at 48 kHz, was found to be $(4.8 \pm 0.1) \times 10^6$. An equivalent circuit was used to model the interaction of the suspension wires with the fundamental longitudinal mode of the mass. This was done in order to determine whether the thermal motion of a test mass, at frequencies in the range of interest for the detection of gravitational waves, would be increased if the test mass was suspended on a loop of wire such that its measured Q was low due to the effect of resonances in the wires. It is concluded that the fundamental level of the thermal motion of the mass is not affected by this apparent degradation in Q. The exact form of the thermal motion spectral density depends upon the assumed frequency dependence of the Q of the materials of both the test mass and the suspension wires.

The equivalent circuit which was developed to model the coupling between the longitudinal mode of the mass and the suspension wires, was adapted to model the pendulum motion of the suspended mass. Combining the results from both equivalent circuits allowed a prediction to be made concerning the sensitivity of a long baseline interferometric gravitational wave detector. If a pendulum has a given Q at its resonant frequency, it is better from the point of view of minimising thermal motion of the pendulum, for the suspension wire Q to be frequency independent. This would then lead to the thermal motion spectral density falling off faster above the pendulum resonance than if the wire Q was inversely proportional to frequency. By contrast, if the test mass has a given Q at its lowest resonant frequency of significance for interferometric detectors (section 2.2.3), it is better to have a material with a Q which is inversely proportional to frequency since this leads to a thermal motion spectral density which is frequency independent below the lowest resonance, rather than inversely proportional to the square root of frequency which would be the case if the Q of the material was constant.

Thus in order to predict the effect of thermal motion on the sensitivity of an interferometric gravitational wave detector, it is necessary to first know how the quality factors of the materials under consideration behave as a function of frequency. It has been conventionally assumed in the design studies for long baseline laser interferometric detectors that the Q of a material is inversely proportional to frequency. Experimental data has been presented as to how the Q of the fundamental longitudinal mode of samples of

aluminium and fused silica behaves. It would appear from these results that the Q of both of these materials is in fact constant over large frequency bandwidths. If this behaviour is confirmed down to lower frequencies this will have implications for the eventual sensitivity of large gravitational wave detectors. Figure 7.1 indicates the the difference in the sensitivity of a detector using pendulums formed from wires and test masses which both have Q values which are inversely proportional to frequency and a detector where these materials have Q values which are frequency independent. It is clear from this that, given a particular value of Q at the resonant frequency of the test mass, it is preferable for the Q of the test mass material to be inversely proportional to frequency - a situation not apparently found in fused silica or aluminium. The frequency dependence of Q for columnar silicon is as yet unknown, however this will be investigated in the future.

It is not only the mechanical properties of the test masses which are important. Optical homogeneity of the beamsplitter, and of the inboard masses if Fabry-perot cavities are used in the arms, is also an important consideration. The results presented in this thesis have allowed an evaluation of the comparative importance of stress induced birefringence and of thermally induced birefringence and thermal lensing as calculated by Winkler (Winkler, 1993). If the effects of thermal lensing can be compensated for, stress birefringence will become important and this may lead to degradation of the sensitivity of interferometric gravitational wave detectors. Thus care must be taken in choosing the material and thickness of the beamsplitter and inboard mirrors, in the case of a Fabry-Perot based system.

This thesis has addressed a number of issues important for the construction of long baseline interferometric gravitational wave detectors. Results and analysis suggest that the thermal noise from the test masses may impose a more severe limit to sensitivity than has been assumed in the present proposals for such detectors. However there may be materials which have a different frequency dependence of Q and clearly there is a need for further experimental work to establish the dependence of Q with frequency for a range of materials, suitable for use in laser interferometric gravitational wave detectors.

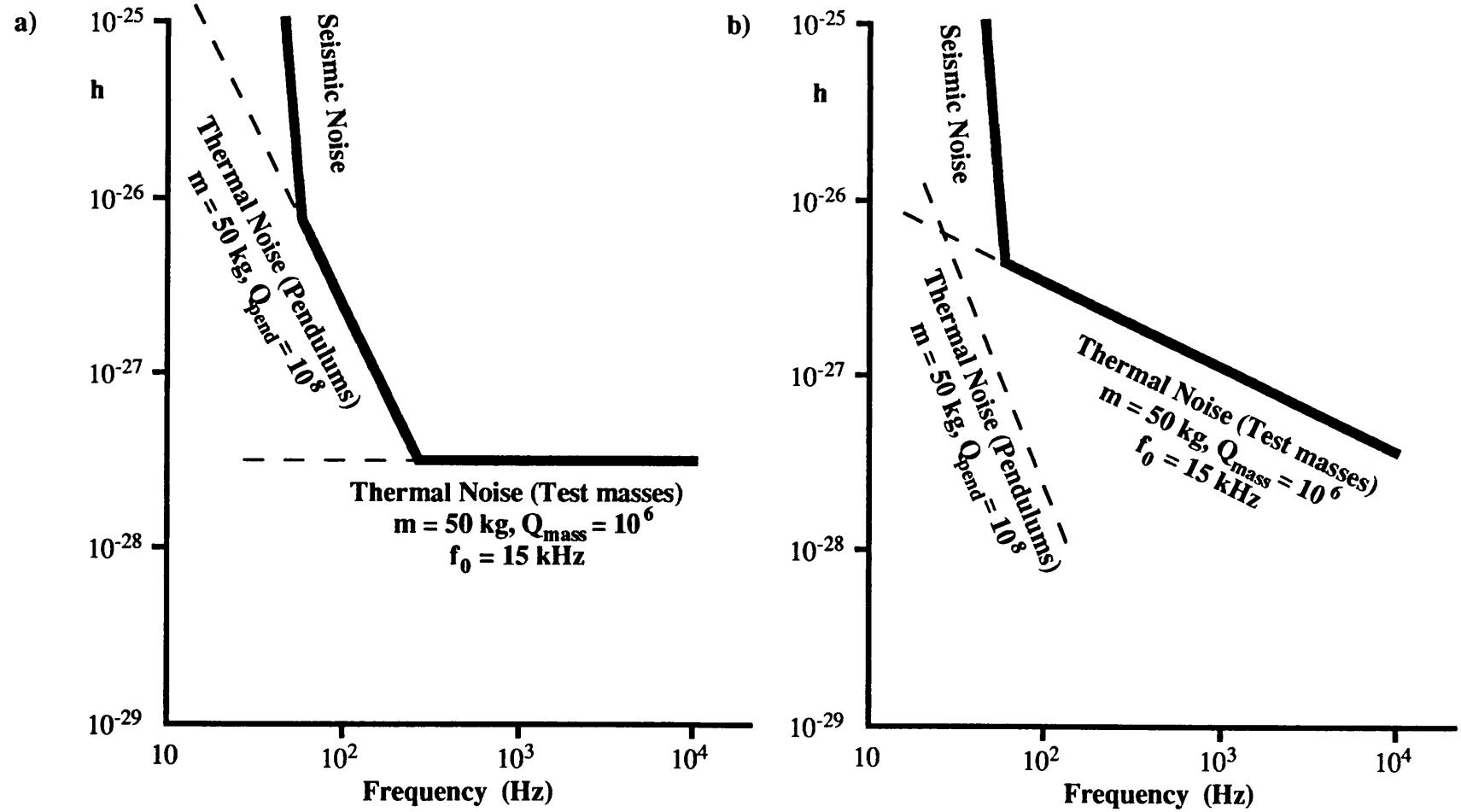

Figure 7.1: The Sensitivity Curves for two Long Baseline Interferometric Gravitational Wave Detectors . *a) is for a detector with the Q values of the pendulums and test masses inversely proportional to frequency. b) is for a detector with both of these Q values frequency independent. The effect of wire resonances has been neglected.*

Appendix A

Damping of Q due to a Magnetic Excitation Mechanism

A.1 Introduction

One method which was used to excite a normal mode of a suspended test sample of material, was to use a coil and magnet mechanism as shown schematically in figure A.1.

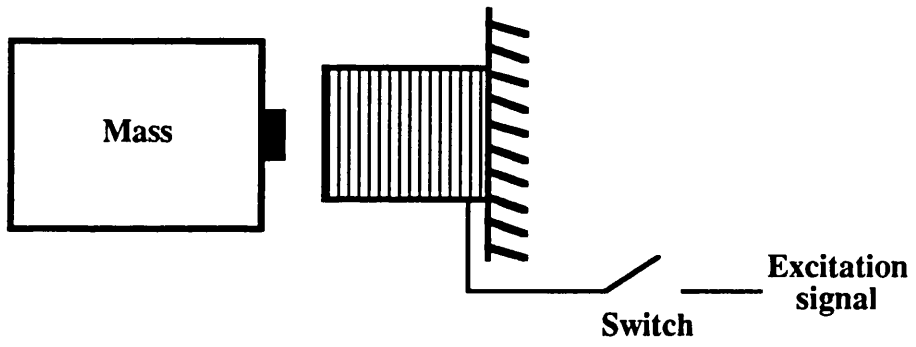

Figure A.1: Coil and Magnet Excitation Mechanism. *The magnet is glued to the rear face of the mass. Note that the size of the coil and magnet have been exaggerated compared to the size of the mass.*

A Michelson interferometer was used, as described in section 2.4, to sense the motion of the front face of the mass. When the mass resonated at the desired normal mode frequency, the excitation signal to the coil was cut-off by means of the switch indicated in figure A.1. The decay of the resonance was then recorded using a chart recorder and the Q of the mode of the sample could thus be calculated.

In this appendix, consideration is given as too how such an excitation mechanism may damp the Q of the fundamental longitudinal mode of the mass.

A.2 Magnetic Damping

A.2.1 Theoretical Calculation of Magnetic Damping

A coil possesses a distributed capacity which may be represented as shown in figure A.2 (Terman, 1943, pp. 84 - 85)

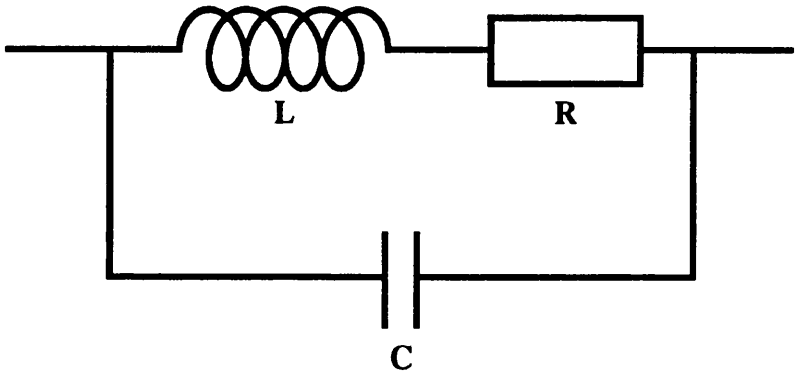

Figure A.2: Representation of the Distributed Capacity of a Coil.

Thus even when such a coil has its terminals open circuit, an induced EMF in the coil can still cause an a.c. current to flow. The motion of the resonating mass causes the magnet, which is attached to the mass, to oscillate in the vicinity of the coil and hence an a.c. current is induced in the coil. Since the coil has some resistance energy is dissipated in it. The limit imposed by such a damping mechanism upon the Q of the mode of the mass may be calculated as follows.

The magnet may be considered as a magnetic dipole with magnetic dipole moment $\underline{p}$. The B field from the magnet normal to the turns of the coil, shown in figure A.3, is given by (e.g. Duffin, 1980, p. 199)

$$B_x = \frac{\mu_o p(2x^2 - y^2)}{4\pi(x^2 + y^2)^{5/2}} \qquad (A.1)$$

where μ_o is the magnetic permeability of vacuum

The magnetic flux cutting the coil

$$\phi = \int_A \underline{B}.d\underline{A}$$

is thus

$$= \frac{\mu_o p a^2}{2(x^2 + a^2)^{3/2}} \qquad (A.2)$$

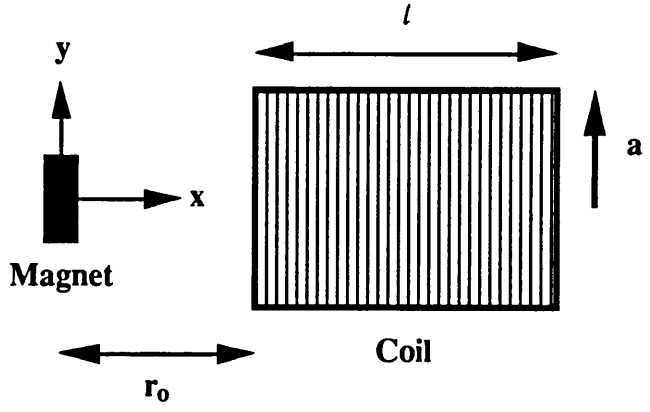

Figure A.3: Coil and Magnet Parameters. *The coil has radius a and length l. The magnet is positioned a distance r_o from the coil.*

If there are N turns of wire on the coil, the EMF, ε, induced in the coil

$$\varepsilon = -\int_{r_o - x_{mag}}^{r_o + l - x_{mag}} \frac{N}{l}\frac{d\phi}{dx}\frac{dx}{dt}\,dx$$

thus

$$\varepsilon = -\frac{\mu_o N p a^2 \omega_o \alpha \cos\omega_o t}{2l}\left[\frac{1}{\left[(r_o + l - x_{mag})^2 + a^2\right]^{3/2}} - \frac{1}{\left[(r_o - x_{mag})^2 + a^2\right]^{3/2}}\right] \qquad (A.3)$$

where $x_{mag} = \alpha\sin\omega_o t$ is the position of the magnet,

α is the amplitude of motion of the mass and hence of the magnet and

ω_o is the angular resonant frequency of the fundamental longitudinal mode of the mass.

Hence, with reference to figure A.2, the current induced in the coil is

$$I = \frac{\varepsilon}{\left[R + j\left(\omega_o L - \frac{1}{\omega_o C}\right)\right]} \tag{A.4}$$

The energy which is dissipated in the coil per cycle, and thus the energy lost from the mass per cycle

$$E_L = \int_0^{2\pi/\omega_o} |I|^2 R \, dt$$

Thus

$$E_L = -\frac{(\mu_o N p a^2 \omega_o \alpha)^2 R \pi}{4\ell^2 \omega_o \left[R^2 + \left(\omega_o L - \frac{1}{\omega_o C}\right)^2\right]} \left[\frac{1}{[(r_o + \ell)^2 + a^2]^{3/2}} - \frac{1}{[r_o^2 + a^2]^{3/2}}\right]^2 \tag{A.5}$$

Thus from the definition of the Q of a resonant system, eq. (2.1), recalling that the energy stored in the fundamental longitudinal mode of a mass $E_T = \frac{1}{4} m\omega_o^2 \alpha^2$, eq. (2.11), the Q of this mode of a mass, limited only by magnetic damping from the excitation mechanism, is

$$Q_{mag} = \frac{2\omega_o m \ell^2}{(\mu_o N p a^2)^2 R} \left[R^2 + \left(\omega_o L - \frac{1}{\omega_o C}\right)^2\right] \left[\frac{1}{[(r_o + \ell)^2 + a^2]^{3/2}} - \frac{1}{[r_o^2 + a^2]^{3/2}}\right]^{-2} \tag{A.6}$$

A.2.2 Evaluation of Q_{mag}

In order to evaluate eq. (A.6), values are required for N, p, L, C and R for the magnet and coil.

The Coil Parameters

The presence of a distributed capacity modifies the apparent inductance, L_{eq}, of the coil as viewed from the terminals. In order to measure L_{eq} of the coil, a capacitor, C_r = 170 pF, was added in series with the coil. The resonant frequency of this combination, f_r, was found to 130 kHz. Hence the inductance of the coil as viewed from the terminals $L_{eq} = (4\pi^2 f_r^2 C_r)^{-1}$ = 8.8 mH. The apparent inductance of the coil is formed from the distributed capacity of the coil, C, in parallel with the true inductance of the coil, L. It

may be shown that

$$L = L_{eq} \frac{(\omega_c^2 - \omega_r^2)}{\omega_c^2} \qquad (A.7)$$

where ω_c is the angular self-resonant frequency of the coil, $\omega_c^2 = (LC)^{-1}$, and

ω_r is the angular frequency at which L_{eq} was measured.

The self-resonant frequency of the coil was found to be 281 kHz and hence from eq. (A.7) L = 7 mH and thus C = 46pF.

The a.c. value of the resistance, R, of the coil will not be equal to its d.c. value, R_{dc}. There are two main reasons for this. The first is due to the fact that at higher frequencies current tends to be distributed closer to the surface of a conductor rather than be uniformly distributed over the wire cross-section. This is known as the skin effect. Thus $R > R_{dc}$ since parts of the conductor are not fully used in carrying the current. For copper wires of diameter 0.5 mm carrying current of frequency 50 kHz the ratio of R to R_{dc} is 1.011 (Terman, 1943, p. 31). Thus at frequencies of interest for the Q measurements in this thesis, this will be a very small effect. The second reason for R not being equal to R_{dc} is the proximity effect (Terman, 1943, p 37) This occurs when there are two or more conductors close to each other, and the current in one conductor is affected by the magnetic flux produced by adjacent conductors i.e. eddy currents are induced. It is difficult to estimate the magnitude of this affect but in general it causes the ratio of a.c to d.c. resistance to be greater than would be predicted by the skin effect.

It is desirable to know the the a.c. resistance of the coil at a frequency at which Q measurements were made. Thus the resonant frequency of the coil was lowered to 55 kHz by connecting a capacitor across its terminals. The Q of the circuit was then measured and hence the value of R was found to be 40 Ω. It was noted that the Q of the circuit was the same irrespective of whether the magnet was brought up close to the coil or was far away from it. Thus very little energy from the system can be lost in the form of eddy currents induced in the magnet.

Measurement of the Product Np for the Coil and Magnet

Consider the forces on a suspended mass as indicated in figure A.4. The horizontal restoring force of the pendulum, for small Δx is

$$F_{pen} = mg\frac{x}{h} \tag{A.8}$$

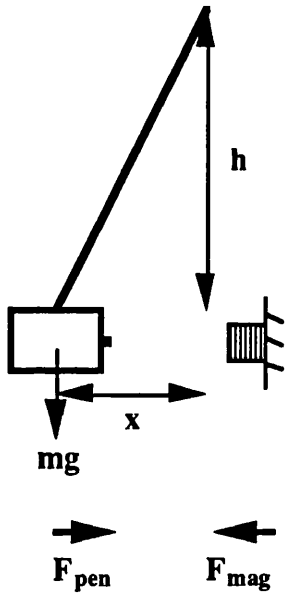

Figure A.4: ***Forces on a Suspended Mass.*** *F_{pen} is the horizontal restoring force of the pendulum. F_{mag} is the horizontal force produced by interaction between the coil and the magnet.*

The gradient of the B field of the coil at the position of the magnet is given by (e.g. Lorrain and Corson, 1970, p.317)

$$\left(\frac{dB_{coil}}{dx}\right)_{x = x_{mag}} = -\frac{I\mu_o N a^2}{2\ell}\left[\frac{1}{\left[(r_o + \ell - x_{mag})^2 + a^2\right]^{3/2}} - \frac{1}{\left[(r_o - x_{mag})^2 + a^2\right]^{3/2}}\right] \tag{A.9}$$

The force on the magnet due to the B field of the coil

$$F_{mag} = p\left(\frac{dB_{coil}}{dx}\right)_{x = x_{mag}} \tag{A.10}$$

Combing eqs. (A.9) and (A. 10), the following expression for Np may be obtained

$$Np = -\frac{F_{mag} 2\ell}{I\mu_o a^2}\left[\frac{1}{\left[(r_o + \ell - x_{mag})^2 + a^2\right]^{3/2}} - \frac{1}{\left[(r_o - x_{mag})^2 + a^2\right]^{3/2}}\right]^{-1} \qquad (A.11)$$

Now

$$\frac{\Delta F_{mag}}{\Delta I} = \frac{\Delta F_{mag}}{\Delta x}\frac{\Delta x}{\Delta V} R$$

$$= -\frac{\Delta F_{pen}}{\Delta x}\frac{\Delta x}{\Delta V} R \qquad (A.12)$$

where V is an applied voltage across the coil

Thus from eqs. (A.8), (A.11) and (A.12)

$$Np = \frac{mg}{h}\frac{\Delta x}{\Delta V} R \frac{2\ell}{\mu_o a^2}\left[\frac{1}{\left[(r_o + \ell)^2 + a^2\right]^{3/2}} - \frac{1}{\left[r_o^2 + a^2\right]^{3/2}}\right]^{-1} \qquad (A.13)$$

In order to measure $\Delta x/\Delta V$, which is the change in position of the magnet as a function of applied voltage, a columnar silicon mass (see section 3.3.1 for a description of this material) 3 inches in diameter by 3 inches long with a samarium cobalt magnet approximately 3 mm square attached to its the rear face, was suspended on a single loop of wire. A d.c. voltage was then supplied to the coil and measurements were taken of the the position of the mass, using a travelling microscope, as a function of applied voltage. For a mass of 0.81 kg, $\Delta x/\Delta V$ was found to be 1×10^{-5} m V^{-1}. Eq. (A.13) was evaluated for the following values

m = 0.81 kg	ℓ = 0.007 m
h = 0.07 m	a = 0.015 m
R_{dc} = 24 Ω	r_o = 0.005 m

From this Np was found to be 13 A m^2.

A.3 Conclusion

Eq. (A.6) was evaluated for the columnar silicon mass using the following values in addition to those given above:

$\omega_o = 52 \times 2\pi \times 10^3$ rad s^{-1} $\quad$ $L = 7$ mH

$R = 40\ \Omega$ $\quad$ $C = 46$ pF

From this it is predicted that the Q of the columnar silicon mass limited only by losses due to the magnetic excitation mechanism is 2×10^{16}. This is many orders of magnitude greater than the Q measurements presented in this thesis and thus magnetic damping due to the excitation mechanism is not predicted to be a limitation to any of the measurements made.

Appendix B

Damping of Q due to a Capacitive Excitation Mechanism

B.1 Introduction

In making Q measurements of suspended samples of columnar silicon, a capacitive excitation method, as indicated in figure B.1, was sometimes employed.

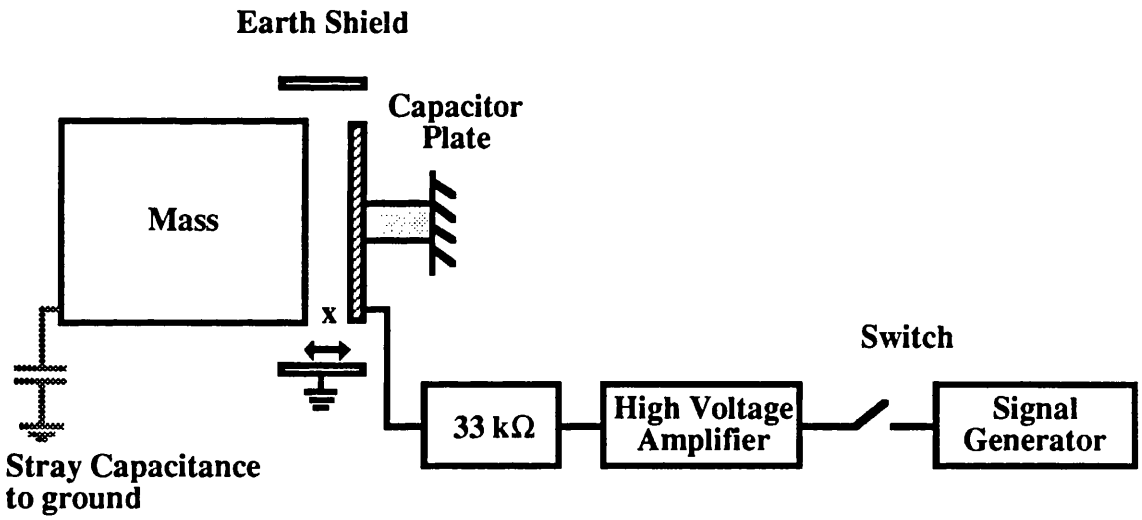

Figure B.1: ***Schematic of Capacitive Excitation Mechanism.*** *The capacitor plate is formed from a copper disc of radius slightly smaller than the mass under study. An earth shield was used to define the edge conditions of the capacitor plate and to provide shielding. The copper earth shield was formed from a strip of copper foil placed around but not in contact with the mass and capacitor plate as indicated in the figure. A gap was left in this shield so that the spacing between the mass and the plate could be easily observed. x denotes the distance between the mass and the capacitor plate.*

A d.c. offset voltage of approximately 250 V and an a.c. voltage of approximately 400 V peak to peak was applied to the capacitor plate in order to excite the desired resonance of the mass. The a.c. signal was then cut-off by means of a switch. A Michelson interferometer sensed the motion of the front face of the mass allowing measurements to be made of the Q of the mode of the mass under study, as described in section 2.4.

As noted in section 2.4, a resistor was placed in series between the high voltage amplifier and the capacitor plate in order to protect the amplifier should the capacitor short circuit. The switch was placed between the signal generator and the high voltage amplifier rather than directly after the amplifier for two reasons: firstly, the switches which were readily obtainable were not rated for such high voltages and secondly, switching off the d.c. component of the signal would have tended to excite the pendulum resonances. Although the motion of the pendulum would be mainly longitudinal, there would also be tilting and rocking of the mass which would cause the decay curve of the amplitude of motion of the mode under study, to be corrupted by movement of the suspended mass as a whole. Note that the feedback circuit which is employed to stabilise the arm lengths of the Michelson interferometer can only compensate for longitudinal motion of the mass.

In this appendix consideration is given as to how such an excitation mechanism may damp the Q of the fundamental longitudinal mode of the mass.

B.2 Theoretical Calculation of Capacitive Damping

When the switch is open circuit the excitation mechanism may be represented as shown in figure B.2. Movement of the mass resonating in its fundamental longitudinal mode will cause the capacitance between the mass and the capacitor plate to change. This will induce an a.c. current which can flow to ground through the amplifier. Energy is then dissipated in the resistor, leading to damping of the longitudinal mode of the mass. The limit that such a damping mechanism places on the Q of the mode may be calculated as follows.

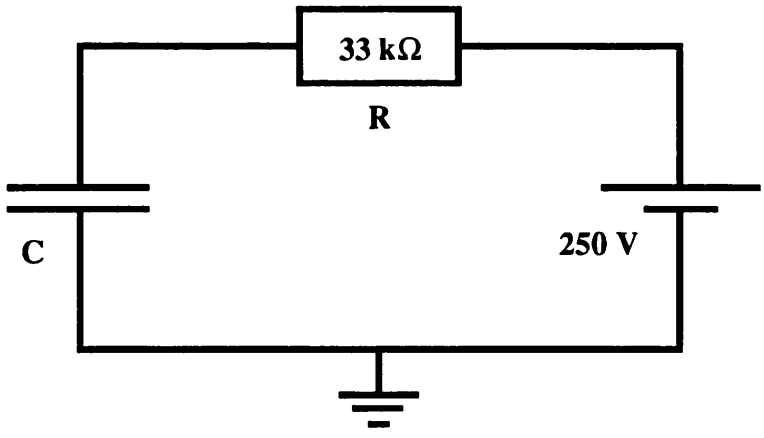

Figure B.2: Circuit Representation of Capacitive Drive Mechanism when the Switch is Open Circuit. *The amplifier has a capacitive output impedance (not shown on the diagram) and thus minimal energy is dissipated in this.*

The charge on the capacitor

$$Q = CV \tag{B.1}$$

and thus the current flowing in the circuit of figure B.2

$$I = V\frac{dC}{dt} = V\frac{\partial C}{\partial x}\frac{\partial x}{\partial t} \tag{B.2}$$

where the separation of the mass and the capacitor plate is denoted by

$$x = x_o + \alpha \sin \omega_o t \tag{B.3}$$

where x_o is the equilibrium distance between the mass and the plate,

α is the amplitude of the fundamental longitudinal mode of the mass and

ω_o is the angular resonant frequency of the fundamental longitudinal mode.

The capacitance of a parallel plate capacitor is expressed as

$$C = \frac{\varepsilon_o S}{x} \tag{B.4}$$

where ε_o is the permittivity of vacuum and

S is the area of the capacitor plates.

(C = 13 pF for x = 5mm and S = 7 x 10^{-3} m^2)

Thus combining eqs (B.2), (B.3) and (B.4) the current flowing in the circuit is

$$I = - \frac{\varepsilon_o S V \alpha \omega_o \cos \omega_o t}{(x_o + \alpha \sin \omega_o t)^2} \tag{B.5}$$

The energy lost per cycle in the circuit is given by

$$E_L = \int_0^{2\pi/\omega_o} I^2 R \, dt$$

$$\approx \frac{(\varepsilon_o S V \alpha \omega_o)^2 R}{x_o^4} \int_0^{2\pi/\omega_o} \cos^2 \omega_o t \left[1 - \frac{4\alpha}{x_o} \sin \omega_o t\right] dt \qquad x_o >> \alpha$$

$$= \frac{(\varepsilon_o S V \alpha)^2 R \pi \omega_o}{x_o^4} \tag{B.6}$$

The energy stored in the fundamental longitudinal mode of the mass is, from eq. (2.11)

$$E_T = \frac{1}{4} m \omega_o^2 \alpha^2 \tag{B.7}$$

Thus from the definition of Q of a resonant system, eq. (2.1), the Q of the fundamental longitudinal mode of the mass limited only by capacitive damping is, from eqs. (B.6) and (B.7)

$$Q_{cap} = \frac{m \omega_o x_o^4}{2 \varepsilon_o^2 S^2 V^2 R} \tag{B.8}$$

B.3 Conclusion

The highest Q measurement made by the author was for the fundamental longitudinal mode of the four inch diameter columnar silicon mass. This was measured to have a Q of 4.8×10^6 using a capacitive drive. For this measurement

$m = 1.39$ kg,

$\omega_o = 2\pi \times 47.4$ kHz,

$x_o = 5$ mm,

$S = 7 \times 10^{-3}$ m^2.

$\varepsilon_o = 8.854 \times 10^{-12}$ C^2 N^{-1} m^{-2},

$R = 33$ kΩ,

$V = 250$ V and

From eq. (B.8) with the above values, it is predicted that the Q of the columnar silicon mass limited only by capacitive damping would be approximately 2×10^{13}. This is many orders of magnitude greater than the value measured experimentally and thus it is concluded that capacitive damping is not a limitation to any of the measurements presented in this thesis.

Appendix C

Diagrams of Circuits used in Q Measurements

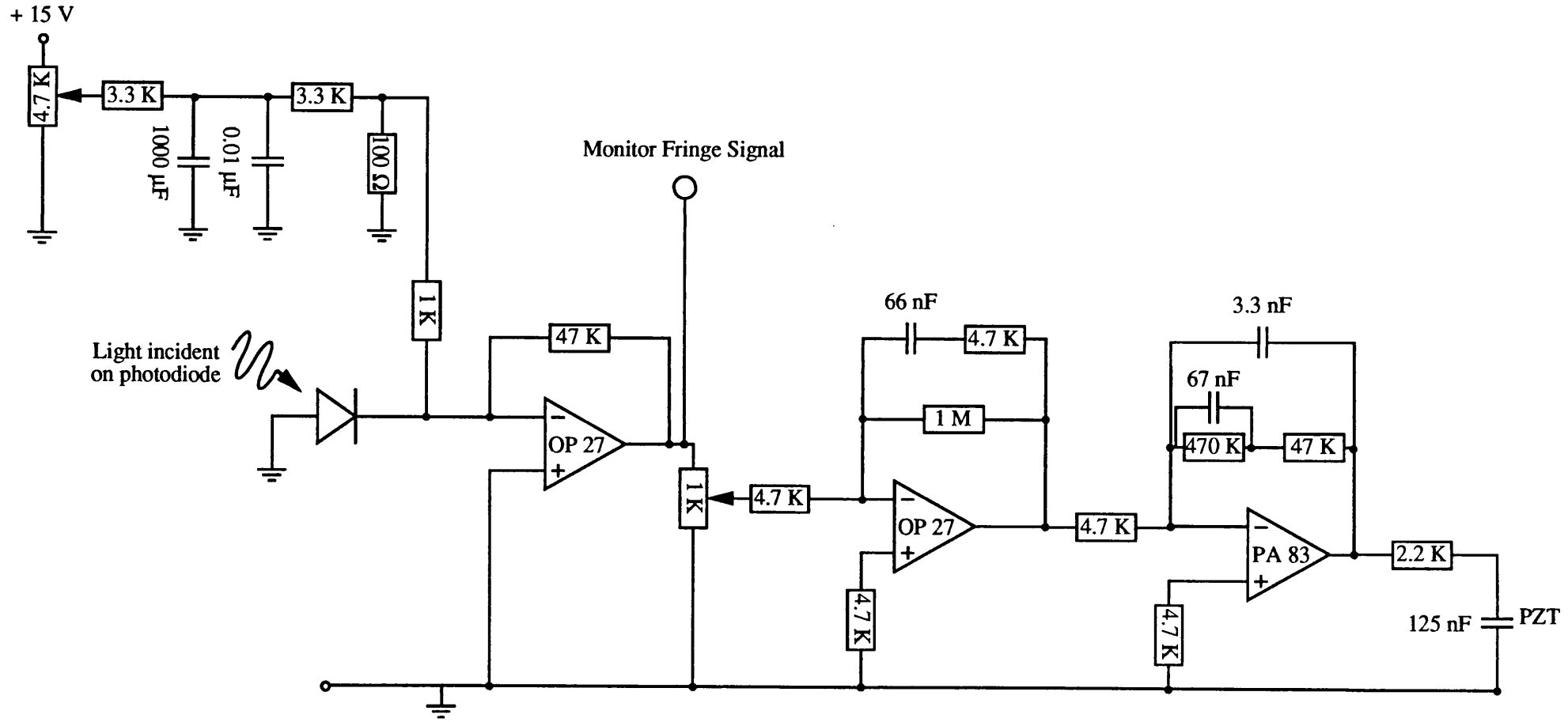

Figure C.1: The Circuit for the PZT Feedback Loop

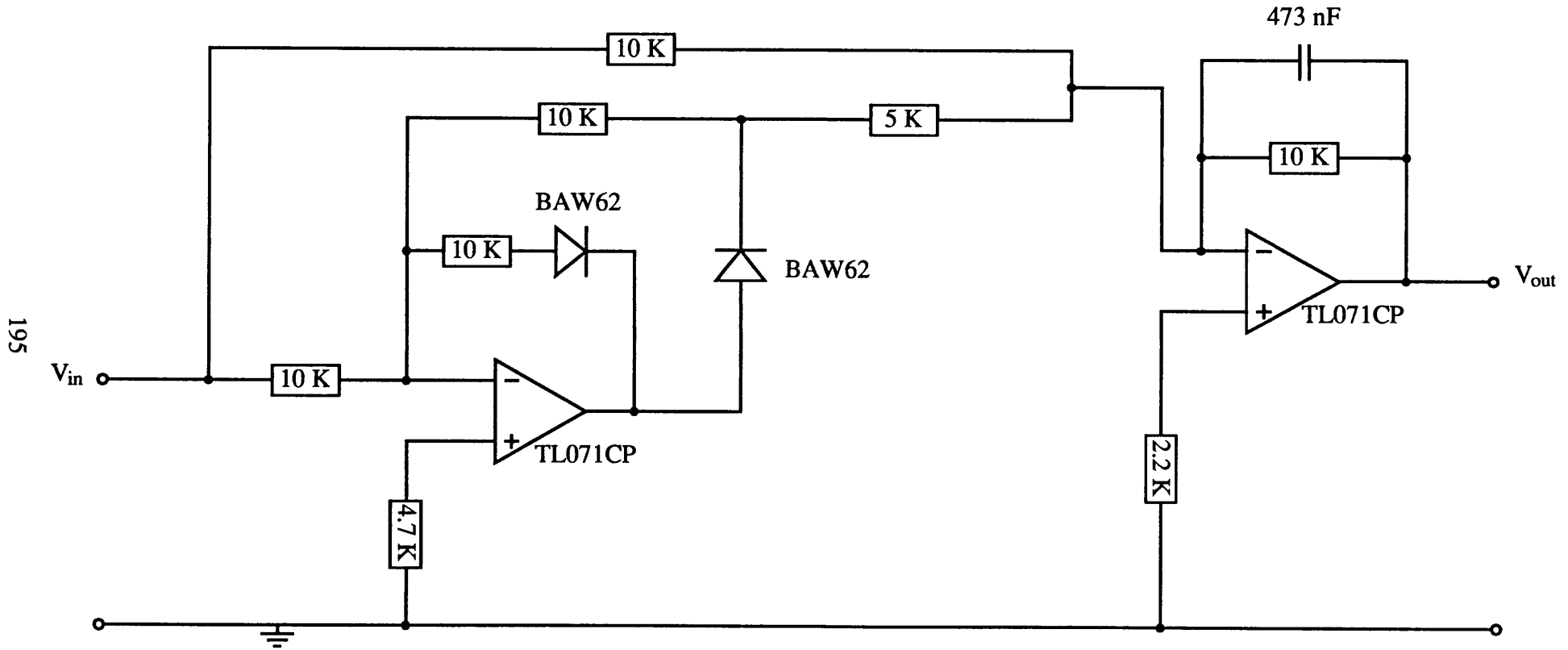

Figure C.2: Circuit Diagram for the Active Rectifier Used when Taking Decay Traces.

Appendix D

An Investigation of Coupled Resonances in Materials Suitable for Test Masses in Gravitational Wave Detectors

Physics Letters A 161 (1991) 101–110
North-Holland

PHYSICS LETTERS A

An investigation of coupled resonances in materials suitable for test masses in gravitational wave detectors

J.E. Logan, N.A. Robertson, J. Hough and P.J. Veitch
Department of Physics and Astronomy, University of Glasgow, Glasgow G12 8QQ, Scotland, UK

Received 8 October 1991; accepted for publication 18 October 1991
Communicated by J.P. Vigier

We report our findings concerning mode coupling, observed during quality factor measurements, in a sample of columnar polycrystalline silicon. This coupling and that produced by an external agent in a sample of aluminium have been investigated using a vibration pattern imager. The coupling in the aluminium has been modelled using an equivalent circuit.

1. Introduction

As part of our work in developing a gravitational wave detector using laser interferometry between free test masses [1] we have been investigated the quality factor of and coupling between internal resonances of certain materials which might be used for the masses. The test masses in such detectors are required to satisfy various criteria. Since the masses act as mirrors in the interferometer, the material must be capable of being polished to a supersmooth finish (~ 1 Å rms roughness). The material should also have a high ratio of thermal conductivity to thermal expansion coefficient in order to minimise distortion effects due to high laser intensities [2]. Finally, to minimise thermal noise effects the test masses should in general have a very high quality factor (of order 10^6) for any internal resonances which could be sensed in the interferometer.

With these criteria in mind we have been investigating the quality factors (Q) of resonances of right circular cylinders of columnar polycrystalline silicon, a material which appears to satisfy the requirements listed above. In the course of developing the best measuring technique for Q values we have also tested a sample of aluminium with the same aspect ratio (aspect ratio = height/radius) as one of the silicon samples. We describe below some of the results of these investigations and in particular report our findings concerning mode coupling.

2. Quality factor measurements

In a gravitational wave detector the thermal noise contributed by the test masses depends on their mechanical losses. These losses are difficult to measure directly in very low loss materials at the operating frequencies of the detector, but an indication of their magnitude is given by the quality factors of the resonances of the samples studied. The modes which are most important in a detector are those in which there is a net movement of the parts of the face interrogated by the sensing beam. One of the chief modes of interest for these quality factor measurements is therefore the fundamental longitudinal mode.

2.1. Experimental technique

Fig. 1 shows our experimental arrangement for measuring the decay curves of oscillating cylinders. The material under test is suspended on a single loop of wire to minimise external damping. This is a possible form of suspension of the test masses in a gravitational wave detector. The test sample may be excited capacitively, as shown, or magnetically by gluing a magnet to the mass and using a driving coil. The

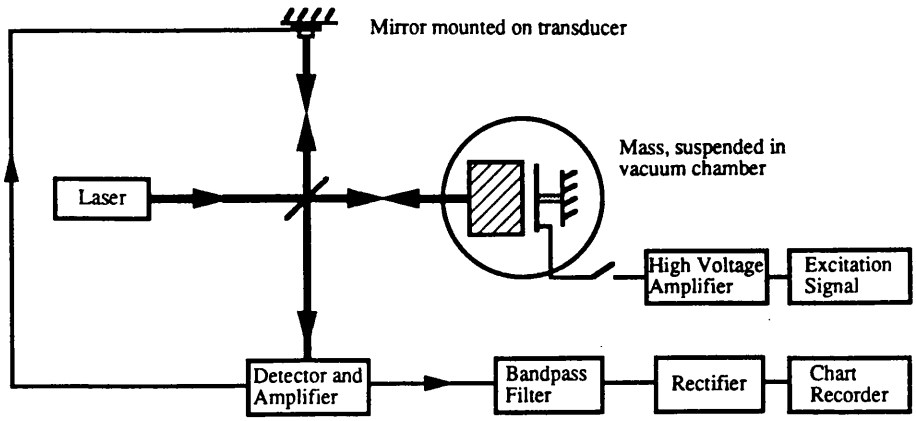

Fig. 1. Schematic diagram of the experimental arrangement for measuring the quality factor of materials. A capacitor plate is placed behind the mass to allow an excitation signal to be applied.

experiments are conducted in vacuum, typically $\sim 10^{-2}$ mbar, in order to reduce gas damping to a level where it does not degrade the Q. A Michelson interferometer forms the sensing system – one arm incorporating the test mass (which may be polished or have a small mirror attached to it) and the other arm a mirror mounted on a piezoelectric transducer. By feeding back a fraction of the signal from the interferometer to the transducer at frequencies up to 1 kHz, this mirror is made to follow the pendulum motion of the suspended mass and hence reduce the effect of this motion in the output signal.

A convenient method of determining the Q is by measuring the time, τ, it takes for the amplitude of the resonance to decay to e^{-1} of its original value and then calculating it from the relation

$$Q = \pi f_0 \tau ,$$

where f_0 is the resonant frequency of the mode of interest.

2.2. Aluminium

An aluminium circular cylinder, of alloy 6082, 3 inches long by 3 inches in diameter was suspended on a single loop of stainless steel wire 0.006 inches in diameter. To ensure well defined break-away points for the suspension wire two small aluminium lugs were glued onto the sides of the cylinder. A small mirror was also attached to the front face.

Excitation of the cylinder using a magnetic drive at frequencies close to that of the longitudinal mode revealed two resonances 70 Hz apart centered on 31 kHz instead of only the expected pure fundamental longitudinal mode. A typical response is shown in fig. 2. Investigation showed that

(1) removal of the lugs resulted in only one resonant frequency;

(2) gluing these lugs to a cylinder of the same alloy but slightly different aspect ratio resulted in only one resonance being observed;

(3) a bad glue joint between the lugs and the cylinder lowered the Q of only the lower resonance; this indicated that the glue joint was being stressed more by this resonance;

(4) decreasing the mass of the lugs resulted in the lower frequency resonance moving up to the frequency of the longitudinal mode as seen without lugs, f_0; while this took place the lower frequency resonance increased in both amplitude and Q and the higher frequency resonance stayed at the same frequency, $\sim f_0$, but decreased in amplitude.

With this knowledge and information about the resonant frequencies of different modes of vibration [3] we postulated that the lugs were coupling the fundamental longitudinal mode and the $n=2$ radial contour mode as shown in fig. 3. It should be noted that without coupling one would not expect to detect the radial contour mode using this measurement technique since the centre of the front face, the point under study, is a node.

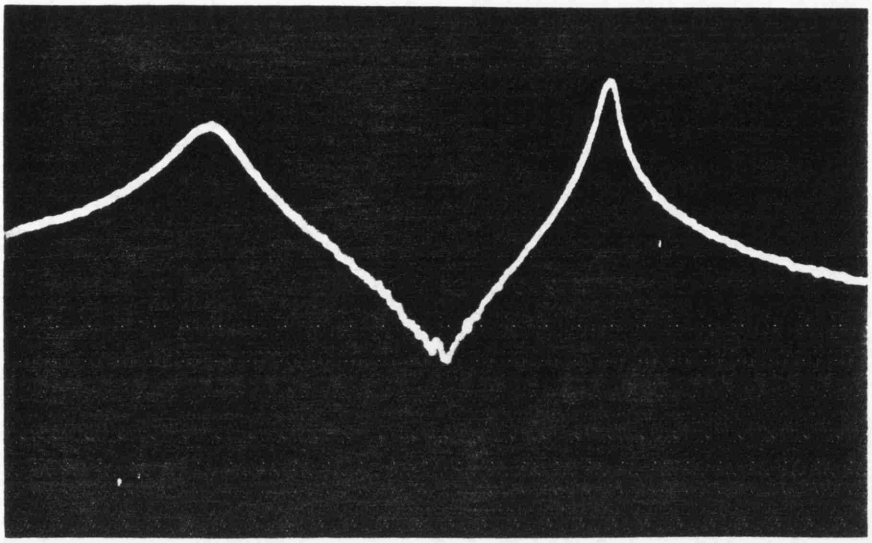

Fig. 2. Typical spectrum of the amplitude of motion of the central point of the front face versus frequency of excitation of the aluminium bar. The resonances occur at 31.10 and 31.20 kHz. Note that the y axis is a log scale.

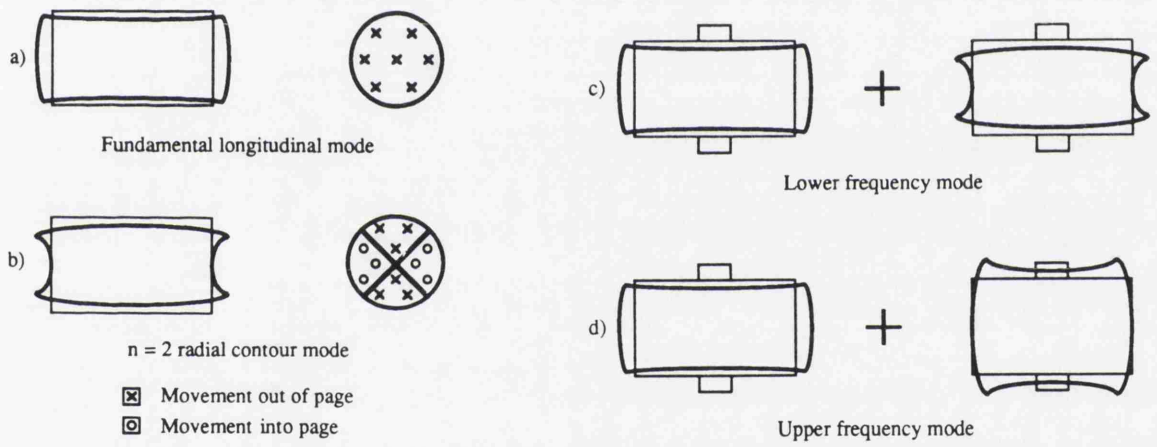

Fig. 3. (a), (b) Pure modes in aluminium. (c), (d) Coupled modes, as seen from above, formed by the addition of lugs on the sides of the bar as indicated.

2.3. Silicon

The Q values of two cylinders of columnar silicon were also measured. Columnar silicon consists of numerous columns of single crystal silicon. In the particular samples studied each of these columns was grown preferentially in the [111] direction but may deviate from this by up to 10°. The crystals are all approximately parallel with the axis of the cylinder.

The first cylinder was 3 inches long by 3 inches in diameter. It was suspended on a single loop of stainless steel wire 0.0035 inches in diameter. No lugs were attached to the cylinder. Measurements were made both with and without mirror and magnet. In all tests it was found that there were two resonances in place of the single longitudinal resonance which was expected. These were 40 Hz apart centered on 51 kHz. The Q for the higher frequency mode was

$(7.3\pm0.1)\times10^5$ and the Q for the lower frequency mode was $(4.3\pm0.1)\times10^5$. It was postulated that the modes involved were again as shown in figs. 3c and 3d.

The dimensions of the second cylinder were chosen to be 2.9 inches long by 4 inches in diameter since the work of McMahon [3] indicated that an aspect ratio of 1.45 seemed to leave a reasonable gap in frequency between the longitudinal resonance and the nearest modes on either side of it. It should be noted that McMahon's work was carried out for isotropic aluminium and steel and so any predictions drawn from it will not be exact for silicon which is anisotropic.

As predicted there was only one resonance at the fundamental longitudinal frequency at 48 kHz, with the nearest other resonance 5 kHz away. Using a magnetic drive the Q was found to be $Q=(3.6\pm0.1)\times10^6$. This value is considerably higher than those measured for the coupled modes. In the 3 inch cylinder the energy in the coupled modes is shared between the contributing pure modes and thus the Q values of the coupled system are degraded by that of the more lossy pure mode [4].

3. Investigations of coupled modes using a vibration pattern imager

3.1. Experimental technique

A commercial vibration pattern imager (VPI) manufactured by Ometron (VPI 9000) was used to investigate the mode structure of the aluminium and silicon cylinders. It is based on a Michelson interferometer in which a laser beam is reflected off the test structure and interfered with a reference laser beam. The resulting optical signal gives information on the velocity at a point on the structure, this being determined by a quadrature phase sensitive optical detection scheme [5]. The laser beam is repeatedly scanned across the surface of the test structure to produce an image of the velocity distribution which is processed and displayed by computer.

The cylinder to be studied was suspended as a pendulum in air, and the front face was scanned by the VPI while the excitation was provided via the rear face. To ensure that we were accurately on resonance our original Michelson interferometer was set up to sense the motion of the rear face of the mass.

3.2. Aluminium

Fig. 4a shows the Ometron picture of the aluminium mass resonating in the pure fundamental longitudinal mode at 31.24 kHz. The form of this is as expected with the centre undergoing more motion than the edges.

Figs. 4b and 4c show the coupled modes which resulted when lugs 10 mm long by 8 mm in diameter were attached to the sides of the mass. Fig. 4b shows the lower frequency mode (mode 1) at 31.12 kHz and fig. 4c the upper frequency mode (mode 2) at 31.24 kHz. Mode 1 shows obvious characteristics of the radial contour mode. Since backward moving quarters are still evident it is clear that this mode is composed mainly of the radial contour mode with a lesser amount of longitudinal motion adding in the phase shown in fig. 3c.

What is taking place in mode 2 is not immediately clear. Based on our earlier deduction that this mode is formed by the radial contour mode adding to the longitudinal mode in the phase shown in fig. 3d, we attempted to reconstruct the pattern in fig. 4c using the velocity information which this picture contains. This was done using the fact that the centre of the pure radial contour mode is a node and thus all the movement at the centre of fig. 4c is due to the longitudinal mode. The velocity at the top and bottom of the VPI picture must then be due to the quarters of the radial contour mode adding in phase with the longitudinal mode whereas the velocity at the left- and right-hand sides are from the radial contour quarters adding in the opposite phase to the longitudinal mode. This gave enough information to draw an approximate map of the velocities of each of these two modes. These maps were then superimposed giving the result shown in fig. 4d which is very similar to fig. 4c. Thus it was deduced that this mode is composed mainly of the longitudinal mode with a small amount of the radial contour mode.

It is instructive to consider how the lugs couple the two pure modes together. To gain some understanding of this, coupling in electrical circuits was studied to see if an analogue to the mass system could be found. Note that in such modelling inductance is

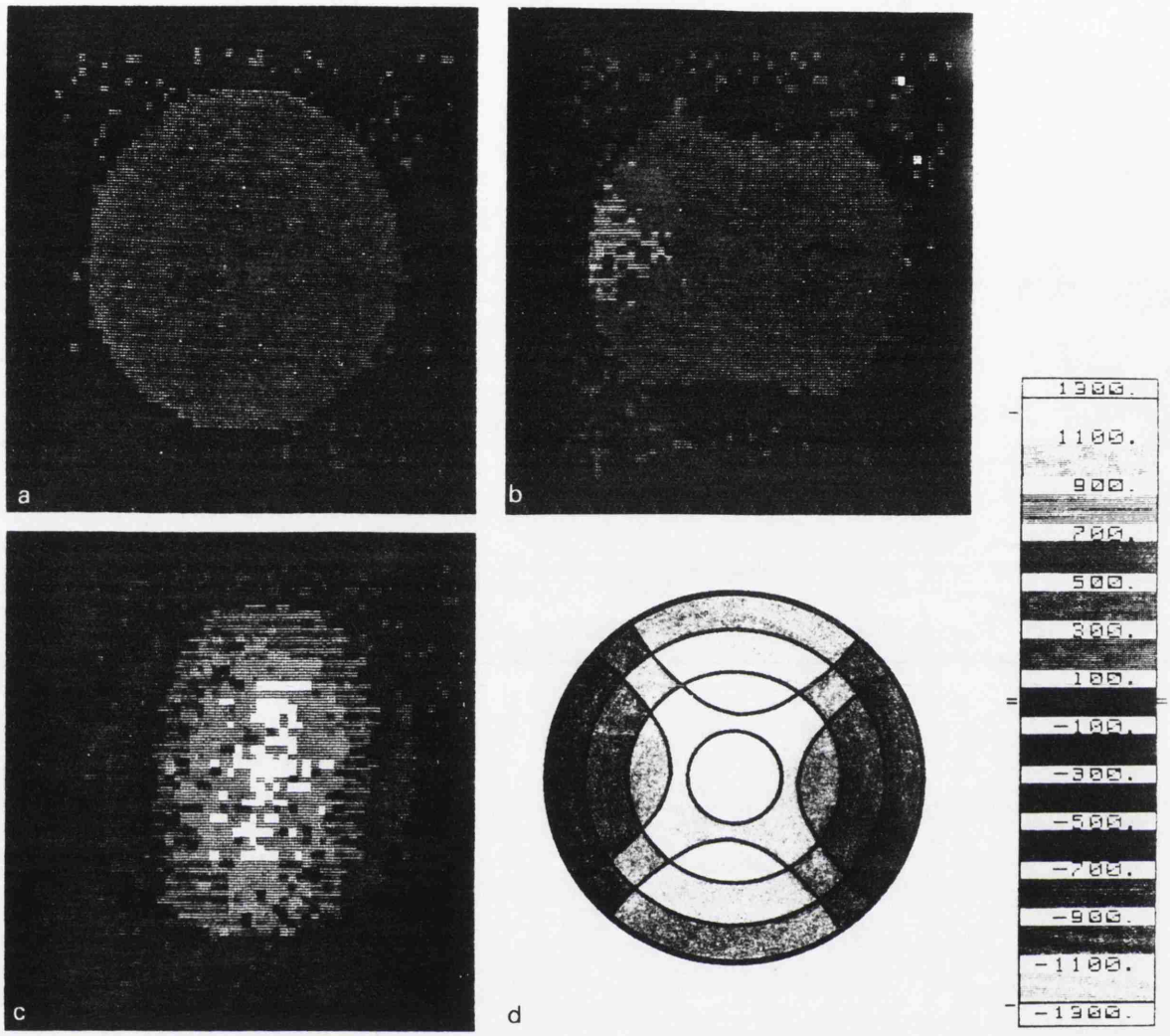

Fig. 4. Image of the front face of the aluminium cylinder resonating in (a) its fundamental longitudinal mode (31.24 kHz), (b) its coupled lower frequency mode (31.12 kHz), (c) its coupled upper frequency mode (31.24 kHz). Scale shows arbitrary units. (d) Reconstruction of the coupled upper frequency mode. When the resolution of the imager is taken into consideration, this velocity map shows a picture very similar to that of (c).

equivalent to mass, capacitance is equivalent to compliance, resistance is equivalent to a damping coefficient and current is equivalent to velocity.

(a) *Equivalent circuit – simple inductive coupling.* Fig. 5 shows the first circuit that was considered. Algebraic analysis of this circuit with no damping present and with the resonant frequencies of the primary and secondary circuits chosen to be equal, f_0, gave the two resonant frequencies of the coupled circuit to be

$$f_1 = \frac{f_0}{\sqrt{1+4\pi^2 f_0^2 L_c (C_p + C_s)}} \quad \text{and} \quad f_2 = f_0 ,$$

where

$$f_0 = \frac{1}{2\pi\sqrt{L_p C_p}} = \frac{1}{2\pi\sqrt{L_s C_s}} .$$

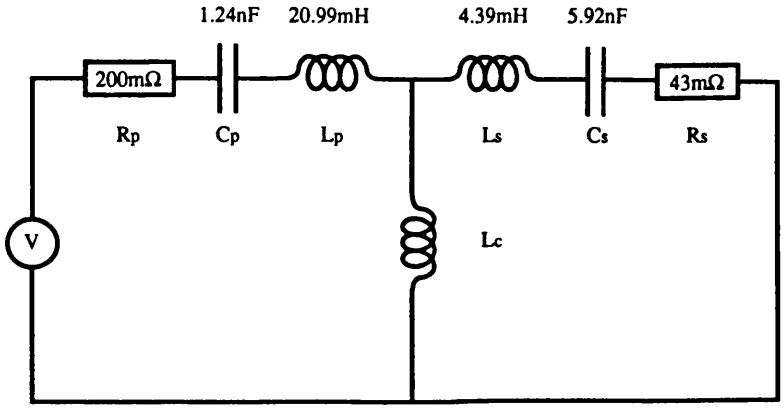

Fig. 5. Circuit with simple inductive coupling. L_c was varied from 6.2 to 63 μH to fit the whole curve shown in fig. 6.

As the coupling decreases the lower resonance, f_1, increases in frequency towards f_0 whilst the upper resonance remains at f_0. Hence the general behaviour of the circuit agrees with the observations of the coupled mode frequencies in the aluminium, as described in section 2.2.

For the lower frequency resonance, f_1, the currents in the primary and secondary circuits are in the ratio of C_p to C_s and are 180° out of phase with each other. For the upper resonant frequency, f_2, these currents are equal and in phase and therefore the net current through L_c is zero. Thus the model is consistent with the predicted phases of the coupled modes shown in figs. 3c and 3d. The physical interpretation of zero current through the coupling inductor, L_c, in the upper frequency mode is that the lugs remain stationary. In order to satisfy this condition the contribution to the radial movement of the lugs from each of the pure modes must be equal and opposite. This agrees with the observation that a bad glue joint does not affect the Q of the upper mode.

Suitable values for the components in the circuit must be chosen to fit the available experimental data. When there are no lugs attached to the mass the only mode excited is the longitudinal resonance. This situation corresponds to L_c being replaced by a wire, i.e. shorting out the secondary circuit, and thus the frequency of the primary circuit must be determined by the frequency of the longitudinal mode. The current in the primary circuit is therefore equivalent to the velocity of the longitudinal mode, v_L. Since the cylinder is a distributed rather than a discrete system, a constant of proportionality, α, is introduced such that

$$v_L = \alpha i_p .$$

Similarly the velocity of the radial contour mode, v_R, for the same point is given by

$$v_R = \beta i_s .$$

Thus

$$\frac{v_R}{v_L} = \frac{\alpha i_s}{\beta i_p} = \gamma \frac{i_s}{i_p} ,$$

where γ is a constant given by the ratio of α to β.

For the upper resonance, f_2, the ratio of the currents is 1 and hence

$$\frac{v_R}{v_L} = \gamma .$$

Average values for v_R and v_L were obtained from the VPI picture for f_2 yielding a value of $\gamma = 9$. This then allowed calculation of the ratio of the capacitor values in the primary and secondary circuits since for the lower resonance

$$\frac{v_R}{v_L} = \gamma \frac{i_s}{i_p} = \gamma \frac{C_s}{C_p} .$$

Average values of v_R and v_L were found from the VPI picture for f_1. This gave

$$C_s = 5C_p .$$

(Note that this result can be obtained using either peak or average velocities since the introduction of α and β allowed for either interpretation.)

Using this information and the fact that the Q in air for the aluminium cylinder was $\sim 2\times 10^4$ the values for circuit components were chosen to be those shown in fig. 5. It was found that in order to obtain resonance curves which closely resembled the experimental spectra in shape, it was necessary to make the frequency of the secondary circuit slightly higher (~ 20 Hz) than that of the primary.

The circuit was analysed using a computer package, "Matlab" (The Maths Work Inc.). It was found that with a frequency split between the two resonances matching that in the VPI data (110 Hz) the coupling strength of the circuit was

$$k_{\text{elec}} = \frac{L_c}{\sqrt{L_p L_s}} = 3.0\times 10^{-3},$$

which compared favourably with the coupling strength

$$k_{\text{mass}} = \frac{\text{mass of lugs}}{\text{mass of bar}} = 2.6\times 10^{-3}.$$

Having established the model using information from the VPI image, the circuit was tested further using results from frequency spectra obtained for three sets of lugs of the same length but differing radii. These spectra gave information on the frequency separations of the two modes and their relative heights. Fig. 6 shows a comparison of these data and the behaviour of the electrical circuit. It is evident that for low coupling values (i.e. a small frequency separation between the resonances) this electrical model does not match the response of the mass system well. The fit is better, however, for larger coupling.

(b) *Equivalent circuit – modification of the simple inductive model.* Several other models were also investigated. Fig. 7 shows the circuit which most closely modelled the experimental data, and is in fact an extension of the first model. The values of L_p, C_p, L_s and C_s are approximately the same as in the first model, and the effect of the lugs is modelled using three small inductors, L_1, L_2 and L_3. The inductors L_1 and L_2 allow the resonant frequencies of the primary and secondary circuits to change with respect to each other as the mass of the lug is varied. The values of the three inductors were required to be pro-

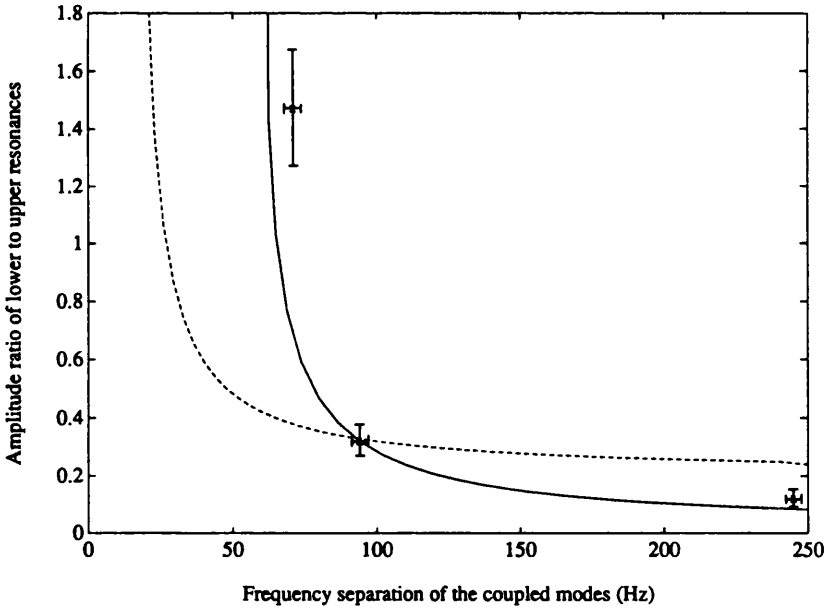

Fig. 6. Comparison of the predictions of equivalent circuits with experimental data. The dashed line shows the behaviour of the simple circuit, the solid line the behaviour of the modified simple circuit. The crosses indicate the experimental points.

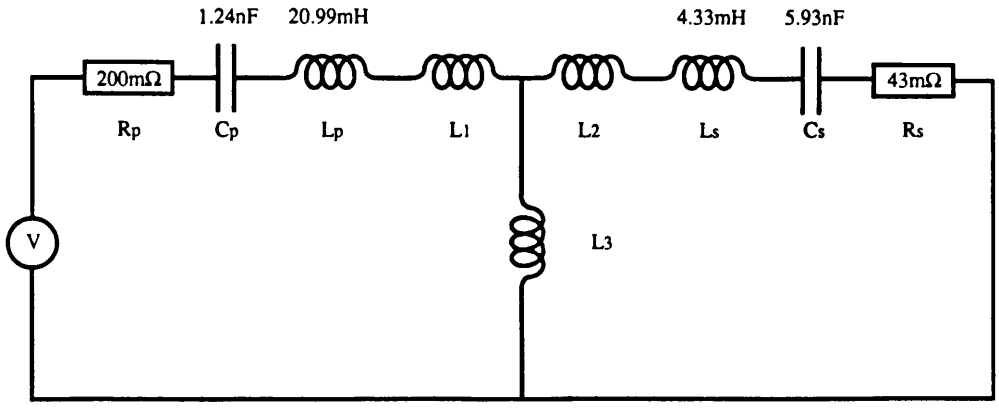

Fig. 7. Modification of simple inductive model. L_3 was varied from 18.3 to 42 μH whilst L_1 was varied from 11.0 to 25 μH and L_2 from 38.4 to 88 μH to fit the whole curve shown in fig. 6.

portional to the mass of the lugs, thus movement from one experimental point to another in fig. 6 required L_1, L_2 and L_3 to be scaled together by the same amount. The relation

$$\frac{L_3}{\sqrt{L_p L_s}} \approx \frac{\text{mass of lugs}}{\text{mass of bar}}$$

allows the value of L_3 to be chosen for a given set of lugs. L_1 and L_2 must then be chosen to allow the model to account for the frequencies of the resonances and the ratios of the resonance heights.

Fig. 6 shows a plot of this circuit's behaviour and the experimental points. It was found that the behaviour of this model gave a very good fit to the experimental data. This implies that the coupling of the modes was predominantly due to the mass of the lugs rather than, for example, their compliance. The quantity L_1+L_3 represents the effective mass of the lugs acting on the longitudinal mode, and L_2+L_3 that acting on the radial contour mode. It was found that in order to fit the experimental results L_2+L_3 had to be approximately twice as large as L_1+L_3 implying that the lugs have a higher effective mass for the radial contour mode than the longitudinal mode.

(c) *Deductions from the equivalent circuit concerning thermal noise.* A consequence of having inductive coupling is that, at frequencies well below the resonances, the coupling decreases with decreasing frequency. At such frequencies, voltage generators placed on each side of the coupled circuit do not significantly affect the other side, since the impedance of L_3 is small. Thermal noise driving forces can be represented by such voltage generators and hence the thermal noise in each side of the coupled circuit at low frequency is essentially independent of that in the other side. Thus from this analogy we can deduce that for the loaded aluminium cylinder, the thermal noise at low frequency due to the fundamental longitudinal mode is essentially unaffected by damping of the mode's apparent Q due to coupling to the radial contour mode.

3.3. Silicon

Figs. 8a and 8b show the mode patterns for the lower and upper resonances, 52.27 and 52.44 kHz respectively, of the silicon mass with aspect ratio 2. The similarity to the patterns seen in aluminium is immediately obvious; however in this case there is no external coupling agent such as lugs, and thus the equivalent circuit need not be the same. We believe that the coupling in this case may be due to the misalignment of the individual crystals in the columnar silicon together with the natural anisotropy of silicon, and that the model may involve a common compliance.

To verify that the coupling was produced by internal anisotropy, the cylinder was rotated about its axis in order to observe the effect on the mode patterns. It was indeed found that the patterns rotated in the same direction and by the same angle as the mass. It must, however, be noted that the mass had

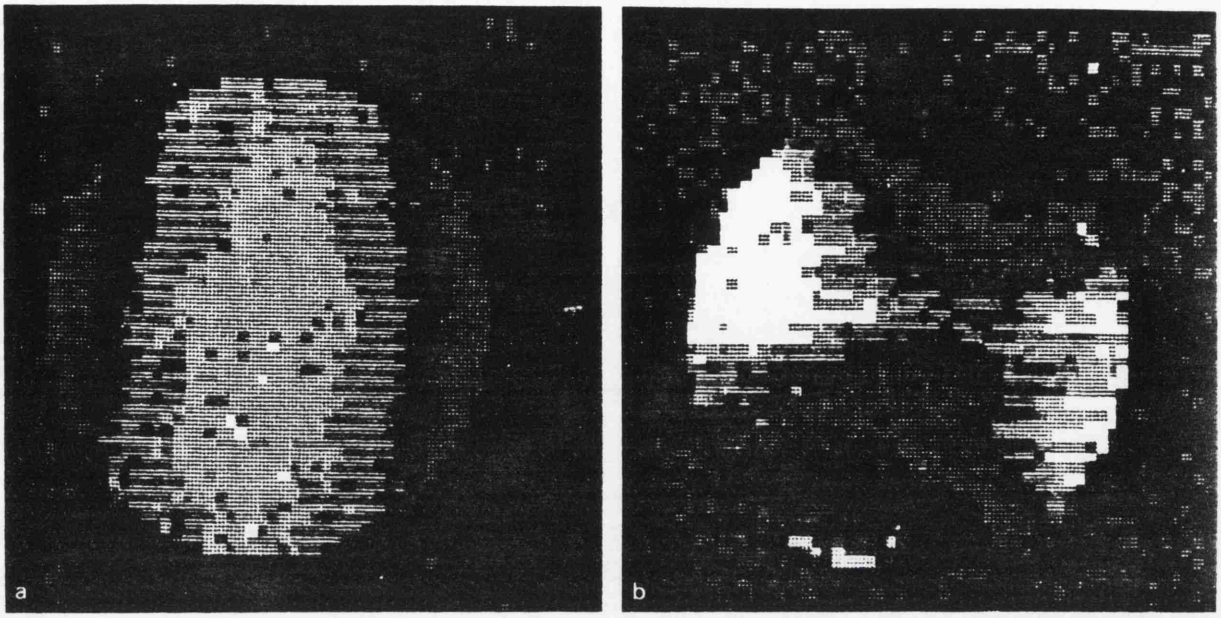

Fig. 8. Image of the front face of the 3 inch diameter silicon cylinder resonating in (a) its coupled lower frequency mode (52.27 kHz) and (b) its coupled upper frequency mode (52.44 kHz). Scale as for fig. 4. Note that the frequency spacing between the resonances is larger than the 40 Hz split mentioned in section 2.3. This is due to the loading of an extra magnet which was added to provide the necessary level of excitation to allow the VPI to detect the cylinder's motion.

sustained a small amount of surface damage at an earlier time. The coupled modes were observed before this occurred and hence the damage is not responsible for producing the coupled system, but it may determine where the nodes lie.

The second silicon mass of aspect ratio 1.45 was also studied using the VPI. It was observed that the longitudinal resonance, at 47.77 kHz, was indeed a pure mode as expected, as were the modes which occurred ~ 5 kHz on either side of it. It was also noted that the anisotropic nature of the mass did not obviously distort the mode patterns from the shapes that would be predicted for an isotropic cylinder.

4. Conclusion

Coupled mode systems have been studied in both aluminium and columnar silicon cylinders using a vibration pattern imager. With the aid of this and electrical models it has been possible to gain some understanding of how, in the aluminium, lugs coupled the two normal modes under consideration. In the columnar silicon of the same aspect ratio it was found that these resonances coupled naturally due the anisotropic nature of the material.

The aspect ratio for the test masses to be used in a gravitational wave detector must be carefully chosen. For the samples examined the presence of two coupled resonances did lead to a reduction of the Q. In the case of the aluminium this coupling would not be expected to increase the observed thermal noise at lower frequency. However this is due to the particular coupling mechanism for our aluminium sample and need not be true for coupling mechanisms in samples of other materials in which coupling is produced by compliance rather than mass. Thus as a general guideline it is best to avoid having resonances lying very close to each other.

Acknowledgement

We would like to thank the Science and Engi-

neering Research Council who made the Ometron VPI 9000 available through their Engineering Board Instrument Loan Pool. We are indebted to John Brandon of the University of Wales College of Cardiff for making available laboratory facilities and technical support, and for assisting us in the operation of the VPI. We are grateful to Bernard Schutz, also of the University of Wales College of Cardiff, for useful discussions. We wish to thank our colleagues in the Gravitational Waves Group for their interest in this work which was supported by an SERC research grant and the University of Glasgow. J.E.L. is in receipt of a SERC studentship.

References

[1] J. Hough, B.J. Meers, G.P. Newton, N.A. Robertson, H. Ward, B.F. Schutz, I.F. Corbett and R.W.P. Drever, Vistas Astron. 30 (1987) 109;
J. Hough, H. Walther, B.F. Schutz, J. Ehlers, H. Welling, I.F. Corbett and V. Kose, Proposal for a joint German–British interferometric gravitational wave detector, Max-Planck-Institut für Quantenoptik/University of Glasgow Report, MPQ 147 GWD/137/JH(89).
[2] W. Winkler, K. Danzmann, T.M. Niebauer, A. Rudiger and R. Schilling, Phys. Rev. A (1991), to be published.
[3] G.W. McMahon, J. Acoust. Soc. Am. 36 (1964) 85.
[4] V.B. Braginsky, V.P. Mitrovanov and V.I. Panov, Systems with small dissipation (University of Chicago Press, Chicago, 1985).
[5] Spate/VPI 9000 Series Operator's Manual, Ometron Limited, London.

Appendix E

An Investigation of Limitations to Quality Factor Measurements of Suspended Masses due to Resonances in the Suspension Wires

Physics Letters A 170 (1992) 352–358
North-Holland

PHYSICS LETTERS A

An investigation of limitations to quality factor measurements of suspended masses due to resonances in the suspension wires

J.E. Logan, N.A. Robertson and J. Hough
Department of Physics and Astronomy, University of Glasgow, Glasgow G12 8QQ, Scotland, UK

Received 24 August 1992; accepted for publication 10 September 1992
Communicated by J.P. Vigier

We report our experimental findings of the variation of measured quality factor with suspension length for a suspended sample of columnar silicon. These observations have been modelled using an equivalent circuit which has allowed predictions to be made concerning the levels of thermal motion associated with the internal modes of the mass.

1. Introduction

As part of our work in developing a gravitational wave detector using laser interferometry between free test masses [1] we have been investigating the quality factor, Q, of columnar polycrystalline silicon, a possible test mass material.

There are various constraints placed on the choice of material to be used for the test masses which incorporate the mirrors for the interferometer. The material should:

(a) have high thermal conductivity and low thermal expansion in order to minimise distortion when high light power is incident upon it [2];

(b) have the ability to be polished to make ultra-high quality, low loss mirrors with surface roughness ~ 1 Å rms;

(c) have a high Q (of order 10^6) for any internal resonances which could be sensed by the interferometer. The dimensions of the test mass should be chosen such that the lowest resonant frequency is well above the frequency band of interest for the detection of gravitational waves (~ 100 Hz to a few kHz). With high Q's, resonances are narrow and so less thermal noise appears in the detector bandwidth;

(d) be such that it is possible to manufacture/grow suitable sized samples (~ 0.5 m diameter, ~ 0.25 m thick) to form mirrors for a long base-line interferometer.

Columnar silicon may satisfy the above criteria. It is a material which consists of numerous columns of single crystal silicon. In the particular sample studied each of these columns was grown preferentially in the [111] direction but may deviate from this by up to 10°. The crystals are all approximately parallel to the axis of the cylinder.

In the course of investigating the Q value of a suspended sample of this material, it was observed that the measured Q varied, apparently randomly by a factor of ~ 30, when the mass was rehung and this was thought to be due to resonances in the suspension wires. Similar effects have been observed elsewhere [3,4]. We describe below the results of our systematic investigations of the hypothesis that measured Q is a function of suspension length. We also make predictions concerning the effect of the suspension wires on thermal motion associated with the internal modes of the test masses at frequencies of interest for the detection of gravitational waves.

2. Experimental technique

The columnar silicon sample under study was a right circular cylinder, 4 inches in diameter by 2.9 inches long. It was suspended, in vacuum, on a single loop of stainless steel wire 0.006 inches in diameter. The sample could be excited in one of two ways,

either magnetically, using a small magnet glued onto the sample, or capacitively. The capacitive drive was achieved using the capacitance between a plate and its image formed in the dielectric bulk of the silicon. The motion of the mass was sensed using laser interferometry which allowed the decay time for the mode under study to be measured and hence its Q value to be calculated [5]. In this set of measurements the mode under study was fundamental longitudinal mode which occurred at 48 kHz.

Figure 1 shows the experimental method for changing the length of the suspension loop. A hook was attached to the wire, placed centrally between the suspension points at the supporting plate. This hook was attached via a cord to the shaft of a small electric motor so that when the shaft turned, the cord wound round it thereby pulling the hook and suspension loop up. A point was also attached to the shaft so that the angle which the shaft was turned could be measured on a scale mounted on the motor. This allowed the suspension loop to be shortened by a known amount and the Q at that length could be measured.

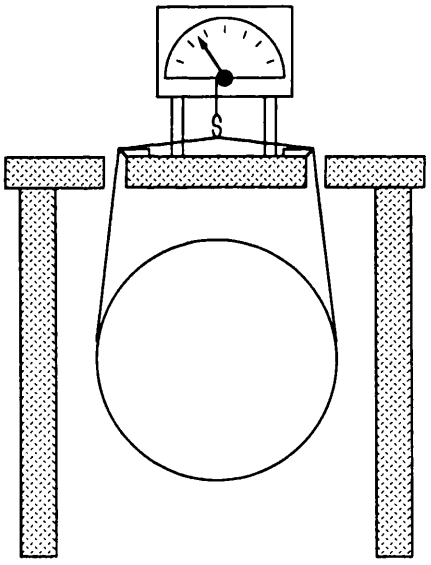

Fig. 1. Experimental arrangement for changing the length of the suspension loop. The mass is suspended on a single loop of wire from a supporting plate with the suspension wires, at the top, being constrained in grooves and breaking away over sharp edges. The length of the suspension wire between the break-away points at the supporting plate and the mass is 0.15 m. The speed of sound in the wire is 280 m s^{-1} and the linear density of the wire is 1.44×10^{-4} kg m^{-1}.

3. Experimental results

Figure 2 shows the variation of Q as function of change in suspension length. It is evident that the Q drops sharply at several points leading to a variation in the measured Q of a factor of ~ 30 with a change in suspension length of only ~ 1.5 mm. The single loop suspension for the mass can be viewed as two separate wires between the break-away points at the mass and those at the supporting plate. If the suspension loop is exactly round the centre of the mass, the wires will be driven radially by the motion of the longitudinal mode. At certain lengths these wires will become resonant and energy from the mass will be transferred to the wires and dissipated, leading to a corresponding drop in the quality factor of the mass. From the results shown in fig. 2 it is evident that there are two sharp dips in the Q in one cycle of the pattern. We believe that the two wires were not exactly the same length, the lengths differing by 0.45 mm, leading to two dips being observed. In the second cycle of the variation it should be noted that there are in fact three dips present. We believe that this may be due to either the mass shifting position slightly in the suspension loop or the wires settling in a slightly different way at the break-away points of the support plate, causing the apparent length of the wires to change and one of them to become resonant again.

It was found that when a magnetic drive was used the maximum Q value in such a series of measurements was not constant but varied by a factor of ~ 1.5. The highest Q value ever measured using a magnetic drive was $(3.6\pm0.1)\times10^6$. To test whether the Q might be limited by the magnet glued to the mass the magnet/coil drive was replaced by a capacitive drive. A variation in Q similar to that in fig. 2 was observed and again some variation was found in the maximum measured Q, with the highest value once more being $(3.6\pm0.1)\times10^6$. From these results there was no indication that the capacitive drive was better than the magnetic drive. It was evident however that some factor, other than variation of suspension length, was affecting the measured Q and

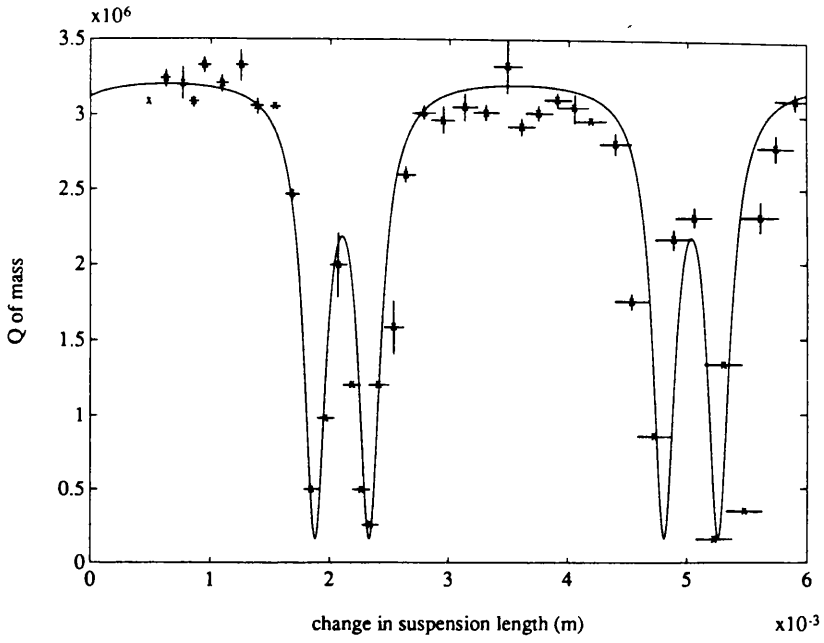

Fig. 2. The variation of Q with changing suspension length. The crosses indicate experimental points. The solid line shows the behaviour of the equivalent circuit. It should be noted that there are in fact three minima in the second cycle of the pattern of the experimental data.

this was thought to be the exact positioning of the break-away points at the mass. If the wires were positioned exactly half-way along the length of the mass they would only be driven radially by the movement of the mass resonating in the fundamental longitudinal mode. If, however, the wires were slightly offset from the centre, the presence of friction ensures they would also be driven longitudinally. This could lead to greater loss of energy from the mass.

In order to investigate this idea a thin layer of grease was applied between the wire and the mass at the break-away points in order to decrease the coupling between them [3]. Again a similar variation in Q to that shown in fig. 2 was observed but this time the minimum Q observed was $(0.61\pm0.01)\times10^6$, compared to $(0.16\pm0.01)\times10^6$ shown on fig. 2, and the maximum Q, $(4.8\pm0.1)\times10^6$, compared to $(3.3\pm0.1)\times10^6$. We believe that the increase in the minimum Q value is due to a smaller fraction of the mass's energy being transferred to the wire when the wire is on resonance, and that the increase in the maximum Q value is due to a decrease in friction effects at the break-away points.

4. Electrical analogue

In order to gain more understanding of the system and to be able to predict the effect of the observed variation in Q on thermal noise levels at lower frequencies, an electrical analogue to the system was developed. Recall that in such modelling, inductance is equivalent to mass, capacitance is equivalent to compliance, resistance is equivalent to a damping coefficient, current is equivalent to velocity and charge is equivalent to displacement.

The suspension wires were modelled as transmission lines which were open-circuit at their far ends to represent a supporting plate of infinite impedance, and the mass was modelled as a series resonant circuit. Figure 3 shows the circuit whose behaviour closely matched the experimental results. Note that the electrical model used has the inputs to the transmission lines in series with the LCR circuit so that the same current passes through all the components. This model was chosen since it represents the situation when the wires are driven by the same displacements and hence same velocities as the sides of the mass.

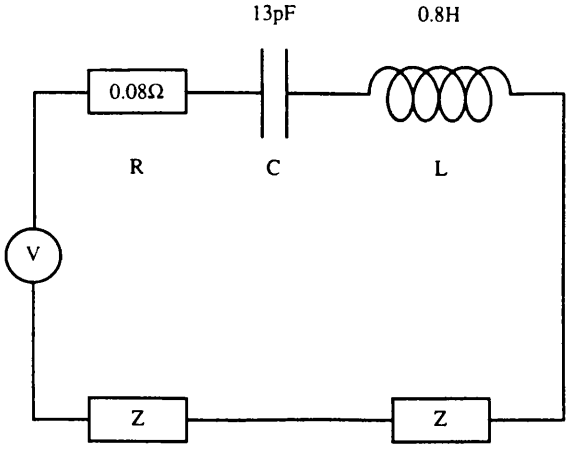

Fig. 3. The equivalent circuit to the mass with suspension wires. Z represents a transmission line. The values shown for L, C and R correspond to the transmission lines having $Q_w = 3 \times 10^3$.

The input impedance, Z, to a lossy, open circuit, transmission line is given by [6]

$$Z = Z_0 \frac{\sinh(2\alpha l) - j \sin(2\beta l)}{\cosh(2\alpha l) - \cos(2\beta l)}, \quad (1)$$

where Z_0 is the characteristic impedance of the line, α is the loss per unit length in the line, l is the line length, $\beta = \omega/v$, ω is the angular frequency of the wave in the line and v is the velocity of propagation of the wave.

It can be shown that such a transmission line behaves like a series tuned circuit when $l = \frac{1}{4}(2n+1)\lambda$, $n \geqslant 0$, where λ is the wavelength in the line [6]. The line is then purely resistive with resistance

$$r_s = Z_0 \alpha l, \quad \alpha l \ll 1, \quad (2)$$

and quality factor

$$Q_w = \pi/\alpha\lambda. \quad (3)$$

When $l = n\lambda/2$, $n \geqslant 1$, the transmission line behaves like a parallel circuit of the form shown in fig. 4. The line has the same Q_w as above but resistance.

$$r_p = Z_0/\alpha l, \quad \alpha l \ll 1. \quad (4)$$

Thus for low losses in the wire $r_p \gg r_s$.

The fraction of energy stored in the transmission lines is very small compared to that stored in the main LCR circuit and thus the resonant frequency of the system is essentially unaffected by the presence of the transmission lines. Hence when both transmission lines have $l = \frac{1}{4}(2n+1)\lambda$, the whole circuit looks like a series resonant circuit with quality factor

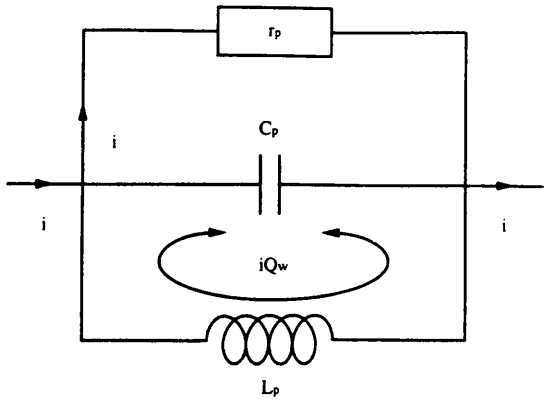

Fig. 4. Representation of a transmission line as a parallel circuit when the line's length is equal to an integral number of half-wavelengths.

$$Q_s = \frac{1}{2r_s + R}\sqrt{L/C}, \quad (5)$$

where R represents the damping in the mass, L represents the mass and C represents the compliance of the mass.

When both transmission lines have $l = n\lambda/2$ the circuit has quality factor

$$Q_p = \frac{1}{2r_p + R}\sqrt{L/C}. \quad (6)$$

When the suspension wires are not exactly the same length eqs. (5) and (6) must be modified. Because of the difference in length, the transmission lines do not resonate together. The highest and lowest Q values of the circuit occur when the sums of the real parts of the impedances of the two transmission lines are at a minimum, r_{min}, and maximum, r_{max}, respectively. r_{min} and r_{max} can be calculated using eq. (1). The term $2r_s$ is replaced by r_{min} in eq. (5) and $2r_p$ is replaced by r_{max} in eq. (6).

4.1. Choice of circuit parameters

An experimentally plausible value for Q_w was initially chosen and α was calculated using eq. (3). The characteristic impedance of a wire is defined to be

$Z_0 = vp$ [7] where ρ is the linear density of the wire. Z_0 was calculated for the suspension wire and this value together with the experimentally determined difference in suspension wire lengths was used to calculate r_{min} and r_{max}. From fig. 2, $Q_p = 0.16 \times 10^6$ and the average value of $Q_s = 3.2 \times 10^6$, and thus the ratio of eqs. (5) and (6), modified as described above for unequal line lengths, allowed calculation of R. This value combined with the resonant frequency of the mass which is represented in the circuit as

$$f_0 = 1/2\pi\sqrt{LC} \qquad (7)$$

allowed the values of L and C to be calculated. Thus all the parameters of the circuit were defined for a given Q_w which was varied in order to provide the best experimental fit.

4.2. Circuit analysis

The circuit was analysed using a computer package, "Matlab" [8]. Figure 2 shows the response of the circuit which closely matched the experimental data, the transmission lines having $Q_w = 3 \times 10^3$ and differing in length by 0.45 mm.

As stated above, when $l = \frac{1}{4}(2n+1)\lambda$ the transmission lines look like series circuits with low resistance. The same current, i, that flows round the main circuit passes through all elements of the series representations of the transmission lines. This enables us to understand what is happening between the mass and suspension wire. When $l = \frac{1}{4}(2n+1)\lambda$ the suspension wire is at an anti-nodal position at the mass, the other end being fixed at the supporting plate, and hence the wire moves easily with the mass and appears to have low impedance. Thus the maximum amplitude of motion of the wire is just that of the mass. Since the impedance of the wire is small there is little energy dissipated in it, and hence the Q of the mass is high.

The opposite case is when $l = n\lambda/2$ and the transmission line behaves like a parallel circuit with high resistance. As indicated in fig. 4 the current, i, which circulates round the rest of the main circuit only flows through the resistive part of the parallel circuit. The L_pC_p loop of the parallel circuit has a current a factor of Q_w higher than this flowing in it. It is thus possible to build up high velocity and hence amplitude on the wire, as indicated in the model by the current iQ_w, and so the wire is on resonance. When the suspension wire has $l \approx n\lambda/2$ the wire is close to a nodal position at the mass and the wire presents a high mechanical impedance to the mass. Thus for a given amplitude of motion, the mass transfers and dissipates much more energy in resonating the wire and the measured Q of the mass is low. Note that the power dissipated in the transmission line is $i^2 r_p$ which is proportional to Q_w for a given current i. Thus the greater Q_w is, the greater the power dissipated in the line and hence the lower the dip in the Q of the circuit.

Thus this electrical analogue provides an understandable model for the suspended mass and fits the experimental data well. It should be noted however that this is not the only possible model. One which could also be used would be to model the suspension wires as lossless with all losses occurring at the supporting plate. The electrical equivalent of this would be lossless transmission lines terminated by an impedance. We have found that such a circuit can also yield a good fit to the experimental data.

5. Thermal noise levels at lower frequency

Using the model discussed above it is possible to calculate the effect of thermal excitation on the displacements of the ends of the bar with respect to its centre of mass at lower frequencies. This allows determination of the possible effect, if any, of the observed variation in Q with suspension length on the level of this motion. It should be noted that when looking over a large frequency band the model outlined above is strictly valid only for situations where the internal damping force in the mass is proportional to velocity. This is due to the fact that the resistance, R, which represents the damping coefficient for the mass is taken to be frequency independent. However the model can be extended to other situations by letting R be a function of frequency.

Thermal displacement in the mechanical system is represented by the fluctuating charge on the capacitor in the circuit of fig. 3. Thermal noise forces are represented by a voltage generator for which it can be shown that [9]

$$\langle V_{th}^2 \rangle = 4k_B TR'\Delta f, \tag{8}$$

where k_B is Boltzmann's constant, T is the temperature, R' is the real part of the impedance in the circuit and Δf is the frequency bandwidth of interest.

Writing the impedance of a transmission line as $Z=r+jX$, $R'=R+2r$, assuming for simplicity that both lines are the same length, the fluctuating charge across the capacitor, q_c, can be shown to be of the form

$$\frac{\langle q_c^2 \rangle}{\Delta f} = 4k_B\sigma TC^2[s^4C^2\gamma^2+2s^3C^2\gamma\sigma + s^2C^2\sigma^2+2s^2C\gamma+2sC\sigma+1]^{-1} \tag{9}$$

where $\gamma=(L+2X/\omega)$, $\sigma=R+2r$ and $s=j\omega$. When $l=(2n+1)\lambda/4$ or $l=n\lambda/2$, Z is purely resistive and eq. (9) may be simplified to

$$\frac{\langle q_c^2 \rangle}{\Delta f} = 4k_B T(R+2r)C^2[s^4C^2L^2 + 2s^3C^2L(R+2r)+s^2C^2(R+2r)^2+2s^2CL + 2sC(R+2r)+1]^{-1} \tag{10}$$

For frequencies very much less than f_0, eq. (10) can be further simplified. When the suspension wire is exactly off resonance, i.e. $f=(2n+1)v/4l$,

$$\frac{\langle q_c^2 \rangle}{\Delta f} \approx 4k_B T(R+2r_s)C^2 . \tag{11}$$

When the wire is on resonance, i.e. $f=nv/2l$,

$$\frac{\langle q_c^2 \rangle}{\Delta f} \approx 4k_B T(R+2r_p)C^2 . \tag{12}$$

For realistic values of $\alpha \ll 1$, $r_s=Z_0\alpha l \ll R$. Hence when the frequency is such that the line is exactly off resonance from eq. (11)

$$\frac{\langle q_c^2 \rangle}{\Delta f} \approx 4k_B TRC^2 . \tag{13}$$

This is independent of the length of the transmission lines and is equal to the thermal noise of the mass alone.

Hence from this electrical analogy it can be seen that away from any resonances in the wires the thermal noise of the system remains essentially unchanged by the presence of the wires. This level of thermal motion remains unaltered, even if the suspension length is such that, at the resonant frequency of the mass, the wires are on resonance and the measured Q of the mass is low.

Using eqs. (3) and (4), r_p may be expressed as

$$r_p = Z_0 Q_w v/\pi f l \tag{14}$$

and so for high Q wires $r_p \gg R$. Thus when the frequency is such that the line is on resonance from (12)

$$\frac{\langle q_c^2 \rangle}{\Delta f} \approx 8k_B Tr_p C^2 = \frac{8k_B TC^2 Z_0 v Q_w}{\pi f l} . \tag{15}$$

We now consider three possible models for the lossy transmission lines which are assumed to be of fixed length, l. Which model is applicable to a given suspension wire will depend on the material chosen and the frequency band considered [10].

(a) Q_w proportional to f (i.e. $Q_w=3\times10^3\times f/(48$ kHz)). This is equivalent to α being frequency independent and implies that $\langle q_c^2 \rangle/\Delta f=$const. Since $r_p \gg R$, it is observed that the level given by eq. (15) is higher than that given by eq. (13). The exact form of the variation is shown in fig. 5, which is drawn for suspension wires 0.15 m in length leading to the first wire resonance occurring at 930 Hz. From this it can be seen that a spectrum of thermal noise spikes of constant height, due to the suspension wires resonating, is superimposed on the fundamental level of thermal noise from the mass.

(b) Q_w frequency independent (i.e. $Q_w=3\times10^3$). This is equivalent to α proportional to frequency and implies that $\langle q_c^2 \rangle/\Delta f \propto 1/f$. For this case, the spectrum of thermal noise spikes, which is superimposed on the fundamental level of thermal noise given by eq. (13), has peak heights which are inversely proportional to frequency leading to increased noise from these spikes at lower frequencies. $\langle q_c^2 \rangle/\Delta f$ is approximately 50 times greater than for (a) for the first resonance of the suspension wires.

(c) Q_w inversely proportional to frequency (i.e. $Q_w=3\times10^3\times(48$ kHz$)/f$). This is equivalent to α proportional to frequency squared and implies that $\langle q_c^2 \rangle/\Delta f \propto 1/f^2$. The spectrum of thermal noise spikes is higher than (a) or (b) and the heights of these peaks are inversely proportional to frequency squared. $\langle q_c^2 \rangle/\Delta f$ is approximately 2600 times greater than for (a) for the suspension wire resonance.

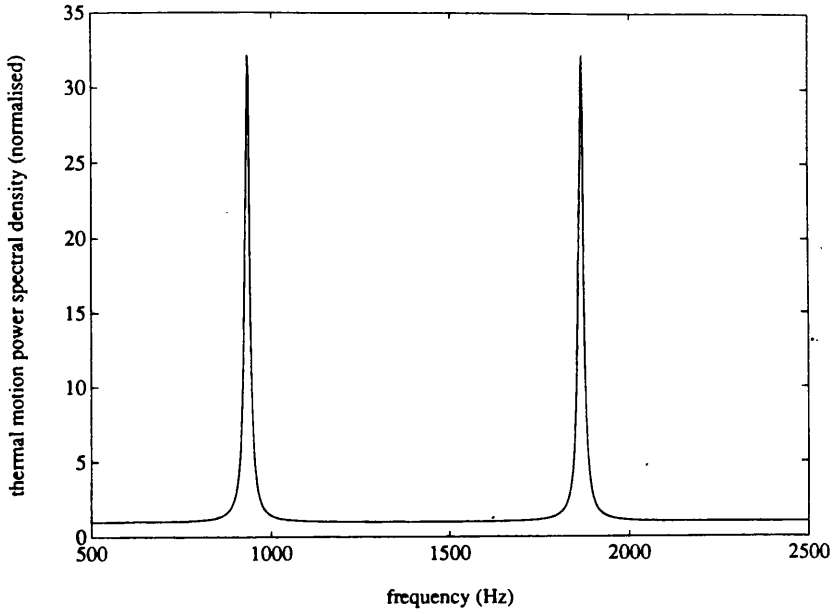

Fig. 5. The form, predicted by the equivalent circuit, eq. (9), for the thermal motion power spectrum associated with internal modes of a mass which has frequency independent internal damping and is suspended by a loop of wire which has a Q proportional to frequency. The spectrum is normalised such that the thermal motion of the mass alone is equal to 1.

6. Conclusion

The models described above predict that the fundamental level of thermal noise in a suspended mass is not affected by the degradation of the measured Q caused by resonances in the suspension wires. The form of the thermal noise spikes which are produced by such resonances depends on how the Q of the wire varies as a function of frequency. The overall situation for a test mass in a laser interferometric gravitational wave detector is more complicated, since thermal energy in the wire resonances can cause further movement of the ends of the bar through their effect on motion of the centre of mass. Similarly, thermal energy in the pendulum mode of the suspension can also produce movement of the ends of the bar. The total thermal noise will be a summation of all these effects.

Acknowledgement

We wish to thank our colleagues in the Gravitational Waves Group for their interest in this work which was supported by an SERC research grant and the University of Glasgow. J.E.L. is in receipt of an SERC studentship.

References

[1] J. Hough, B.J. Meers, G.P. Newton, N.A. Robertson, H. Ward, B.F. Schutz, I.F. Corbett and R.W.P. Drever, Vistas Astron. 30 (1987) 109;
J. Hough et al., Proposal for a joint German–British Interferometric Gravitational wave detector, Max-Planck-Institut für Quantenoptik/University of Glasgow Report, MPQ 147 GWD/137/JH(89).
[2] W. Winkler, K. Danzmann, T.M. Niebauer, A. Rudiger and R. Schilling, Phys. Rev. A 44 (1991) 7022.
[3] V.B. Braginsky, V.P. Mitrofanov and V.I. Panov, Systems with small dissipation (Univ. of Chicago Press, Chicago, 1985) pp. 26–29.
[4] P.F. Michelson, Stanford University, Private communication (1992).
[5] J.E. Logan, N.A. Robertson, J. Hough and P.J. Veitch, Phys. Lett. A 161 (1991) 101.
[6] B.I. Bleaney and B. Bleaney, Electricity and magnetism (Oxford Univ. Press, Oxford, 1959) pp. 279–293.
[7] H.J. Pain, The physics of vibrations and waves, 3rd Ed. (Wiley, New York, 1983) pp. 109–110.
[8] The MathWorks Inc. Natick, MA 01760, USA.
[9] F.R. Connor, Noise (Arnold, London, 1973) p. 39.
[10] P.R. Saulson, Phys. Rev. D 42 (1990) 2437.

References

Abramovici, 1990

A. Abramovici, "Aspect Ratio and Internal Thermal Noise in Test Masses", unpublished report.

Alers and Thompson, 1961

G.A. Alers and D.O. Thompson, "Dislocation Contributions to the Modulus and Damping in Copper at Megacycle Frequencies", **32** (1961) 283.

Allen, 1988

B. Allen, "Stochastic Gravity - Wave Background in Inflationary - Universe Models", Physical review D, **37** (1988) 2078.

Amaldi et al, 1977

E. Amaldi, C. Cosmelli, U. Giovanardi, I. Modena, G.V. Pallottino and G. Pizzella, "Measurements of the Merit Factor Q of an Aluminium Gravitational-Wave Antenna between 4.2 and 1.1 K", Il Nuovo Cimento, **41B** (1977) 327.

American Society for Metals, 1984

"American Society for Metals Reference Book", 2nd edition (American Society for Metals Publications, Ohio 1984).

Anderson et al, 1990

S.B. Anderson, P.W. Gorham, S.R. Kulkarni, T.A. Prince and A. Wolszczan, "Discovery of Two Radio Pulsars in The Global Cluster M15", Nature **346** (1990) 42.

Astone et al, 1993

P. Astone, M. Bassan, P. Bonifazi, P. Carelli, M.G. Castellano, G. Cavallari, E. Coccia, C. Cosmelli, V. Fafone, S. Frasca, E. Majorana, I. Modena,

G.V. Pallottino, G. Pizzella, P. Rapagnani, F. Ricci and M. Visco, "Long-term Operation of the Rome "Explorer" Cryogenic Gravitational Wave Detector", Physical Review D, **12** (1993) 5.

Bagdasarov et al, 1977

Kh.S. Bagdasarov, V.B. Braginsky, V.P. Mitrofanov and V.S. Shian, "A High Q Mechanical Resonator Built from a Single Sapphire Crystal", Vestnik Moskovskovo Universiteta, Seria Fizika Astronomia, **18** (1977) 98 (in Russian). The result is also quoted by V.B. Braginsky, V.P. Mitrofanov and V.I. Panov in "Systems with Small Dissipation" (The University of Chicago Press, Chicago 1985), p30.

Baur and Benoit, 1987

J. Baur and W. Benoit, "Study of the Dislocation Contribution to the Internal Friction Background of Gold", Journal of Applied Physics, **61** (1987) 2463.

Blair et al, 1990

D.G. Blair, R.J. Sandeman and J. Collet "Australia International Gravitational Research Centre" (1990).

Blair, 1991

"The Detection of Gravitational Waves" edited by D.G. Blair (Cambridge University Press, Cambridge 1991).

Bleaney and Bleaney, 1959

B.I. Bleaney and B. Bleaney, "Electricity and Magnetism" (Oxford University Press, Oxford 1959).

Braginsky et al, 1985

V.B. Braginsky, V.P. Mitrofanov and V.I. Panov, "Systems with Small Dissipation" (The University of Chicago Press, Chicago 1985).

Brillet et al, 1990

A. Brillet, C.N. Man and D. Ivanov, "An Optical Method for Measuring Virgo

Mirror' Resonance Frequencies and Q - Factor", Virgo report 10.2*.01a (unpublished).

Brillet, 1992

A. Brillet, Universite de Paris-Sud, Centre d'Orsay, private communication, 1992.

British Nuclear Fuels

"REFEL Silicon Carbide Data Sheet", British Nuclear Fuels, Cheshire.

Cadez and Abramovici, 1988

A. Cadez and A. Abramovici, "Measuring High Mechanical Quality Factors of Bodies Made of Bare Insulating Materials", Journal of Physics E: Scientific Instruments, **21** (1988) 453.

Callen and Welton, 1951

H.B. Callen and T.A. Welton, "Irreversibility and Generalized Noise", Physical Review, **83** (1951) 34.

Callen and Greene, 1952

H.B. Callen and R.F. Greene, "On a Theorem of Irreversible Thermodynamics", Physical Review, **86** (1952) 702.

Caves, 1981

C.M. Caves, "Quantum-Mechanical Noise in an Interferometer", Physical Review D, **23** (1981) 1693.

Caves, 1982

C.M. Caves, "Quantum Limits on Noise in Linear Amplifiers", Physical Review D, **26** (1982) 1817.

Chree, 1886

C. Chree, "Longitudinal Vibrations of a Circular Bar", Quarterly Journal of Mathematics, **21** (1886) 287.

Coherent Associates

Laser Noise Reduction System, Model 307, Coherent Associates, Danbury CT 06810, U.S.A..

Corning

Corning Glass Works, Corning, New York 14830, U.S.A..

Crystal Systems

"HEM Sapphire Data Sheet", Crystal Systems Ltd, Massachusetts, U.S.A..

Dialinas, 1991

M. Dialinas, "Miroirs d'Entrée", Virgo report I.12.A.3 (unpublished).

Drever, 1983

R.W.P. Drever, "Interferometric Detectors for Gravitational Radiation" in "Gravitational Radiation" Proceedings of the Les Houches NATO Advanced Study Institute (1982), edited by T. Piran and N. Derouelle (North Holland Publishing Company, Amsterdam 1983).

Drever et al, 1983

R.W.P. Drever, G.M. Ford, J. Hough, I.M. Kerr, A.J. Munley, J.R. Pugh, N.A. Robertson and H.Ward, "A Gravity-Wave Detector Using Optical Cavity Sensing", Proceedings of the Ninth International Conference on General Relativity and Gravitation (Jena, 1980) edited by E. Schmutzer (VEB Deutscher Verlag der Wissenschaften, Berlin 1983).

Duffin 1980

W.J. Duffin, "Electricity and Magnetism", 3rd edition (McGraw-Hill Book Company Ltd, London 1980).

Edelstein, 1978

W.A. Edelstein, J. Hough, J.R. Pugh and W. Martin, "Limits to the Measurement of Displacement in an Interferometric Gravitational Radiation Detector", Journal of Physics E: Scientific Instruments, **11** (1978) 710.

Einstein, 1916

A. Einstein, "Die Grundlage der Allgemeinen Relativitätstheorie", Annalen der Physik, **49** (1916) 769.

Ferreirinho, 1991

J. Ferreirinho, "Internal Friction in High Q Materials" in "The Detection of Gravitational Waves" edited by D.G. Blair (Cambridge University Press, Cambridge 1991).

Forward, 1978

R.L. Forward, "Wideband Laser-Interferometer Gravitational-Radiation Experiment", Physical Review D, **17** (1978) 379.

French, 1986

A.P. French, "Vibrations and Waves" (Van Nostrand Reinhold Co. Ltd., Wokingham 1986).

Friedel, 1964

J. Friedel, "Dislocations" (Pergamon Press, Oxford 1964).

Giazotto et al, 1989

A. Giazotto, A. Brillet, L. Milano, P. Tourrenc, L. Pinto, T. Damour, F. Fuligni, L.E. Holloway et al, "The Virgo Project" (1989).

Gladwell and Vijay, 1975

G.M.L. Gladwell and D.K. Vijay, "Natural Frequencies of Free Finite-length Circular Cylinders", Journal of Sound and Vibration, **42** (1975) 387.

Granato and Lücke, 1956

A. Granato and K. Lücke, "Theory of Mechanical Damping due to Dislocations", Journal of Applied Physics, **27** (1956) 583.

Gray, 1972

"American Institute of Physics Handbook", 3rd edition, edited by D.E. Gray

(McGraw-Hill Book Company, New York 1972).

Hecht, 1987

E. Hecht, "Optics", 2nd edition (Addison-Wesley Publishing Company, Massachusetts, 1987).

Heraeus

"Fused Quartz and Fused Silica Data Sheet", Heraues Silica and Metals Ltd., Surrey.

Hikata et al 1970

A. Hikata, R.A. Johnson and C. Elbaum, "Interactions of Dislocations with Electrons and with Phonons", Physical Review Letters, **24** (1970) 215.

Hough et al, 1897

J. Hough, B.J. Meers, G.P. Newton, N.A. Robertson, H. Ward, B.F. Schutz, I.F. Corbett and R.W.P. Drever, "Gravitational Wave Astronomy - Potential and Possible Realisation", Vistas in Astronomy, **30** (1987) 109.

Hough et al, 1989

J. Hough, H. Walther, B.F. Schutz, J. Ehlers, H. Welling, I.F. Corbett, V. Kose et al, "Proposal for a Joint German-British Interferometric Gravitational Wave Detector", Max-Planck-Institut für Quantenoptik Report 147 and GWD/137/JH(89) (1989).

Hull, 1975

D. Hull, "Introduction to Dislocations", 2nd edition (Pergamon Press, Oxford 1975).

Johnson, 1928

J.B. Jonhnson, "Thermal Agitation of Electricity in Conductors", Physical Review, **32** (1928) 97.

Kaye and Laby, 1986

"Tables of Physical and Chemical Constants", 15th edition, edited by G.W.C. Kaye and T.H. Laby (Longman Group Ltd., London 1986).

Kimball and Lovell, 1927

A.L. Kimball and D.E. Lovell, "Internal Friction in Solids", Physical Review, **30** (1927) 948.

Koehler, 1952

J.S. Koehler, "The Influence of Dislocations and Impurities on the Damping and the Elastic Constants of Metal Single Crystals" in "Imperfections in Nearly Perfect Crystals" edited by W. Schockley (John Wiley and Sons Inc., New York 1952).

Kuske and Robertson, 1974

A. Kuske and G. Robertson, "Photoelastic Stress Analysis" (John Wiley and Sons, London 1974).

Logan et al, 1991

J.E. Logan, N.A. Robertson, J. Hough and P.J. Veitch, "An Investigation of Coupled Resonances in Materials Suitable for Test Masses in Gravitational Wave Detectors", Physics Letters A, **161** (1991) 101.

Logan et al, 1992

J.E. Logan, N.A. Robertson and J. Hough, "An Investigation of Limitations to Quality Factor Measurements of Suspended Masses Due to Resonances in the Suspension Wires", Physics Letters A, **170** (1992) 352.

Longhurst, 1973

R.S. Longhurst, "Geometrical and Physical Optics", 3rd edtion (Longman Group Ltd, 1973)

Lorrain and Corson, 1970

P. Lorrain and D. Corson, "Electromagnetic Fields and Waves", 2nd edition (W.H. Freeman and Company, New York 1970).

Martin, 1978

W. Martin, "Experiments and Techniques for the Detection of Gravitational and Pulsed Electromagnetic Radiation from Astrophysical Sources", PhD Thesis, University of Glasgow, 1978.

Mason and Wher, 1970

W.P. Mason and J. Wher, "Internal Friction and Ultrasonic Yield Stress of the Alloy 90Ti6Al4V", Journal of Physics and Chemistry of Solids, **31** (1970) 1925.

Mason, 1971

W.P. Mason, "Internal Friction at Low Frequencies due to Dislocations: Applications to Metals and Rock Mechanics", in "Physical Acoustics: Principles and Methods" Vol. VIII edited by W.P. Mason and R.N. Thurston (Academic Press, New York 1971).

Mathematica, Wolfram Research, Inc.

Mathematica, Wolfram Research, Inc, Champaign, Illinois 61820-7273, U.S.A..

Matlab, The MathsWork Inc.

Matlab, The MathWorks Inc, Natick, Massachusetts 01760, U.S.A..

McCourt, 1976

J. McCourt, "Searches for Gravitational and Electromagnetic Waves from Extra-terrestrial Sources", MSc Thesis, University of Glasgow, 1976.

McGuigan et al, 1978

D.F. McGuigan, C.C. Lam, R.Q. Gram, A.W. Hoffman and D.H.Douglass, "Measurements of the Mechanical Q of Single-Crystal Silicon at Low Temperatures", Journal of Low Temperature Physics, **30** (1978) 621.

McMahon, 1964

G.W. McMahon, "Experimental Study of the Vibrations of Solid, Isotropic, Elastic Cylinders", Journal of the Acoustical Society of America, **36** (1964) 85.

Meegan et al, 1992

C.A. Meegan, G.J. Fishman, R.B. Wilson, W.S. Paciesas, G.N. Pendleton, J.M. Horack, M.N. Brock and C. Kouveliotou, "Spatial Distribution of γ-ray Bursts Observed by BATSE", Nature, **355** (1992) 143

Meers, 1988

B.J. Meers, "Recycling in Laser-interferometric Gravitational Wave Detectors", Physical Review D, **38** (1988) 2317.

Michelson, 1992

P.F. Michelson, Stanford University, Private communication, 1992.

Misner et al, 1973

C.W. Misner, K.S. Thorne and J.A. Archibald, "Gravitation" (W.H. Freeman and Company, San Francisco 1973).

Mitrofanov and Frontov, 1974

V.P. Mitrofanov and V.N. Frontov in "Systems with Small Dissipation", V.B. Braginsky, V.P. Mitrovanov and V.I, Panov (The University of Chicago Press, Chicago 1985), p 18.

Mochkovitch et al, 1993

R. Mochovitch, M. Hernanz, J. Isern and X. Martin, "Gamma-ray Bursts as Collimated Jets from Neutron star / Black Hole Mergers", Nature, **361** (1993) 236.

Nowick and Berry, 1972

A.S. Nowick and B.S. Berry, "Anelastic Relaxation in Crystalline Solids" (Academic Press, New York 1972).

Nyquist, 1928

H. Nyquist, "Thermal Agitation of Electric Charge In Conductors", Physical Review, **32** (1928) 110.

Paik, 1974

H.J. Paik, "Analysis and Development of a Very Sensitive Low Temperature Gravitational Radiation Detector", PhD Thesis, Stanford University, 1974.

Pain, 1983

H.J. Pain, "The Physics of Vibrations and Waves", 3rd edition (John Wiley and Sons Ltd., Chichester 1983).

Pandharipande et al, 1976

V.R. Pandharipande, D. Pines and R.A. Smith, "Neutron Star Structure: Theory Observation and Speculation", The Astrophysical Journal, **208** (1976) 550.

Pochhammer, 1876

L. Pochhammer, "Beitrag zur Theorie der Biegung des Kreiscylinders", Journal für die Reine und Angewandte Mathematik, Crelle - Borchardt, **81** (1876) 324. An account of this treatment is given by e.g. H. Kolsky in "Stress Waves in Solids" (Dover Publications Inc., New York 1963), pp. 54 - 65.

Reed-Hill, 1973

"Physical Metallurgy Principles", 2nd edition, R.E. Reed-Hill (D. Van Nostrand Company, New York 1973).

Robertson, 1991

N.A. Robertson, "Vibration Isolation for the Test Masses in Interferometric Gravitational Wave Detectors" in "The Detection of Gravitational Waves" edited by D.G. Blair (Cambridge University Press, Cambridge 1991).

Routbort and Sack, 1966

J.L. Routbort and H.S. Sack, "Background Internal Friction of Some Pure Metals at Low Frequencies", Journal of Applied Physics, **37** (1966) 4803.

Saulson, 1990

P.R. Saulson, "Thermal Noise in Mechanical Experiments", Physical Review D, **42** (1990) 2437.

Schockley, 1952

W. Shockley, "Solid State Physics in Electronics and Metallurgy", Transactions of the American Mining and Metallurgical Engineers, **194** (1952) 829.

Schutz, 1986

B.F. Schutz, "Determining the Hubble Constant from Gravitational Wave Observations", Nature, **323** (1986) 310.

Schutz, 1989a

B.F. Shutz, "Sources of Gravitational Radiation" in "Gravitational Wave Data Analysis" Proceedings of the NATO Advanced Research Workshop on Gravitational Wave Data Analysis, Cardiff 1987, edited by B.F. Schutz (Kluwer Academic Publishers, Dordrecht 1989).

Schutz, 1989b

B.F. Schutz, "Gravitational Wave Sources and their Detectability", Classical and Quantum Gravity, **6** (1989) 1761.

Shoemaker, 1987

D.H. Shoemaker, "Contributions à l'étude de la Détection interférométrique des Ondes de Gravitation", PhD Thesis, Universite de Paris-Sud, Centre d'Orsay, 1987.

Shoemaker et al, 1988

D. Shoemaker, R. Schilling, L. Schnupp, W. Winkler, K. Maischberger and A. Rüdiger, "Noise Behavior of the Garching 30-meter Prototype Gravitational-Wave Detector", Physical Review D, **38** (1988) 423.

Strain, 1990

K.A. Strain, "Techniques in Laser Interferometery for the Detection of Gravitational Radiation", PhD Thesis, University of Glasgow, 1990

Strain and Meers, 1990

K.A. Strain and B.J. Meers, "Experimental Demonstration of Dual Recycling for

Interferometric Gravitational-Wave Detectors", Physical Review Letters, **66** (1990) 1391.

Suzuki, 1983

T. Suzuki, "Practical Cryogenic Environment for Gravitational Radiational Detector with Parametric Transducer", Proceedings of the Third Marcel Grossmann Meeting on General Relativity, edited by H. Ning (Science Press and North Holland Publishing Company, Amsterdam 1983).

Taylor and Weisberg, 1982

J.H. Taylor and J.M. Weisberg, "A New Test of General Relativity: Gravitational Radiation and the Binary Pulsar PSR1913 + 16", The Astrophysical Journal, **253** (1982) 908.

Terman, 1943

F.E. Terman, "Radio Engineers' Handbook" (McGraw-Hill Book Company Inc., New York 1943).

Thorne et al, 1979

K.S. Thorne, C.M. Caves, V.D. Sandberg, M. Zimmerman, R.W.P. Drever, "The Quantum Limit for Gravitational Wave Detectors and Methods of Circumventing It" in "Sources of Gravitational Radiation" edited by L.M. Smarr (Cambridge University Press, Cambridge 1979).

Thorne, 1987

K.S. Thorne, "Gravitational Radiation" in "300 Years of Gravitation" edited by S.W. Hawking and W. Israel (Cambridge University Press, Cambridge 1987).

Vachaspati and Vilenkin, 1985

T. Vachaspati and A. Vilenkin, "Gravitational Radiation from Cosmic Strings", Physics Review D, **31** (1985) 3052.

Van Bueren, 1960

H.G. Van Bueren, "Imperfections in Crystals" (North-Holland Publishing

Company, Amsterdam 1960).

Vogt et al, 1989

R.E. Vogt, R.W.P. Drever, K.S. Thorne, F.J. Raab and R. Weiss, "A Laser Interferometer Gravitational-Wave Observatory (LIGO)" (1989).

VPI 9000, Ometron Limited

Spate / VPI 9000 Series, Ometron Limited, London.

Wagoner, 1984

R.V. Wagoner, "Gravitational Radiation from Accreting Neutron Stars", The Astrophysical Journal, **278** (1984) 345.

Weber, 1960

J. Weber, "Detection and Generation of Gravitational Waves", Physical Review, **117** (1960) 306.

Weiss, 1972

R. Weiss, "Electromagnetically Coupled Broadband Gravitational Antenna", Massachusetts Institute of Technology Quarterly Progress Report, **105** (1972) 54.

Winkler, 1991

W. Winkler, "A Michelson Interferometer Using Delay Lines" in "The Detection of Gravitational Waves" edited by D.G. Blair (Cambridge University Press, Cambridge 1991).

Winkler et al, 1991

W. Winkler, K. Danzmann, T.M. Niebauer, A. Rudiger and R. Schilling, "Heating by Optical Absorption and the Performance of Interferometric Gravitational Wave Detectors", Physical Review A, **44** (1991) 7022.

Winkler, 1993

W. Winkler, paper in preparation, 1993.

Wolszczan, 1991

A. Wolszczan, "A Nearby 37.9ms Radio Pulsar in a Relativistic Binary System", Nature, **350** (1991) 688.

Zener, 1948

C. Zener, "Elasticity and Anelasticity of Metals" (The University of Chicago Press, Chicago 1948).

Zimmermann, 1978

M. Zimmermann, "Revised Estimate of Gravitational Radiation from Crab and Vela Pulsars", Nature, **271** (1978) 524.

Separate reference lists are included in appendices D and E.